Electric Field Mediated Instabilities for On-Demand Microfluidic Mixing and Separation

A thesis submitted
in partial fulfillment of the requirements
for the degree of

Doctor of Philosophy

by

Satarupa Dutta

DEPARTMENT OF CHEMICAL ENGINEERING
INDIAN INSTITUTE OF TECHNOLOGY GUWAHATI
March 2021

CERTIFICATE

It is certified that the work contained in the thesis entitled **"Electric Field Mediated Instabilities for On-Demand Microfluidic Mixing and Separation"**, by Satarupa Dutta (Roll no. 156107006) has been carried out under our supervision and that this work has not been submitted elsewhere for a Ph.D degree.

Thesis Supervisors

Dr. Dipankar Bandyopadhyay
Professor
Department of Chemical Engineering
Indian Institute of Technology Guwahati

Dr. Partho Sarathi Gooh Pattader
Assistant Professor
Department of Chemical Engineering
Indian Institute of Technology Guwahati

September 2021

Dedicated to my parents

Acknowledgements

The entire tenure of my doctoral study has been an enriching experience filled with opportunities, obstacles and a cornucopia of invaluable lessons. As I now step into the end of my beginning as a researcher, I express my heartfelt gratitude to the people who have inspired and supported me in my journey till now. First and foremost, I express my sincere gratitude to my thesis supervisor Dr. Dipankar Bandyopadhyay for his support, suggestions and criticisms which help me to better myself each day. I thank him for his unwavering faith in me and for being my guiding light all throughout. I am also immensely thankful to my thesis supervisor Dr. Partho Sarathi Gooh Pattader for his helpful suggestions and constant support. I am also grateful to the members of my doctoral committee, Dr. Tapas Kumar Mandal, Dr. Siddhartha Sankar Ghosh and Dr. Nageshwara Rao Peela for their meticulous evaluation of my thesis and their insightful comments. I also express my gratitude to all the faculty and staff members of Department of Chemical Engineering and Centre for Nanotechnology, IIT Guwahati. The financial support from DST-SERB, MHRD, and MeitY of Government of India are also gratefully acknowledged.

I am immensely grateful to all my colleagues and lab-mates for creating a very congenial atmosphere in the workplace. I will always cherish the stimulating discussions and the friendly banters during our tea breaks. I am extremely grateful to my friends Mahasweta, Mousumi, Mitradip and Snigdha for their constant support and encouragement. I am thankful to Joydip for being my best friend, colleague and for always raising the bar.

I thank my parents for placing their utmost trust in me and for being my biggest cheerleaders. I also thank my brother and sister for their love and support. Last but not the least, I thank my niece Ritvika and little nephew Krishnil for bringing me immense joy and laughter.

Satarupa Dutta

Synopsis

Chapter 1: Introduction

We live in an age where one of the major aims of technological progress has been rapid miniaturization. The saying that "big things come in small packages", is literally evident in almost all routine as well as high-tech gadgets. From tests being conducted in labs, we have moved forward to tests being conducted on chips. In this regard, the fortes of micro/nano science are routinely exploited for a plurality of microuidic applications such as clinical diagnostics, cell cultures and vesicle formation, immuno-assays, micro-reactions, separation using electro-coalescence, DNA analysis, environmental monitoring, sensing, amongst a lot. Microfluidics deals with the control and handling of very low volumes of fluids in devices of the dimensions of a few microns. In particular, this field has garnered significant scientific curiosity owing to some distinct advantages over their macroscopic counterparts such as, (i) usage and control of lesser amounts of samples, (ii) availability of higher surface to volume ratio, (iii) high performance due to process intensication, and (iv) superior control over the process parameters. Assembly of different microfluidic devices on a single chip create avenues for 'μTAS' or 'lab-on-a-chip' for a host of biological and chemical assays.

The conventional pressure-driven microfluidic flows are inherently characterized by low velocities owing to the dominance of the viscous force over the inertial one. The cutting-edge microscale applications demand improvement of the rate limiting diffusive transports for proficient mixing, dissolution, reaction, separation, cooling, or heating. In this regard, the innovations associated with the groovy or twisted channels, multi-lamination of flow paths, serpentine channels, or viscous fingering of fluids disclose various passive pathways to enhance momentum transport. In comparison, the active mode of enhanced transport requires the support from the external fields such as the applications of thermal or acoustic waves, magnetic or electric fields or electro-kinetic forces. However, the enhancement of momentum, heat and mass diffusivities with the help of in situ disturbances inside microfluidic devices remains one of the long-standing challenges of fluid dynamical research.

Apart from the single or multicomponent channel flows, bubble/droplet/particle laden multi-phase flows are essential platforms which can be harnessed for a variety of microfluidic applications.

Droplet or bubble laden ternary systems are frequently encountered in a variety of industrial and laboratory processes such as emulsification, liquid-liquid extraction, electro-coalescence, encapsulation and coating, drug delivery etc. In such processes, the migration of droplets from liquid to the other, are often desirable. Microparticle laden flows are also very common in a plethora of biological and industrial processes, some of which are - flow of blood corpuscles in blood serum, movement of bacterial colonies, fluorescence-activated cell sorting, separation of nanoparticles, suspension polymerizations and fluidized bed reactions. It is often desirable to apply external fields to effectively manoeuvre various particle motions inside microfluidic devices.

Thus, it is clear under the light of the above discussion that, an effective external stimulus is instrumental in achieving optimum functionality of a microfluidic process. In this dissertation, externally applied electric field has been harnessed to study the salient features of some selected microfluidic phenomena with the aid of micro and mesoscale model set-ups. Experimental investigations are validated using suitable numerical and analytical models to gain in-depth knowledge about the physics associated with them. The point wise objective of the present work are as follows,

- Investigations of electric field mediated instabilities in viscosity stratified miscible microflows for applications in mixing.
- Study of the genesis of electric field mediated micro-particle assemblage in a dielectric fluid.
- Investigations of electric field mediated modes of active droplet transport across a liquid-liquid interface.
- Investigations of mechanisms of contact during electric field mediated drop coalescence/non-coalescence.

The details of the thesis objectives are provided in the following four chapters. A brief summary of the dissertation along with the prospective scope of the investigated phenomena are provided at the end of the fifth chapter.

Chapter 2: Electric Field Mediated von Kármán Vortices in Stratified Microflows: Transition from Linear Instabilities to Coherent Mixing

Application of an electric field across the pressure-driven stratified flow of a pair of miscible fluids inside a microchannel manifests interesting electrohydrodynamic (EHD) instabilities. Experiments uncover distinctive instability regimes with an increase in electric field Rayleigh number (Ra^{ψ}) - linear-onset regime, time-periodic non-linear regime analogous to von Kármán vortex street at the downstream, and a regime with coherent flow patterns. The experiments also reveal that such linear and nonlinear instabilities can be stimulated non-invasively in a microchannel to mix or de-mix fluids simply by turning the electric field on or off, indicating the suitability of the process for on-demand micromixing. The characteristics of these instabilities have been theoretically investigated with the help of an Orr-Sommerfeld framework, which discloses the possibility of five distinctive finite-wavenumber modes for the instability. The EHD stresses originating due to the application of electric field stimulate a pair of shorter-wavelength electric field modes beyond a critical value of Ra^{ψ}. Increase in the levels of charge injection and EHD stresses lower the critical Ra^{ψ} of these modes. The relatively longer wavelength viscous-mode is found to appear when the viscosity stratification between the fluid layers is high. Beyond a threshold Schmidt number (Sc), a diffusive-mode is also found to appear near the mixed interfacial region. A thinner interface between the fluids at a higher Sc helps this mode to behave as the interfacial mode of immiscible fluids. Constrast of ionic mobility in the fluids leads to the appearance of the K-mode of instability at much shorter wavelengths. The reported phenomena can be of significance in the domains of microscale mixing, pumping, heat-exchange, mass transfer, and reaction engineering.

Chapter 3: Genesis of Electric Field assisted Microparticle Assemblage in a Dielectric Fluid

This chapter deals with the oscillatory motions of charged particles inside a liquid under the influence of an electric field emulating the field-induced particle-laden fluid flows. The properties of the surrounding fluid are found to play key roles in the kinetics of such a particle aggregation process. While the weakly conducting or insulating liquids promote high frequency oscillations of charged particles followed by a quick assemblage, the viscosity and relative permittivity of the liquid play sig-

nificant roles in modulating the time scales. In fact, the origin of such motions in a multi-particle system is very similar to a system with single charged particle wherein the particle gathers charge from one of the electrodes before moving towards the other of opposite polarity. Interestingly, in the multi-particle system, an unprecedented charge-reversal is observed wherein a charged particle reverses its direction of motion after colliding with another particle of opposite polarity. Experiments together with simulations further reveal that, while the equal sized particles undergo an electric field driven 'elastic' collision and show synchronized motions with nearly similar speeds of approach and separation, the motions of unequal sized particles are rather non-uniform after undergoing an 'inelastic' collision. Importantly, the simulations with two-particle systems uncover the presence of counter-rotating-vortices surrounding the charged particles. The results reported not only usher the genesis of the chain like assemblage in the multi-particle systems but also open up the possibility of generation of on-demand power-law liquid properties through 'chaining' or 'layering' of the charged particles.

Chapter 4: Electric Field Mediated Modes of Active Droplet Transport across a Deformable Interface

We explore the migrations of a droplet across the interface of a pair of immiscible liquids under electric field. The electrohydrodynamic stress conditionally deforms the droplet, while the migration of the droplet deforms, stretches, and ruptures the biphasic carrier-target interface. The dynamics of the interfaces in such a ternary system have been analysed through high-speed imaging and simulations. Experiments together with simulations reveal the presence of the rupture and tailing modes of droplet transport across the interface. In the rupture mode, below a critical electric field Weber number (We_{E}), a quasi-steady rupture and hole-growth of the carrier film is observed, wherein the hole-radius r_{h} at the interface follow a viscosity dominated kinetics of, $r_{\mathrm{h}} \sim t$. In contrast, beyond this critical We_{E}, a fast moving prolate shaped droplet induce an inertia dominated hole-growth kinetics following, $r_{\mathrm{h}} \sim t^{0.5}$. Film drainage occurs in two stages, with the rate diminishing significantly after the film thickness nears 0.3 times the droplet radius. An analytical model, reveals velocity profiles resembling the Couette flow within the draining film during the various stages of carrier-film drainage. In the tailing mode, the droplet entrains carrier liquid approximately equal to its own volume into the target

liquid, wherein the length of tail can be as high as eight times the drop radius. The interfacial-tensions, density and viscosity of the liquids of the ternary system are the key parameters influencing the dynamics of both the modes of migrations. The phenomena may find applications in liquid-liquid extraction, micro-reactions, ultra-low tensiometry, among others.

Chapter 5: Mechanisms of Electric Field Mediated Drop Coalescence or Non-coalescence

Experimental investigations with high-speed imaging reveal asymmetric interfacial deformations of the approaching uneven sized oppositely charged drops during field induced coalescence and separation. Experiments suggest diverse novel mechanism of Taylor cone formation during the drop coalescence and separation, which are very much specific to the joining of the charged droplets of asymmetric size. Three dimensional simulations and an analytical model corroborate and confirm the finer details of such a phenomenon unveiling the diverse mechanisms of field induced drop coalescence and separation.

Chapter 6: Conclusions and Future Scope of Work

The thesis unravels some of the salient features associated with the electric field triggered responses in a host of liquid-liquid and solid-liquid systems. A combined theoretical and experimental study in the second chapter uncovers the salient features of electric field induced instabilities associated with the viscosity stratified flow of a pair of miscible fluids inside microchannels. Experiments uncover four distinct regimes of instabilities. The linear regime I corresponds to the onset of instability waves beyond a critical field intensity. With increase in the applied voltage, the regime II marks the initiation of the nonlinear regime with the appearance of time-periodic vortices in the downstream. On further increasing the electric field a regime III appears where smaller vortices are generated at higher frequencies leading to intermixing of the flow patterns. At still higher field intensities, the flow becomes unstructured in regime IV leading to total mixing of the two fluids. CFD simulations also predict the appearance of vortices which are qualitatively similar to the experimental observations of regime II and III. A general linear stability analysis reveals that the EHD uncovers the presence of five distinctive instability modes, which are

identified as electric field mode I (E-I), electric field mode II (E-II), viscous mode (V), diffusive mode (D) and the K-mode. From the perspective of mixing, among all the regimes, the chaotic regime IV with coherent flow patterns is found to be the most suitable one. The mixing efficiency is found to increase with the increase in the strength of the applied field and the number of electrodes inserted across the channel.

The third chapter explores the pathways to the self-organization of a collection of microparticles inside a dielectric fluid under the influence of an external electric field. In the multi-particle system, the particles also gather charge during the collisions in between themselves. The experiments together with the numerical simulations for such systems uncover that the time of contact and charge reversal increases with reduction in the applied field intensity or the surface conductivity of the particles. The equal sized particles undergo electric field driven 'elastic' collisions, while the collisions between unequal particles are rather 'inelastic'. The equal sized particles exhibit a synchronized oscillatory pattern with similar speeds of approach and separation. Unequal sized particles on the other hand show asymmetric trajectories, in such a manner that the speed of the smaller particle increases marginally after contact, while the bigger particle demonstrates a rather sluggish behaviour after contact. Experiments with unequal sized particles, also reveal that after contact between the particles, the union of particles moves in the direction of the bigger particle briefly, before the charge reversal and separation of the particles take place. The non-slipping particle-liquid interface ensure the generation of symmetric vortices around equal particles and asymmetric vortices around unequal particles.

In the fourth chapter the dynamics of an electric field induced droplet migration in an immiscible carrier-target liquid interface have been explored. Experiments and CFD simulations reveal that the electric field induced droplet migrations from a carrier to a target liquid can be broadly divided into the rupture and tailing modes. An undeformed droplet at a low electric field cause a viscosity dominated quasi-static carrier film drainage and rupture, with the hole radius growing as $r_h \sim t$. At a higher electric field, a deformed prolate shaped droplet impinges on the interface at a much higher speed to stimulate an inertia dominated carrier film rupture and drainage with relation $r_h \sim t^{0.5}$. In the rupture mode, the drainage of the film proceeds in two distinct stages. The rate of film-drainage is faster until the film thickness reduces to $\sim$0.3 times the drop radius, after which there is a significant reduction in the rate of film drainage. Analytical model predicts nearly parabolic velocity profiles

for thicker films, which eventually becomes almost linear with decrease in film thickness, resembling that of Couette flow. The tailing mode is observed for very low values of interfacial tensions between the carrier and target phases. Both experiments and simulations predict the maximum volume of the carrier liquid entrained by the droplet to be approximately equal to the volume of the droplet itself. The maximum occurs at a distance of approximately 8 times the droplet radius, from the undisturbed interface.

The fifth chapter discloses the pre-contact and contact dynamics of two uneven and opposingly charged droplets during their coalescence and separation under the electric field. Experiments reveal asymmetric interfacial deformations and subsequent nonlinear effects of Taylor cone formation with decreasing distance between the charged droplets. Simulations in conjunction with GLSA corroborate such experimental observations, which happen before the final contact between the droplets. Experiments and simulations together disclose the formation of asymmetric bridges from the Taylor cone on the smaller droplet, which eventually extend into the bigger droplet forming a liquid bridge between the droplets.

The phenomena studied in the present dissertation open up the avenues for a number of prospective fundamental research and applications. Investigations of electric field induced instabilities in miscible flows uncover pathways to integrate the influence of an external electrostatic field with a microfluidic device in order to remotely control the mixing of the fluid layers. The phenomenon can be of significance in improving the efficiency of multifarious cutting-edge microfluidic applications which include mixing, pumping, heat exchange, mass transfer and reaction engineering. The electric field induced micro-particle assemblage can be harnessed for a number of futuristic applications such as microfluidic vortex generators or flow control valves, on-demand catalyst beds for reaction engineering, extraction of solid from liquid and microrheology. The in-depth analysis on the mechanisms of charge transfer, charge reversal between the particles, and the role of the flow patterns in the liquid medium on such phenomena can be a very potent area of future research. The electric field induced migrations of aqueous drops across liquid-liquid interfaces can be harnessed for a variety of applications such as liquid-liquid extraction, separation and purification, micro-reactions, tensiometry. In depth analysis with a wider range of liquids along with the study of secondary electric field effects on the migration of drops can be a lucrative area of research. Investigations of electric field mediated asymmetric contact of drops may be instrumental in realizing more

practical models to accurately map the finer details of the contact phase dynamics of coalescing/non-coalescing drops.

Contents

List of Figures

Chapter 1

Introduction

1.1 Overview

In the recent times, majority of the technological innovations are centred on the 'scaling down' or 'miniaturization' of the end products. With the advancement of science and technology, miniaturization is being witnessed in most of the day-to-day use gadgets as well as the high-end sophisticated equipments. Most of the miniaturized applications in the present era utilize the distinct advantages of diverse micro or nanoscale phenomena such as low sample consumption, low reaction times owing to high surface to volume ratio, and ease of sample control and manipulation [1–4]. Assembly of different microfluidic devices on a single chip create avenues for 'micro total analysis systems (μTAS)' or 'lab-on-chip' applications [5]. These 'μTAS' or 'lab-on-chip' devices serve as hosts to a plethora of microfluidic applications such as clinical diagnostics, point-of-care testing, cell cultures and vesicle formation, immuno-assays, micro-reactions, separation using electro-coalescence, DNA analysis, environmental monitoring and sensing [6–18].

1.1.1 Microfluidic Mixing

Microfluidics deals with the control and handling of very low volumes of fluids in devices of the dimensions of a few microns [3, 19–21]. Thus, the pressure-driven microfluidic flows are inherently characterized by low velocities owing to the dominance of the viscous force over the inertial one, such that the mixing between fluid streams is purely due to diffusion [22–25]. Diffusive mixing being slow is generally characterized by large mixing lengths ($\gg 1$ cm) [22]. Thus, the cutting-edge microscale applications demand improvement of the rate limiting diffusive transports for proficient mixing, dissolution, reaction, separation, cooling, or heating [4, 26]. The mixing of fluid streams inside the microfluidic devices is intrumental for the efficient and time bound operations of a plethora of existing microscale chemical or biological applications [4, 26, 27]. In the macroscopic processes, the diffusion limited large mixing lengths are routinely reduced by the introduction of auxiliary momentum, heat, and mass diffusivities through turbulence. However, the solution is not that simple in the micro-processes because the generation of the pressure drop to achieve a large Reynolds number (Re) becomes challenging due to the large viscous resistance orig-

inating from the confining boundaries. Over the past decade, researchers have put forth many strategies to decrease the mixing length by facilitating convective mixing in microchannels. Passive micromixers with grooved or twisted channels [22,28,29], multilamination techniques involving rearrangement of flow paths [30], serpentine channels [31] and viscous fingering [32] facilitate local rotation of the fluids causing convective mixing. Active mixing inside micro channels have been attempted to achieve via application of acoustic waves [33], magnetohydrodynamic stirring [34] and electro osmosis [35–37]. Electro kinetic instabilities triggered by electrical conductivity stratification between two fluids have by far been the most ventured route to generate active mixing in micro-channels [38–43].

However, in the present scenario, the enhancement of momentum, heat, and mass diffusivities with the help of the *in-situ* turbulence inside the microfluidic devices [39,41,43] remains to be one of the major challenges. In this regard, electric field can serve as an efficient stimulus to promote convective mixing in various microfluidic flows. Prior art suggests that various EHD phenomena can improve the performance of microscale electrowetting [44], rheological devices [45], electrospinning [46], and drug delivery systems [47]. In this direction, one particularly interesting phenomenon is the the electroconvection inside an insulating fluid originating from the ion injections from the electrode [48–53]. In insulating liquids with high values of electrical resistivity, electrical conduction at high electric fields is mainly controlled by creation of charge carriers at the metal-liquid interface. The creation and subsequent injection of charge from the surface of the electrodes takes place due to complex electrochemical reactions at the metal-liquid interface [54,55]. The Coulombic force acting on the injected ions stimulate an auxiliary advection inside the fluid and chaotic advection is observed [56–58]. The Coulomb force driven electro convection phenomena due to ion injection has been harnessed to enhance heat transfer [59,60] and in the construction of EHD ion-drag pumps [61].

In this direction, herein, we attempt to couple the consequence of electrohydrodynamic (EHD) phenomena originating from the ion injections, in a stratified flow of a pair of miscible fluids inside a microchannel to develop laminar, transitional, and turbulent flow regimes. The mentioned stratified pressure-driven flow [62,63] has deliberately been chosen as the experimental and theoretical systems owing to the following distinctive advantages, (i) at the microscale they show a purely laminar flow; (ii) a diffused interface demarcates the high and low viscosity fluids even though they are miscible; (iii) the length scales of diffusive mixing of such flows are

large; and (iv) onset of any convective influence near the interface disturbing the diffusion limited momentum transport can readily be followed.

1.1.2 Particle Laden Micro-flows

Particle laden flows are encountered in a host of natural processes such as motion of dust particles in air, movement of cloud or molten lava, ocean waves near sea shore, propagation of smoke plumes, and the moving sand dunes in desserts [64–66]. The flow of blood corpuscles with the serum in blood vessels [67], movement of bacterial colonies [68] are examples of particle laden biological flows. Some of the industrial processes which host such flows include suspension polymerization [69], separations of nucleic acids [70] and fluidized bed reactors [71]. Particle laden flows are also the predominant components of many important micro-scale phenomena such as flow cytometry [72], fluorescence-activated cell sorting (FACS) [73], zeta-potential analyser [74], separation of nanoparticles [75], self-propelling objects [76], and emulsifiers [77].

In such processes, it is often desirable to manoeuvre the particles for achieving multifarious applications. In this regard, electrical field serves to be a very efficient external stimulus to induce particle motions of sundry types. Electrophoresis of charged particles embedded in electrolytes, under the influence of a uniformly applied electric field, has been harnessed for the measurement of zeta potential [74], DNA separation [70] and purification and separation of nanoparticles [75]. Electrophoretic particle-particle interaction studies reveal that particles with the line of centers perpendicular to the applied field mutually attract each other, whereas particles aligned to the applied field direction experience mutual repulsion [78,79]

Dielectrophoretic motions of uncharged particles under non-uniform electric fields have been utilized for a host of applications such as particle and cell separation, sorting, trapping, formation of cell and particle arrays [80–87], organization of colloidal mixtures and controlling crystallization of colloids [88–90]. Particle chain formation is a remarkable facet of dielectrophoretic particle-particle interactions, wherein the induced dipoles of closely spaced particles interact to eventually align the particles in the direction of the applied field [91–95]. It is established that the nature of such interactive force is attractive and similar particles always align in the direction of the applied field [96–100]. Heterogeneous mixtures of particles with higher and lower polarizabilities than the suspending liquid, however, form chains in the direction per-

pendicular to the applied field [101, 102]. It is noteworthy that chains of dielectric particles are also formed in insulating fluids under uniform electric field [103–105]. This class of fluids commonly referred to as electrorheological (ER) fluids was first discovered by Winslow [103] who demonstrated that the effective viscosity of ER fluids could be varied by varying the applied field.

Contact charging of charged/uncharged particles on metallic electrodes on application of AC/DC (alternative current/direct current) electric fields and the subsequent oscillatory motions between them have been researched by many groups [106–114]. In this phenomenon, an uncharged particle acquires charge from an electrode on contact and undergoes an electrophoretic motion towards the electrode of opposite polarity, where it again transfers charge and moves towards the other electrode. Such oscillatory motion necessitates the suspending fluid to be nearly non-conductive for the particle charge to remain intact during the motion. The theoretical expression for the charge acquired by a conductive particle from an electrode under uniform electric field is given by, $Q_0 = \left(\frac{2\pi^3}{3}\right) \varepsilon_f r_p^2 E_0$ [115–117], where Q_0 is the total charge, ε_f, r_p and E_0 are the liquid permittivity, particle radius and average applied electric field intensity, respectively.

The mechanisms of chain formations in electrophoretic and dielectrophoretic mptions are widely studied. For oscillations through contact charging, although the charging and discharging mechanisms and the subsequent movements of a single particle have been studied extensively in the past, the mechanisms associated with the dynamics of multiple particles remain relatively less explored and understood. The study of the oscillatory motions of a mixture of particles opens up the possibility of exploring the simultaneous charging and discharging between the particles or the chains of the particles. Further, such a system is instrumental to study their interactions with the electrodes as well while undergoing the oscillatory motions between the electrodes. In fact, analysing the physics behind such occurrences can help in the improvement of understanding of the aggregation and segregation of cells or micro/nanoparticles of a suspension in a more comprehensive manner.

1.1.3 Droplet Laden Micro-flows

1.1.3.1 Droplet Laden Ternary Systems

Droplet laden ternary liquid systems are expected to be encountered in a plurality industrial and laboratory processes. Some of the processes include liquid-liquid ex-

traction [118–120], separation process involving electro-coalescence [121,122], microreactors [26,123,124], encapsulation and coating [125], and drug delivery [126]. Migration of a droplet from a carrier liquid to a target liquid may be opted for a variety of applications such as preparation of vesicles [127], cell research [128–130] and fabrication of microreactors. Thus, various active as well as passive routes to effect droplet migrations across liquid-liquid interfaces, have been explored.

One of the most exploited routes of passive droplet transfer is based on driving droplet via inertial forces, with specialized geometric modifications such as, branched channels [131], railed channels [132] and pillars [133]. Several other strategies have been reported for droplet transfer by using non-inertial lift force [134–136], interfacial tension directed method [137], magnetic field [138], surface acoustic waves [139] and laser [140]. While passive methods of droplet transfer involving grooves or pillars are operationally simple and cost-effective, but the fabrication of the channels requires huge precision. The interfacial tension directed droplet transfer offers advantages in applications, where the change in chemical composition of the fluids do not significantly hamper the process [137]. Active methods relying on application of magnetic fields, have only been tested for low interfacial tension fluids. For high interfacial tensions between the carrier and target medium, the requirement of strong magnetic force may create a bottleneck for such techniques. Laser guided techniques are operationally expensive.

The study of the migration dynamics of liquid drops via a liquid-liquid interface is also lucrative from the point of view of fundamental research. The migration dynamics of solid particles [141–153] and bubbles [144,154–166] via liquid-liquid interfaces have been explored extensively in previous studies. The breakthrough of a solid particle past the fluid-fluid interface involves two main regimes, (a) the film drainage and (b) the tailing [167]. In the former, the sphere crosses the interface in a quasi-static manner, with the drainage and subsequent rupture of the film of the carrier liquid ahead of it. In the tailing regime, the particle tows a column of the carrier liquid into the target liquid, with the film ahead of it intact. Though the characteristics of migrations of solid particles and bubbles are widely explored, the dynamics of droplet migration across a liquid-liquid interface have been very less explored and the only known experimental investigation has been reported by Shah *et al.* [168]. In case of droplets, the major focus of most of the reported studies has been on the characteristics of the film drainage and rupture, prior to drop coalescence into a bath of the same liquid [122,159,169–181].

With the above discussed background, this thesis focuses on gaining insights into the relatively less explored dynamics of droplet migrations in immiscible ternary liquid systems. This configuration is particularly interesting because (a) due to the presence of three different liquids, with different densities, viscosities and interfacial tensions, it is anticipated that the drainage and film rupturing characteristics will be different than the coalescence systems and (b) as the droplet breakthroughs the liquid-liquid interface, the tailing regime may unveil new dynamics.

1.1.3.2 Droplet Laden Binary Systems

Drop coalescence/noncoalescence are pertinent to a multitude of processes such as dehydration in petroleum industry [182], ink-jet printing technology [183], electrowetting [184] and chemical and biological essays on lab-on-chip platforms [185]. In this regard, the physics associated with electric field driven drop coalescence or separation has attracted immense research attention, owing to its applicability in a variety of microscale processes. Conventional electro-coalescence studies are focussed at unveiling the dynamics associated with interstitial film drainage and rupture [122] during the motion of the droplets towards each other. One of the major focus of the electric field induced drop non-coalescence studies is the determination of the critical conditions leading to the non-coalescence of drops [186, 187]. The dynamics of the liquid bridge between the droplets are also widely studied [186–191]. After a careful examination of the prior art related to this field, it is observed that all studies in this front are motivated for symmetric mode of contact between the drops. However, in applications, the drops are rarely equal sized. Thus, it can be anticipated that the assumption of symmetric contact may not always hold true. Thus, in this regard, the study of the contact dynamics of unequal sized droplets can lead to the revelation of novel and scientifically relevant information.

1.2 Objectives of the Thesis

In view of the above discussion, it can be inferred that in a plurality of microfluidic processes, an effective external stimulus may be instrumental in achieving an optimum functionality. In this dissertation, we strive to study the effects of externally applied electric field in some selected microfluidic phenomena with the aid of micro and mesoscale model set-ups. Experimental investigations are validated using suitable numerical and analytical models to gain in-depth knowledge about the physics

associated with them. The point wise objective of the present work are as follows,

1. Experimental and theoretical investigations of electric field mediated instabilities in the stratified microflows of two miscible fluids for applications in mixing.

2. Experimental and numerical studies of the characteristics of electric field mediated assemblies of mixtures of micro-particles suspended in an insulating fluid.

3. Experimental and numerical investigations of the different modes of electric field mediated active transport of droplets across a liquid-liquid interface.

4. Experimental and theoretical investigations of the salient features of electric field mediated coalescence/non-coalescence of uneven sized oppositely charged droplets suspended in an insulating medium.

1.3 Layout of the Thesis

The present dissertation is divided into six chapters. The present first chapter details an introduction of the thesis with a brief literature review, the main objectives of the thesis and the layout of the thesis.

In the second chapter, the electric field induced instabilities in stratified microchannel flows is discussed. Application of an electric field across the pressure-driven stratified flow of a pair of miscible fluids inside a microchannel manifests interesting electrohydrodynamic (EHD) instabilities. Experiments uncover distinctive instability regimes with an increase in electric field Rayleigh number (Ra^{ψ}) - linear-onset regime, time-periodic non-linear regime analogous to von Kármán vortex street at the downstream, and a regime with coherent flow patterns. The experiments also reveal that such linear and nonlinear instabilities can be stimulated non-invasively in a microchannel to mix or de-mix fluids simply by turning the electric field on or off, indicating the suitability of the process for on-demand micromixing. The characteristics of these instabilities have been theoretically investigated with the help of an Orr-Sommerfeld framework, which discloses the possibility of five distinctive finite-wavenumber modes for the instability. The EHD stresses originating due to the application of electric field stimulate a pair of shorter-wavelength electric field modes beyond a critical value of Ra^{ψ}. Increase in the levels of charge injection and

EHD stresses lower the critical Ra^{ψ} of these modes. The relatively longer wavelength viscous-mode is found to appear when the viscosity stratification between the fluid layers is high. Beyond a threshold Schmidt number (Sc), a diffusive-mode is also found to appear near the mixed interfacial region. A thinner interface between the fluids at a higher Sc helps this mode to behave as the interfacial mode of immiscible fluids. Constrast of ionic mobility in the fluids leads to the appearance of the K-mode of instability at much shorter wavelengths. The reported phenomena can be of significance in the domains of microscale mixing, pumping, heat-exchange, mass transfer, and reaction engineering..

In the third chapter, oscillatory motions of charged particles inside a liquid medium have been explored under the influence of an electric field emulating the field-induced particle-laden fluid flows. The properties of the surrounding fluid are found to play key roles in the kinetics of such a particle aggregation process. While the weakly conducting or insulating liquids promote high frequency oscillations of charged particles followed by a quick assemblage, the viscosity and relative permittivity of the liquid play significant roles in modulating the time scale. In fact, the origin of such motions in a multi-particle system is very similar to a system with single charged particle wherein the particle gathers charge from one of the electrodes before moving towards the other of opposite polarity. Interestingly, in the multi-particle system, an unprecedented charge-reversal is observed wherein a charged particle reverse its direction of motion after colliding with another particle of opposite polarity. Experiments together with simulations further reveal that, while the equal sized particles undergo an electric field driven 'elastic' collision and show synchronized motions with nearly similar speeds of approach and separation, the motions of unequal sized particles are rather non-uniform after undergoing an 'inelastic' collision. Importantly, the simulations with two-particle system uncover the presence of counter-rotating-vortices surrounding the charged particles. The results reported not only usher the genesis of the chain like assemblage in the multi-particle systems but also open up the possibility of generation of on-demand power-law liquid properties through 'chaining' or 'layering' of the charged particles.

In the fourth chapter, the migration dynamics of a droplet across the interface of a pair of immiscible liquids under electric field have been explored. The electrohydrodynamic stress conditionally deforms the droplet, while the migration of the droplet deforms, stretches, and ruptures the biphasic carrier-target interface. The dynamics of the interfaces in such a ternary system have been analysed through

high-speed imaging and simulations. Experiments together with simulations reveal the presence of the rupture and tailing modes of droplet transport across the interface. In the rupture mode, below a critical electric field Weber number (We_{E}), a quasi-steady rupture and hole-growth of the carrier film is observed, wherein the hole-radius r_{h} at the interface follow a viscosity dominated kinetics of, $r_{\mathrm{h}} \sim t$. In contrast, beyond this critical We_{E}, a fast moving prolate shaped droplet induce an inertia dominated hole-growth kinetics following, $r_{\mathrm{h}} \sim t^{0.5}$. Film drainage occurs in two stages, with the rate diminishing significantly after the film thickness nears 0.3 times the droplet radius. An analytical model, reveals velocity profiles resembling the Couette flow within the draining film during the various stages of carrier-film drainage. In the tailing mode, the droplet entrains carrier liquid approximately equal to its own volume into the target liquid, wherein the length of tail can be as high as eight times the drop radius. The interfacial-tensions, density and viscosity of the liquids of the ternary system are the key parameters influencing the dynamics of both the modes of migrations. The phenomena may find applications in liquid-liquid extraction, micro-reactions, ultra-low tensiometry, among others.

In the fifth chapter, the contact dynamics of two oppositely charged aqueous droplets suspended in insulating oil under electric field is detailed. Experimental investigations with high-speed imaging reveal asymmetric 'cone-cone' to 'cone-groove' deformations of the approaching poles of two uneven sized oppositely charged drops during electro-coalescence/non-coalescence. Three dimensional simulations and an analytical model confirm the occurrence of a third 'groove-groove' configuration at close proximity. Experiments corroborated with simulations show the emergence of asymmetric liquid 'tentacles' on the Taylor cone of the smaller droplet prior to contact.

In the sixth chapter of the dissertation, the key results of the four main research problems of the thesis are summarized. The prospects of future research arising from the discussed problems along with the potential applications of the same are also discussed in chapter six.

Chapter 2

Electric Field Mediated von Kármán Vortices in Stratified Microflows: Transition from Linear Instabilities to Coherent Mixing

2.1 Abstract

Application of an electric field across the pressure-driven stratified flow of a pair of miscible fluids inside a microchannel manifests interesting electrohydrodynamic (EHD) instabilities. Experiments uncover distinctive instability regimes with an increase in electric field Rayleigh number (Ra^{ψ}) - linear-onset regime, time-periodic non-linear regime analogous to von Kármán vortex street at the downstream, and a regime with coherent flow patterns. The experiments also reveal that such linear and nonlinear instabilities can be stimulated non-invasively in a microchannel to mix or de-mix fluids simply by turning the electric field on or off, indicating the suitability of the process for on-demand micromixing. The characteristics of these instabilities have been theoretically investigated with the help of an Orr-Sommerfeld framework, which discloses the possibility of five distinctive finite-wavenumber modes for the instability. The EHD stresses originating due to the application of electric field stimulate a pair of shorter-wavelength electric field modes beyond a critical value of Ra^{ψ}. Increase in the levels of charge injection and EHD stresses lower the critical Ra^{ψ} of these modes. The relatively longer wavelength viscous-mode is found to appear when the viscosity stratification between the fluid layers is high. Beyond a threshold Schmidt number (Sc), a diffusive-mode is also found to appear near the mixed interfacial region. A thinner interface between the fluids at a higher Sc helps this mode to behave as the interfacial mode of immiscible fluids. Constrast of ionic mobility in the fluids leads to the appearance of the K-mode of instability at much shorter wavelengths. The reported phenomena can be of significance in the domains of microscale mixing, pumping, heat-exchange, mass transfer, and reaction engineering.

The contents in this chapter have been published as S. Dutta, A. Ghosh, P. S. G. Pattader and D. Bandyopadhyay, (2019) 'Electric Field Mediated von Kármán Vortices in Stratified Microflows: Transition from Linear Instabilities to Coherent Mixing', *J. Fluid Mech.*, vol. **865**, pp. 169-211.

2.2 Introduction

In the recent years, the specialities of micro or nanoscale science have been routinely exploited in diverse microfluidic applications such as cell culture [9], clinical diagnostics [8], immunoassays [6], DNA analysis [7], and environmental monitoring [10]. The microscale applications are found to have some distinct advantages over their macroscopic counterparts such as, (i) usage and control of lesser amount of materials [2]; (ii) availability of higher surface to volume ratio; (iii) high-performance due to process intensification [3]; and (iv) superior control over the process parameters [1]. It is now well understood that for efficient and time bound operations, the existing microscale chemical or biological applications require rapid mixing of fluid streams inside the microfluidic devices [4, 26, 27]. However, the conventional pressure-driven microfluidic flows are often limited by low values of Reynolds number (Re), which results in large diffusive time and length scales of mixing owing to the dominance of the viscous force over the inertial one [22, 23]. In the macroscopic processes, the diffusion limited mixing lengths are improved by the generation of auxiliary transport pathways such as turbulence. In contrast, for the microscale processes, the large frictional resistance originating from the confining boundaries pose multifarious challenges towards this end. Thus, of late, the enhancement of momentum, heat, and mass transport in the microscale processes have become one of the major areas of fluid dynamical research [19].

Various pathways have been explored to engender auxiliary transport mechanisms in the microfluidic flows with the help of active and passive triggers. For example, the innovations associated with the groovy or twisted channels [22, 28, 29], multi-lamination of flow paths [30], serpentine channels [31], or viscous fingering of fluids [32] disclose passive modes of enhanced momentum transport. In comparison, the active triggers require the support from the external fields such as the applications of thermal [192], or acoustic waves [33], magnetic [34], or electrokinetic forces [35–43]. However, the enhancement of momentum, heat, and mass diffusivities with the help of in situ disturbances inside microfluidic devices remains to be one of the long standing challenges in this regard. For example, the electrohydrodynamic (EHD) instabilities due to electrokinetic phenomena instigated by conductivity gradients between the fluids have been explored only recently [40–43].

In the present study, we investigate the consequence of an EHD phenomenon to develop laminar, transitional, and chaotic flow regimes. The phenomenon originates

due to injection of ions into a pair of miscible fluids undergoing a pressure-driven stratified flow in a microchannel. The miscible fluids are considered to have higher viscosity contrast and lower electrical conductivities to explore the cumulative effects of electric field stress and viscosity stratification. The major interests here are two-fold, (i) to experimentally investigate the various regimes of instabilities in the aforementioned system leading to chaotic mixing of the fluid streams, and (ii) to theoretically analyse the linear regime of instability to predict their nature and onset conditions. The study is pertinent due to its significance in a plurality of futuristic applications such as microfluidic mixing in drug delivery systems, heat transfer enhancement, reactions in micro reactors, among others.

The prior art related to the stability of viscosity stratified miscible flows suggests that Craik [193] was among the pioneers who identified that these flows can be more stable than the immiscible ones owing to the damping of the perturbations near the interface due to molecular diffusion. Much later, Ranganathan & Govindarajan [194] theoretically identified the influence of the location of the viscosity stratified layer with respect to the critical layer of the perturbation. Subsequently, Ern, Charru & Luchini [195] showed that the effect of molecular diffusion is not always stabilizing. They identified that for moderate values of Peclet number ($400 \leq Pe \leq 10000$), the perturbation at a thicker interface might grow to destabilize the system. Later, Govindarajan [196] identified an overlap mode mode of instability, distinct from the classical Tollmien Schlichting (TS) and inviscid modes, obtained when the critical layer of the most dominant disturbance merges with the viscosity stratified layer. More recently, Selvam *et al.* [197, 198] noted that the miscible core-annular flows can be unstable beyond a critical viscosity ratio, when the lighter phase occupies the annular region. The observations in this study uncovered some of the exceptions to the claims of Ranganathan & Govindarajan [194]. Talon & Meiburg [199] performed the stability analysis of miscible fluids with strong viscosity stratification in the Stokes flow regime ($Re \to 0$), and observed four distinct modes of instabilities in which two were interfacial while the other two were bulk modes. They proposed that these instabilities grew due to the phase shift between vorticity and interfacial perturbations. Subsequently, a number of works showed the influence of miscibility [63], inclination [200–202], and variable density [203] on the different modes of instability. Apart from the macroscopic flows, the microscale flows of the miscible fluids have also been explored theoretically [204–206], as well as experimentally [62, 207]. Interestingly, these studies indicate that the dominance (weakness)

of the frictional (inertial) force at the microscale often disallow intermixing of the fluid layers to provide a kinetic stability at the stratified interface, even when the molecular diffusivities of the fluid layers are high, leading to a weaker capacity of heat, mass, and momentum transfer.

In this regard, the use of an external electric field is found to be an efficient alternative to promote disturbance in various microfluidic flows. Previous studies indicate that various EHD phenomena can improve the performance of microscale electrowetting [44], rheological devices [45], electrospinning [46], and drug delivery systems [47]. In particular, the electroconvection inside a fluid originating from the ionic or charge injections from an electrode to a dielectric fluid has attracted a lot of attention [48–53]. In such processes, the electrical conduction is controlled by the creation of charge carriers at high electric field intensities through electrochemical reaction at the electrode-fluid interface for the fluids having higher electrical resistivity [54, 55]. The Coulombic force acting on the injected ions stimulate an auxiliary advection inside the fluidic medium [56–58] to enhance momentum, heat, and mass transfer [59, 60] as well as throughputs [61].

The onset of electroconvection in the fluid flows has been traditionally analysed from the magnitudes of the following dimensionless numbers, (i) electric field Rayleigh number $Ra^{\psi}\left(=\dfrac{\varepsilon \Psi_0}{K\mu}\right)$ - the ratio of Coulombic to viscous force and (ii) injection level $I^{q}\left(=\dfrac{Q_0 L^2}{\varepsilon \Psi_0}\right)$. Here, the notations ε, Ψ_0, K, μ, Q_0, and L denote electrical permittivity, applied voltage, ionic mobility, fluid viscosity, volumetric charge density at the injecting electrode, and distance between the electrodes respectively. The instability of dielectric quiescent fluids subjected to unipolar ion injections was first reported by Schneider & Watson [208] neglecting the effects of diffusion. Subsequently, Watson *et al.* [49], performed an experimental analysis by creating strong ion injections ($I^{q} \gg 1$) on the surface of a liquid with electron beam, to identify the critical voltage ψ_0, for onset of electroconvection to be about 99. Later, Atten & Moreau [209] established for the case of weak injections ($I^{q} \ll 1$), a stability criterion $Ra^{\psi} I^{q2} = 220.7$, whereas for strong injections ($I^{q} \gg 1$) the stability criterion was defined by $Ra^{\psi} = 160.75$. However, the experiments performed by Atten & Lacroix [210] reported the critical Ra^{ψ} to be 100 for the space charge limited regime. Following this, a number of analytical and numerical investigations of the process of electroconvection due to unipolar injection of ions have been reported by many groups [211–217].

The literature discussed so far indicate that, while the contributions of inertial and molecular diffusive forces have been explored in detail in the past, arguably, there is no report as such of the influence of electric field induced instabilities on stratified two-layer miscible flows inside microchannels. In the present study, with the help of a combined experimental as well as theoretical analyses, the effects of electroconvection on a two-layer viscosity stratified miscible flow inside a microchannel have been explored. We report the experimental investigations of the various regimes of instabilities produced due to ion injections from electrodes into a viscosity stratified flow of miscible fluids, which subsequently lead to the coherent mixing of the fluid streams. Experiments uncover three different instability regimes with increase in electric field intensity, namely, linear-onset regime, time-periodic nonlinear regime with the formation of von Kármán vortices, and a chaotic flow regime. An Orr-Sommerfeld analysis of the governing equations with appropriate boundary conditions has also been performed to identify the various linear modes of instabilities of the system, which helps in the identification of the onset conditions of the EHD instabilities.

2.3 Experimental Section

2.3.1 Materials and Methods

Experiments were carried out in a cylindrical microchannel of 420 μm diameter built on a PDMS (poly-dimethylsiloxane) platform. The channels were fabricated by template moulding technique [218] employing a silicone elastomer (SLYGARD 184 silicone elastomer, Dow Corning). For the fabrication of the channels, templates were first prepared with the help of copper wires (Cu) of the same dimension, as required for the channel. A rectangular well was then formed with double sided tapes, with the Cu wire template fixed into the well. Liquid PDMS mixed with a cross linker in the ratio 10:1 was then poured inside the well before curing the system in a vacuum oven at 80°C for 2 h. The template was then pulled out of the solid PDMS block to form the channels of required configuration. The Cu wire electrodes of 420 μm diameter were integrated across the channel wall, for application of electric field potential. Experiments were conducted using different liquid pairs. Benzene [analytical grade, procured from Merck Ltd. (India), viscosity, $\mu_1 \approx 0.603$ cP at 25°C; dielectric constant, $\varepsilon_{r1} \approx 2.284$ [219]] formed the lower

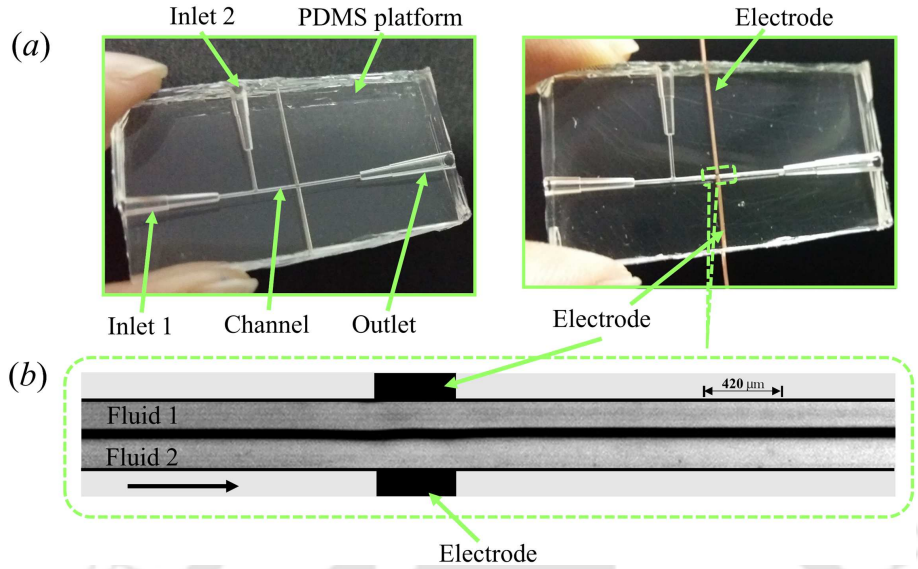

Figure 2.1: Image (a) shows the top-view of the experimental microchannel on a PDMS platform. Fluids 1 and 2 with viscosities μ_1 and μ_2 ($\mu_2 > \mu_1$), respectively, entered the channel through their respective inlets, and were subjected to an electric field applied from a direct current (DC) high voltage source through the Cu wire electrodes as shown. Image (b) shows the experimental micrograph of the top view of the region marked on the image (a). Fluids 1 and 2 formed a stratified flow in the channel (side by side), and were subjected to an electric field via Cu wire electrodes. The diameter of the channel and the electrodes were 420 μm. The average Re of the flow was maintained at 0.5. The arrow on image b indicates the direction of the flow.

viscosity phase. Oleic acid [analytical grade, procured from Merck Ltd. (India), viscosity, $\mu_2 \approx 18$ cP at 25°C; dielectric constant, $\varepsilon_{r2} \approx 2.32$ [220]], silicone oil [analytical grade, procured from Merck Ltd. (India), viscosity, $\mu_2 \approx 317$ cP at 25°C; dielectric constant, $\varepsilon_{r2} \approx 2.5$ [221]], and soybean oil [procured from local vendor, viscosity, $\mu_2 \approx 50$ cP at 25°C; dielectric constant, $\varepsilon_{r2} \approx 3.3$ [222]] formed the higher viscosity phases. The viscosities of the liquids were measured using interfacial rheometer (Anton Paar, Physica MCR 301).

Figure 2.1(a) shows the photographs of the experimental channel, before and after electrode integration. The two liquids were flown through the inlets 1 and 2 of the PDMS channel with the help of a syringe pump (Harvard Apparatus, PHD 2000). Electric field was applied from a high voltage direct current (DC) source (SES Instruments Pvt. Ltd, EHT-II) via Cu wire electrodes of 420 μm diameter as shown figure 2.1(a). The flow of the liquids through the channel was recorded

with a high speed camera (Photron, Fastcam Mini UX-100). A picoammeter (SES Instruments Pvt. Ltd, Model DPM-111) was used to measure the electric current across the electrodes. Figure 2.1(b) demonstrates the experimental micrograph of the highlighted portion in figure 2.1(a), which shows the stratified flow of the fluids 1 and 2 in absence of electric field. Before and after every experiment the channels were first cleaned by ultra-sonication in an acetone bath for 10 min. It was followed by treatment with 10% (v/v) dilute piranha solution ($H_2SO_4 : H_2O_2$, 3 : 1) for 15 min. The channels were then repeatedly washed with DI water (Merck Millipore, grade I), dried by blowing nitrogen gas, and kept in an air oven at 70°C for 20 min.

2.3.2 Calculation of Injection Level

Previous studies indicate that strong unipolar injections ($I^q \gg 1$) with space charge limited currents can be achieved experimentally by covering the electrodes with suitable perm selective membranes and varnishes [48, 223]. In comparison, for the nonpolar liquids, moderate and weak injections have been achieved by doping the liquids with appropriate salts [53, 224]. It has also been shown that intense localized

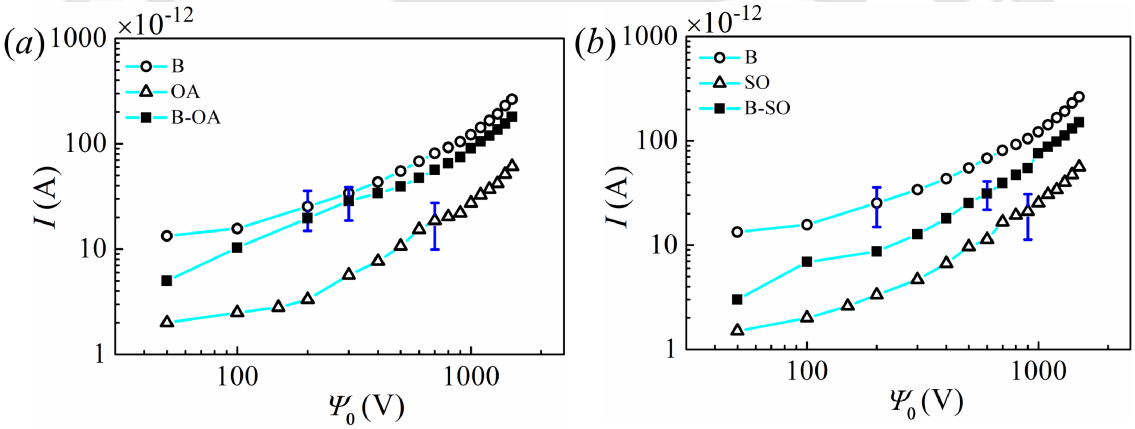

Figure 2.2: Images (a) and (b) show the current (I) vs. voltage (Ψ_0) curves for different combinations of flows. Image (a) shows the combination of single component flows of benzene (B), oleic acid (OA), and a stratified flow of benzene and oleic acid (B-OA). Image (b) shows the combination of single component flows of benzene (B), silicone oil (SO), and a stratified flow of benzene and silicone oil (B-SO). The error bar represents the maximum standard deviation obtained from three experiments.

injections of charge can be achieved by concentrating the electric field with the use of blade or needle electrodes [225–228]. In the reported experiments, DC voltage was applied from a high voltage source with the help of wire electrodes for the

injection of charge into the dielectric experimental fluids. Since the electrodes were in contact with the experimental fluids, the injection of charge in the regions of high electric fields, was inevitable [229]. In order to measure the injection level, a stratified flow of the lower viscosity phase composed of benzene, and higher viscosity phase composed of oleic acid (or silicone oil) was maintained in the microchannel with the help of a syringe pump. DC voltage input was applied to the system with the help of the copper wire electrodes, while the electric current was measured across the electrodes with the help of a picoammeter. The current-voltage curves for the cases: (i) benzene-oleic acid and (ii) benzene-silicone oil are shown in figure 2.2. The electric field intensity between the electrodes was obtained by dividing the applied voltage by the distance between the electrodes (420 μm). The value of electric current across the electrodes was recorded for each applied voltage across each liquid separately before the same was repeated for the stratified flows. It has been shown in previous literature that for electric fields within the range $5\times10^2 \leq E \leq 5\times10^4$ kV/cm, the charge density at the injector remains almost constant and independent of the electric field [58]. Hence, the assumption of autonomous injection for the present analysis seems to be reasonably valid. The measured electrical current in the quiescent liquid is due to the contribution of two processes, (i) residual conduction and (ii) migration of injected ions [53,59]. Previously, [53] showed that conduction current can be considered negligible if the ratio of conduction current to injection current, $C_0 \left(= \dfrac{\sigma L^2}{2K\varepsilon\Psi_0}\right)$, is less than 0.5. The working liquids benzene and oleic (or silicone oil) acid have conductivities of the order of $\sim10^{-13}$ Sm^{-1} [230,231], while the value of ionic mobility K in the working liquids is of the order of $\sim(10^{-8} - 10^{-10})$ $\mathrm{m^2s^{-1}V^{-1}}$ [53]. In such a situation, the value of C_0 was found to be less than 0.5 for the experiments reported in the present work. Thus, the total current was considered to be due to ionic injections from the electrodes only. Thereafter, the injection level I^q was calculated from eq. (2.9), using the current voltage curves shown in figure 2.2. The injection levels I^q for the experiments shown in the present study were found to be in the range of 0.5−1.15, indicating a moderate injection.

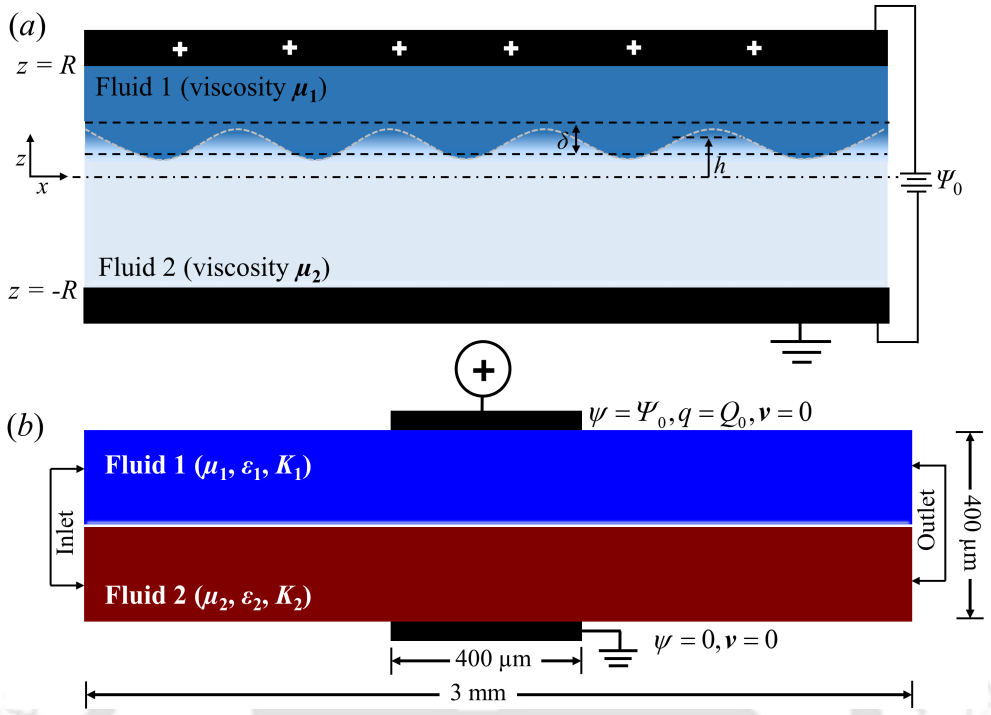

Figure 2.3: Images (a) and (b) show the current (I) vs. voltage (Ψ_0) curves for different combinations of flows. Image (a) shows the combination of single component flows of benzene (B), oleic acid (OA), and a stratified flow of benzene and oleic acid (B-OA). Image (b) shows the combination of single component flows of benzene (B), silicone oil (SO), and a stratified flow of benzene and silicone oil (B-SO). The error bar represents the maximum standard deviation obtained from three experiments.

2.4 Theoretical Formulation

2.4.1 Problem Formulation

The experiments were carried out in a cylindrical microchannel (420 μm diameter) as already discussed in section 2.3.1. To get an in-depth information about the nature and onset conditions of the reported EHD instabilities, a scrupulous investigation considering similar flow geometry as the experimental channel is required. However, the mathematical treatment of the problem considering cylindrical coordinate system, is seemingly cumbersome, especially, because the experimental flow configuration is non-axisymmetric, due to integration of the electrodes on the channel walls. This calls for a complete three-dimensional formulation of the problem in the cylindrical-coordinate system followed by a global stability analysis, which in the context of the reported problem will be extremely involved. We thus, resorted to

a two-dimensional planar geometry. Figure 2.3(a) depicts the laminar flow of a pair of miscible fluids flowing through a channel, before subjected to a DC voltage Ψ_0. A Cartesian coordinate system is chosen as the reference frame with x and z axes perpendicular to each other on the same plane. The distance between the two electrodes is $2R$, while the electric field is applied in the z direction. The fluids, namely, fluid 1 of viscosity μ_1 and fluid 2 of viscosity μ_2 ($\mu_2 > \mu_1$), are assumed to be of equal density, and dielectric permittivity, and the ionic mobility is considered same in both the fluids. For two miscible fluids flowing inside a microchannel, the associated mass transfer Peclet number $\left[Pe = \frac{ul}{\kappa}\right]$, is of the order of $\sim 10^2$ or higher [22], leading to a slow diffusive mixing between the fluids. Thus, in the present study, which is motivated for flow inside microchannels, the thickness of the mixed interface can be effectively assumed to be constant. The interface between the two fluids grows diffusively to a distance δ in such a manner that fluid 1 occupies the region between $h + \delta/2 \leq z \leq R$ and fluid 2 occupies the region $-R \leq z \leq h - \delta/2$, where h is the distance of the mixed interface from the datum line $z = 0$.

The viscosity of the fluids is formulated as an exponential function of the concentration scalar S, such that the base values of the scalar S_0 are 0 and 1 in the top and bottom layers, respectively. The viscosity μ is modelled as,

$$\mu = \mu_1 \exp(SV^L), \tag{2.1}$$

where, V^L is the log viscosity ratio of the fluids defined as, $V^L = \ln\left(\frac{\mu_2}{\mu_1}\right)$ [63]. The Reynolds number (Re) is defined as $Re = \frac{Q}{R\eta_1}$, where Q is the volumetric flow rate and η_1 is the kinematic viscosity of fluid 1. In order to bring homogeneity between the theoretical and experimental analyses, the strength of injection, characterized by the injection parameter, I^q, is calculated experimentally (refer to section 2.3.2), and used for the theoretical analysis. It is observed that the injection is homogeneous and autonomous in the experiments. Assuming a medium injection level, the value of injection parameter I^q, is fixed at 1 for the theoretical analysis unless otherwise stated. In the formulation, 't' represents time, the bold variables indicate vectors, and the dashed variables denote derivative with respect to 'z'.

2.4.2 Governing Equations

The fluids are assumed to be Newtonian and incompressible, thereby the flow field can be defined by the following continuity and momentum equations neglecting the effect of gravity,

$$\boldsymbol{\nabla} \cdot \boldsymbol{v} = 0, \tag{2.2}$$

$$\rho \left(\frac{\partial \boldsymbol{v}}{\partial t} + \boldsymbol{v} \cdot \boldsymbol{\nabla} \boldsymbol{v} \right) = -\boldsymbol{\nabla} p + \boldsymbol{\nabla} \cdot \left[\mu \left(\boldsymbol{\nabla} \boldsymbol{v} + \boldsymbol{\nabla} \boldsymbol{v}^{\mathrm{T}} \right) \right] + \boldsymbol{F_e}. \tag{2.3}$$

Where, $\boldsymbol{v}$ is the velocity vector, ρ is the density, p is the pressure, and $\boldsymbol{F_e}$ is the electrical body force term given by,

$$\boldsymbol{F_e} = q\boldsymbol{E} - \frac{1}{2}|\boldsymbol{E}|^2 \boldsymbol{\nabla} \varepsilon + \boldsymbol{\nabla} \left(\rho \frac{|\boldsymbol{E}|^2}{2} \frac{\partial \varepsilon}{\partial \rho} \right). \tag{2.4}$$

Here, q represents the volumetric charge density, $\boldsymbol{E}$ is the electric field intensity, and ε is the electrical permittivity. The first term of eq. (2.4) represents the Coulombic force exerted by the electric field on the free charges, and is generally the strongest in case of DC supplied voltage. The second term of eq. (2.4) is the dielectric force exerted by the electric field on the bound charges, and is neglected in the present analysis due to the negligible gradient of dielectric permittivity. The third term of eq. (2.4) is the electrostrictive force which is included with the pressure term of the Navier-Stokes equation. The irrotational electric field $\boldsymbol{E}$ is assumed to follow the field, $\boldsymbol{E} = -\boldsymbol{\nabla} \psi$, which leads to the following Poisson's equation originating from the governing Gauss's law in which the electric field potential is defined as ψ,

$$q = \boldsymbol{\nabla} \cdot \varepsilon \boldsymbol{E}, \tag{2.5}$$

$$\nabla^2 \psi = -\frac{q}{\varepsilon}. \tag{2.6}$$

The continuity equation for charge density is given by,

$$\frac{\partial q}{\partial t} + \boldsymbol{\nabla} \cdot \boldsymbol{J} = 0, \tag{2.7}$$

where, the current density $\boldsymbol{J}$ is given by,

$$\boldsymbol{J} = q\boldsymbol{v} + qK\boldsymbol{E} - D\boldsymbol{\nabla} q + \sigma \boldsymbol{E}. \tag{2.8}$$

The first term of eq. (2.8) accounts for the convection of charges due to motion of the fluid moving with a velocity $\boldsymbol{v}$. The second term accounts for the drift transport of charges under the effect of electric field, where K is the mobility of the ions moving with velocity $K\boldsymbol{E}$. The third term accounts for the diffusive transport of the ions with diffusion coefficient D, which is neglected because of its smaller magnitude as compared to the other terms [52, 53, 58]. In the present analysis, the fluids under study are considered to be nearly electrically non-conductive ($\sigma \leq 10^{-13}\ \mathrm{Sm}^{-1}$), thereby making the last term of eq. (2.8) negligible. Therefore, the constitutive relation for current density reduces to,

$$\boldsymbol{J} = q\boldsymbol{v} + qK\boldsymbol{E}. \tag{2.9}$$

Substituting eq. (2.9) into eq. (2.7), and using eq. (2.2), we obtain the conservation equation for the charge density as,

$$\frac{\partial q}{\partial t} + \boldsymbol{v}\cdot(\boldsymbol{\nabla} q) + K\left[q\left(\boldsymbol{\nabla}\cdot\boldsymbol{E}\right) + \boldsymbol{E}\cdot(\boldsymbol{\nabla} q)\right] = 0. \tag{2.10}$$

The advection-diffusion equation for the concentration scalar S gives,

$$\frac{\partial S}{\partial t} + \boldsymbol{v}\cdot\boldsymbol{\nabla} S = \kappa\nabla^2 S. \tag{2.11}$$

Here, κ is the diffusion coefficient of the scalar. For the velocity field, no-slip and no penetration boundary conditions are enforced at the channel walls, i.e. $[\boldsymbol{v}(\pm R) = 0,\ \boldsymbol{v}'(\pm R) = 0]$. The boundary conditions used to solve for the electric potential ψ are: $\psi(R) = \Psi_0,\ \psi(-R) = 0$.

2.4.3 Non-Dimensional Governing Equations

The equations are reduced to dimensionless forms by using the following scheme,

$$\left.\begin{aligned} &(x, z, h, \delta) = R\left(x^*, z^*, h^*, \delta^*\right), \quad (u, w) = \frac{K\Psi_0}{R}\left(u^*, w^*\right), \quad \psi = \Psi_0\psi^*, \\ &q = Q_0 q^*, \quad t = \frac{R^2}{K\Psi_0}t^*, \quad p = \frac{\rho K^2\Psi_0^2}{R^2}p^*, \quad \mu = \mu_1\mu^*. \end{aligned}\right\} \tag{2.12}$$

The asterisk symbol depicts dimensionless quantities. Here, Ψ_0 and Q_0 represent the applied voltage and the charge density at the injector, respectively. The dimen-

sionless governing equations after dropping the asterisk symbol are,

$$\boldsymbol{\nabla} \cdot \boldsymbol{v} = 0, \tag{2.13}$$

$$\frac{\partial \boldsymbol{v}}{\partial t} + \boldsymbol{v} \cdot \boldsymbol{\nabla} \boldsymbol{v} = -\boldsymbol{\nabla} p + \frac{1}{Re^{\psi}} \boldsymbol{\nabla} \cdot \left[\mu \left(\boldsymbol{\nabla} \boldsymbol{v} + \boldsymbol{\nabla} \boldsymbol{v}^{\mathrm{T}} \right) \right] + I^{q} {R_M}^2 \left(q \boldsymbol{E} \right), \tag{2.14}$$

$$\nabla^2 \psi = -I^{q} q, \tag{2.15}$$

$$\frac{\partial q}{\partial t} + \boldsymbol{v} \cdot (\boldsymbol{\nabla} q) + q \left(\boldsymbol{\nabla} \cdot \boldsymbol{E} \right) + \boldsymbol{E} \cdot (\boldsymbol{\nabla} q) = 0, \tag{2.16}$$

$$\frac{\partial S}{\partial t} + \boldsymbol{v} \cdot \boldsymbol{\nabla} S = \frac{1}{Re^{\psi} Sc} \nabla^2 S, \tag{2.17}$$

where,

$$Re^{\psi} = \frac{K \Psi_0}{\eta_1}, \quad R_M = \frac{(\varepsilon/\rho)^{1/2}}{K}, \quad I^{q} = \frac{Q_0 R^2}{\varepsilon \Psi_0}, \quad Sc = \frac{\eta_1}{\kappa}. \tag{2.18}$$

Here, Re^{ψ} is defined as the electric Reynolds number, R_M is defined as the ratio between hydrodynamic mobility $\left[\left(\frac{\varepsilon}{\rho} \right)^{1/2} \right]$ to the true ionic mobility K, I^{q} is the charge injection level, and Sc is the Schmidt number. The electric field Rayleigh number Ra^{ψ} is defined as $Ra^{\psi} = Re^{\psi} {R_M}^2 = \frac{\varepsilon \Psi_0}{\mu_1 K}$, and gives the ratio between electrostatic to viscous force. The non-dimensional boundary conditions used to solve the velocity field are: $\boldsymbol{v}(\pm 1) = 0$, $\boldsymbol{v}'(\pm 1) = 0$. For the solution of the electric potential ψ, the non-dimensional boundary conditions used are: $\psi(1) = 1$, $\psi(-1) = 0$.

2.4.4 Stability Theory

A general linear stability analysis (LSA) has been carried out by splitting the flow and electric field variables into base-state and perturbed-state quantities. We consider only the transversal modes because the existing literature suggests that the longitudinal modes remain unaffected by the parallel shear flow or the other parameters of interest reported in the present study [63, 232, 233]. In such a scenario a two-dimensional (2-D) stability analysis is found to be sufficient to qualitatively uncover the underlying physics and predict the onset conditions. The formulation considering three- dimensional (3-D) perturbations is also shown in the appendix

A.2. The governing equations are linearized considering the following linear modes:

$$\begin{aligned}[u, w, p, \psi, S, \mu](x, z, t) &= [u_0(z), 0, p_0, \psi_0(z), S_0(z), \mu_0(z)] \\ &+ \left[\tilde{u}, \tilde{w}, \tilde{p}, \tilde{\psi}, \tilde{S}, \tilde{\mu}\right](z)\, e^{(\omega t + \mathrm{i}kx)}. \end{aligned} \tag{2.19}$$

The variables with subscript '0' denote the base-state quantities and the variables with 'tilde' are the perturbed quantities. Here, u and w are x- and z- directional velocities, respectively. The symbols ω and k are the growth coefficient and the wavenumber of the perturbation, respectively. The parameter ω is a complex quantity ($\omega = \omega_r + \mathrm{i}\omega_i$). A perturbation is unstable when $\omega_r > 0$, stable when $\omega_r < 0$, and neutrally stable when $\omega_r = 0$. The perturbation viscosity $\tilde{\mu}$ is modelled as, $\tilde{\mu} = \frac{\mathrm{d}\mu_0}{\mathrm{d}S_0}\tilde{S}$ [63].

2.4.4.1 Base-State Analysis

It is assumed that the diffusive interface between the two miscible fluids is of thickness δ. If $\delta \ll 1$, then the base-state profile of the concentration scalar can be estimated following a quasi-steady approximation $\left[\omega \gg \frac{\kappa}{\delta^2}\right]$ [197, 204] as,

$$S_0 = 0.5 - 0.5\mathrm{erf}\left(\frac{z-h}{\delta}\right). \tag{2.20}$$

Here, the variable, h, is the dimensionless distance of the diffused interface from the datum, $z = 0$. The base-state profile of the concentration scalar is shown in figure 2.4(a). The base-state profiles for viscosity μ_0, are then obtained from the relation,

$$\mu_0 = \exp(S_0 V^L). \tag{2.21}$$

The base-state velocity profile u_0, is then obtained by solving eq. (2.14) for steady state, after dropping the electrical body force term, which gives,

$$\mu_0\left(u_0'' + V^L u_0' S_0'\right) = Re^{\psi}\frac{\mathrm{d}p_0}{\mathrm{d}x}. \tag{2.22}$$

Equation (2.22) is solved with no slip boundary conditions at the channel walls, $u_0(\pm 1) = 0$, in which the non-dimensional pressure gradient, $\left(\frac{\mathrm{d}p_0}{\mathrm{d}x}\right)$, is fixed by assuming a constant volumetric flow rate. From eq. (2.16) the base state equation

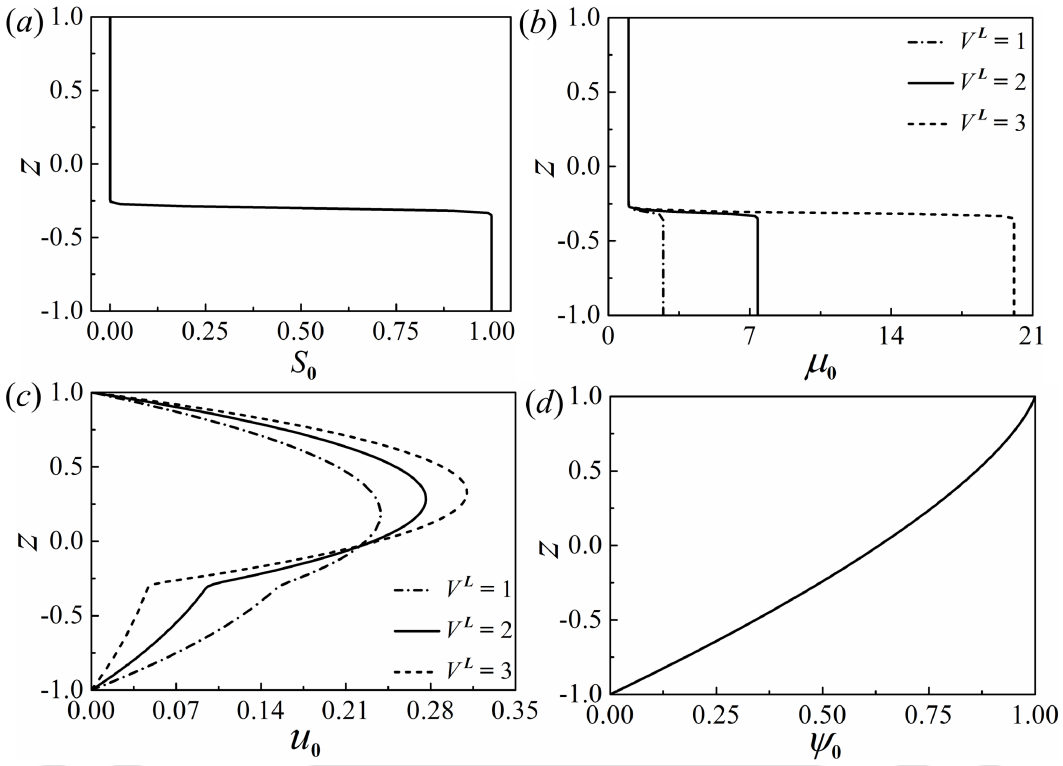

Figure 2.4: Base-state profiles for, (a) concentration scalar S_0, (b) viscosity μ_0, (c) velocity u_0, and (d) potential ψ_0, for $h = -0.3$ and $\delta = 0.02$.

for electric potential is obtained as,

$$(\psi_0'')^2 + \psi_0'\psi_0''' = 0. \tag{2.23}$$

Equation (2.23) is solved numerically with the boundary conditions: $[\psi_0(1) = 1;\ \psi_0(-1) = 0;\ \psi_0''(1) = -I^q]$. The base state profiles for viscosity (μ_0), velocity (u_0), and electric potential (ψ_0) are shown in figures 2.4(a)–(d) . The plot (a) in this figure shows that S_0 is zero at the layer 1 and it is one at the layer 2 while the variation across the diffused interface is sharp but continuous. A similar trend of the variation in the dimensionless viscosity μ_0 can also be seen in plot (b). Further, plot (c) shows the dimensionless velocity profile u_0, at the base-state under varied conditions. The plot (d) shows the variation of the base state electric field potential ψ_0, across the fluid layers.

2.4.4.2 Perturbed-State Analysis

The governing equations (2.13)−(2.17) are perturbed with the variables mentioned in eq.(2.19) in which the growth coefficient, ω, is represented in terms of the wave speed c as, $\omega = -\mathrm{i}kc$. The dimensionless linearized equations of motion and continuity equation after eliminating the pressure perturbation term is given by,

$$\begin{aligned} &Re^{\psi}\mathrm{i}k\left[(u_0-c)\left(\tilde{w}''-k^2\tilde{w}\right)-u_0''\tilde{w}\right]+Ra^{\psi}k^2\left[\psi_0'\tilde{\psi}''-\left(\psi_0'''+k^2\psi_0'\right)\tilde{\psi}\right]= \\ &\mu_0\tilde{w}''''+2\mu_0'\tilde{w}'''+\left(\mu_0''-2k^2\mu_0\right)\tilde{w}''-2k^2\mu_0'\tilde{w}'+\left(k^2\mu_0''+k^4\mu_0\right)\tilde{w} \\ &-\mathrm{i}ku_0'\tilde{\mu}''-2\mathrm{i}ku_0''\tilde{\mu}'-\left(\mathrm{i}ku_0'''+\mathrm{i}k^3u_0'\right)\tilde{\mu}. \end{aligned} \tag{2.24}$$

Equation (2.16) and eq. (2.17) reduce to the following equations,

$$\begin{aligned} \mathrm{i}k\left[(u_0-c)\left(\tilde{\psi}''-k^2\tilde{\psi}\right)-\frac{\mathrm{i}}{k}\psi_0'''\tilde{w}\right] &= \psi_0'\tilde{\psi}'''+2\psi_0''\tilde{\psi}''+\left(\psi_0'''-k^2\psi_0'\right)\tilde{\psi}' \\ &\quad -2k^2\psi_0''\tilde{\psi}, \end{aligned} \tag{2.25}$$

$$\mathrm{i}kRe^{\psi}Sc\left[(u_0-c)\,\tilde{S}-\frac{\mathrm{i}}{k}S_0'\tilde{w}\right]=\tilde{S}''-k^2\tilde{S}. \tag{2.26}$$

The boundary conditions employed to solve eqs. (2.24)−(2.26) are,

$$\tilde{w}\,(\pm1)=0, \quad \tilde{w}'\,(\pm1)=0, \tag{2.27}$$

$$\tilde{\psi}\,(\pm1)=0, \quad \tilde{\psi}''\,(1)=0, \tag{2.28}$$

$$\tilde{S}'\,(\pm1)=0. \tag{2.29}$$

2.4.4.3 Numerical Method

The domain is discretized employing a spectral collocation method based on Chebyshev polynomials [234, 235]. The three ordinary differential equations defined by eqs. (2.24)−(2.26) reduce to the following eigenvalue form upon discretization,

$$A\tilde{\phi}=\omega B\tilde{\phi}, \tag{2.30}$$

where A and B are 3×3 matrices, and $\tilde{\phi}$ is a vector given by,

$$\boldsymbol{A} = \begin{bmatrix} A_{11} & A_{12} & A_{13} \\ -Re^{\psi} ScS_0' & A_{22} & 0 \\ -\psi_0''' & 0 & A_{33} \end{bmatrix}, \tag{2.31}$$

$$\boldsymbol{B} = \begin{bmatrix} Re_{\psi}\left(\mathrm{D}_2 - k^2\right) & 0 & 0 \\ 0 & Re^{\psi} Sc & 0 \\ 0 & 0 & \left(\mathrm{D}_2 - k^2\right) \end{bmatrix}, \tag{2.32}$$

$$\tilde{\phi} = \begin{bmatrix} \tilde{w} \\ \tilde{S} \\ \tilde{\psi} \end{bmatrix}. \tag{2.33}$$

Here, $\mathrm{D}_1 = \dfrac{\mathrm{d}}{\mathrm{d}z}$, $\mathrm{D}_2 = \dfrac{\mathrm{d}^2}{\mathrm{d}z^2}$, $\mathrm{D}_3 = \dfrac{\mathrm{d}^3}{\mathrm{d}z^3}$, $\mathrm{D}_4 = \dfrac{\mathrm{d}^4}{\mathrm{d}z^4}$, and,

$$A_{11} = \mu_0 \mathrm{D}_4 + 2\mu_0' \mathrm{D}_3 + \left(\mu_0'' - \mathrm{i}kRe^{\psi} u_0 - 2k^2\mu_0\right)\mathrm{D}_2 - 2k^2\mu_0' \mathrm{D}_1 + \mathrm{i}k\left(Re^{\psi} u_0'' + \frac{k}{\mathrm{i}}\mu_0'' + Re^{\psi} k^2 u_0 + \frac{k^3}{\mathrm{i}}\mu_0\right),$$

$$A_{12} = -\mathrm{i}kV^L \mu_0 u_0' \mathrm{D}_2 - 2\mathrm{i}kV^L\left(\mu_0 u_0'' + u_0'\mu_0'\right)\mathrm{D}_1 - \mathrm{i}kV^L\left(\mu_0 u_0''' + k^2\mu_0 u_0' + u_0'\mu_0'' + 2u_0''\mu_0'\right),$$

$$A_{13} = Ra^{\psi} k^2\left(\psi_0''' + k^2\psi_0' - \psi_0' \mathrm{D}_2\right),$$

$$A_{22} = \mathrm{D}_2 - k^2 - \mathrm{i}kRe^{\psi} Scu_0,$$

$$A_{33} = \psi_0' \mathrm{D}_3 + \left(2\psi_0'' - \mathrm{i}ku_0\right)\mathrm{D}_2 + \left(\psi_0''' - k^2\psi_0'\right)\mathrm{D}_1 - 2k^2\psi_0'' + \mathrm{i}k^3 u_0.$$

The eigenvalue problem defined by eq. (2.30) has been solved with the help of a MATLAB$^{\mathrm{TM}}$ code to obtain variation in the grow rate, ω, with the wave number,

k, for the unstable modes. In general, it is a common practice to cluster the grid in the viscosity stratified region by using a stretching function to reduce the number of grid points required for convergence [63]. However, in the present analysis, even in absence of clustering, a satisfactory convergence has been achieved with about 200 collocation points.

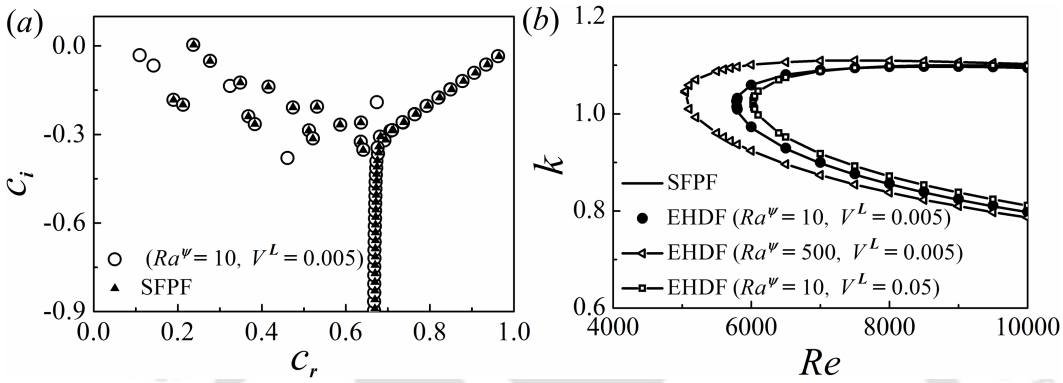

Figure 2.5: Plots showing, (a) eigenspectra depicting the real part (c_r) vs. imaginary part (c_i) of the complex wave speed c, for single fluid plane Poiseuille flow (SFPF) and EHD flow (EHDF) when $Re = 10000$ and $k = 1$, and (b) neutral stability curves showing the variation of k with Re for SFPF and EHDF. The other parameters considered for EHDF are, $h = -0.3$, $\delta = 0.02$, and $Sc = 10$.

2.4.4.4 Validation of Numerical Method

In order to validate the results obtained from the numerical method, we draw a parallel between the EHD flow (abbreviated as, EHDF) studied in the present report with the single fluid plane Poiseuille flow (abbreviated as, SFPF), as described in Schmid & Henningson [236] for $Re = 10000$. The consistency of the numerical method is checked by setting significantly lower values for V^L, representing negligible viscosity gradient in the flow, so that the flow can be essentially considered to be composed of a single fluid. The electric field force is turned off by assigning extremely low values to Ra^ψ. Hence, for imposed constraints of very low V^L and Ra^ψ, EHDF asymptotically emulates the SFPF. Figure 2.5 shows the eigenspectra and neutral stability plots for SFPF in tandem with EHDF considered in the present analysis. Figure 2.5(a) shows the comparison between the eigenspectra depicting the imaginary part (c_i) vs. the real part (c_r) of the complex wave speed c, for the SFPF and the EHDF. The plot shows that for a lower electric field potential ($Ra^\psi = 10$) and marginal viscosity difference ($V^L = 0.005$), the SFPF and EHDF generate

almost similar eigenspectra. The latter produce a few extra eigenvalues owing to the marginal influence originating from the electric body force term of the momentum equation. Figure 2.5(b) depicts the neutral stability curves showing wavenumber (k) as function of Reynolds number (Re) for SFPF and EHDF. For very low values of electric field and viscosity stratification ($Ra^{\psi} = 10$, $V^L = 0.005$), the EHDF depicts a similar behaviour as the SFPF, yielding a critical Re of approximately 5772, as can be seen in figure 2.5(b). An increase in Ra^{ψ} signals increment in the destabilizing electric field force, which is reflected as a decreasing trend of the critical Re with increasing Ra^{ψ}, in the figure 2.5(b). However, for a marginal increase in the viscosity difference between the fluids ($V^L = 0.05$) and for a lower electric field potential ($Ra^{\psi} = 10$), the critical Re for instability is found to increase, suggesting a kinetic stabilization of the system. Figure 2.5 shows the accuracy of the numerical analysis presented in this work, which has been employed to generate the results shown in the manuscript.

2.4.4.5 Variable Ionic Mobility

It may be noted here that, the ionic mobility parameter can strongly depend on the viscosity of the fluid [237]. Thus, it is likely that the ionic mobility values may differ in the fluids of interest in a practical setting. Though in the present analysis, for the purpose of mathematical simplification, most of the results are presented assuming equal ionic mobility, however, it is lucrative to study the effect of difference in ionic mobility values in order to simulate a physical system with more precision. In order to investigate the effect of ion mobility values on the stability characteristics, we assume the ion mobility to be K_1 in the lower viscosity fluid 1 and K_2 in the higher viscosity fluid 2. The ionic mobility in the mixed interfacial is modelled as $K = K_1 \exp(SK^L)$, where S is the same scalar used for defining the viscosity μ, and $K^L = \ln\left(\frac{K_2}{K_1}\right)$, is defined as the log-mobility ratio. Subsequently, the perturbation scheme described by eq. (2.19) becomes,

$$\begin{aligned}[u, w, p, \psi, S, \mu, K](x, z, t) &= [u_0(z), 0, p_0, \psi_0(z), S_0(z), \mu_0(z), K_0(z)] \\ &+ \left[\tilde{u}, \tilde{w}, \tilde{p}, \tilde{\psi}, \tilde{S}, \tilde{\mu}, \tilde{K}\right](z)\, e^{(\omega t + \mathrm{i}kx)}. \end{aligned} \tag{2.34}$$

The modified governing equation for the conservation of charge density q [eq. (2.10) and eq. (2.16)] can now be written as,

$$\frac{\partial q}{\partial t} + \boldsymbol{v} \cdot (\boldsymbol{\nabla} q) + Kq\,(\boldsymbol{\nabla} \cdot \boldsymbol{E}) + \boldsymbol{E} \cdot (K \boldsymbol{\nabla} q + q \boldsymbol{\nabla} K) = 0. \tag{2.35}$$

The base-state profile of the ionic mobility K_0 is obtained from the base-state solution of S_0 [eq. (2.20)] as,

$$K_0 = \exp(S_0 K^L). \tag{2.36}$$

The base-state of electric potential ψ_0 is obtained by solving the steady state form of eq. (2.35), given by,

$$K_0 \left(\psi_0''\right)^2 + K_0 \psi_0' \psi_0''' + K_0' \psi_0' \psi_0'' = 0, \tag{2.37}$$

with the boundary conditions: $[\psi_0(1) = 1;\ \psi_0(-1) = 0;\ \psi_0''(1) = -I^q]$ as already mentioned previously. Upon perturbing the governing equations with the variables mentioned in eq. (2.34), the modified dimensionless linearized charge conservation equation is given by,

$$\begin{aligned} \mathrm{i}k \left[(u_0 - c)\left(\tilde{\psi}'' - k^2 \tilde{\psi}\right) - \frac{\mathrm{i}}{k} \psi_0''' \tilde{w}\right] = {} & K_0 \psi_0' \tilde{\psi}''' + \left(2K_0 \psi_0'' + K_0' \psi_0'\right) \tilde{\psi}'' + \\ & \left(K_0 \psi_0''' + K_0' \psi_0'' - k^2 K_0 \psi_0'\right) \tilde{\psi}' - \left(2k^2 K_0 \psi_0'' + k^2 K_0' \psi_0'\right) \tilde{\psi} + \psi_0' \psi_0'' \tilde{K}' \\ & + \left[\left(\psi_0''\right)^2 + \psi_0' \psi_0'''\right] \tilde{K}. \end{aligned} \tag{2.38}$$

The linearized non-dimensional governing equations defined by eqs. (2.24), (2.38) and (2.26) along with the boundary conditions defined by eqs. (2.27–2.29), are solved using the numerical method described in section 2.4.4.3.

2.4.4.6 Variable Dielectric Constant

As the case of ionic mobility, it is also quite likely that the experimental fluids may seldom have similar dielectric constants. In order to investigate the effect of variable dielectric constants on the stability characteristics, we assume dielectric constants ε_1 and ε_2 for the fluids 1 and 2, respectively. In the mixed interfacial region, dielectric constant is modelled as, $\varepsilon = \varepsilon_1 \exp(SE^L)$, where $E^L = \ln\left(\frac{\varepsilon_2}{\varepsilon_1}\right)$, is defined as log

permittivity ratio. The perturbation scheme shown in eq. (2.19) transforms into,

$$\begin{aligned}[u, w, p, \psi, S, \mu, \varepsilon](x, z, t) &= [u_0(z), 0, p_0, \psi_0(z), S_0(z), \mu_0(z), \varepsilon_0(z)] \\ &+ \left[\tilde{u}, \tilde{w}, \tilde{p}, \tilde{\psi}, \tilde{S}, \tilde{\mu}, \tilde{\varepsilon}\right](z)\, e^{(\omega t + \mathrm{i}kx)}. \end{aligned} \tag{2.39}$$

The base-state profile of dielectric constant ε_0 is obtained from the base-state of the concentration scalar S_0 as,

$$\varepsilon_0 = \exp(S_0 E^L). \tag{2.40}$$

The base state electric potential ψ_0 is obtained by solving the steady state form of eq. (2.16), given by,

$$\varepsilon_0 (\psi_0'')^2 + 3\varepsilon_0' \psi_0' \psi_0'' + \varepsilon_0 \psi_0' \psi_0''' + \varepsilon_0'' (\psi_0')^2 = 0. \tag{2.41}$$

Equation (2.41) is solved using the boundary conditions: $[\psi_0(1) = 1;\ \psi_0(-1) = 0;\ \psi_0''(1) = -I^q]$. The modified dimensionless linearized momentum equation is given by,

$$\begin{aligned} &Re^{\psi} \mathrm{i}k \left[(u_0 - c)\left(\tilde{w}'' - k^2 \tilde{w}\right) - u_0'' \tilde{w}\right] + \\ &Ra^{\psi} k^2 \left[\varepsilon_0 \psi_0' \tilde{\psi}'' - \left(\varepsilon_0 \psi_0''' + k^2 \varepsilon_0 \psi_0' + 2\varepsilon_0' \psi_0'' + \varepsilon_0'' \psi_0'\right) \tilde{\psi} + (\psi_0')^2 \tilde{\varepsilon}' + 2\psi_0' \psi_0'' \tilde{\varepsilon}\right] \\ &= \mu_0 \tilde{w}'''' + 2\mu_0' \tilde{w}''' + \left(\mu_0'' - 2k^2 \mu_0\right) \tilde{w}'' - 2k^2 \mu_0' \tilde{w}' + \left(k^2 \mu_0'' + k^4 \mu_0\right) \tilde{w} - \mathrm{i}k u_0' \tilde{\mu}'' \\ &- 2\mathrm{i}k u_0'' \tilde{\mu}' - \left(\mathrm{i}k u_0''' + \mathrm{i}k^3 u_0'\right) \tilde{\mu}. \end{aligned} \tag{2.42}$$

The linearized charge conservation equation is given by,

$$\begin{aligned} &\mathrm{i}k \left[(u_0 - c)\left(\varepsilon_0 \tilde{\psi}'' + \varepsilon_0' \tilde{\psi}' - k^2 \varepsilon_0 \tilde{\psi} + \psi_0' \tilde{\varepsilon}' + \psi_0'' \tilde{\varepsilon}\right) - \frac{\mathrm{i}}{k}\left(\varepsilon_0 \psi_0''' + 2\varepsilon_0' \psi_0'' + \varepsilon_0'' \psi_0'\right) \tilde{w}\right] \\ &= \varepsilon_0 \psi_0' \tilde{\psi}''' + \left(2\varepsilon_0 \psi_0'' + 3\varepsilon_0' \psi_0'\right) \tilde{\psi}'' + \left(\varepsilon_0 \psi_0''' + 2\varepsilon_0'' \psi_0' + 3\varepsilon_0' \psi_0'' - k^2 \varepsilon_0 \psi_0'\right) \tilde{\psi}' \\ &- \left(2k^2 \varepsilon_0 \psi_0'' + 2k^2 \varepsilon_0' \psi_0'\right) \tilde{\psi} + (\psi_0')^2 \tilde{\varepsilon}'' + 3\psi_0' \psi_0'' \tilde{\varepsilon}' + \left(\psi_0' \psi_0''' + \psi_0''^2\right) \tilde{\varepsilon}. \end{aligned} \tag{2.43}$$

Equations (2.42) and (2.43) along with eq. (2.26) are solved using the boundary conditions mentioned in eqs. (2.27–2.29) applying the numerical method discussed in section 2.4.4.3.

2.4.5 Non-linear Simulations

The computational domain for the non-linear simulations is shown in the figure 2.3(b). The properties of the fluids are modelled as, $X = X_1 \exp(SX^L)$, where X is a physical property [viscosity (μ_1, μ_2), dielectric constant (ε_1, ε_2), and ionic mobility (K_1, K_2)], S is any scalar, and X^L is the log ratio. The governing equations simulated for the system are same as defined in section 2.4.2 [eqs. (2.2)−(2.11)].

For the flow field [eqs. (2.2) and (2.3)], no slip ($\boldsymbol{v} = 0$) condition was enforced at the walls. For the advection-diffusion equation [eq. (2.11)], inlet concentration was fixed at 1 for the higher viscosity (dielectric constant, electrical permittivity) fluid and at 0 for the lower one. For the electric field [eq. (2.6)], $\psi = \Psi_0$ and $\psi = 0$, boundary conditions had been enforced at the top and bottom electrodes, respectively. The injection was considered autonomous and homogenous [refer to section 2.3.2]. Thus, for the charge conservation equation defined by eq. (2.7), constant charge density, $q = Q_0$ was maintained at the injector (top). It was also assumed that the ions discharged immediately on reaching the collector electrode [213, 214].

The set of partial differential equations defined by eqs. (2.2)−(2.11) were solved using the finite element method employing the commercial software COMSOL Multiphysics for a 2-D geometry shown in figure 2.3(b). The domain was discretized with $\sim 4.5 \times 10^4$ finite elements with refinement along the walls, mixed interface, and electrode regions. Second order elements for velocity, concentration, potential, and volume charge density, and first order elements for pressure, were used for discretization. The MUltifrontal Massively Parallel Sparse direct solver (MUMPS) was used for solving the equations. The time dependent solver was adjusted to backward difference formula with free time stepping for integrating the equations.

2.5 Results and Discussion

2.5.1 Experimental Observations

We initiate the discussion with one of the experimental results in which benzene-silicone oil system ($V^L \approx 6$) was flown through a microchannel before the EHD field was generated by the application of a DC voltage of 300 V ($Ra^\psi = 225$) across the electrodes. Figure 2.6 shows the images of the experiment, which correspond to the top-view of the flow while the electrodes were inserted into the channel horizontally from the sides, as previously mentioned in figure 2.1. The experiments were visu-

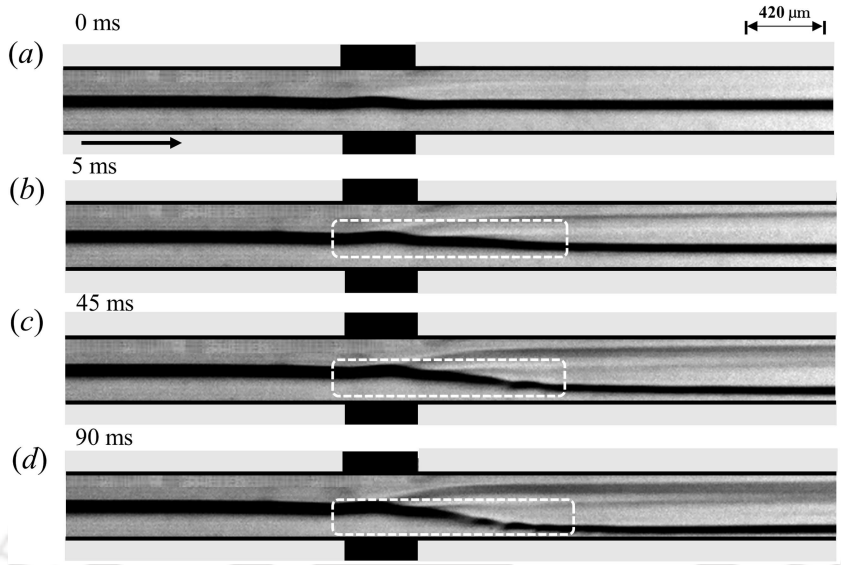

Figure 2.6: Images $(a)-(d)$ show the experimental snapshots after 0 ms, 5 ms, 45 ms, and 90 ms, respectively, depicting the response of a stratified flow of benzene-silicone oil system through the microchannel under applied potential of 300 V ($Ra^{\psi} = 225$). Here, the first image (a) corresponds to the system under 0 V electric potential. The top layer on the image corresponds to benzene and the bottom layer corresponds to silicone oil. The fluids flowed side by side in the channel while the images were taken from the top. The average Re of the base flow was maintained approximately at 0.5. The arrow indicates the direction of flow.

alised using a microscope under 2.5x magnification and recorded using a high speed camera at 500 fps at a resolution of 1280×120 pixels unless stated otherwise. It may be noted here that a higher difference in the viscosities of benzene and silicone oil helped us in capturing the high quality grayscale videos, as reported here. The phenomenon was reproducible for benzene-oleic acid and benzene-soybean oil systems too. However, those results are not reported for the sake of brevity. Figure 2.6(a) shows that the pressure-driven flow rates of the fluids were attuned in such a manner that a steady stratified flow was formed in absence of the external field. Figures 2.6$(b)-(d)$ show the typical evolution of the miscible benzene-silicone oil interface under the influence of electric field. It may be noted here that the top layer shown on the image is benzene while the bottom one is silicone oil. However, in reality the fluids were flown side by side in the channel while the images were taken from the top. On application of the electric field potential through the electrodes, the flow becomes unstable to develop the instabilities, as shown with the help of highlighted rectangular boxes on the images. The images suggest that the applied field

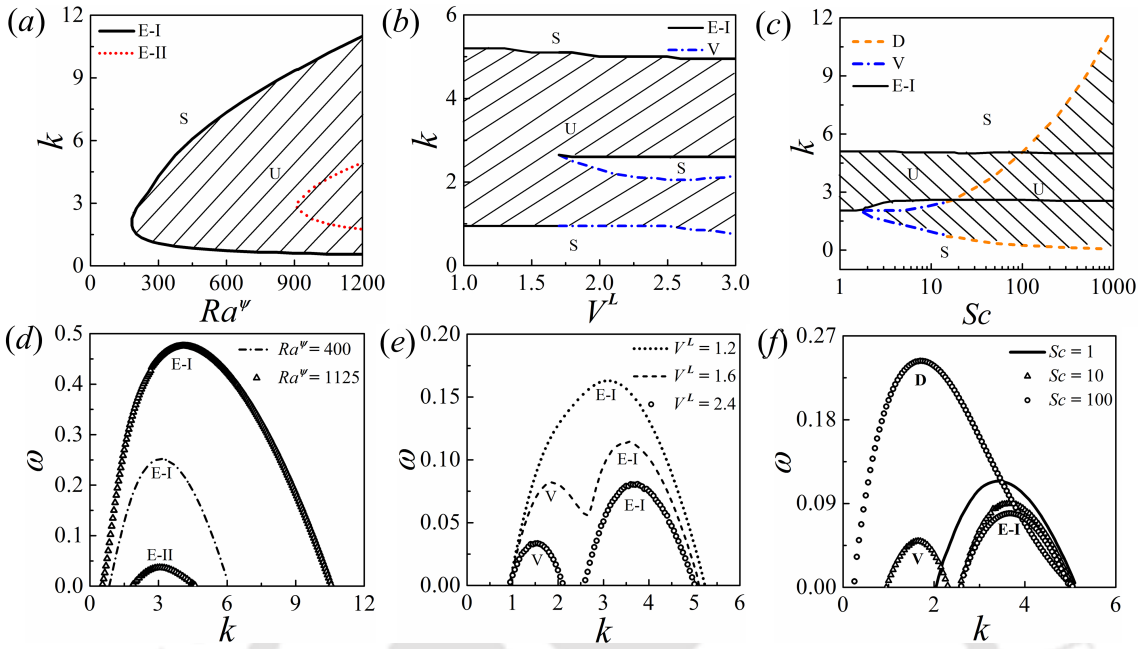

Figure 2.7: Neutral stability plots showing the variations of wavenumber (k) with, (a) electric Rayleigh number Ra^{ψ}, (b) log viscosity ratio V^L, and (c) Schmidt number Sc. The dispersion curves showing the growth rate (ω) versus the wavenumber (k) of the unstable modes with, (d) Ra^{ψ}, (e) V^L, and (f) Sc. In plot (a), the solid line represents the electric field mode I (E-I) and the broken line represents the electric field mode II (E-II). The other parameters for the plots (a) and (d) are, $V^L = 1$, $h = -0.3$, $\delta = 0.02$, $Sc = 10$, and $Re = 0.5$. In the plot (b), the solid lines represent electric field mode I (E-I) and the unevenly broken lines represent the viscous mode (V). The other parameters for the plots (b) and (e) are, $h = -0.3$, $\delta = 0.02$, $Sc = 10$, $Ra^{\psi} = 375$, and $Re = 0.5$. In the plot (c), the solid lines represent E-I-mode, the unevenly broken line represents the V-mode, and the evenly broken line denotes the diffusive mode (D). The other parameters for the plots (c) and (f) are, $V^L = 2$, $h = -0.3$, $\delta = 0.02$, $Ra^{\psi} = 375$, and $Re = 0.5$. The hatched U-regions denote unstable zones whereas S-regions denote the stable zones.

destabilizes the lower viscosity benzene layer and subsequently shifts the diffused interface towards the more viscous silicone oil layer. Under the exposure of a constant electric field intensity, the instability possesses convective waves propagating towards the downstream of the channel owing to the presence of the pressure-driven flow inside the channel. After the onset, the speed of these waves increase with time before reaching a constant value for given field intensity, as shown in the figures 2.6(b)$-$(d).

2.5.2 Theoretical Outlook

The details of the theoretical formulation are deliberated in § 2.4 while the results obtained from the LSA are discussed in this section. We have identified that for the proposed system the effects of Ra^{ψ}, V^L, and Sc, are perhaps the most significant ones because all the different modes of instabilities pertaining to this system are obtained with the variations in the magnitudes of these parameters. The results (except figures 2.13−2.15) correspond to $K_L = 0$ and $E_L = 0$, unless otherwise stated.

Figure 2.7(a) depicts the neutral stability plot showing the variation of the wavenumber (k) with Ra^{ψ} for $V^L = 1$. The plot suggests that the system is unstable to a finite wavenumber mode of instability at low and intermediate values of Ra^{ψ} (solid line). We term this mode as electric field mode I (E-I). At higher values of Ra^{ψ} the system becomes unstable to another finite wavenumber mode of instability (broken line) termed as the electric field mode II (E-II). The wave speed (c_r) of the E-I-mode is found to match with the theoretical average velocity (u_0) of the lower viscosity fluid (1) whereas the wave speed of E-II-mode matches with the mean flow of the higher viscosity fluid (2). This observation helps in inferring that the EHD field can destabilize the lower viscosity fluid at much lower values of Ra^{ψ} to manifest the E-I-mode while the E-II-mode appears at a much higher value of Ra^{ψ} in the higher viscosity fluid 2. The typical ω versus k plots with the variation in Ra^{ψ} are shown in the figure 2.7(d). At $Ra^{\psi} = 400$, only E-I-mode exists (unevenly broken line) whereas at $Ra^{\psi} = 1125$, both E-I and E-II modes (triangular symbols) are present with the E-I-mode characterized by significantly higher growth rates than the E-II-mode.

Figure 2.7(b) illustrates the variation of wavenumber against log viscosity ratio (V^L) for $Ra^{\psi} = 375$. The plot suggests that, at lower values of V^L only the E-I-mode (solid line) can destabilize the flow. In comparison, at higher values of V^L, a much longer wavelength viscous mode (V) (unevenly broken line) appears alongside the E-I-mode (dotted line). At the intermediate values of V^L, ranging from 1.3 until 1.6, a unique bimodal behaviour is observed, as shown by ω versus k plots in figure 2.7(e). The plots clearly suggest that the V-mode arises only when there is a higher viscosity contrast across the diffused interface. Figure 2.7(c) shows the variation of k with Sc for $V^L = 2$ and $Ra^{\psi} = 375$. In this situation, apart from the E-I-mode (solid line), the diffusive D-mode becomes unstable beyond a threshold value of Sc.

The D-mode exhibits a finite wavenumber type behaviour for low to intermediate values of Sc, which signifies a thick and diffusive interface. At higher values of Sc, when the interface is much sharper and thin, the D-mode behaves as a long-wave mode, frequently observed for the immiscible two-phase flows [63,195]. The ω versus k plots in figure 2.7(f) shows the transition of the length scale from the shorter to longer wavelength regime with the increase in the Sc.

In summary, figure 2.7 uncovers four distinctive finite-wavenumber modes to destabilize a two-layer viscosity stratified flow of miscible fluids under the influence of an externally applied electric field. The results suggest the existence of two distinct electric field modes, E-I and E-II, beyond a critical value of Ra^{ψ}. Further, the presence of the V- and D-modes are also observed due to the viscosity stratification and convective transport of the perturbed concentration near the interface, respectively.

In order to evaluate the contributions of the various forces towards the growth of the instability modes discussed above, an energy analysis is carried out. A brief outline of the analysis is provided in appendix A.1. The energy equation relates the rate of change of the disturbance kinetic energy (E_{KE}), with energy changes associated with the Reynolds stress (E_{RS}) , viscous dissipation (E_{VD}), viscosity stratification (E_V), and electric force component (E_E). Figure 2.8 describes the variation of the normalized energy associated with the various terms (E_N) with Ra^{ψ}, V^L, and Sc. It may be noted here that the eigenfunctions used for the energy calculations correspond to that of the most unstable modes. Further, the eigenfunctions are normalized with their maximum absolute values while the energy terms are normalized by the total kinetic energy $\int_{-1}^{1} \left(\left|\tilde{u}\right|^2 + \left|\tilde{w}\right|^2 \right) \mathrm{d}z$. The variation of E_{RS} is not shown in the plots because the energy associated with the Reynolds stresses are negligible for the flows with low Re, reported in this work.

Figure 2.8(a) shows that for the situation with a lower viscosity stratification ($V^L = 1$), the major part of the disturbance energy is generated by the applied electric force, which is reflected in the higher values of E_E. With the increase in electric force (Ra^{ψ}), E_E increases monotonically, which is the cause of the onset of the E-I and E-II modes. In this case, the energy associated with viscosity stratification (E_V), is negligible, and remains nearly unchanged with increment in Ra^{ψ}. The trends of the variation in E_E and E_V with Ra^{ψ} explain well the occurrence of the electric field modes at lower viscosity stratifications, as previously discussed

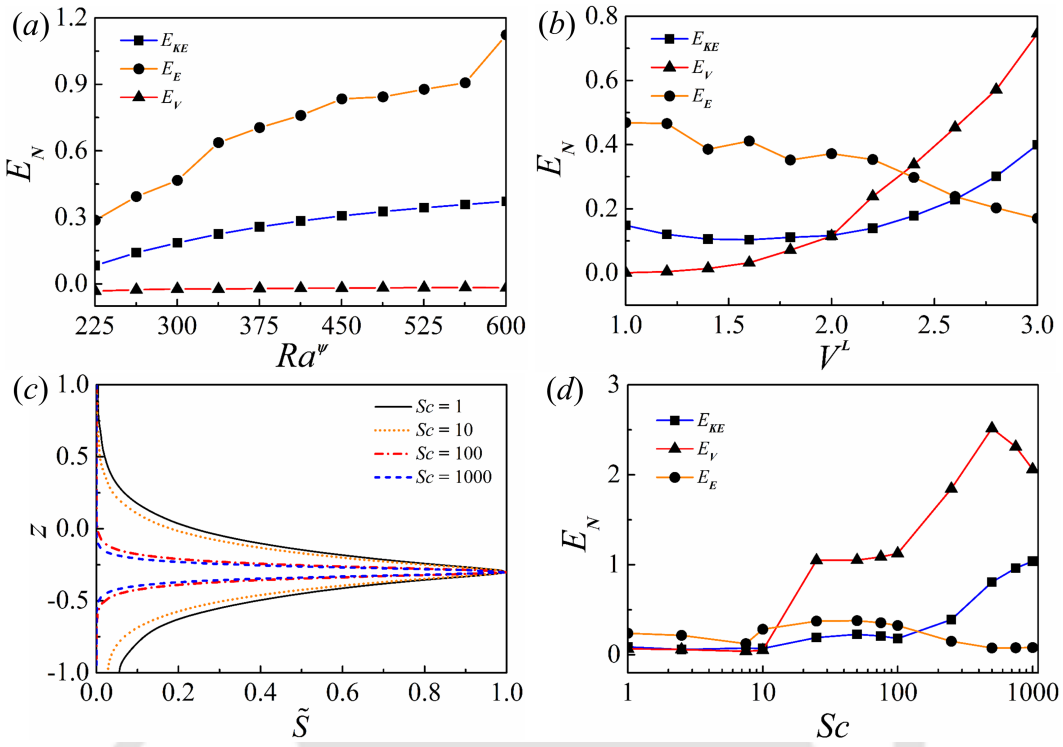

Figure 2.8: The variations of, (a) normalized energy (E_N) with Ra^ψ, (b) normalized energy with V^L, (c) absolute values of normalized perturbation concentration $(\tilde{S})$ with Sc, and (d) normalized energy with Sc. The other parameters for (a) are, $V^L = 1$, $h = -0.7$, $\delta = 0.02$, $Sc = 10$, and $Re = 0.5$. The other parameters for (b) are, $h = -0.3$, $\delta = 0.02$, $Sc = 10$, $Ra^\psi = 375$, and $Re = 0.5$. The other parameters for (c) and (d) are, $V^L = 3$, $h = -0.3$, $\delta = 0.02$, $Ra^\psi = 375$, and $Re = 0.5$.

with the figures 2.7(a) and (d). Figure 2.8(b) depicts the variations of E_N with V^L, which reveals that electric force remains to be the major source of disturbance at lower values of V^L. Hence, for lower viscosity stratifications, only the E-I-mode of instability manifests in the system as depicted in figures 2.7(b) and (e). With the increase in V^L, the energy associated with viscosity stratification increases rapidly, leading to the occurrence of the V-mode of instability along with the E-I-mode. Figure 2.8(c) shows the variation of the absolute values of the normalized perturbation concentration $(\tilde{S})$ for different values of Sc. At lower values of Sc the variation in $\tilde{S}$ is found to be progressive and less steeper near the mixed interface. The variation in $\tilde{S}$ becomes steeper across the interface at higher values of Sc, which gives rise to the onset of the D-mode of instability. Figure 2.8(d) shows the variation of E_N with Sc. The plot suggests that at lower values of Sc, the disturbance kinetic energy is produced mainly by the applied electric force, which is indicated by the higher

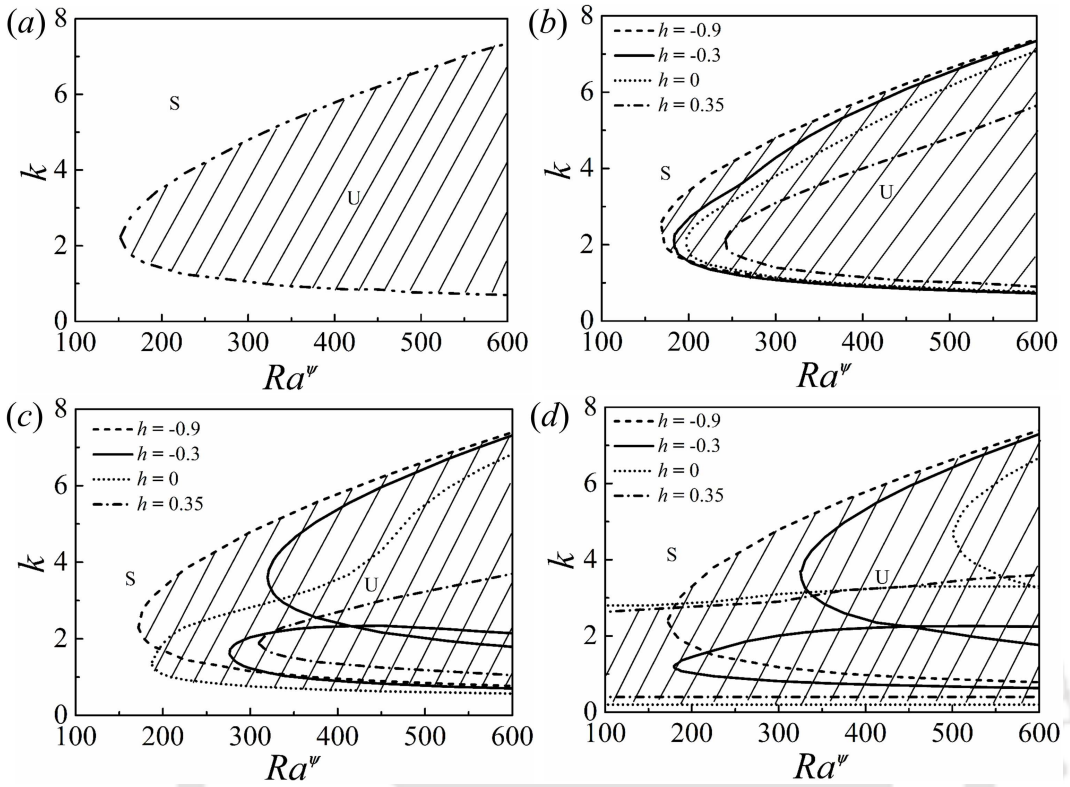

Figure 2.9: Neutral stability plots showing the variation of wavenumber (k) vs. electric field Rayleigh number (Ra^{ψ}) for, (a) $V^L = 0$, (b) $V^L = 1$, (c) $V^L = 2$, and (d) $V^L = 3$. In the plots (b)−(d) the evenly broken, solid, dotted, and unevenly broken lines show the situations with $h = -0.9, -0.3, 0,$ and 0.35, respectively. The other parameters are $Sc = 10$, $\delta = 0.02$, and $Re = 0.5$. The hatched U-regions denote unstable zones whereas S-regions denote the stable zones.

values of E_E. At higher values of Sc, E_V contributes more towards the generation of disturbance energy compared to E_E, which causes the D-mode to occur alongside the E-I-mode as previously observed in figures 2.7(c) and 2.7(f).

2.5.2.1 Parametric Study

In this section we discuss the role of various parameters in influencing the stability of the system. Figure 2.9(b) shows the variation of k with Ra^{ψ}, for different values of h, which signifies the distance of the diffused interface from the datum, $z = 0$, as previously shown in figure 2.3(a). It may be noted here that the variation of h from -1 to 1 also signifies the progressive filling of the channel with a more viscous fluid. Figure 2.9(a) shows the situation when $V^L = 0$, which indicates

that the channel is entirely filled with the low viscosity fluid. The plot shows that the system is unstable to the E-I-mode of instability. In the figures 2.9(b)−(d) the evenly broken, solid, dotted, and unevenly broken lines show the situations with $h = -0.9,\ -0.3,\ 0,$ and 0.35, respectively, which signify that the channel is filled with thin (e.g. $h = -0.9$) to thick (e.g. $h = 0.35$) layer of more viscous fluid in the fully developed stratified flow.

Figure 2.9(b) shows the neutral stability curves when $V^L = 1$, for different values of h. The plot suggests that as the proportion of the more viscous fluid increases inside the channel, the critical Ra^ψ for the E-I-mode progressively increases owing to the increase in the overall viscous resistance. The neutral stability curves in figure 2.9(c) for $V^L = 2$ show the presence of the E-I-mode for the situations with a thinner layer of more viscous fluid. The plot shows the appearance of the twin E-I and V-modes with shorter and longer wavelengths, respectively, as the thickness of the layer with more viscosity is increased at $h = -0.3$. The V-mode arises due to the viscosity stratification across the diffused interface, while the origin of the E-I-mode can be attributed to the externally applied electric field, as discussed previously. Notably, the E-I-mode is found to have a much shorter wavelength, compared to the V-mode. The V-mode becomes unstable at a much lower value of Ra^ψ when the thickness of the more and less viscous fluids are identical at $h = 0$. With further increase in the thickness of the higher viscosity fluid, the increase in the viscous resistance inside the channel enforces the V-mode to appear at a higher value of Ra^ψ for $h = 0.35$. Again, the E-I-mode for this plot appears at a much higher value of Ra^ψ, which is not shown. Figure 2.9(d) shows the results for $V^L = 3$, which are very similar in nature as it is observed in the figure 2.9(c). However, for $V^L = 3$, the V-mode becomes unstable even in the absence of externally applied electric field beyond a value of h as can be seen for $h = 0$ and $h = 0.35$. Thus, the V-mode is found to have similar characteristics as the shear mode of instability in the viscosity stratified flow of miscible fluids, which has been reported in previous works [199].

Figure 2.10(a) depicts the variations of the dominant growth rate (ω_m) and wavelength (λ_m) representing the most unstable disturbances with Ra^ψ for $V^L = 1$. The plot suggests that for low and intermediate values of Ra^ψ, the system manifests the E-I-mode (black symbols) whereas at higher values of field intensities E-II-mode (red symbols) appears along with the E-I-mode. Figure 2.10(b) shows the variations of ω_m and λ_m with h across the channel for three different values of Ra^ψ. Again, in this plot the variation of h from -1 to 1 signify the progressive filling of the channel

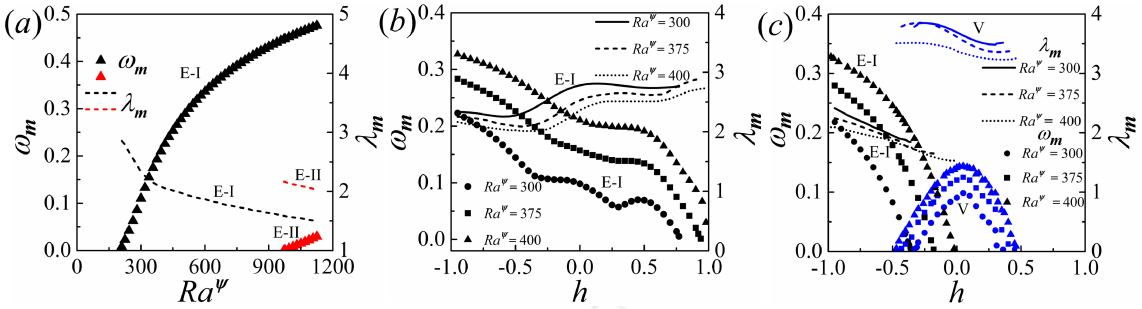

Figure 2.10: The plot (a) shows the variations of dominant growth rate (ω_m, denoted by symbols) and wavelength (λ_m, denoted by lines) with Ra^{ψ}. The plots (b) and (c) show the variations of dominant growth rate (ω_m, denoted by symbols) and wavelength (λ_m, denoted by lines) with h, at different values of Ra^{ψ} for $V^L = 1$ and $V^L = 2$, respectively. The other parameters considered for (a) are, $V^L = 1$, $h = -0.3$, $\delta = 0.02$, $Sc = 10$, and $Re = 0.5$. The other parameters considered for (b) and (c) are, $h = -0.3$, $\delta = 0.02$, $Sc = 10$, and $Re = 0.5$.

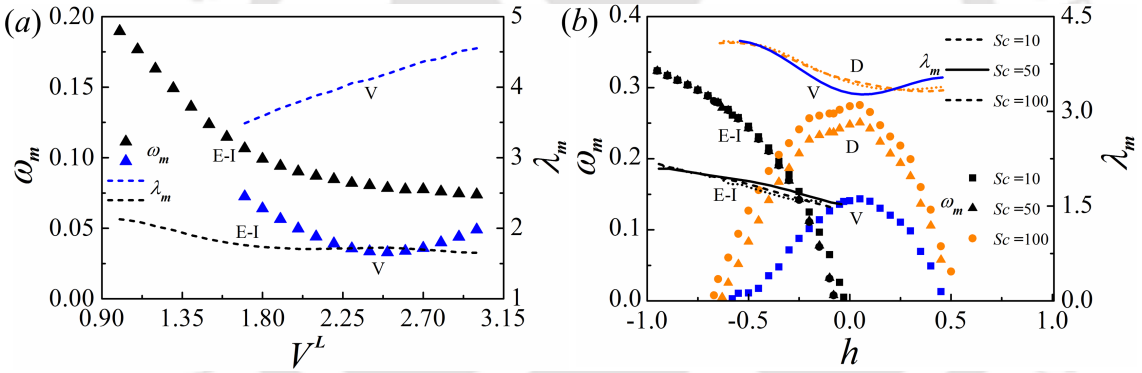

Figure 2.11: The plot (a) shows the variations of dominant growth rate (ω_m, denoted by symbols), and wavelength (λ_m, denoted by lines) with V^L. The other parameters considered are, $h = -0.3$, $\delta = 0.02$, $Sc = 10$, $Ra^{\psi} = 375$, and $Re = 0.5$. The plot (b) shows the variations of dominant growth rate (ω_m, denoted by symbols) and wavelength (λ_m, denoted by lines) with h for different values of Sc. The other parameters are, $V^L = 2$, $\delta = 0.02$, $Ra^{\psi} = 375$, and $Re = 0.5$.

with the more viscous fluid. The plot suggests that when $V^L = 1$, the E-I-mode progressively loses its strength (ω_m reduces) when the channel is filled with the more viscous fluid provided Ra^{ψ} is kept constant. Subsequently, a marginal increase in λ_m of the E-I-mode is also observed. The plot also shows that the time and length scales of the E-I-mode reduce with the increase Ra^{ψ} because the magnitude of ω_m increases and λ_m reduces with the increase in Ra^{ψ}. In comparison, the plot (c) shows that for higher values of $V^L (V^L = 2)$, the E-I-mode is the dominant one

at lower values of h. However, the reduction in ω_m of the E-I-mode happens at a much faster rate with the increase in h while a subdominant V-mode appears due to the combined influence of electric field and viscosity stratification at intermediate values of h. At even higher values of h, the E-I-mode disappears, and the V-mode becomes the dominant mode. Interestingly, at intermediate values of h both the modes co-exist to engender a bimodal instability. The plot suggests that the time and length scales of both the E-I-mode and V-mode reduce with the increase in Ra^{ψ} because the magnitude of ω_m increases and λ_m reduces with the increase in Ra^{ψ} as previously observed in the case of $V^L = 1$. Thus, externally applied electric field can stimulate both of these finite wavenumber E-I-mode and V-mode at lower Re of the stratified flow of miscible fluids.

Another important parameter, which majorly influences the nature of the in-

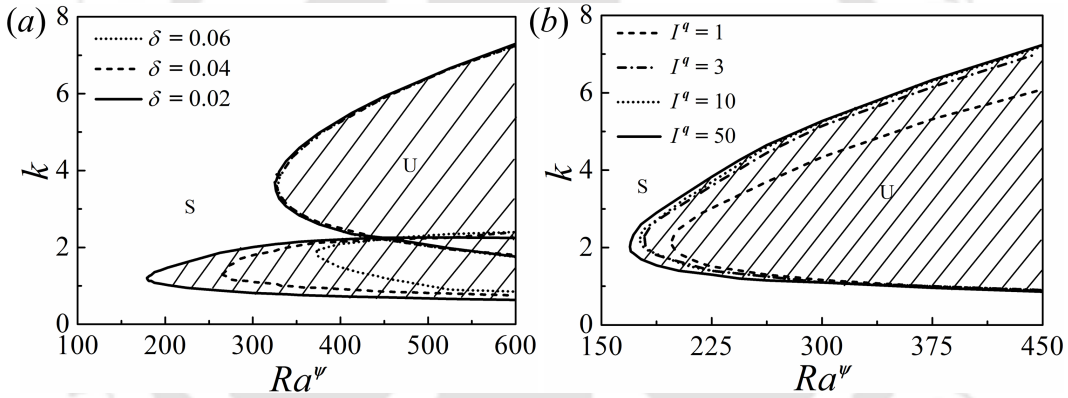

Figure 2.12: Neutral stability plots showing the variation of k with Ra^{ψ} for, (a) different values of thickness of the mixed interface, δ, and (b) different values of injection level I^q. The other parameters for the plot (a) are, $V^L = 2$, $h = -0.3$, $Sc = 10$, and $Re = 0.5$ and (b) are, $V^L = 1$, $h = -0.3$, $\delta = 0.02$, $Sc = 10$, and $Re = 0.5$. The hatched U-regions denote unstable zones whereas S-regions denote the stable zones.

stabilities in the present setting, is the viscosity contrast between the fluids defined by log viscosity ratio V^L. Figure 2.11(a) shows the variations of ω_m and λ_m with V^L. The plot suggests that when the viscosity contrast across the diffused interface is less the E-I-mode is the dominant one whereas with progressive increase in V^L, the V-mode can become the dominant one (not shown here). The plot also shows a much smaller length scale of the E-I-mode as compared to the V-mode. It is important to note here that Sc is another crucial parameter for defining the stability of miscible flows. The effect of Sc on various configurations of miscible flows have been

discussed in detail in previous literature [63]. However, the presence of electric field in this regard makes the study more interesting. It has been discussed earlier that Sc number contributes to the appearance of the D-mode beyond a critical threshold. Figure 2.11(b) shows the variation of ω_m and λ_m with h for three different values of Sc. It can be inferred from the figure that the E-I-mode remains almost unaffected by the increase in Sc. However, as the interface becomes thinner and less diffusive (higher Sc, filled circular and triangular symbols) the V-mode which occurs at $Sc = 10$ undergoes transition to the D-mode which is accompanied by a drastic increase in the growth rates of the most unstable perturbations. At higher values of h, again the increase in the viscous resistance owing to the presence of the more viscous liquid reduces the growth rate of the D-mode.

It is now well understood that the thickness of the mixed interface plays a sig-

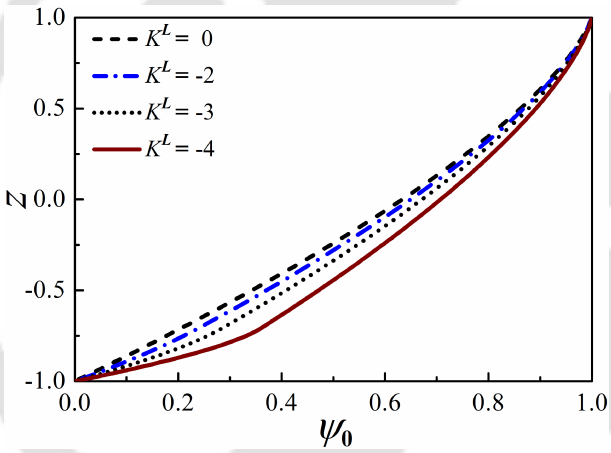

Figure 2.13: Base-state profile for electric potential (ψ_0) for different values of log mobility ratio K^L. The other parameters are, $h = -0.3$ and $\delta = 0.02$.

nificant role in determining the stability characteristics of the system [199]. While a thicker mixed interface damps a perturbation due to molecular diffusion, a thin interface with restricted diffusion makes a perturbation unstable owing to steep viscosity profiles near the interfacial region. The neutral stability plot shown in figure 2.12(a) describes the effect of δ on the stability behaviour for $V^L = 2$. While the E-I-mode remains unaffected by δ, the V-mode exhibits profound stabilization with increase in δ. Apart from the interfacial thickness, the level of charge injection, I^q, can also influence the critical conditions of the E-I-mode. Figure 2.12(b) shows that the critical Ra^ψ reduces significantly with the increase in I^q. This observation is in qualitative agreement with the results of Zhang *et al.* [215] for a single fluid.

The difference in ionic mobility in the two fluids can be a critical parameter in governing the stability characteristics of the system under study. The base-state profile for electric potential ψ_0 is shown in figure 2.13 for different values of K^L. The variation of ionic mobility across the channel is consequential in the distribution electric potential across the channel. In case of uniform mobility across the channel ($K^L = 0$), the base-state profile of electric potential is progressive, as shown in figure 2.13. However, with decrease in the value of ionic mobility in the higher viscosity fluid, there is a build-up of charge in the mixed interfacial region, which is depicted by the cusps in the profiles of the electric potential ψ_0 near the mixed interfacial region for $K^L = -2$, $K^L = -3$, and $K^L = -4$. Figure 2.14(a) depicts the neutral stability plots for different values of K^L, at $V^L = 1$ and $h = -0.7$. It can be inferred from the plot that, as the mobility values decrease in the higher viscosity fluid, the critical electric field needed to trigger the E-I-mode of instability increases. However, with increase in the proportion of more viscous fluid ($h = -0.3$), there is substantial increase in the growth rates (ω_m) at $K^L = -3$ and $K^L = -4$, compared to $K^L = 0$ as seen from figures 2.14(b) and 2.14(c). The instabilities also exhibit much shorter wavelengths compared to the finite wavenumber E-I-mode of instability. We hereafter, refer to this mode as the K-mode of instability.

Figure 2.14(d) shows the variation of ω_m with the location of the mixed layer (h). It can be inferred from the plot that, for greater proportions of less viscous (higher mobility) fluid inside the channel, the system becomes unstable to the E-I-mode of instability (triangular symbols). The interface is located close to the walls when the proportion of either fluid is very high inside the channel. Thus, any perturbation occurring within the interfacial region due to difference in ionic mobility is stabilized by viscous dissipation. Thus, only E-I-mode occurs for high proportions of less viscous fluid inside the channel. With increase in the proportion of the more viscous (lesser mobility) fluid, as the location of the interface h shifts towards the centre of the channel, the instability is governed by the K-mode with higher growth rates and lower wavelength as compared to the E-I-mode. The K-mode occurs in the mixed interfacial region due the steep gradient in charge density in the region caused by the difference in ionic mobility between the fluids. Again, it can be seen from figures 2.14(e) and 2.14(f) that for higher viscosity stratification the stability characteristics change on varying the ionic mobility of the fluids. For $K^L = -4$, as depicted by figure 2.14(f), only the K-mode of instability exists, unlike the V-mode and the E-I-mode depicted by figure 2.14(e) for ($K^L = 0$). It may be noted that

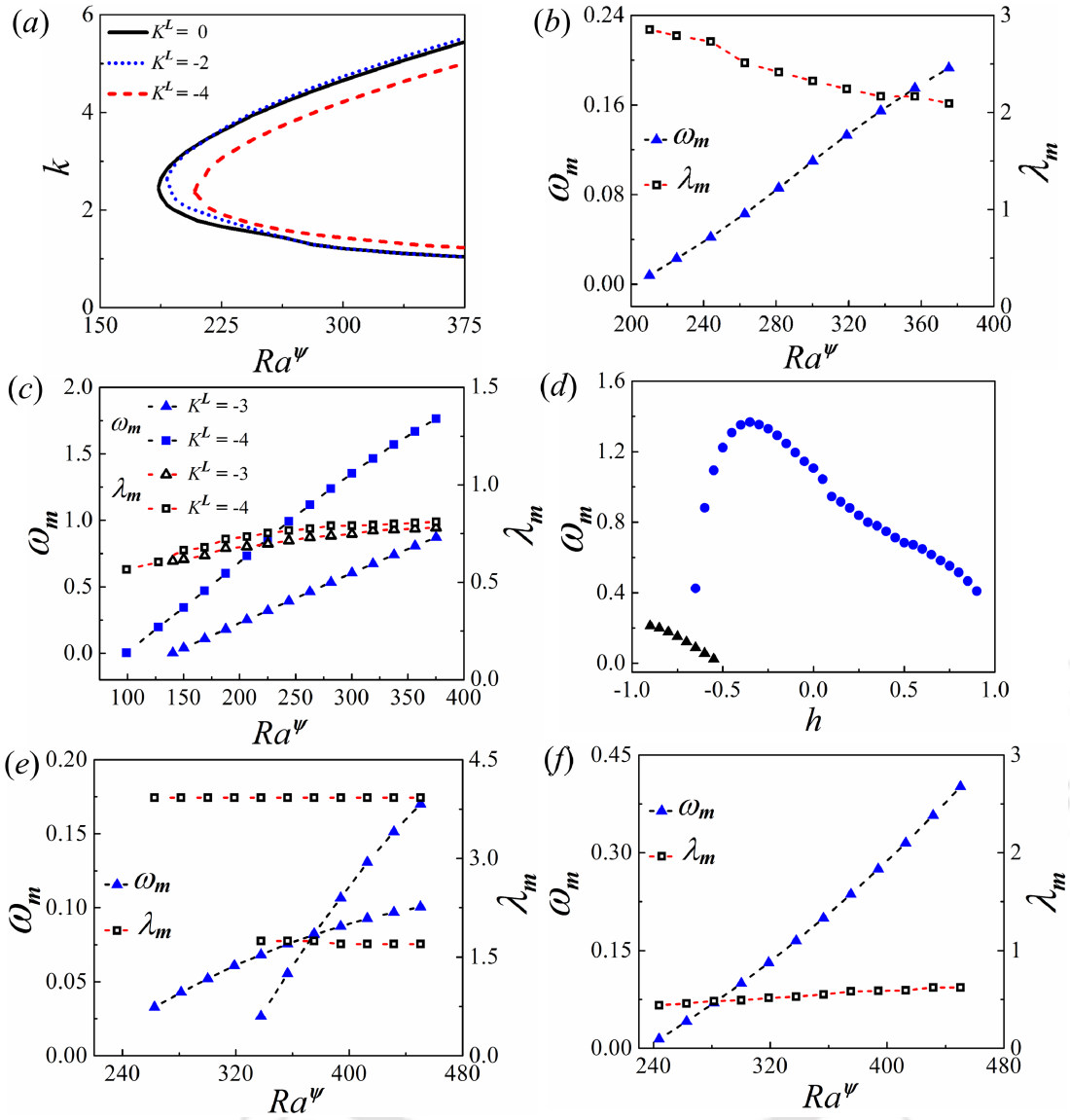

Figure 2.14: (a) Neutral stability curves showing the variation of wavenumber (k) with electric Rayleigh number (Ra^ψ) for different values of K^L. The other parameters are, $V^L = 1$, $h = -0.7$, $\delta = 0.02$, $Sc = 10$, and $Re = 0.5$. Variation of the growth rate of the most unstable modes (ω_m) with Ra^ψ for (b) $K^L = 0$, (c) $K^L = -3$ and $K^L = -4$. The other parameters used for (b) and (c) are,$V^L = 1$, $h = -0.3$, $\delta = 0.02$, $Sc = 10$, and $Re = 0.5$. (d) Variation of the growth rate of the most unstable modes (ω_m) for different values of h. The other parameters used are, $V^L = 1$, $K^L = -4$, $Ra^\psi = 300$, $\delta = 0.02$, $Sc = 10$, and $Re = 0.5$. Variation of the growth rate of the most unstable modes (ω_m) with Ra^ψ for $V^L = 2$ and (e) $K^L = 0$ and (f) $K^L = -4$. The other parameters are, $h = -0.3$, $\delta = 0.02$, $Sc = 10$, and $Re = 0.5$.

with further increase in viscosity stratification, the V-mode also occurs in conjunction with the K-mode (not shown here).

Dielectric constant is another important parameter that can be consequential to

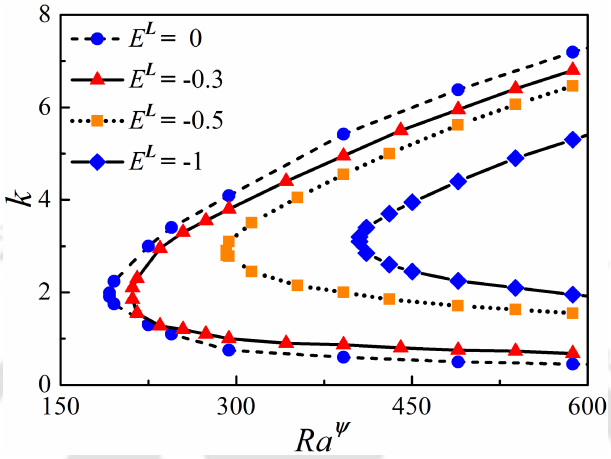

Figure 2.15: (a) Neutral stability curves showing the variation of wavenumber (k) with electric Rayleigh number (Ra^ψ) for different values of E^L. The other parameters are, $V^L = 1$, $K^L = 0$, $h = -0.3$, $\delta = 0.02$, $Sc = 10$, and $Re = 0.5$.

the stability characteristics of the system under study. Figure 2.15 shows the neutral stability curves depicting the variation of k with Ra^ψ for different values of E^L. The plot predicts increase in the critical values of Ra^ψ with increase in the permittivity stratification inside the channel compared to the case of uniform permittivity ($E^L = 0$). It may be noted here that, in this work the higher permittivity is used as the characteristic permittivity. Hence, negative (positive) sign in the values of E^L, signifies that the permittivity of fluid 2 is lesser (higher) than that of fluid 1. It can be inferred from figure 2.15 that, for slight differences in the values of electric permittivity of the two fluids, the critical conditions for the onset of the instabilities remain very close to each other. Significant changes in the onset conditions are only observed for larger differences in the values of dielectric constants of the two fluids. Since, this study is motivated for fluids with nearly similar dielectric constants, we restrain an in depth analysis of the consequences of larger contrasts in dielectric constants.

2.5.3 A Comparison between Experiments and Theory

In this section, a comparison between the data obtained from the experiments, LSA, and numerical simulations has been reported. Here, we particularly focus on the

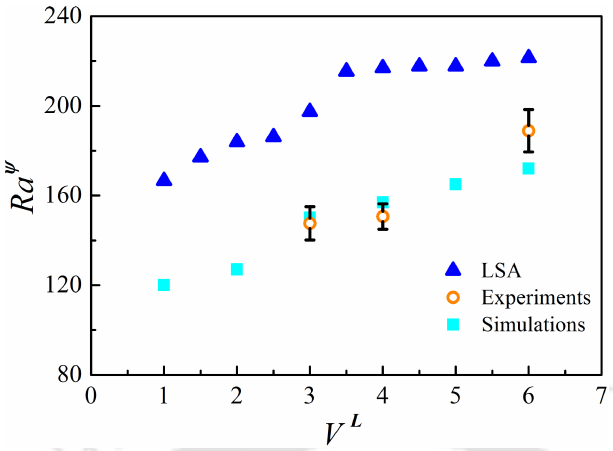

Figure 2.16: Variation of Ra^{ψ} with V^L depicted by LSA, experiments, and numerical simulations. . The other parameters used for LSA are, $h = -0.6$, $\delta = 0.04$, $K^L = 0$, $E^L = 0$, $Sc = 500$, and $Re = 0.5$. The other parameters used for simulations are, $K^L = 0$, $E^L = 0$, $Sc = 500$, and $Re = 0.5$. The experimental values denote benzene-oleic acid ($V^L = 3$), benzene-soybean oil ($V^L = 4$), and benzene-silicone oil ($V^L = 6$) fluid pairs. The average Re maintained during the experiments was 0.5. The error bar represents the standard deviation of three experiments.

critical voltage required to initiate the instability in the two-layer stratified flow of miscible fluids. Due to limitations in measurement techniques, the values of h and δ used for the theoretical calculations are assumed to emulate the experimental conditions closely. The precise calculation of thickness of the mixed layer δ, for a dynamic interface developed inside a microchannel is challenging. Further, the characterizations of such a diffuse interface between miscible fluids require sophisticated techniques, and thus, not attempted. In such a scenario, the value of δ was not measured directly from the experiments, but rather approximated with a simple order-of-magnitude analysis and CFD simulations the details of which are provided in appendix A.3. The three experimental values denote benzene-oleic acid ($V^L \approx 3$), benzene-soybean oil ($V^L \approx 4$), and benzene-silicone oil ($V^L \approx 6$) fluid pairs. Figure 2.16 shows that the LSA over-predicts the corresponding experimental and simulation values. It is expected since the non-linearity associated with the actual experimental phenomena are not considered in the LSA. In addition, the other parameters such as the location of the mixed layer (h), thickness of the mixed layer (δ), the value of Sc, are set for the LSA, to tentatively emulate the experimental conditions, as the measurement of these quantities is exceedingly challenging in the reported experimental set up. Variation in ionic mobility and dielectric constants

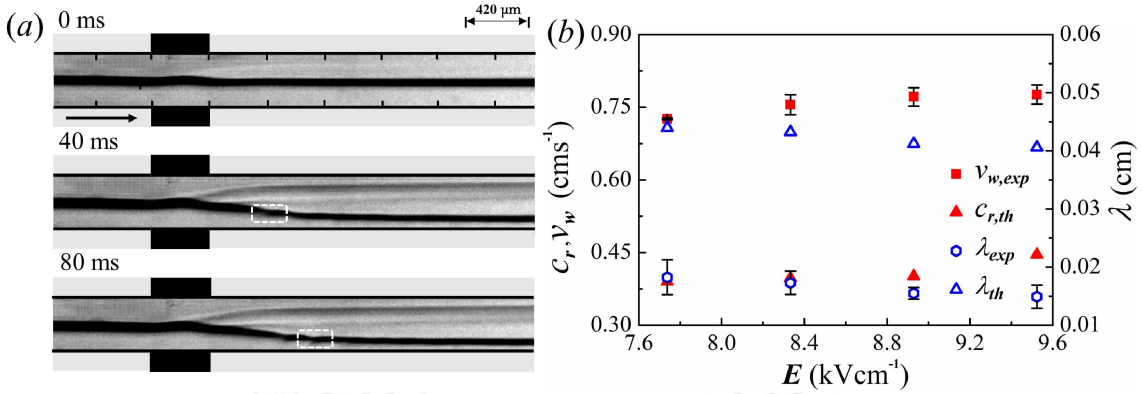

Figure 2.17: The plot (a) shows the experimental snapshots of a silicone oil-benzene system under application an electric field of 9.5 kVcm^{-1} at different time instances. The plot (b) demonstrates the variation of experimental and theoretical wave speeds (v_w, c_r) and wavelengths (λ) with increasing electric field intensity ($\boldsymbol{E}$). The hollow symbols (blue) denote the values of wavelengths, whereas the solid symbols (red) denote the wave speeds. The theoretical parameters used for the plot are, $h = -0.6$, $\delta = 0.02$, $Sc = 500$, and $V^L = 6$. The error bars in the experimental points are twice the standard deviations obtained from three experiments. The average Re maintained during the experiments was 0.5. The images in (a) correspond to the top view of the flow configuration. In the image the top (bottom) layer corresponds to benzene (silicone oil) while in reality they were flown side by side. The videos were recorded at 500 fps under 2.5x magnification. The arrow in (a) indicates the direction of the flow.

of the fluids, which are not considered in the LSA, can also be instrumental in determining the onset conditions as hinted in the figures 2.14 and 2.15. In absence of exact experimentally measured values of the ionic mobility and dielectric constant, the LSA was carried out considering equal ionic mobility and dielectric constant for both the fluids. Further, the injection of charges from the electrodes is considered to be autonomous. However, it has been shown in earlier literature [224] that, for moderate injection levels, a realistic field-dependent injection law can yield results different from that of the autonomous injection case. Nevertheless, it can be seen that there is a reasonable qualitative agreement between the onset conditions obtained from theory and experiments. It is anticipated that, various assumptions made, for the purpose of simplification of the mathematical model, when addressed accurately, would yield better agreement between the experimental and theoretical predictions.

Figure 2.17(a) shows experimental snapshots of the top view of the instabilities

of a benzene-silicone oil system at different time intervals when exposed to an electric field potential of 400 V ($\boldsymbol{E}$ = 9.5 kVcm^{-1}). Again, it may be noted here that the top layer shown in the image is benzene while the bottom one is silicone oil. However, in reality the fluids were flown side by side while the images were taken from the top. The images show the progressive linear undulations near the interface and subsequent travelling waves towards the downstream of the channel under the exposure of electric field. Figure 2.17(b) shows a comparison between the theoretically calculated wavelengths (λ) and wave speeds (c_r), and their corresponding experimental values. In order to experimentally measure the wavelength and wave speed of the unstable waves, the system was subjected to DC electric fields before the response was recorded. The frames extracted from the videos were then analysed to measure the required quantities. The wave speed was measured by tracking a wave over a particular distance towards the downstream, and then estimating the time required for the motion, as shown by the boxes in figure 2.17(a).

The experimental wavelength and wave speed was compared with the wavelength and speed of the E-I-mode obtained from linear stability analysis. It can be seen from figure 2.17(b) that the experimental and theoretical wavelengths are of the order of $\sim 10^{-2}$ cm, while the wave speeds are found to be of the order of $\sim 10^{-1}$ cms^{-1}. The plot also shows that the wavelengths obtained from the experimental and theoretical analyses show the same qualitative decreasing trend, whereas the wave speeds exhibit an increasing trend, with increase in the strength of the applied electric field. Again, the plot shows that the experimentally observed quantities are slightly different from the values predicted theoretically, which can be attributed to various factors mentioned previously.

2.5.4 Experimental and Simulation Results: Non-linear, Time-periodic, and Unsteady Regimes

Apart from the unstable linear modes, the experiments also uncovered the presence of interesting non-linear, time-periodic, and unsteady regimes in the two-layer stratified flow of miscible fluids under the influence of external EHD field inside a microchannel. In this section, we investigate the various flow patterns obtained during electroconvection when the applied field intensity is on the higher side. Upon application of electric potential to the system after development of a steady flow profile, four distinctive disturbance patterns are observed in the system as demonstrated

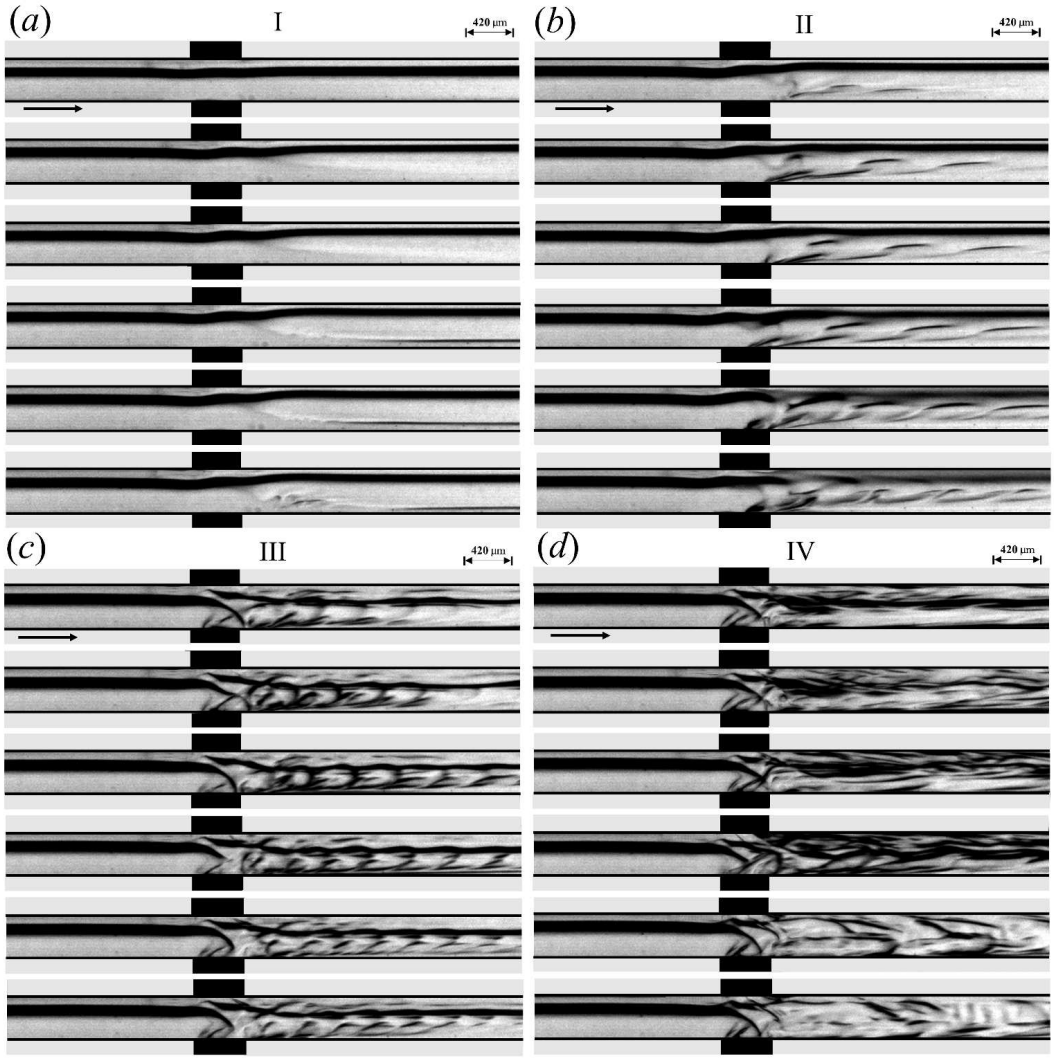

Figure 2.18: Experimental micrographs showing the response of a stratified flow of benzene-silicone oil system through the channel under application of ramp electric fields of strengths, (*a*) 0−300 V, (*b*) 300−600 V, (*c*) 600−900 V, and (*d*) 900−1500 V. The first image in the image-set (*a*) corresponds to the system under 0 V electric field potential. The four regimes were distinguished, namely I, II, III, and IV, as shown on the image-sets. The applied voltage was gradually increased from 0 V−1500 V in 20 s, allowing 5 s to stabilize each. Experiments were viewed with the help of a microscope under 2.5x magnification under the transmission mode. The videos were recorded at 500 fps. The images correspond to the top view of the flow configuration. The top layer corresponds to benzene and the bottom layer corresponds to silicone oil. The average *Re* maintained during the experiments was 0.5. The arrow indicates the direction of the flow.

in figure 2.18. The image-sets in the figures 2.18(a)−2.18(d) qualitatively identifies these instability regimes labelled as I, II, III, and IV, observed upon application of electric field from 0−35 kVcm^{-1}. In these images the layer shown at the top (bottom) corresponds to benzene (silicone oil). In these experiments, the voltage was ramped up in 20 s in such a manner that the four quarters correspond to ramps of 0−300 V, 300−600 V, 600−900 V, 900−1500 V, respectively. The image-set shown in figure 2.18(a) corresponds to the regime I, which is in response to the application of 0−300 V electric potential. In this regime, upon crossing a threshold voltage, the linear instability is first triggered in the less viscous fluid layer, which grows with the increase in the applied voltage. The characteristics of the instabilities in this regime have already been discussed in the previous sections. It may be noted here that these instabilities are reversible in nature because turning off the electric field again leads to the formation of the two-layer stratified flow in short time. The image-set in figure 2.18(b) corresponds to the regime II, obtained during application of 300−600 V electric potential. This regime is marked by the generation of repeated instability patterns at the downstream of the channel, which qualitatively resemble the time-periodic von Kármán vortex street in appearance. Upon further increase in voltage from 600−900 V, regime III is identified as shown in the image-set in the figure 2.18(c). In this situation, the time-periodic flow patterns start mixing with each other alongside having a smaller length scale and higher frequency of ejection of flow structures as compared to regime II. Finally, the voltage increment in the range of 900−1500 V, results in regime IV, depicted in the image-set of figure 2.18(d). The images illustrate the onset of a chaotic regime of flow instability where the periodic ejections of flow patterns having higher frequency and smaller length scale intermix to stimulate a ready mixing of the miscible layers.

The CFD simulations also predict qualitatively similar flow structures upon application of electric field to a stratified flow of two miscible fluids through a channel. Figure 2.19 depicts the concentration surface plot of a stratified flow of benzene-silicone oil ($V^L = 6$) at $Ra^\psi = 225$. The flow is undisturbed at $t^* = 0$ in the absence of electric field. The EHD instability sets into the system upon application of electric field, and a vortex street similar to the experimental regimes II and III have been observed in the figure 2.19. The simulations mimic the experimental findings of reduction of the size and time scale of vortex generation on increasing the electric field, which is depicted in figure 2.20. The figure shows the concentration surface plots of the benzene-silicone oil system at different values of Ra^ψ. It can be seen

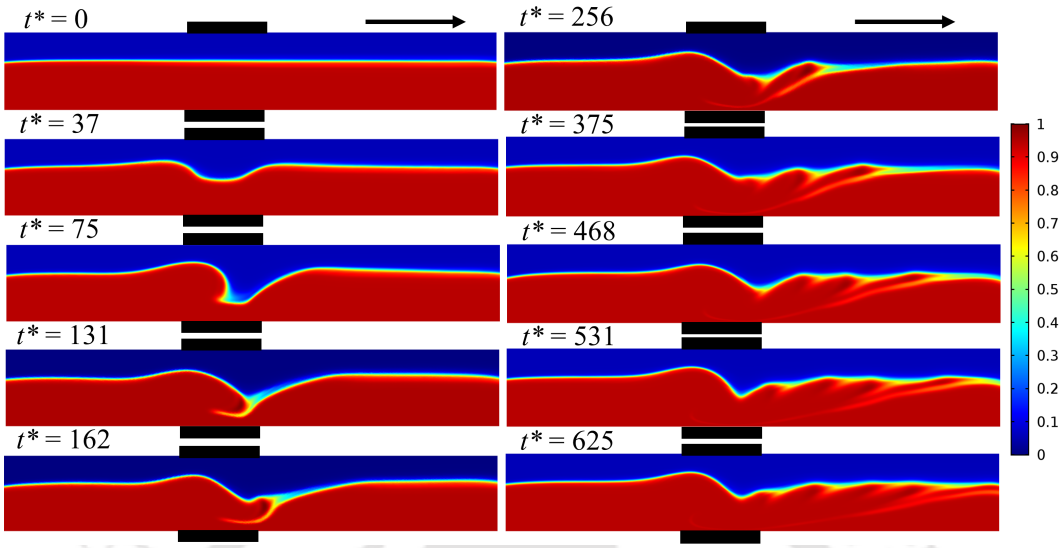

Figure 2.19: Computational snapshots showing the concentration surface plot of a stratified flow of silicone oil-benzene ($V^L = 6$) through the channel at $Ra^\psi = 225$. Here, t^* represents non-dimensional time. The other parameters used for the simulation are, $K^L = -4$, $E^L = -0.15$, $Sc = 700$, $I^q = 1$, and $Re = 0.5$. The arrows on the images indicate the direction of the flow. The black rectangles outside the channel represent the electrodes. A positive potential is applied to the top electrode while the bottom electrode is grounded.

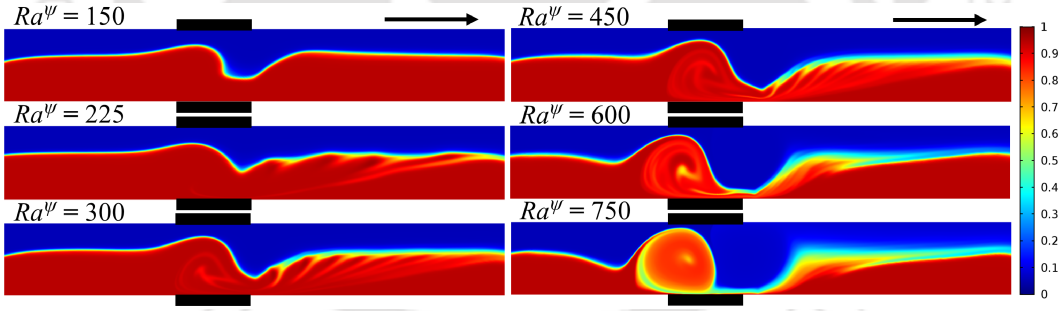

Figure 2.20: Computational snapshots showing the concentration surface plot of a stratified flow of silicone oil-benzene ($V^L = 6$) through the channel at different values of Ra^ψ at $t^* = 300$. It may be noted here t is normalized considering $\Psi_0 = 300$ for maintaining uniformity in reporting the results. The other parameters used for the simulation are, $K^L = -4$, $E^L = -0.15$, $Sc = 700$, $I^q = 1$, and $Re = 0.5$. The arrows on the images indicate the direction of the flow. The black rectangles outside the channel represent the locations of the electrodes. A positive potential is applied to the top electrode while the bottom electrode is grounded.

from the figure that the size of the vortices decrease with increasing from $Ra^\psi = 225$ to $Ra^\psi = 450$ accompanied by increase in the frequency of vortex shedding. This

behaviour is qualitatively similar to the experimental observations reported in figure 2.18. It may be noted here that the simulation results are reproducible with other fluid pairs (different V^L) and also considering liquids with equal ionic mobility ($K^L = 0$), however, the results are not discussed here for the sake of brevity.

In order to characterize regimes II and III shown in figure 2.18, the frequency

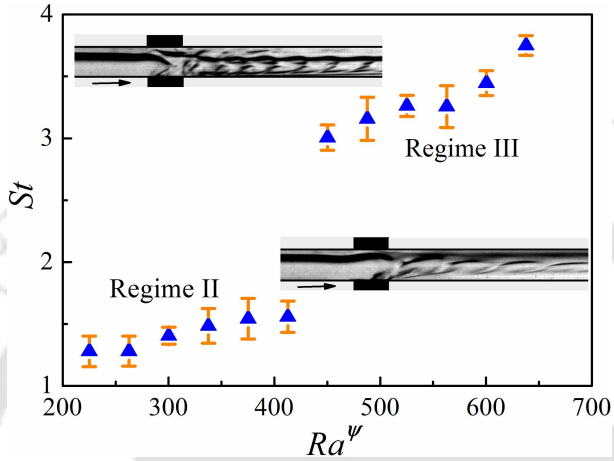

Figure 2.21: Variation of Strouhal number (St) with electric field Rayleigh number (Ra^{ψ}) in regimes II and III, for a benzene-silicone oil system under DC voltage input. The average Re maintained during the experiments was 0.5. The arrow indicates the direction of the flow.

of vortex shedding is correlated to the strength of the applied electric field. For this purpose, we analyse the variation of Strouhal number (St) with electric field Rayleigh number (Ra^{ψ}). The experimental Strouhal number (St) is defined as, $St = \dfrac{fR}{U}$, where f is the frequency of shedding, R is the characteristic length, and U is the average flow velocity. In these experiments, the benzene-silicone oil system was subjected to DC voltage input in the range of 300−850 V at increments of 50 V. The system responded by the generation of vortices, which were recorded and analysed simultaneously. The frequency of the vortex cycles generated per second (f) at each of the applied electric field was calculated from the frames extracted from the recorded videos. Figure 2.21 shows the variation of St with Ra^{ψ}, for regimes II and III. The figure suggests that for both the regimes II and III, the frequency of vortex generation increases (increasing St) with the strength of the applied field (increasing Ra^{ψ}). The higher values of St in regime III indicate larger frequencies of the vortices as compared to regime II, which can be attributed to higher electrical force in regime III compared to regime II. Further, the regimes II and III can also

be differentiated by abrupt jump observed in the values of St. Interestingly, the experimental time scale of vortex generation, $t_v \sim \mathrm{O}\,(10^{-2}\,\mathrm{s})$, is found to be very close to the theoretical one as, $t_v \sim \mathrm{O}\,(10^{-2}\,\mathrm{s}) \sim \dfrac{RV^L\eta_1}{K\psi_0 U}$.

We introduce a parameter ξ to quantify the amount of perturbation instilled

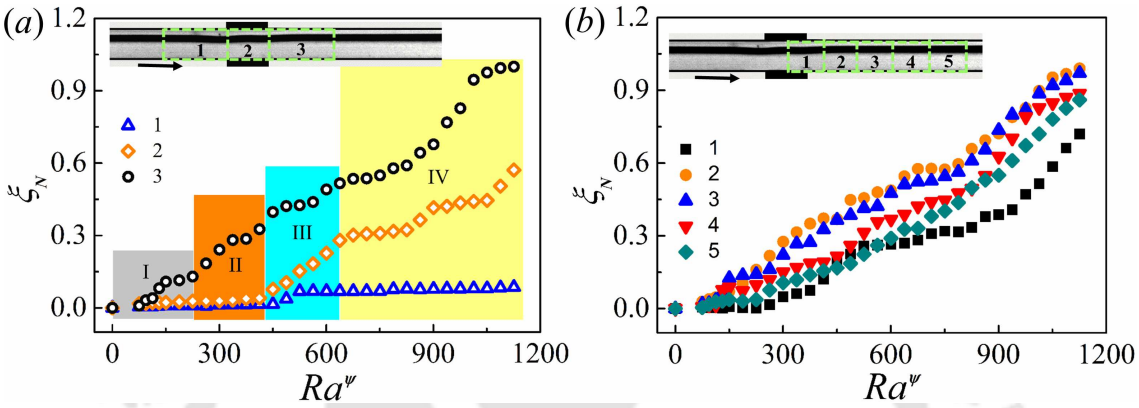

Figure 2.22: Variation of Strouhal number (St) with electric field Rayleigh number (Ra^ψ) in regimes II and III, for a benzene-silicone oil system under DC voltage input. The average Re maintained during the experiments was 0.5. The arrow indicates the direction of the flow.

into the system upon application of electric fields of varying strengths for the regimes I–IV, discussed in figure 2.18. For this purpose, initially, the benzene-silicone oil system was subjected to DC voltage application in the range of 0-1500 V, at increments of 50 V, and the response was recorded simultaneously. We define, $\xi = 1 - \dfrac{I_e}{I_i}$, where I_i is the mean grey scale level in absence of electric field and I_e is the mean grey scale level in the presence of electric field. The parameter, ξ_N represents the normalized values of ξ, obtained by dividing the latter by the maximum value of ξ. The grey scale intensities were measured by image analysis of the extracted frames using the commercial software MATLAB. Figure 2.22(a) shows the variation of ξ_N with Ra^ψ. The ξ_N in this plot were calculated for three distinct regions marked 1, 2, and 3, located upstream, within, and downstream of the area of application of electric field, respectively, as shown in the plot by the rectangular boxes. The intensity values represent the mean intensity of all the pixels contained within the regions of interest namely, regions 1, 2, and 3.

The plot suggests that, while ξ_N remains nearly constant at the upstream of the electrodes, the same increases with increase in Ra^ψ within the electrode and downstream regions. Further, at lower values of Ra^ψ, when there is little perturbation in

the system, the grey scale levels do not change significantly, yielding lower values of ξ_N. With the increase in Ra^{ψ}, the development of the instability modes yield higher values of ξ_N. The region 3 in the downstream, where all the unstable perturbations travel with the fluid, shows a much rapid increase in the values of ξ_N with Ra^{ψ}, as compared to regions 1 and 2. Further, the regions 2 and 3 show significantly higher values of ξ_N in instability regimes III and IV owing to the chaotic nature of instabilities. Figure 2.22(b) shows the variation of ξ_N with Ra^{ψ} in five different regions immediately downstream to the electrode region, as shown by boxes in the figure. The figure suggests that ξ_N is minimum near the region 1, then increases sharply in the regions 2 and 3 before again reducing in the regions 4 and 5. The plots infer that perturbation strength is maximum in the region 2, which is the immediate downstream of the region of application of electric force. The image suggests that the electric field induced perturbations in these systems can only grow up to a certain part of the downstream of the electrodes before they are transported downstream due to pressure-driven flow of the fluid layers. It is important to note here that ξ_N is also a measure of mixing of the fluids in the downstream of the channel. A higher value of ξ_N signifies a larger amount of mixing between the layers. Thus, both the plots in figure 2.22 suggest that the increase in the electric field intensity can cause a rapid mixing of the fluids at the immediate downstream of the channel. Further, the plots also suggest that the mixing length reduces with the increase in the field intensity. The experiments also uncover that the liquid can immediately be de-mixed when the electric field is turned off, i.e. the perturbations die out immediately upon removal of electric field.

Concisely, the figures 2.18−2.22 show the EHD induced steady, time-periodic, and chaotic instabilities in a pressure-driven viscosity stratified flow of a pair of miscible fluids inside a microchannel, which can be employed for rapid mixing of the fluids inside microfluidic devices. The method is found to be reversible in nature because immediate de-mixing of the layers take place upon the removal of the electric field influence.

Figure 2.23 shows the use of multiple electrodes to cause a rapid mixing of the miscible fluids undergoing a stratified flow inside a microchannel. The optical micrographs (a)−(f) show the response of a benzene-silicone oil stratified flow when a DC voltage of 0−500 V is ramped up through five pairs of electrodes integrated in a staggered manner along the microchannel wall, as shown in the figure. The electrode separation distance in these experiments has been optimized based on the

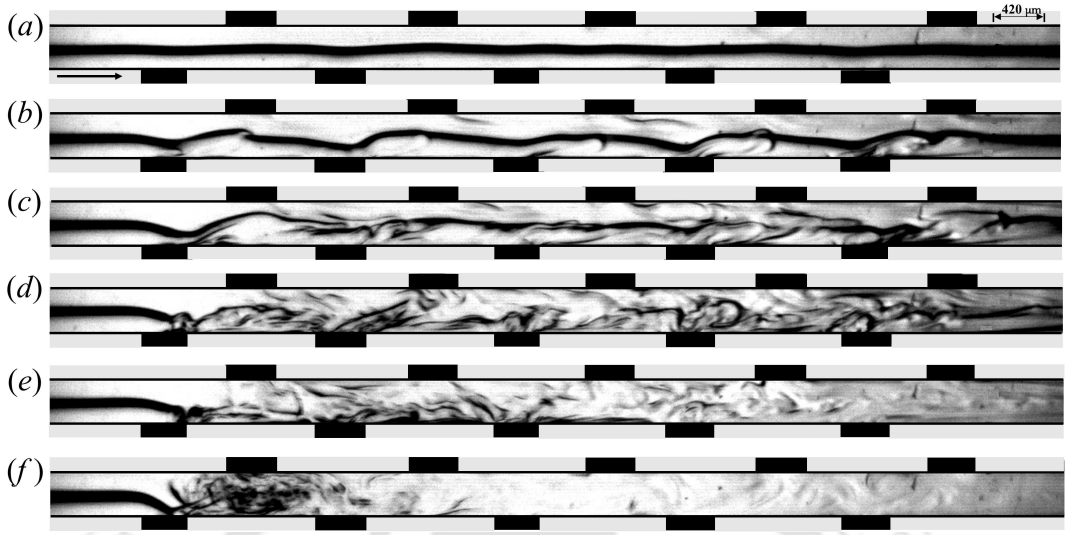

Figure 2.23: The experimental micrographs $(a)-(f)$ show the response of a benzene-silicone oil stratified flow upon application of ramp DC voltage of 0−500 V, through five pairs of electrodes integrated along the channel wall in a staggered fashion. The images correspond to the top view of the flow configuration. The top layer corresponds to benzene and the bottom layer corresponds to silicone oil. The image (a) corresponds to the system at 0 V. The average Re maintained during the experiments was 0.5.

observations made with the single electrode experiments. Again, the top (bottom) layer shown in the image corresponds to benzene (silicone oil). In these experiments, the voltage was ramped up in 5 s to cause the phenomena. Image (a) corresponds to the pressure-driven situation in absence of the electric field while the image (a) shows the onset of the electric field induced mixing. The images $(c)-(f)$ show the progressive reduction in the mixing length owing to the generation of time-periodic and unsteady flow patterns with the progressive increase in the field intensity. The multiple electrode arrangement ensure an amplified perturbation in this system induced by the electric field as compared to a single electrode system. Thus, a more efficient mixing of the fluids can be achieved at a much lower voltage in the multi-electrode system. The figure shows the use of the proposed methodology to rapidly mix fluids layers inside the microfluidic devices.

2.6 Conclusions

A combined theoretical and experimental study uncovers the salient features of electric field induced instabilities associated with the viscosity stratified flow of a pair of miscible fluids inside microchannels. The major conclusions are,

1. A general linear stability analysis reveals that the EHD instabilities of such systems appear only beyond a critical field intensity. The analysis also uncovers the presence of five distinctive instability modes, which are identified as electric field mode I (E-I), electric field mode II (E-II), viscous mode (V), diffusive mode (D), and the K-mode. Mode E-I-mode appears in the bulk of the lower viscosity fluid at the lower values of Ra^{ψ} while the E-II-mode manifests in the higher viscosity fluid at very high values of Ra^{ψ}. The V-mode appears when the viscosity difference between the fluids are high. Presence of the electric field facilitates the onset of the V-mode when compared with the regular pressure driven flows. The D-mode appears in the mixed interfacial region at higher values of Sc, due to steep variation of perturbation concentration across the interface. Again, presence of the electric field facilitates the onset of the D-mode when compared with the regular pressure driven flows. A contrast of the ionic mobility in the fluids cause the appearance of the much shorter wavelength K-mode.

2. The location of the interface (h), thickness of the interface (δ), level of charge injection (I^{q}), strength of the applied EHD field (Ra^{ψ}), viscosity contrast across the diffused interface (V^{L}), and diffusivity across the interface (Sc), are found to be some of the very important parameters for these type of instabilities. For relatively small variations in the dielectric constants of the fluids (E^{L}), the E-I-mode remains nearly unaffected. In particular, the E-I-mode and E-II-modes can be facilitated by increasing the applied field intensity, charge injection levels, and reducing the overall viscosity of the fluids. In the linear regime, the experimental and theoretical values obtained for the critical electric field strength, wave speed, and wavelength of the E-I-mode of instability are found to be in reasonable qualitative agreement.

3. Experiments uncover four distinct regimes of instabilities. The linear regime I corresponds to onset of instability waves beyond a critical field intensity. With

further increase in the applied voltage, the regime II marks the initiation of the non-linear regime with the appearance of time-periodic vortices in the downstream of the electrode region. On further increasing the electric field intensity a regime III appears where smaller vortices are generated at higher frequencies leading to intermixing of the flow patterns. The transition of regime II to III is marked by an abrupt jump in the Strouhal number. Two-dimensional non-linear CFD simulations also predict the appearance of vortices which are qualitatively similar to the experimental observations of regime II and III. The simulated results show reduction in size and increment in frequency of shedding with the increase in the electric field intensity. At still higher field intensities, the flow becomes unstructured and chaotic in regime IV leading to total mixing of the two fluids downstream the region of application of electric potential.

4. From the perspective of mixing, among all the regimes, the chaotic regime IV with coherent flow patterns is found to be the most suitable one. The mixing is found to happen at the immediate downstream of the electrodes inserted in the channel where electric field can engender a strong intermixing of the layers. The mixing decrease at the far downstream of the channel due to viscous damping of the perturbations induced by the electric field. Interestingly, the mixing and de-mixing processes has been observed to be reversible because the flow immediately restores to its stratified configuration on switching off the electric field. The mixing efficiency is found to increase with the increase in the strength of the applied field and the number of electrodes inserted across the channel.

In summary, the study uncovers a pathway to integrate the influence of an external electrostatic field with a microfluidic device in order to remotely control the mixing of the fluid layers. The phenomenon can be of significance in improving the efficiency of multifarious cutting-edge microfluidic applications which include mixing, pumping, heat-exchange, mass transfer, and reaction engineering. In depth investigation of the coherent and chaotic regimes, alongwith a spatial stability analysis of the system has been kept as future scope of research work.

Chapter 3

Genesis of Electric Field assisted Microparticle Assemblage in a Dielectric Fluid

3.1 Abstract

Oscillatory motions of charged particles inside a liquid medium have been explored under the influence of an electric field emulating the field-induced particle-laden fluid flows. The properties of the surrounding fluid are found to play key roles in the kinetics of such a particle aggregation process. While the weakly conducting or insulating liquids promote high frequency oscillations of charged particles followed by a quick assemblage, the viscosity and relative permittivity of the liquid play significant roles in modulating the time scale. In fact, the origin of such motions in a multi-particle system is very similar to a system with single charged particle wherein the particle gathers charge from one of the electrodes before moving towards the other of opposite polarity. Interestingly, in the multi-particle system, an unprecedented charge-reversal is observed wherein a charged particle reverse its direction of motion after colliding with another particle of opposite polarity. Experiments together with simulations further reveal that, while the equal sized particles undergo an electric field driven 'elastic' collision and show synchronized motions with nearly similar speeds of approach and separation, the motions of unequal sized particles are rather non-uniform after undergoing an 'inelastic' collision. Importantly, the simulations with two-particle system uncover the presence of counter-rotating-vortices surrounding the charged particles. The results reported not only usher the genesis of the chain like assemblage in the multi-particle systems but also open up the possibility of generation of on-demand power-law liquid properties through 'chaining' or 'layering' of the charged particles.

The contents in this chapter have been accepted for publication as S. Dutta, A. K. Singh, P. S. G. Pattader, and D. Bandyopadhyay, (2021) 'Genesis of Electric Field assisted Microparticle Assemblage in a Dielectric Fluid', *J. Fluid Mech.*, vol. **915**, pp. 1-36.

3.2 Introduction

Suspended microparticles undergoing motions inside a bulk liquid medium, namely the microparticle laden fluid flows, are often encountered in a plethora of natural processes, which include the motion of dust particles in air, movement of cloud or molten lava, ocean waves near sea shore, propagation of smoke plumes, and the moving sand dunes in deserts [64–66]. The particle laden fluid flows (PLFF) are also very common in the biological realm, for example, the flow of blood corpuscles with the serum in blood vessels [67] or movement of bacterial colonies [68]. Further, many of the industrial processes are also found to host such flows which include suspension polymerization [69], separations of nucleic acids [70], or fluidized bed reactors [71], among others. Of late, the state-of-art microfluidic applications encounter a variety of PLFF flows in flow cytometry [72], fluorescence-activated cell sorting (FACS) [73], zeta-potential analyser [74], separation of nanoparticles [75], self-propelling objects [76], or emulsifiers [77]. Fundamentally, such flows are also very attractive because of the physics associated with the, (i) interplay of friction and surface tension dominated flows under weak inertial and gravitational influences [151, 238–240]; (ii) non-Newtonian nature of the flows embedded with particles [241–243] ; (iii) liquid-particle or particle-particle interactions [244–247]; and (iv) diverse hydrodynamic, non-hydrodynamic, and stochastic forces [248, 249].

Importantly, at the microscopic length scale, it is often desirable to apply external fields to effectively manoeuvre the particle motions inside a liquid [86, 250, 251]. A set of prior seminal contributions initiated by Winslow [103–105, 252] report the formation of smart electrorheological liquids when a suspension of solid microparticles in a liquid is exposed to an electric field. In such systems, the electric field help in tuning the viscosity of the liquid in a non-invasive manner. Interestingly, such capacitive systems also find mention in the lecture series of Prof. Richard Feynman [253]. A few recent experimental studies have uncovered the mixing of liquids due to the rotational motion of a glass particle inside a microchannel under the influence of an externally applied electric field [110]. In similar lines, a collection of pancreatic adenocarcinoma cells has also been concentrated between a pair of electrodes using electric field in a microfluidic platform [254].

Such electric field induced motions and subsequent assemblage of the microparticles inside the liquid mediums can largely be classified into electrostatic or Coulombic, electrophoretic (EP), dielectrophoretic (DEP), and electrohydrodynamic (EHD)

types. The EP flows manifest when a charged microparticle is immersed in a weak electrolyte leading to the formation of a charged electrical double layer (EDL) surrounding the same, which helps the particle to move under the influence of an externally applied field [70,74,75]. On the other hand, DEP originates when a conducting or insulating particle in an electrolyte or insulating fluid, is placed inside a non-uniform electric field, owing to the presence of a finite liquid-particle dielectric contrast and a spatial gradient of the applied field [82,87,94].

While the electric field motions of a single particle suspended in a liquid medium are fairly well explored, the physics behind the movements of a collection of microparticles in a liquid medium is rather complex. In particular, one of the very long-standing challenges has been to study the dynamics of the alignment of multiple microparticles in between a pair of electrodes. Previous studies reveal that during EP interactions, the particles with the line of centres aligned in the perpendicular (parallel) direction of applied field mutually attract (repel) each other [78,79,255]. In such a scenario, increase (reduction) in the local electric field between the particles increases (reduces) the Smoluchowski slip velocity on the particle surface to cause a reduction (increase) in the local hydrodynamic pressure, which can facilitate aggregation (segregation) of particles. Formation of a particle chain in a PLFF is a remarkable facet of dielectrophoretic particle-particle interactions, wherein the induced dipoles of closely spaced particles interact to eventually align the particles in the direction of the applied field [91–95,101]. It is now established that the nature of such interactive force is attractive and similar particles always align parallel to the direction of the applied field [96–100]. Heterogeneous mixtures of particles with higher and lower polarizabilities than the suspending liquid, however, form chains in the direction perpendicular to the applied field [101,102].

Contact charging at the electrodes and subsequent oscillatory motions of suspended particles inside an insulating liquid medium under an AC or DC (alternating or direct current) field have recently been studied by many groups [106–114]. When a microparticle suspended in a non-conducting fluid is subjected to an electric field, the particle moves towards the nearest electrode where it acquires/loses charge, until the potential difference between them equals the contact potential difference of the two materials [111,112,114]. The particle is then repelled by the electrode and moves towards the one of opposite polarity, to maintain an oscillatory motion. These motions initiate beyond a critical applied field intensity and the frequency of oscillation increases with the intensity of electric field [256]. It has been reported

that a conductive particle in contact with a plane electrode acquires a free charge of, $Q_0 = \left(\frac{2\pi^3}{3}\right)\varepsilon_f r_p^2 E_0$ [115–117], where Q_0 is the total charge, ε_f, r_p and E_0 are the liquid permittivity, particle radius and average applied electric field intensity, respectively. However, experiments with different materials report over- [106,108,257] and under-charging [109,111,258]. Further, as the particle with some free charge on the surface approaches either of the electrodes, the local electrode-particle field intensity increases by many folds owing to the narrowing of the gap [112]. Thus, a dielectric breakdown of the intermediate liquid is a possibility before their mechanical contact, which may lead to a micro-discharge near the contact point. The conductive pathway thus created, facilitates the movement of charges to/from the particle [257–259]. Such charging and discharging cycles are also found to cause meltdown to create pits on the electrodes [260].

Although the charging and discharging mechanisms and the subsequent oscillatory movements of a single particle in a fluid have been studied extensively in the past, the mechanisms associated with the dynamics of multiple particles in a PLFF is relatively less explored and understood [114,261]. Recently Bishop *et al.* [114] have reported a preliminary experiment with equal sized spheres undergoing oscillations inside a mineral oil. In their experiments, it has been observed that the spheres undergo elastic collision at low *Re* (Reynolds number). The charges on the spheres redistribute during the collisions to conserve the total charge, while they move apart when they become equipotential. The results reported by Bishop *et al.* [114] are qualitative and the report does not reveal the nature of interactions between unequal particles, non-conductive particles and dissimilar particles. In view of this background, using the set-up shown in the figure 3.1(*a*), we attempt to unravel different regimes of motions of the different types of charged particles in a PLFF, under the influence of a DC electric field in a non-conducting liquid medium. The microparticles in the proposed PLFF experiments are chosen from, (i) rigid and dielectric glass particle, (ii) soft-elastic and dielectric amberlite-resin, (iii) silver (Ag) or nickel (Ni) coated amberlite with an electrically conducting surface, or (iv) an iron-oxide coated amberlite-resin with an electrically non-conducting surface. Experiments are conducted with a pair of particles to study the finer aspects of the host of phenomena that occur during the oscillations of mixtures of particles. Further, the roles of the viscosity and dielectric permittivity of the surrounding liquid medium on the kinetics of the assemblage and separation of the particles of the

PLFF have also been explored in detail. In a way, analysing the physics behind such occurrences can help in the improvement of understanding of the aggregation and segregation of cells or micro/nanoparticles of a suspension, which eventually lead to the manifestation of on-demand electrorheological properties inside a PLFF under electric field.

In order to explain the underlying physics of the aforementioned phenomena, we also perform computational fluid dynamics (CFD) simulations of the proposed PLFF employing the geometry shown in the figure 3.1(b). A robust and accurate Galerkin finite element method [262–265] has been utilized to capture the essential features of the particle-particle, liquid-particle, and electrode-particle electrostatic interactions alongside resolving the necessary hydrodynamic interactions to uncover the spatiotemporal dynamics of oscillation, collision, migration, and charging-discharging of the particles between the electrodes resembling the experiments. Concisely, the experimental and theoretical results reported can be a significant step forward in the understanding of the electric field driven multi-particle dynamics of a PLFF inside a microfluidic device.

3.3 Experimental Methodology

Figure 3.1(a) shows the experimental setup where a cavity of 5 mm $\times$ 5 mm $\times$ 10 mm ($l \times b \times h$) was replica-moulded inside a poly-dimethyl-siloxane (PDMS) block [266] using a silicone elastomer (SLYGARD 184 silicone elastomer, Dow Corning). In order to prepare this setup, initially, a template of the size of the required pool was attached to a clean glass sheet and the Aluminium (Al) electrodes were carefully attached to the sides of the template, before the entire set-up was surrounded by double sided tapes to prepare a rectangular well with solid boundaries. The well was then filled with liquid PDMS mixed with a cross linker in 10:1 ratio and cured inside a vacuum oven at 80°C for 3 h. Following this, the template was carefully pulled out before the well was washed repeatedly with de-ionized (DI) water and ethanol to remove any extraneous matter.

The pair of Al electrodes embedded on the opposite walls of the block were used to generate the electric field. Thus, one of the plates was connected to the positive terminal of a high voltage source (SES Instruments Pvt. Ltd, EHT-II), while the other was grounded. The solid particles used in the experiments were glass particles (∼100 μm diameter, Merck) and amberlite resin particles (IR-120,

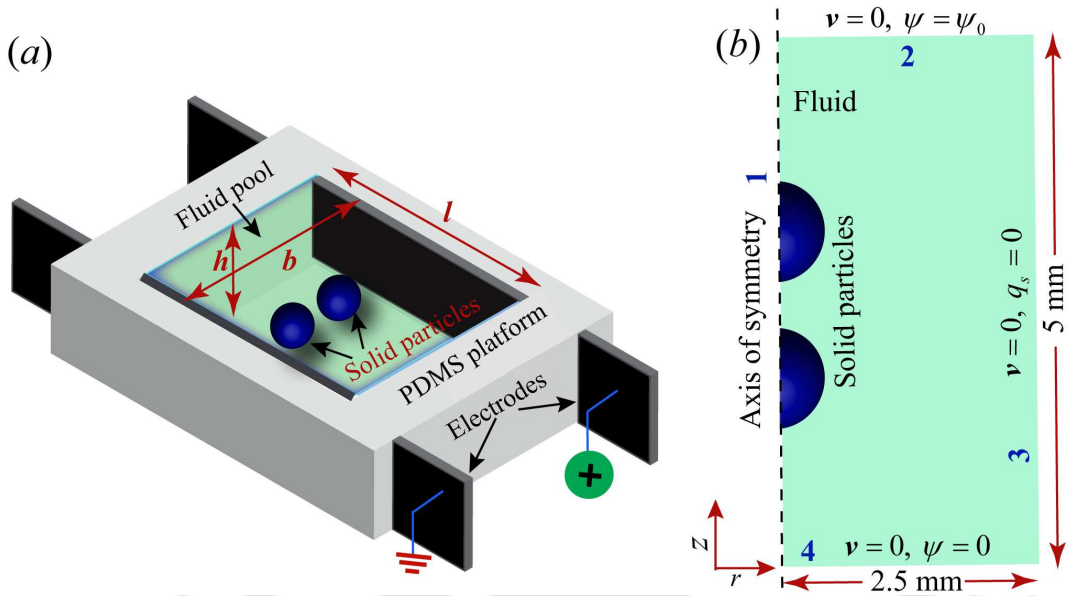

Figure 3.1: (*a*)Schematic diagram of the experimental set-up. Two solid particles are suspended inside a non-conductive high viscosity liquid contained in a 5 mm × 5 mm × 10 mm ($l \times b \times h$) pool carved in a PDMS (polydimethyl siloxane) block. Two aluminium plate electrodes are embedded on two opposite sides of the block. One of the plates is connected to the positive terminal of a high voltage source, while the other plate is grounded. (*b*) Schematic diagram of the axisymmetric computational domain.

Merck) coated with various metal films. The protocols of metal deposition and comprehensive characterization of the experimental particles are given in section 1.3 of the supplementary information. Silicone oil (Merck, density, $\rho_f \approx 960$ kgm^{-3}, viscosity at 25°C, $\mu_f \approx 317$ cP, electrical conductivity, $\sigma_f \approx 10^{-13}$ Sm^{-1} [231], and dielectric constant $\varepsilon_{rf} \approx 2.5$ [221] was used to suspend the particles in the pool. The experiments were conducted under a microscope (Leica) and recorded using a high-speed camera (Photron, Fastcam Mini UX-100).

3.4 Theoretical Formulation

3.4.1 Governing Equations

The liquid used in the experiment is considered incompressible and Newtonian. Thus, the flow field is defined by the continuity and momentum equations as,

$$\nabla \cdot \boldsymbol{v}_f = 0, \tag{3.1}$$

$$\rho_f \left(\frac{\partial \boldsymbol{v}_f}{\partial t} + \boldsymbol{v}_f \cdot \boldsymbol{\nabla} \boldsymbol{v}_f \right) = -\boldsymbol{\nabla} p + \boldsymbol{\nabla} \cdot \left[\mu_f \left(\boldsymbol{\nabla} \boldsymbol{v}_f + \boldsymbol{\nabla} \boldsymbol{v}_f{}^{\mathrm{T}} \right) \right]. \tag{3.2}$$

Here, ρ_f, $\boldsymbol{v}_f$, p, and μ_f denote the density, velocity, pressure, and viscosity of the liquid, respectively. The motions of the solid particles are governed by following Newton's second law as,

$$\rho_s \frac{\partial^2 \boldsymbol{u}}{\partial t^2} = \boldsymbol{\nabla} \cdot \overline{\overline{\boldsymbol{\sigma}}} + \boldsymbol{f}_e. \tag{3.3}$$

Here, ρ_s is the density of the particle, $\boldsymbol{u}$ is the solid displacement vector, $\overline{\overline{\boldsymbol{\sigma}}}$ is the Cauchy stress tensor, and $\boldsymbol{f}_e$ is the electrical force per unit volume acting on the particles. The particles used in the experiments were $\gg 10$ µm in size, hence the adhesive force between the particles and the electrodes is not considered [108]. The gravitational force acting on a particle is of the order of $\sim \left(\frac{4\pi {r_s}^3 g(\rho_s - \rho_f)}{3} \approx 10^{-6}\mathrm{N} \right)$, while the electrical force is $\sim \left(\frac{2\pi^3 \varepsilon_f {r_s}^2 {E_0}^2}{3} \approx 10^{-4}\mathrm{N} \right)$. Here, r_s and g denote the particle radius and acceleration due to gravity, respectively. As shown in figure 3.1(a), the electrical field was applied in the horizontal direction and the experiments were carefully conducted each time the particle was well suspended in the fluid. Thus, the time scale of the electrical force acting on the particle to cause the horizontal oscillations, was lower compared to the gravitational force tending to settle it to the bottom of the well. Hence, the gravitational force acting on the particles is not considered in the simulations. The strain-displacement relation for the solid is given by,

$$\overline{\overline{\boldsymbol{\epsilon}}}_s = \frac{1}{2} \left[(\boldsymbol{\nabla} \boldsymbol{u})^{\mathrm{T}} + (\boldsymbol{\nabla} \boldsymbol{u}) + (\boldsymbol{\nabla} \boldsymbol{u})^{\mathrm{T}} (\boldsymbol{\nabla} \boldsymbol{u}) \right]. \tag{3.4}$$

Here, $\overline{\overline{\boldsymbol{\epsilon}}}_s$ is the strain tensor. The stress-strain relationship of the solid is considered as [267],

$$\overline{\overline{\boldsymbol{\sigma}}} = C \overline{\overline{\boldsymbol{\epsilon}}}_s. \tag{3.5}$$

Here, C is the stiffness matrix. The total electrical force acting on the particles is expressed as,

$$\boldsymbol{F}_E = \int \left(\overline{\overline{\tau}} \cdot \boldsymbol{n} \right) \mathrm{d}S = \int \left[\left(\varepsilon \boldsymbol{E}\boldsymbol{E} - \frac{1}{2} \varepsilon \boldsymbol{E} \cdot \boldsymbol{E} \overline{\overline{I}} \right) \cdot \boldsymbol{n} \right] \mathrm{d}S. \tag{3.6}$$

By multipole expansion of the particle field, $\boldsymbol{F}_E$ can be alternatively written as,

$$\boldsymbol{F}_E = q\boldsymbol{E} + (\boldsymbol{p}\cdot\boldsymbol{\nabla})\,\boldsymbol{E}. \tag{3.7}$$

Here, $\overline{\overline{\boldsymbol{\tau}}}$ is the Maxwell stress tensor, q is the net charge on the particle, $\boldsymbol{E}$ is the electric field intensity and $\boldsymbol{p}$ is the dipole moment. The first term of (3.7) is the Coulomb force exerted by the external field on the particle net charge and the second one denotes the force exerted by the external field on the induced bound charge. Considering the particles to be nearly spherical, the polarization force can be expressed as [268],

$$\boldsymbol{F}_p = 2\pi {r_s}^3 \varepsilon_f K \boldsymbol{\nabla}\left|\boldsymbol{E}\right|^2, \tag{3.8}$$

where, K is the Clausius-Mossotti factor expressed as, $K = \dfrac{\varepsilon_s - \varepsilon_f}{\varepsilon_s + 2\varepsilon_f}$, where ε_s and ε_f denote the permittivity of the particles and the liquid, respectively. The liquid is considered to be dielectric with no net free charge density. Thus, the electric field inside the liquid and the solid are governed by the Laplace's equations as,

$$\boldsymbol{\nabla}\cdot\boldsymbol{D}_f = 0, \tag{3.9}$$

$$\boldsymbol{\nabla}\cdot\boldsymbol{D}_s = 0, \tag{3.10}$$

where, the electric displacement is given by, $\boldsymbol{D} = \varepsilon\boldsymbol{E}$. The electric field is governed by the Gauss' law as,

$$\boldsymbol{E} = -\boldsymbol{\nabla}\psi. \tag{3.11}$$

Here, ψ is the electrical potential. It is assumed that the charge contained in the particle resides on its surface such that,

$$q_s = \boldsymbol{n}\cdot\left(\boldsymbol{D}_f - \boldsymbol{D}_s\right). \tag{3.12}$$

Here, q_s is the surface charge density of the particles and $\boldsymbol{n}$ is the outward unit normal vector.

3.4.2 Boundary Conditions and Solution Methodology

The oscillations of the particles between the parallel electrodes in the horizontal direction, as shown in figure 3.1(a), was found to be reasonably axisymmetric. Hence, to reduce the computational load, instead of a three-dimensional domain, an ax-

isymmetric geometry mimicking the dimensions of the experiments was used for the numerical simulations. The axisymmetric boundary conditions were enforced for all the variables at the axis of symmetry (boundary 1) shown in figure 3.1(b). No-slip ($\boldsymbol{v}_f = 0$) and wetted wall boundary conditions were enforced at the boundaries 2, 3 and 4 for the solution of the flow field. The solid particles were modelled as linear elastic material. The motion of the solid particles was tracked using an arbitrary Lagrangian Eulerian (ALE) method. This combines the Eulerian description of the flow field using a spatial frame and the solid mechanics equations formulated using Lagrangian description with a material frame. The dynamics of the moving solid particles were handled using the moving mesh technique wherein, based on the movement of the solid boundary new mesh coordinates are created to solve the momentum equations for the modified flow field. At the boundary of the solid particle(s), no-slip boundary condition of the form, $\boldsymbol{v}_f = \boldsymbol{v}_s$, was enforced, where $\boldsymbol{v}_s \left(= \dfrac{\partial \boldsymbol{u}}{\partial t} \right)$ is the solid velocity. The liquid load on the boundary of the solid was defined by, $\boldsymbol{f}_s = -\boldsymbol{n} \cdot \left[-p\boldsymbol{I} + \left\{ \mu_f \left(\boldsymbol{\nabla} \boldsymbol{v}_f + \boldsymbol{\nabla} \boldsymbol{v}_f{}^{\mathrm{T}} \right) \right\} \right]$ where $\boldsymbol{n}$ is the normal vector to the boundary. For the electric field equations (3.6 – 3.12), Dirichlet boundary conditions of $\psi = 0$ and $\psi = \psi_0$ were maintained at boundaries 2 and 4, respectively. Here, ψ_0 refers to the applied electric potential. Insulating wall ($\boldsymbol{n} \cdot \boldsymbol{D} = \boldsymbol{0}$) boundary condition was enforced at boundary 3.

The governing equations for the flow and electric fields along with the associated boundary conditions were solved using the Galerkin finite element method with the aid of commercial software package COMSOL Multiphysics$^{\mathrm{TM}}$. A quadratic discretization method was used for the flow field in the liquid, displacement field of the particles and the electric field variables. First order elements were used for the pressure calculations in the liquid. The momentum equation was stabilized using the streamline and crosswind stabilization schemes. Further, moving mesh boundary conditions were enforced at the boundaries 2, 3 and 4 along with zero normal mesh displacement boundary condition enforced at the line of symmetry. The mesh in the liquid domain was allowed to deform with a hyper-elastic smoothing technique. The time dependent equations were solved in a segregated manner with backward difference formula for the time stepping and backward Euler for consistent initialization. Free time steps were taken by the solver with relative tolerance of 10^{-5}. The domain was re-meshed every time the mesh quality degraded beyond 0.8. The validation of the numerical method and the grid convergence study are given in appendices

B.1 and B.2, respectively. It must be noted that in the numerical simulations a gap of 10 μm was maintained between the particles during contact to avoid numerical singularities.

3.5 Results and Discussion

Figure 3.2(a) shows the assemblage of a collection of non-conducting glass particles of different sizes in silicone oil under the influence of a DC field, in the setup shown in figure 3.1(a). The experiment shows that, initially, the segregated particles tend to form a chain like assembly between the electrodes under the influence of the electric field [104]. Over a period of time, relatively stable and static chains are formed when adequate amount of glass particles are accumulated between the electrodes. The particle assemblies within each chain undergo incessant to-and-fro oscillatory motions. Figure 3.2(b) shows another interesting case wherein an assemblage of smaller glass particles and larger Ag-coated amberlite particles in silicone oil is investigated. The experiment shows that some of the larger Ag-coated amberlite particles migrate faster towards the electrodes to acquire charge at the initial stages of evolution. Subsequently, they help in assembling the glass and other Ag-coated amberlite particles after having repeated collisions between them. In fact, the progressive integration of the larger Ag-coated amberlite particles in the chain help in increasing the packing density of the glass particles in between the Ag-coated amberlite particles and the electrodes. Finally, a heterogeneous assembly composed of the bigger Ag-coated amberlite particles 'chained' by a collection of smaller glass particles of high packing density is formed.

The figures 3.2(c) and 3.2(d) show that the phenomenon remain qualitatively similar when Ag-coated amberlite with a conducting surface and non-conductive amberlite (conductivity $\approx 10^{-10}$ Sm^{-1}) particles are employed. In these motions, initially, the randomly placed microparticles move towards the nearest electrode where they undergo charge acquisition or reversal. Subsequently, the charged particles are attracted by the electrode of opposite polarity during which they start colliding with the other charged or uncharged particles. A few particles do not contact any other particle during the motions and thus, continue their usual oscillation between the electrodes. During the formative stage of the chain, the Coulombic interaction of a charged particle with the bounding pair of charged particles of opposing polarity generate a motion of relatively higher frequency, as it is previously observed for a

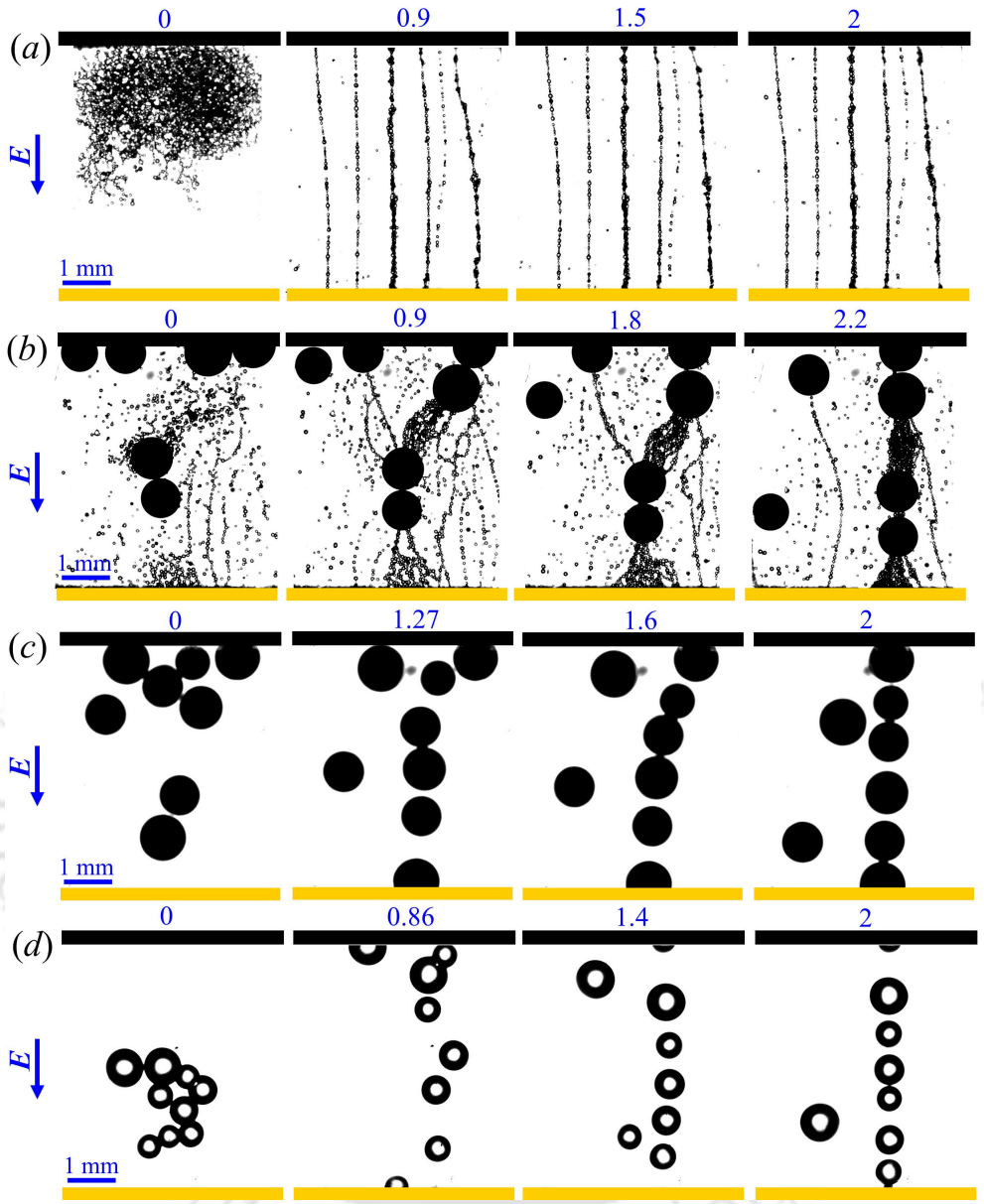

Figure 3.2: Experimental time sequence micrographs depicting alignment of (a) a collection glass particles (b) a mixture of glass particles and Ag-coated amberlite particles (c) Ag-coated amberlite particles, and (d) uncoated amberlite particles under application of 6 kVcm^{-1}, 5 kVcm^{-1}, 5 kVcm^{-1}, and 6 kVcm^{-1} average electric fields, respectively. The glass particles were ∼100 µm in diameter. The times indicated have unit of second (s). The experiments were visualized under a microscope at 2.5x magnification. The images correspond to the top view of the particles.

single particle oscillation between a pair of electrodes [112]. In fact, a small chain of charged particles also oscillates between the bounding pair of charged particles

(or charged chains) of opposing polarity, in the similar manner, as the particles do. Concisely, figure 3.2 uncovers a host of interesting phenomena displayed by multiple charged particles inside a microparticle laden fluid flow.

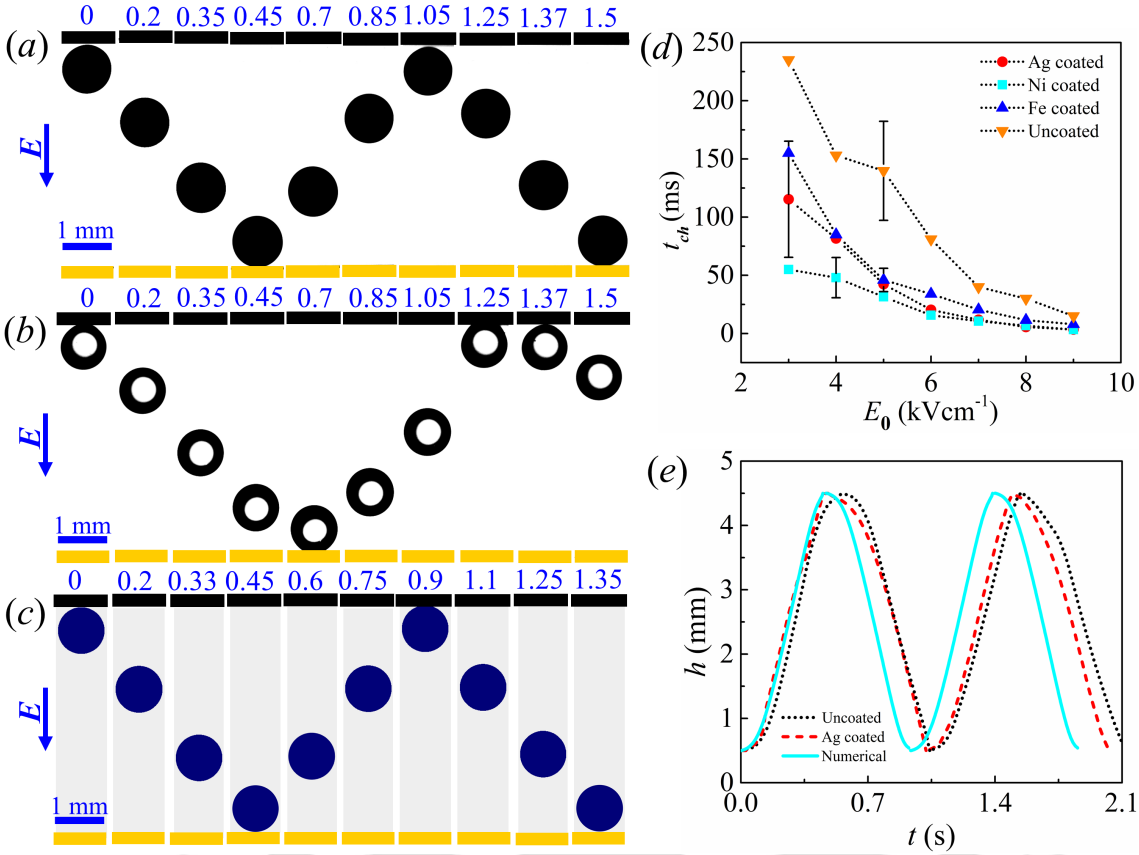

Figure 3.3: Time sequence snapshots of (a) a Ag-coated (b) an uncoated, amberlite resin particle of ∼500 µm radius each under application of 9 kVcm^{-1} average electric field. (c) Simulated time sequence snapshots of a 500 µm particle under application of 9 kVcm^{-1} average electric field. The time indicated above each micrograph has unit of second (s). The plot (d) shows the variations of the charging time (t_{ch}) of a ∼500 µm radius amberlite resin particle coated with different material with average applied electric field. The error bar represents the maximum standard deviations obtained from five sets of experiments. The plot (e) shows the variations of the positions of the centres (h) of the particles from the bottom electrode at $z = 0$, with time (t) corresponding to (a), (b) and (c). The broken (solid) lines correspond to the experimental (simulated) values, respectively. The experiments were visualized under a microscope at 2.5x magnification. The image panels shown in (a) and (b) correspond to the top view of the particles.

3.5.1 Single Particle Phenomena

The results shown in the figure 3.2 have multiple layers of scientific information, which are rather difficult to comprehend at one go. Thus, in order to elucidate the origin of such migrations of the charged particles inside a microparticle laden fluid flow, a series of experiments have been performed involving either a single particle or a pair of particles. We initiate the discussions with the motions of single particles under electric field with conducting and non-conducting surfaces. The experimental time sequence snapshots of a silver coated (Ag-coated) and an uncoated amberlite resin particle of ∼500 μm radius each, under application of 9 kVcm^{-1} average electric field are demonstrated in figures 3.3(a) and 3.3(b), respectively. The oscillatory motion of the conductive Ag-coated particle is expected and studied in earlier literature [111, 112]. However, the uncoated amberlite particle also shows similar oscillatory behaviour, as shown by the figures 3.3(b) and 3.3(e). This observation is particularly interesting, given that fact that the conductivity of the uncoated amberlite particle is rather limited ($\sim 10^{-10}$ Sm^{-1}). Figure 3.3(c) demonstrates the simulated time sequence snapshots of a 500 μm radius conductive particle under application of 9 kVcm^{-1} average electric field.

This experiment raises an important question on the mechanism, which causes the reversal of the direction of the particles immediately after contact. In this regard, a collisional rebound may be thought of as one of the possibilities. However, the Stokes number (ratio of particle inertia to viscous forces), $St\left(=\frac{1}{9}\frac{\rho_s}{\rho_f}Re_s\right)$ (where, $Re_s=\frac{\rho_s D_s U_i}{\mu_f}$ and D_s and U_i denote particle diameter and impact velocity, respectively), for the experiments reported here, are found to be $O(10^{-3})$. Prior-art [269–271] suggest that below a critical value of St ($\sim$ 10) the particles may not rebound after collision. Hence, any possibility of rebound due to an electrode-particle elastic collision can be safely ignored. The more probable reason can be that, the non-conductive amberlite particles too undergo some charge transfer during contact with the electrodes, in a fashion similar to the Ag-coated conductive particles.

Figure 3.3(d) demonstrates the experimentally evaluated values of average charging time (t_{ch}) of an amberlite particle (r_s∼500 μm) during the contact with the electrodes. The results are reported for the particles coated with different materials and at different electric fields (E_0). Two additional types of particles, a conductive

Ni-coated (nickel coated) and a non-conductive Fe-coated (iron coated) particle, were experimented with to get an approximate knowledge of the oscillatory trends shown by different materials. The Fe-coated particles were kept for 2 days at room temperature to reduce their conductivity due to oxidation. Figure 3.3(d) shows that both the conductive Ag-coated and Ni-coated particles show lesser charging times (t_{ch}) at the electrodes as compared to the non-conductive Fe-coated and uncoated particles. In these experiments, (t_{ch}) was evaluated by noting the difference in the time of zero approach velocity and the same for a marginal rebound velocity. The experiments suggest that the electrical conductivity of the particle at the surface has a significant influence on the charging time of the particles at the electrodes. Figure 3.3(e) shows the experimental trajectories of the Ag-coated and uncoated particles corresponding to figures 3.3(a) and 3.3(b), respectively. The figure 3.3(e)

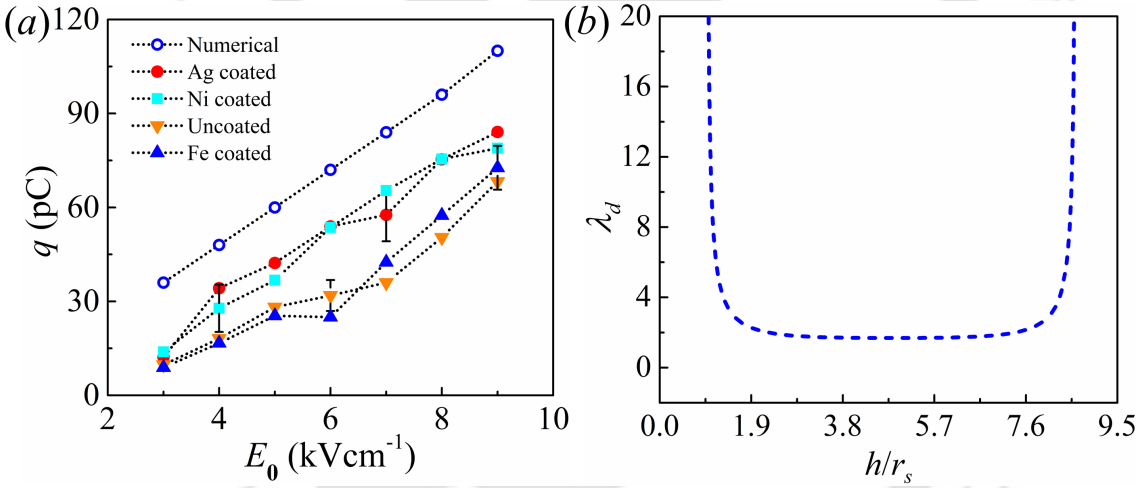

Figure 3.4: (a) The variation of the net charge (q) acquired by amberlite particles of ∼550 μm radius, coated with a variety of materials, with the average applied electric field. The solid (hollow) symbols denote the experimental (numerical) values, respectively. The error bar represents the the maximum standard deviations obtained from five sets of experiments. (b) The variation of the simulated values of dimensionless drag coefficient (λ_d) with the dimensionless position (h/r_s) of a sphere ($r_s = 500$ μm) moving between two electrodes 5 mm apart. Here, h is the position of the centre of the sphere measured from the lower electrode at $z = 0$.

also shows the numerically simulated trajectories for the geometry shown in figure 3.1(b), which is very similar to the experimental set-up shown in figure 3.1(a). It may be noted that in the simulations the particles were modelled as conductive. The dimensions shown in the schematic diagram of the computational domain in

figure 3.1(b) were used for all the simulations, unless otherwise stated. The physical properties of the surrounding liquid and the particles were assigned similar to those mentioned for the experiments, in section 3.3, unless otherwise stated. The particles were assigned the simulated theoretical values of charge given in figure 3.4(a), which depicts the charge acquired by a conductive particle in contact with the electrode, unless otherwise stated.

It can be inferred from figure 3.3(e) that the motion of the uncoated particle is slightly sluggish compared to the Ag-coated particle. The numerically simulated trajectory again predicts higher particle speeds than both the uncoated and Ag-coated particles. The reason behind this trend can be better understood from figure 3.4(a), which depicts the average charge (q) acquired by the particles at different values of average applied electric field (E_0). The method to calculate charge from the experiments is given in appendix B.4. The drag force on the particles was experimentally estimated using the numerically simulated values of drag coefficient across the channel as depicted in figure 3.4(b). The hollow symbols in the plot (a) correspond to the numerically simulated values of charge, which are approximately equal to the theoretical charge Q_0 described above. The Ag-coated and the Ni-coated particles and found to acquire ∼73% while the Fe-coated and uncoated particles are found to contain ∼48% of the theoretical value of charge Q_0. As the uncoated particle acquires less charge compared to the Ag-coated particles and both the particles acquire significantly less charge compared to the theoretical values, they are acted upon by less electric force compared to the simulated particle. Hence, the experimental trajectories show sluggish behaviour compared to the numerical one.

3.5.2 Two-particle Phenomena

Figures 3.5(a) and 3.5(b) demonstrate the experimental time sequence snapshots of Ag-coated amberlite resin particle pairs moving inside a liquid medium under application of 9 kVcm^{-1} average electric field. The image panel in (a) shows a pair of equal sized particles of ∼550 μm radius each, while the smaller particle in (b) is ∼400 μm. The trajectories in the image panel (a) suggest that the particles after reversal of charge at the respective electrodes after contact, move towards the electrodes of opposite polarity. During the motion, they appear to undergo an 'elastic' collision with each other before reversing their directions of motion. The behaviour is found to be very similar for the setup with particles having different sizes in the

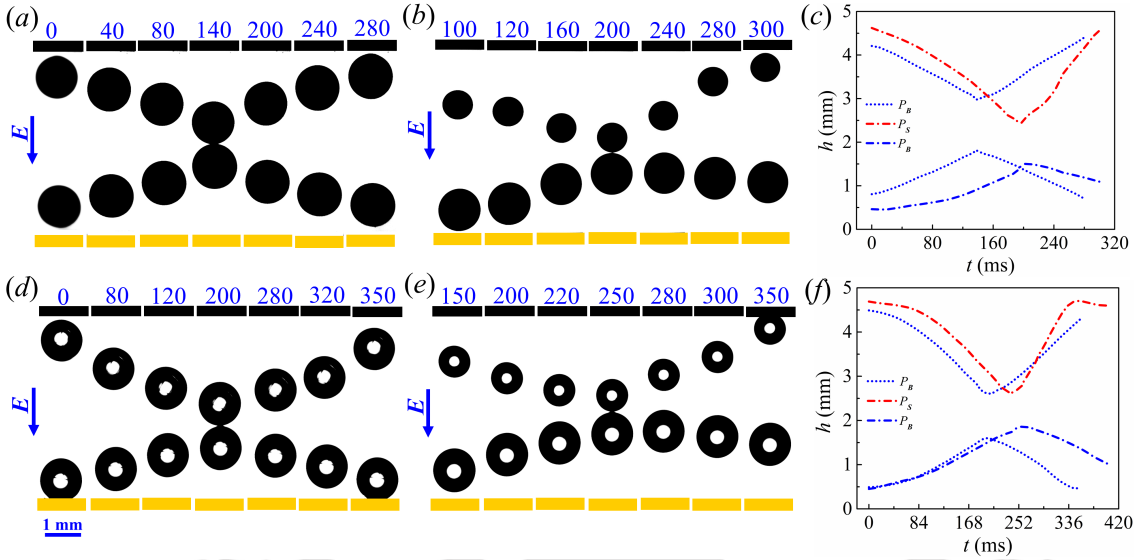

Figure 3.5: Experimental time sequence snapshots of two Ag-coated particles of (a) equal sizes of ∼550 µm radius each (b) unequal sizes with radii of the smaller and bigger particles of ∼400 µm and ∼550 µm, respectively, under application of 9 kVcm^{-1} average electric field. The time indicated above each micrograph has unit of millisecond (ms). Variations of the positions of the centres (h) of the particles measured from the lower electrode at $z = 0$, with time (t) for the image panels shown in (a) and (b). Experimental time sequence snapshots of two uncoated particles of (d) equal sizes of ∼550 µm radius each (e) unequal sizes with radii of the smaller and bigger particles of ∼400 µm and ∼550 µm, respectively, under application of 9 kVcm^{-1} electric field. (f) Variations of the positions of the centres (h) of the particles with time (t) for the image panels shown in (d) and (e). The evenly broken (unevenly broken) lines correspond to the case of equal (unequal) sized particles, respectively. The suffix S (B) correspond to the smaller (bigger) particles, respectively. The experiments were visualized under a microscope at 2.5x magnification. The image panels shown in (a), (b), (d) and (e) correspond to the top view of the particles.

image panel (b) with difference in the location of the point of contact and the path length of oscillations of the individual particles. In such a scenario, the prior-art suggests the possibility of the presence of a thin fluid layer in between the particles [108, 111, 112, 257, 269–271].

Figure 3.5(c) demonstrates the trajectories shown by the particle pairs in (a) and (b). The trajectories are reported in terms of positions of the centres (h) of the particles measured from the lower electrode at $z = 0$, as a function of time (t). The figures 3.5(a) and 3.5(c) clearly indicate that the equal sized particle pairs show a rather synchronized oscillatory behaviour. They approach each other with

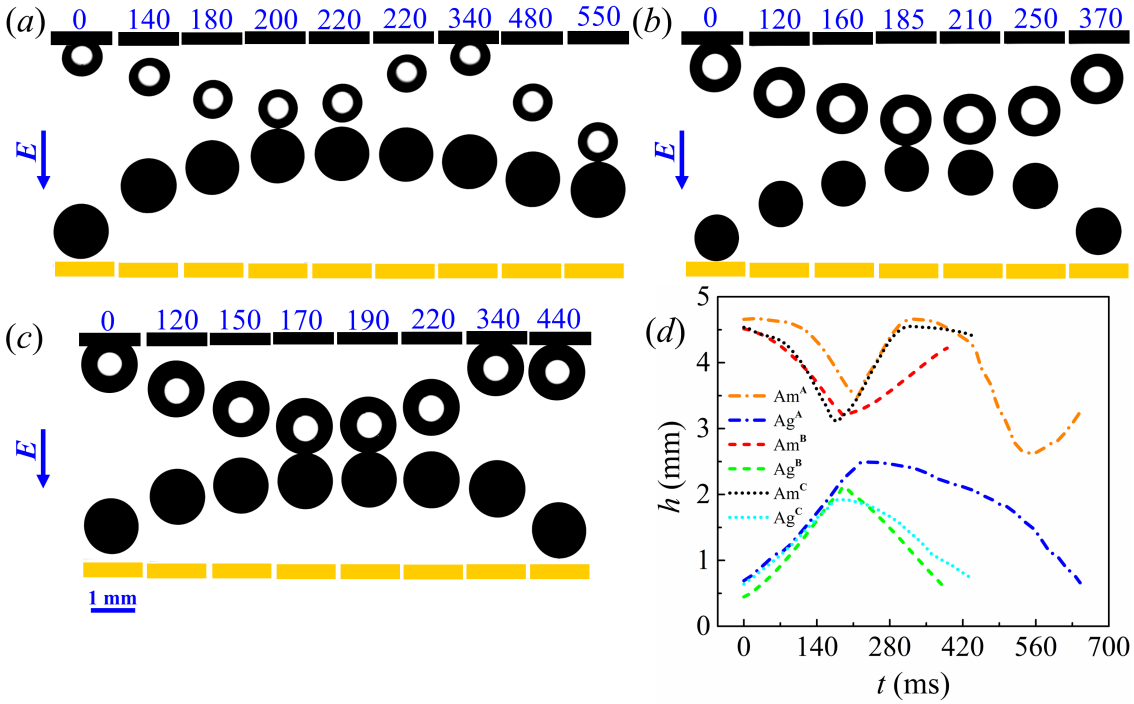

Figure 3.6: Experimental time sequence snapshots of a Ag-coated and an uncoated particle of (a) unequal sizes with radii of the smaller uncoated and bigger Ag-coated particles of ∼400 µm and ∼550 µm, respectively (b) unequal sizes with radii of the smaller Ag-coated and bigger uncoated particles of ∼450 µm and ∼550 µm, respectively and (c) almost equal sizes of ∼550 µm radius each, under application of 9 kVcm^{-1} average electric field. The time indicated above each micrograph has unit of millisecond (ms). (d) Variations of the positions of the centres (h) of the particles measured from the lower electrode at $z = 0$, with time (t), for the image panels shown in $(a-c)$. Superscripts A, B and C in the legend indicate the particles shown in (a), (b) and (c), respectively, and Am corresponds to the uncoated particle and Ag corresponds to the Ag-coated particle. The black (yellow) rectangle represents the positive electrode (grounded electrode), respectively. The experiments were visualized under a microscope at 2.5x magnification. The image panels shown in (a), (b) and (c) correspond to the top view of the particles.

nearly similar speeds until the middle of the channel. After collision, they maintain reasonably same speed of separation during their reverse motions. Figures 3.5(b) and 3.5(c) show that for the unequal sized particles, the smaller particle accelerates after contact whereas the bigger particle moves rather sluggishly. Interestingly, the motions of the uncoated particles shown in figures 3.5$(d-f)$ are found to be very similar to the Ag-coated particles, as shown in the figures 3.5$(a-c)$.

Further interesting behaviours are observed when particles of two different types

are placed. For example, the oscillation characteristics of a Ag-coated amberlite particle and an uncoated particle under 9 kVcm^{-1} electric field are shown in figures 3.6($a-d$). Again, as observed in the figure 3.5, the smaller amberlite particle hastens its speed of return towards the electrode after collision while the bigger Ag coated particle moves rather slowly after contact, as shown in the 3.6(a). This behavior is more clearly indicated in the position versus time plots depicted in figure 3.6(d). In comparison, in the case of a bigger uncoated particle and a slightly smaller Ag-coated particle, the trajectories of the motion of the particles are found to be rather symmetric, as shown in the figures 3.6(b) and 3.6(d). For equal sized combination of a Ag-coated particle and an uncoated amberlite particle, figures 3.6(c) and 3.6(d) depict very marginal acceleration of the amberlite particle and deceleration of the Ag-coated particle after contact.

The experiments with equal sized Ag-coated particles shown in figure 3.5(a) are qualitatively similar to that reported in previous studies [114, 261]. Bishop *et al.* [114] observed that two equal conductive particles undergo electric field driven elastic collisions with redistribution of charge on their surfaces, keeping the total charge conserved. In addition to this, the results presented above reveal that (i) even non-conductive and dissimilar (a conductive and a non-conductive) particles and (ii) unequal sized similar or dissimilar particles, also undergo such field driven collisions with charge reversals. To gain more insight into the nature of such field driven collisions, quantitative estimations of charge contained by the particles before and after collisions are necessary. Figures 3.7($a-d$) show the variations of the average velocities (v_s) and the fraction of the initial charge retained by the particles after collisions (q^*) as functions of the average electric field intensity (E_0) for different combination of particles. Figures 3.7(a) and (b) refer to two equal Ag-coated and uncoated particles of $\sim$550 μm radius each, respectively. Both the figures suggest that the the velocities of approach and separation in case of equal sized particles remain reasonably similar as the particles retain approximately the initial amount charge of opposite polarity after collision. Thus, the equal sized particles undergo elastic collision irrespective of the the particle type. Figures 3.7(c) and (d) show the variations of unequal sized Ag-coated and uncoated particles, respectively. As discussed in figures 3.5 and 3.6, figures (c) and (d) show that the velocity of the smaller particle increases and the that of the bigger particles decreases after collision. The bigger particle retains almost 30$-$40% of its initial charge, while the smaller particle retains approximately 120$-$150%. The dotted (dashed) line refers

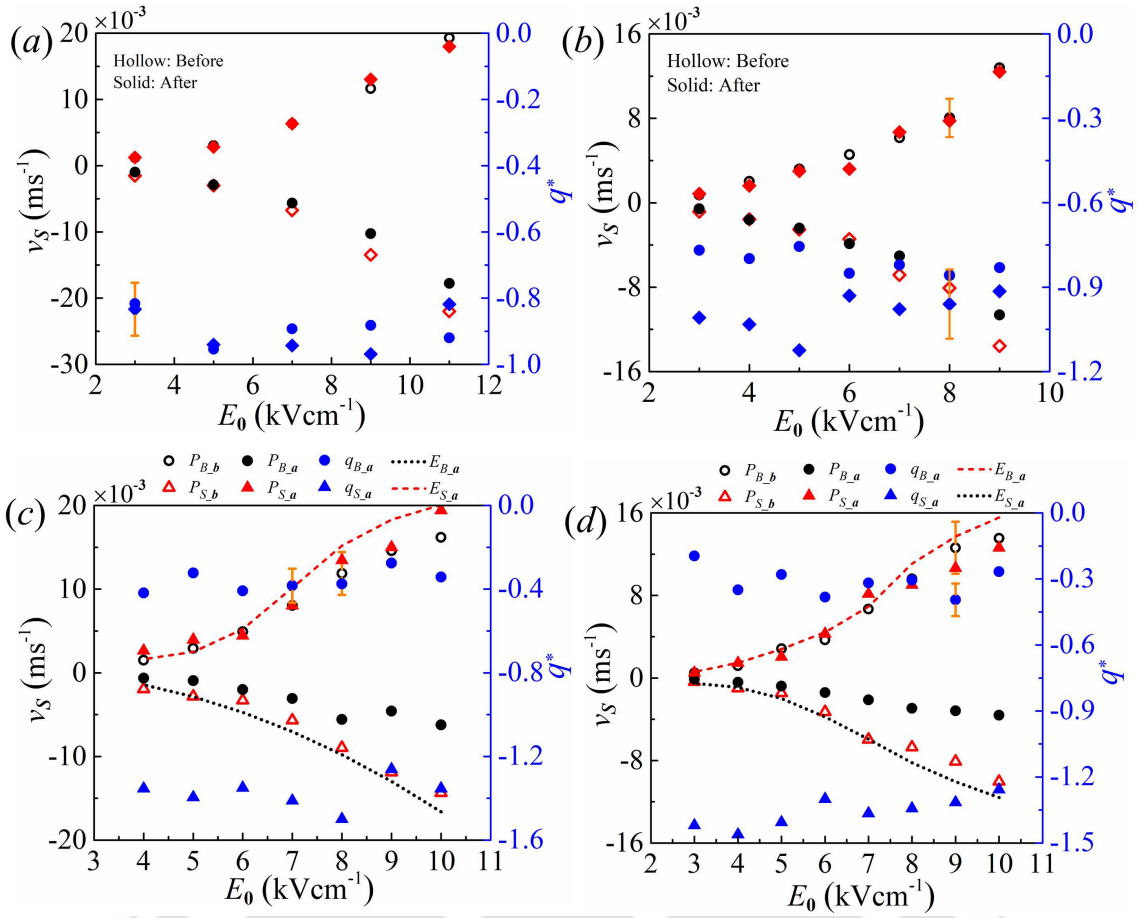

Figure 3.7: Variation of the average velocity (v_s) of the particles and the fraction of the initial amount of charge retained after collision (q^*) with average electric field (E_0) for (a) equal sized Ag-coated particles with radius ∼550 μm each, (b) equal sized uncoated particles with radius ∼550 μm each, (c) unequal sized Ag-coated particles with the radius of the smaller being ∼400 μm and bigger being ∼550 μm, respectively and (d) unequal sized uncoated particles with the radius of the smaller being ∼400 μm and bigger being ∼550 μm, respectively. In figures (c) and (d) the notations specify the following: P_{B_b} (respectively, P_{S_b}): velocities of bigger (respectively, smaller) particle before collision, P_{B_a} (respectively, P_{S_a}): velocities of bigger (respectively, smaller) particle after collision, q_{B_a} (respectively, q_{S_a}): fraction of the initial charge retained by the bigger (respectively, smaller) particle after collision, E_{B_a} (respectively, E_{S_a}): velocity of the bigger (respectively, smaller) particle after elastic collision between them.

to the separation velocity of the bigger (smaller) particle, predicted by the elastic collision theory. It can be seen that the v_s of the smaller particle resemble the elastic collision velocities, but the v_s of the bigger particle are substantially less compared

to the elastic collisions. Thus, it can be inferred that (i) equal sized particles of similar type, undergo 'elastic' electric field driven collisions and (ii) the collisions between unequal sized particles are essentially 'inelastic'.

We further explore some of the other interesting characteristics of the charge

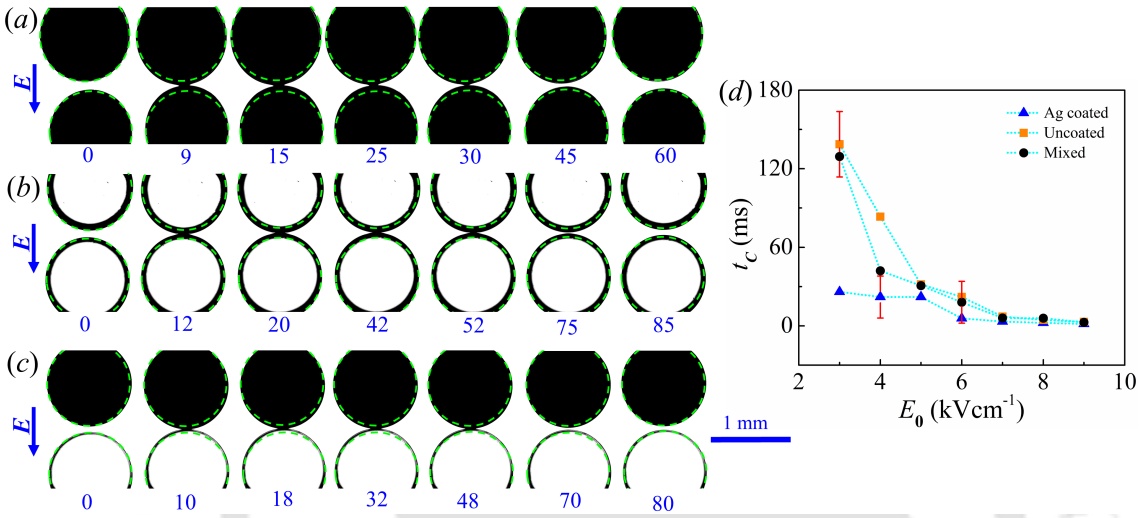

Figure 3.8: Experimental time sequence snapshots show the contact dynamics of (a) two Ag-coated (b) two uncoated and (c) a Ag-coated and an uncoated particle of ∼550 μm radius each under application of 5 kVcm^{-1} average electric field. The time indicated below each micrograph has unit of millisecond (ms). (d) Variations of the time periods for charge reversals (t_c) for the particle pairs shown in $(a-c)$ with the average applied electric field. The experiments were visualized under a microscope at 10x magnification. The image panels shown in (a), (b) and (c) correspond to the top view of the particles. The dashed lines in the image panels of $(a-c)$ indicate the initial positions of the particles during their close approach with each other.

reversal for a set of two-particle systems. For this purpose, we report the magnified time sequence experimental snapshots during the charge reversals of two particles, under application of 5 kVcm^{-1}, in figures 3.8$(a-c)$. The image panel in figure 3.8(a) denotes two equal sized Ag-coated particles of ∼550 μm radius each, while 3.8(b) corresponds to two equal sized uncoated amberlite particles of the same size, as mentioned above. Figure 3.8(c) captures the dynamics of a Ag-coated (darker shade) and an uncoated amberlite (lighter shade) particle of ∼550 μm radius each. It can be inferred from figures 3.8$(a-c)$ that both the particles in each panel show synchronized motions before and after collisions in all cases. The positively charged upper particle (returning from the positive upper electrode), first shows apparent contact with the negatively charged bottom sphere (returning from the grounded

electrode), after which both the particles reverse their trajectory, as demonstrated in figures 3.5 and 3.6. The time periods for charge reversals of the particles last for $10^{-2} - 10^{-1}$ s. However, it may be noted here, that such time measurements reported are not exact due to experimental artefacts while capturing the videos such as optical aberrations.

Figure 3.8(d) shows the variations of the time periods for charge reversals (t_c) for the particle pairs shown in 3.8($a - c$). The plot suggests that for all the three cases shown in 3.8($a - c$), t_c decrease with increasing field intensity, suggesting that the charge reversal kinetics during collision, is directly proportional to the applied electric field. A higher value of electric field, thus, provides a greater driving force for rapid charge transfer between the particles. Experiments suggest that at high electric fields, the local enhancement of electric field between the particles becomes progressively higher as they approach each other. This provides a relatively higher driving force for charge transfer, leading to shorter t_c, as illustrated in the computational study by Flittner & Pŕibyl [272] for the case of an oscillating droplet. Further, figure 3.8(d) suggests that the uncoated particles show slightly higher contact times, than the Ag-coated particles. The Ag-coated particles with greater amounts of surface charge compared to the uncoated particles, are expected to result in greater local field enhancements during their collision. This may be a possible reason for the smaller t_c than the corresponding uncoated particles. The higher surface conductivity of the Ag-coated particles compared to the uncoated ones may also play a key role in these phenomena.

The image panels in the figures 3.9($a - d$) depict the flight of two unequal sized particles inside a liquid medium under 5 kVcm^{-1} electric field. The time sequence experimental snapshots in panel (a) correspond to Ag-coated particles of which the radius of the bigger particle is ∼550 μm and the smaller particle is ∼450 μm. Panel (b) shows the response for uncoated particles of approximately the same size as in (a). Panels (c) and (d) depict bigger (smaller) Ag-coated (uncoated) particles, respectively. It is interesting to note that the contact dynamics shown by the unequal sized particles are remarkably different from that observed in the case of equal sized particles discussed above in figure 3.8. Figure 3.9 depicts that, even after the contact, the bigger particle carrying larger amount of charge continues its motion while in contact with the smaller particle for a brief period before reversing its direction towards the oppositely charged electrode. The smaller particle, however, reverses its direction of motion, almost immediately after the charge reversal.

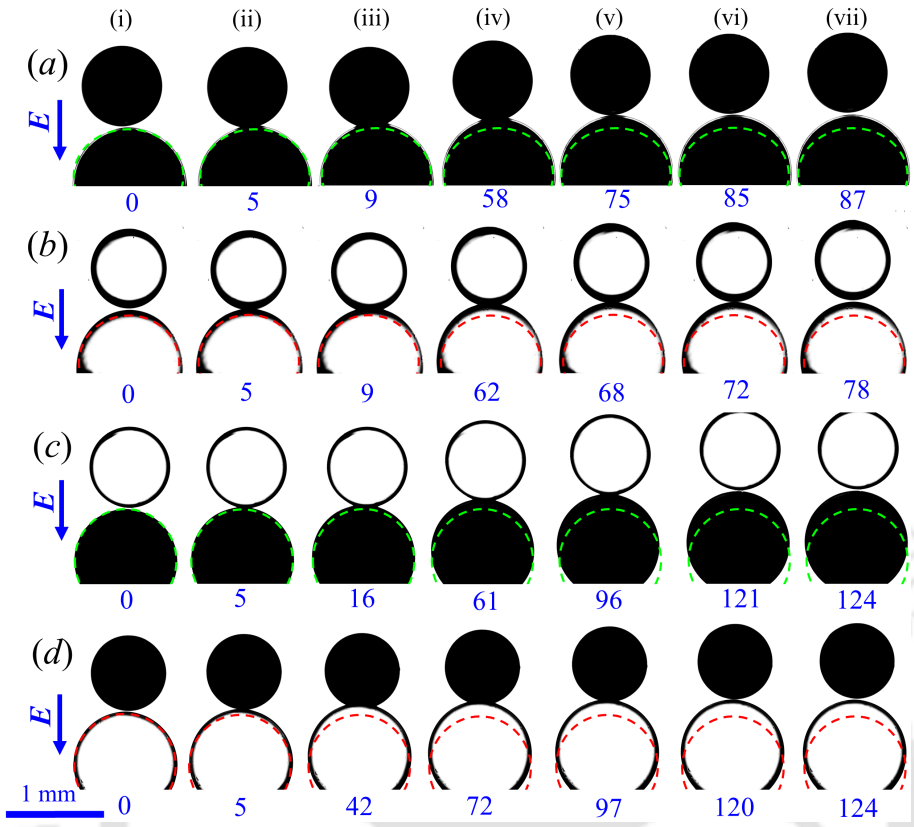

Figure 3.9: Experimental time sequence snapshots of (a) two unequal Ag-coated (b) two unequal uncoated (c) a bigger Ag-coated and smaller uncoated, and (d) a smaller Ag-coated and a bigger uncoated amberlite resin particles under application of 5 kVcm^{-1} average electric field. The time indicated below each micrograph has unit of millisecond (ms). The radii of the big and small particles are $\sim$550 μm and $\sim$450 μm, respectively. The experiments were visualized under a microscope at 10x magnification. The images correspond to the top view of the particles. The dashed lines in the image panels of ($a-d$) indicate the initial positions of the bigger particle during its close approach with the smaller one.

In view of these observations, the 'inelastic' collision characteristics of significantly different sized particles can be summarized as, (a) the bigger particle after its engagement with the smaller particle approaching from the opposite direction, briefly continues its motion in the original direction along with the smaller particle, at a much reduced speed (images (ii)-(iv) of each panel); (b) the smaller particle then detaches itself from the union and reverses it direction of motion at a slightly higher speed than that of its approach (images (iv)-(vii); (c) after its disengagement from the smaller particle, the bigger particle still continues its flight towards the smaller particle for a very brief period of time (images (vi) and (vii)) before finally

reversing its direction towards the opposite electrode; and (d) the bigger particle exhibits a much smaller speed after colliding with the smaller one. The experiments shown so far suggest that the charge reversal mechanisms between a pair of equal or unequal sized particles are very different. While it is observed that, the case of equal sized particles temporarily freeze for a very brief period of time, during the anticipated charge reversal (figures 3.8($a-c$)), the unequal sized particles form a union and move briefly along the direction of the bigger particle, during which the charge reversal is expected to take place.

In fact, the multi-particle PLFF systems shown in the figure 3.2 also show such pair-wise repeated 'elastic' and 'inelastic' collisions inside the liquid medium, for equal and unequal sized particles. With the progress in time, a combination of these types of pair-wise motions and charge reversals during the collision lead to the large-scale assemblage of the particles inside a liquid medium. The charged particles keep showing this pair-wise oscillatory behaviour with repeated reversal of motions after charge reversals till there are some void spaces available during the chain formation.

3.5.3 Numerical Investigations

The experiments on the pairs of equal and unequal sized particles, shown in the figures 3.5 – 3.9, uncover the following key details: (a) the equal sized particles acquire charge of nearly equal quantity of opposite sign; (b) there is a disparity of charge acquired by unevenly sized particles with the smaller particle getting overcharged while the bigger particle getting undercharged after collision. In order to obtain a physical explanation of such observations on the charge reversal and subsequent motions of the particle pairs, a set of numerical simulations were carried out using parameters that largely emulate the experimental conditions. The model employed a system of two particles suspended in a liquid medium to qualitatively uncover the salient features of the oscillatory motions between a pair of electrodes under electric field. The results shown here help in identifying the underlying mechanism of the formation of particle chains, as shown previously in figure 3.2.

In the first simulation, a pair of uniformly sized particles oscillating between two parallel electrodes is considered, as schematically shown in the figure 3.1(b). The simulated time sequence snapshots shown in figures 3.10(a) and 3.10(b) demonstrate the response of two equal sized spheres 1 (negatively charged) and 2 (positively

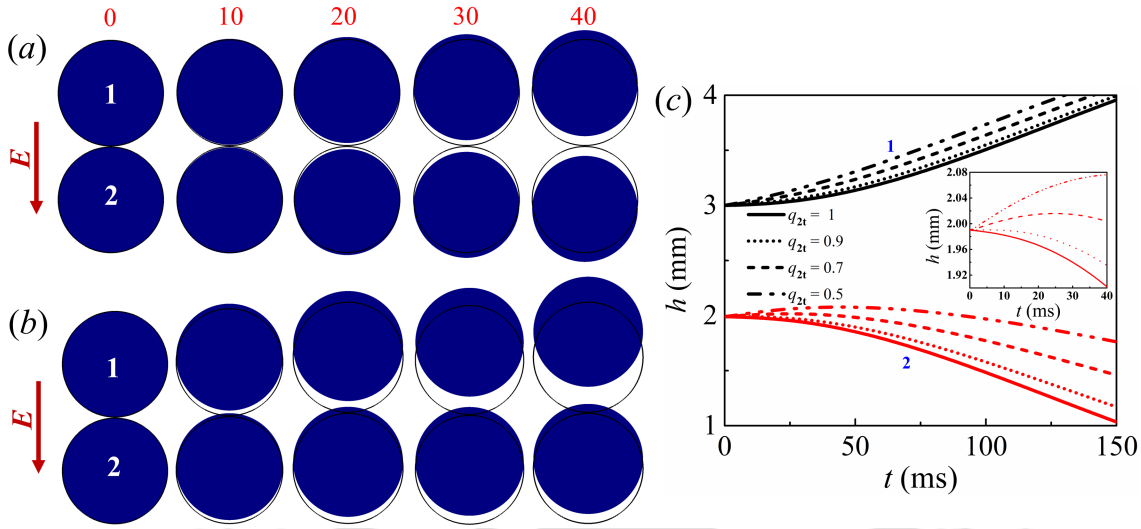

Figure 3.10: Time sequence snapshots of two equal sized particles 1 and 2 of 500 μm radius each, under application of 9 kVcm^{-1} average electric field for (a) $q_{2t} = 1$ and (b) $q_{2t} = 0.5$. Here, q_{2t} represents the ratio of charge (q) contained by particle 2 to the theoretical value of charge. Particle 1 contains the theoretical value of charge of opposite sign. The time indicated above each micrograph has unit of millisecond (ms). The solid lines in the image panels of (a) and (b) indicate the initial positions of the particles during their close approach with each other. (c) The positions of the centres of two spheres (h) measured from the bottom electrode at $z = 0$, with time for different values of q_{2t}. The upper (black) graphs correspond to particle 1 and the lower (red) plots correspond to particle 2. The inset plot represents the variation of h of particle 2 during the initial time. The simulations were carried out employing an axisymmetric domain.

charged) of 500 μm diameter each, under 9 kVcm^{-1} electric field for $q_{2t} = 1$ and $q_{2t} = 0.5$, respectively. Here, q_{2t} is defined as the ratio of surface charge density of the particle 2 to its theoretical value. Figure 3.10(a) shows the variation of the positions of the centres (h) of particles 1 and 2, measured from the electrode at $z = 0$, with time, under 9 kVcm^{-1} electric field for different values of q_{2t}. It can be inferred from the plot (a) that for $q_{2t} = 1$, when the particles contain equal and opposite charge, the displacements of the particles from their initial positions are similar. The negatively charged sphere moves towards the positively charged anode, while the positively charged particle migrates towards the cathode.

This synchronized motion of equal sized particles is qualitatively confirmed from the experimental trajectory plots depicted in figures 3.5–3.9. For $q_{2t} = 0.5$, wherein particle 2 contains half the amount of charge contained by particle 1, figures 3.10(b)

and 3.10(c) demonstrate that the trajectories are not similar. Particle 1 containing higher charge shows expected motion towards the oppositely charged electrode. In contrast, the particle 2 containing less charge, follows particle 1 for a brief period of time, before migrating towards the oppositely charged lower electrode. Thus, the results in the simulated image set (b) is found to be very similar to the experimental results involving the unevenly sized particles in the figures 3.5, 3.6 and 3.9. This observation leads to a reasonable confirmation that, during the process of dynamic charge reversals of the particles of unequal sizes, the charge distribution is rather unequal. The bigger particle shows a relatively slower motion after the 'inelastic' collision because it gains a relatively less charge of opposite polarity.

Figures 3.11(a) and 3.11(b), demonstrate the simulated time sequence snap-

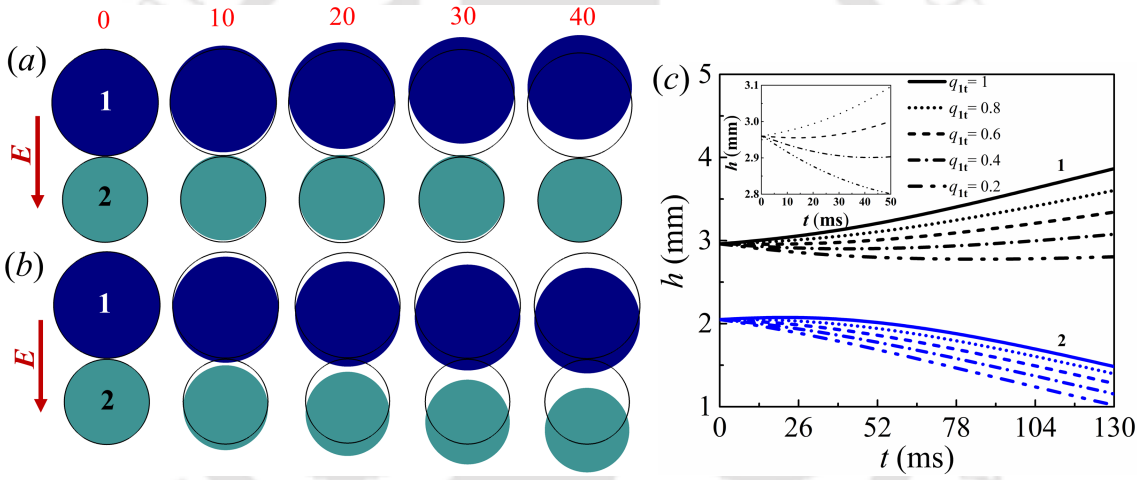

Figure 3.11: Simulated time sequence snapshots of two unequal sized particles 1 and 2 of radii 500 μm and 400 μm, respectively under application of 9 kVcm^{-1} average electric field for (a) $q_{1t} = 1$ and (b) $q_{1t} = 0.2$. Here, q_{1t} represents the ratio of charge (q) contained by particle 1 to the theoretical value of charge. Particle 2 contains the theoretical amount of charge of opposite sign. The time indicated above each snapshot has unit of millisecond (ms). The solid lines in the image panels of (a) and (b) indicate the initial positions of the particles during their close approach with each other. (c) The positions of the centres of the two spheres (h) measured from the bottom electrode at $z = 0$, with time for different values of q_{1t}. The upper (black) graphs correspond to particle 1 and the lower (blue) plots correspond to particle 2. The inset plot represents the variation of h of particle 1 during the initial time. The simulations were carried out employing an axisymmetric domain.

shots of a bigger sphere 1 (negatively charged) and a smaller sphere 2 (positively charged) of radii 500 μm and 400 μm, respectively, under 9 kVcm^{-1} electric field for

$q_{1t} = 1$ and $q_{1t} = 0.2$, respectively. Here, q_{1t} represents the ratio of charge contained by particle 1 to the theoretical value of charge. Particle 2 contains the theoretical amount of charge in all the cases. In the first case wherein, the smaller particle 2 contains lesser magnitude of charge compared to particle 1, similar results are obtained as previously shown in figure 3.10(b). The negatively charged particle 1 rapidly moves towards the positively charged upper electrode, while the positively charged particle 2 follows particle 1 for a very brief period of time, before migrating towards the grounded electrode. However, experiments contradict this observation, thus suggesting that the bigger particle contains less amount of charge after the collision. This results is further validated by the observations shown in figure 3.11(b) where the bigger particle contains 20% of the theoretical value of charge. In this case, in line with the experimental observations shown in figure 3.9, the bigger particle follows the smaller one for a brief period of time before reversing its direction.

Figure 3.11(c) demonstrates the variations of the positions of the centres of two spheres (h) measured from the electrode at $z = 0$, with time for different values of q_{1t}. The inset plot shows that particle 1 shows motion towards particle 2 only if the net charge on particle 1 is less than that of 2. The plots suggest that the larger the difference between the charges on the particles, the greater is the distance traversed by particle 1 in direction of particle 2. Another key observation is that as the charge on 1 decreases, the speed of particle 2 increases, although the magnitude of charge on particle 2 remains constant. This observation is qualitatively similar to the experimental observations shown in figures 3.5 and 3.6 where the smaller particles show slight increment in speed compared to their original after charge reversal.

Figure 3.12 compares the simulated velocities of Ag-coated particles with the experimental ones shown in figure 3.7. Figure 3.12(a) shows that in case of the equal sized particles, the simulated velocities predict the experimental ones with reasonable accuracy. It may be noted here that charge assigned to each particle was Q_0. In case of the unequal sized particles, based on the observations made in figures 3.7(c) and 3.7(d), the simulated particles were assigned Q_0 charge before collision and after collision the charge assigned to the bigger particle was $0.35Q_0$ and that to smaller particle was $1.35Q_0$. With these assigned values of charges figure 3.12(b) shows that the simulated values of v_s mimic the experimental values very well. The slight differences between the experimental and simulated values may be attributed to factors such as, (i) the effect of low but finite liquid conductivity is not included in the simulations in which the liquid is assumed to be non-conductive, (ii) the effect

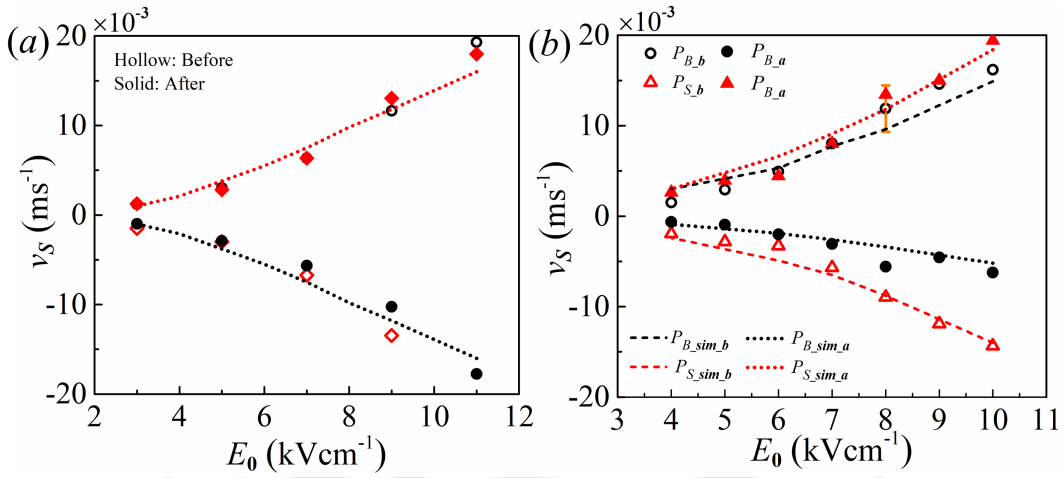

Figure 3.12: Variation of the average velocity (v_s) of the particles with average electric field (E_0) for (a) equal sized Ag-coated particles with radius 550 μm each and (b) unequal sized Ag-coated particles with the radius of the smaller being 400 μm and bigger being 550 μm, respectively. In figure (a) the dotted lines refer to simulated velocities. In figure (b) the notations specify the following: P_{B_b} (respectively, P_{S_b}): velocities of bigger (respectively, smaller) particle before collision, P_{B_a} (respectively, P_{S_a}): velocities of bigger (respectively, smaller) particle after collision, $P_{B\_sim\_b}$ (respectively, $P_{S\_sim\_b}$): simulated velocities of bigger (respectively, smaller) particle before collision, $P_{B\_sim\_a}$ (respectively, $P_{S\_sim\_a}$): simulated velocities of bigger (respectively, smaller) particle after collision.

of gravity is ignored in the simulations, (iii) the particles in the experiments are not perfect conductors as assumed in the simulations, and (iv) there are inaccuracies associated with assignment of values of parameters such as liquid viscosity, particle charge and liquid permittivity in the simulations.

Figures 3.13(a) and 3.13(b) demonstrate the experimental time sequence snapshots of two Ag-coated particles under 8 kVcm^{-1} and 5 kVcm^{-1} electric fields, respectively. The diameters of the big and small particles are ∼550 μm and ∼450 μm, respectively. The image panels (a) and (b) show that the average displacement of the bigger particle towards the smaller particle under two different electric fields are rather similar. However, in case of the lower electric field as shown in (b), the contact time between the particles as well as the time of retraction of the bigger particle, is much higher compared to higher electric field situation demonstrated in (a). This behaviour is intuitive for lower field values as charge reversal kinetics is expected to be slow, leading to an 'inelastic' collision with a higher contact time. The sluggish return of the bigger particle can be attributed directly to the lower

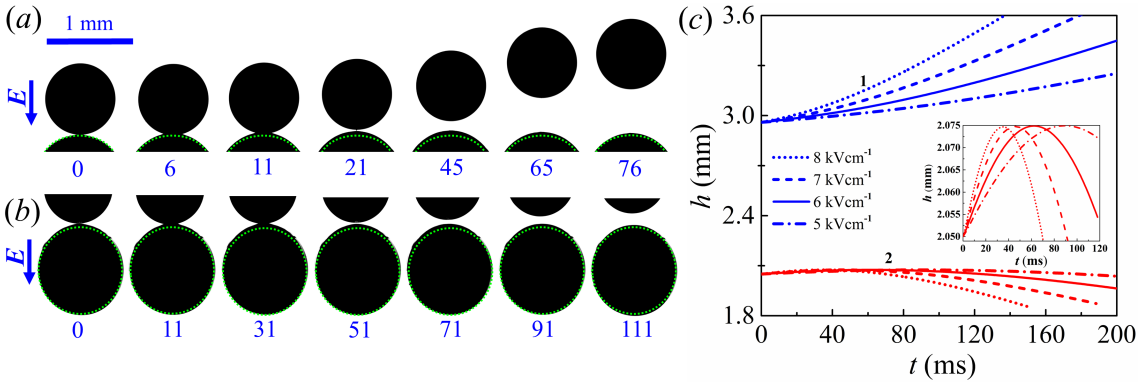

Figure 3.13: Experimental time sequence snapshots of Ag-coated amberlite resin particles under application of (*a*) 8 kVcm^{-1} and (*b*) 5 kVcm^{-1} average electric fields. The time indicated below each micrograph has unit of millisecond (ms). The diameters of the big and small particles are ∼550 µm and ∼450 µm, respectively. The experiments were visualized under a microscope at 10x magnification. The images correspond to the top view of the particles. The dashed lines in the image panels of (*a*) and (*b*) indicate the initial position of the bigger particle during its close approach with the smaller one. (*c*) Simulated values of the variations of the positions of the centres (h) measured from the lower electrode at $z = 0$, of a 400 µm sphere 1 and a 500 µm sphere 2 with time (t), at different applied electric field intensities. The upper (blue) graphs correspond to sphere 1 and the lower (red) plots correspond to a sphere 2. The inset plot represents the magnified view of the positions of sphere 2 during the initial time period. The simulations were carried out employing an axisymmetric domain.

value of electric force acting on it at lower field intensity. These observations are qualitatively confirmed by the simulated values of the variations of the positions of the centres of a negatively charged (400 µm) sphere 1 and a positively charged (500 µm) sphere 2 ($q_{2t} = 0.5$) with time at different applied electric field intensities, as demonstrated in figure 3.13(*c*). The inset plot in (*c*) clearly demonstrates that, while the bigger particle 2 undergoes similar displacement towards the smaller particle 1 at all studied field strengths, the time of flight of particle 2 increases with decreasing field.

Having discussed the origins of the oscillatory behaviours of the particles alongside their charge reversal dynamics under electric field, we now shift our focus to explore some of the important factors that drive the proposed phenomena. Figures 3.14(*a*) and 3.14(*b*) demonstrate the simulated distribution of the z-component of the Maxwell stress tensor (τ_z) over two equal sized particles 1 (negatively charged) and 2 (positively charged) of 500 µm radius each, under application of 9 kVcm^{-1} av-

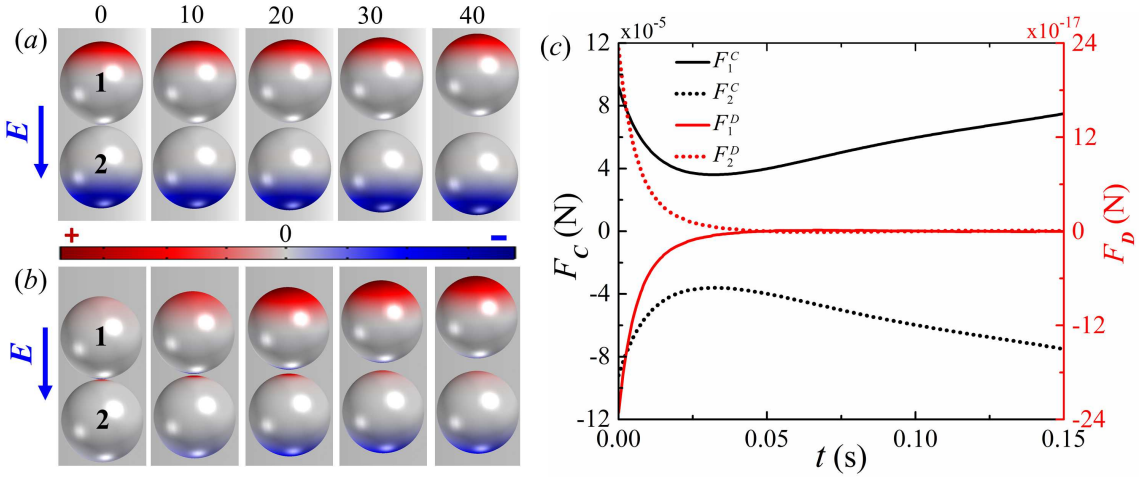

Figure 3.14: Simulated time sequence snapshots of the distribution of the z-component of the Maxwell stress tensor (τ_z) over two equal sized particles 1 and 2 of 500 μm diameter under application of 9 kVcm^{-1} average electric field for (a) $q_{2t} = 1$ and (b) $q_{2t} = 0.5$. Here, q_{2t} represents the ratio of charge contained by particle 2 to its theoretical value of charge. Particle 1 contains the theoretical values of charge. The time indicated above each snapshot has unit of millisecond (ms). (c) Variations of the Coulomb force (F_C) and the dielectrophoretic force (F_D) acting at points 1^t and 2^b with time. The simulations were carried out employing an axisymmetric domain.

erage electric field. Here, the sphere 1 is assigned the theoretical amount of charge. Figure 3.14(c) demonstrates that the magnitude of the Coulomb force (F_C) acting on the particles is very large compared to the dielectrophoretic force (F_D), and thus, the former almost entirely contributes to the electrical forces acting on the particles. Figure 3.14(a) correspond to $q_{2t} = 1$, wherein both the spheres contain equal charge of opposite polarity. The images suggest that the negatively charged particle 1 experiences an attractive force towards the anode, while the positively charged particle 2 experiences a pull towards the cathode. This eventually leads to the separation of the spheres from each other.

In order to a more in-depth information regarding the distribution of electric force on the spheres, we consider points 1^t (2^t) at the topmost point of sphere 1 (sphere 2) and 1^b (2^b) at the bottommost point of sphere 1 (sphere 2), respectively. It may be noted here that the usage of the words 'top' and 'bottom' in this write-up is only directed towards describing the results because the gravitational influence has been neglected in the formulation. Figure 3.15(a) corresponding to the case shown in figure 3.14(a), depicts the variation of τ_z with time at the topmost and bottommost

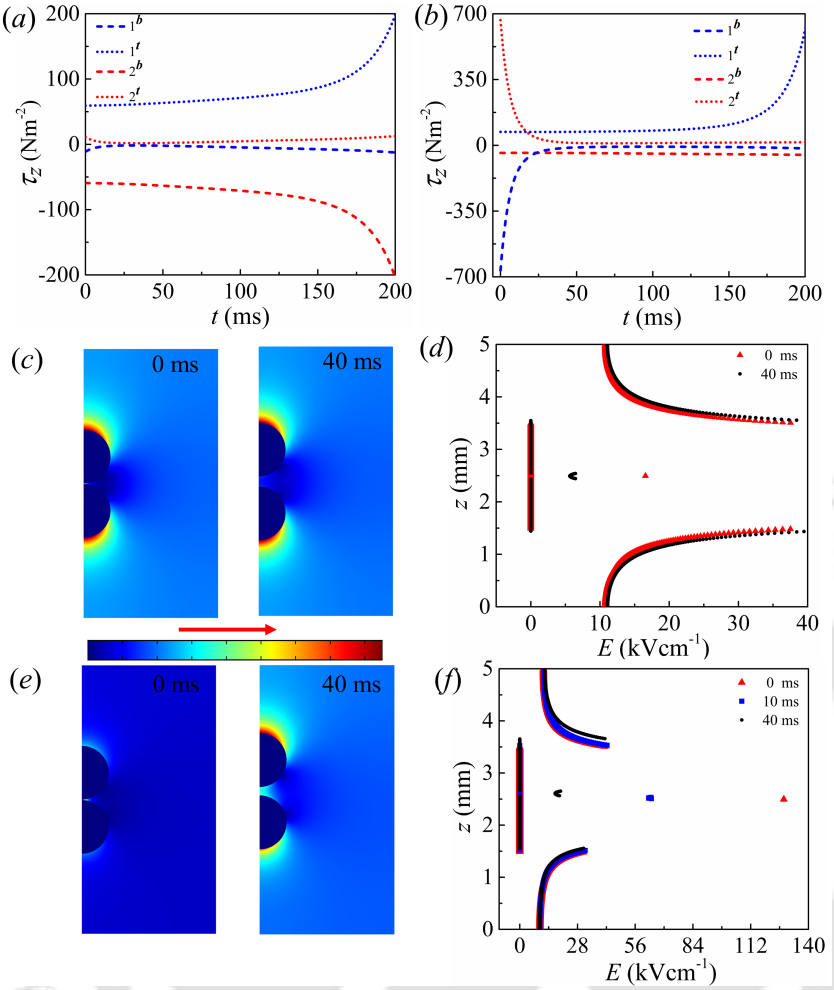

Figure 3.15: Variations of the z-component of the Maxwell stress tensor (τ_z) at the topmost and bottommost points of two equal sized particles 1 and 2 of 500 μm diameter under 9 kVcm^{-1} electric field for (a) $q_{2t} = 1$ and (b) $q_{2t} = 0.5$. Here, q_{2t} represents the ratio of charge contained by particle 2 to its theoretical value of charge. Particle 1 contains the theoretical values of charge. The subscripts t and b in the legends denote the topmost and bottommost point of spheres 1 and 2 corresponding to figure 3.14. (c) Surface plot showing the variations of the magnitude of the electric field intensity (E) and (d) variations of E along a cut line passing through the centres of the spheres 1 and 2 (axis of symmetry shown in figure 1(b) at average applied field intensity of 9 kVcm^{-1} corresponding to the case shown in 3.14(a). (e) Surface plot showing the variations of E and (f) variations of E along a cut line passing through the centres of the spheres 1 and 2 (axis of symmetry shown in figure 1(b)) at average applied field intensity of 9 kVcm^{-1} corresponding to the case shown in 3.14(b). The colour scale in (c) and (e) from blue to red indicates increasing magnitude of E. The simulations were carried out employing an axisymmetric domain.

points of the two spheres. It can be seen from the plot that the top-pole of sphere 1 experiences a strong attractive force towards the anode, while the bottommost point experiences a weak attractive force towards the sphere 2. This facilitates the net movement of the particle towards the anode. On the other hand the bottom pole of sphere 2 experiences a strong attractive force towards the cathode, while the topmost point experiences a weak attractive force towards the sphere 1. This facilitates the net movement of the particle towards the cathode. In a nut-shell, when the particles carrying opposing charges of equal magnitude move in a close proximity under an electric field, they experience a mutual attraction as well as an attractive force towards the electrodes of opposite polarity. While the brief association during the charge reversal is caused due to the particle-particle attractive force, they move apart towards the electrodes owing to the larger particle-electrode attractive force.

Figure 3.15(d) depicts the distribution of electric field magnitude (E) along a cut line passing through the centres of the spheres (axis of symmetry shown in figure 3.1(b)). The plots show that the electric field magnitude is highest at the topmost part of sphere 1 and the bottommost part of sphere 2, which increase as the spheres approach the respective electrodes. Thus, the points 1^t and 2^b experience larger attractive force from the electrodes, which progressively increase as the particles move towards them. The electric field in the gap between the spheres gradually decrease as the spheres move apart indicating reduction in the mutual attraction between the spheres.

Figure 3.14(b) demonstrates the simulated distribution of the z-component of the Maxwell stress tensor (τ_z) over spheres 1 and 2 for $q_{2t} = 0.5$, wherein the sphere 2 contains half of the charge contained by sphere 1 of opposite polarity. In this situation, the negatively charged sphere 1 experiences a pull towards the positive electrode, while the positively charged sphere 2 containing less charge briefly experiences a pull towards particle 1 and moves along its direction. The distributions of the stress due to electric field on the topmost and bottommost points of spheres 1 and 2, depicted in figure 3.15(b), reveals that the positive upward force acting on point 2^t is significantly larger than the downward force acting on point 2^b during the initial time period when the spheres arrive at near proximity, and eventually decrease with increase in the separation distance. Thus, sphere 2 briefly moves towards sphere 1, before reversing its motion towards the oppositely charged electrode. The variation of the magnitude of electric field corresponding to this situation are depicted in figures 3.15(e) and 3.15(f), which suggest a significant increment of electric

field between the spheres during their close proximity. The electric field in the gap decreases as the particles move apart, leading to the decrease in the upward force experienced by 2^t compared to downward force experienced by 2^b, thus, causing it to move away from the other particle. In this case, contrary to the case for $q_{2t} = 1$, 1^b experiences a significantly larger downward force compared to the upward force experienced by 1^t, during their close proximity, for a very brief period of time. However, sphere 1 still experiences a larger net positive force, which causes it to move towards the upper electrode.

The simulated results shown in figures 3.14(b) and 3.15(b) can be summarized as - when two spheres carrying unequal amount of charges of the opposite polarity, are placed in close proximity under the influence of an externally applied electric field, under the conditions mentioned, the spheres experience mutual attraction towards each other and towards the respective electrodes of opposite polarity. When their separation distance is small, the attraction experienced by the sphere of less charge towards the sphere of higher charge, is larger than its attraction towards the electrode of opposite polarity. Thus, it follows the sphere of higher charge briefly, until the separation between them increases to the extent that it experiences more attractive force towards the electrode of opposite polarity, after which the sphere starts moving towards electrode. The net force on the sphere of greater charge always acts towards the electrode of opposite polarity and it moves towards the electrode.

3.5.3.1 Flow Patterns and Role of Fluid Properties

Thus far, the major focus of the discussion has been to elucidate the motions of the particles inside the liquid medium under electric field. In this direction, the surrounding liquid medium is found to play a key role. For example, the dielectric contrast at the liquid-particle interface decides the capacity of the particles to retain charges, which is a crucial factor in deciding the extent of Coulombic force experienced by them. Further, formation of interesting flow patterns can also be envisaged during their periodic approach and reversal of the spherical particles between the electrodes. Such flow patterns may not only be important in deciding the speeds of particle migration, however, they may also help in deciding the directions of the particle motion. In such a scenario, the viscosity of the liquid is expected to play a crucial role especially when the particles sizes are different.

Figures 3.16 and 3.17 show the velocity and streamlines fields in the surrounding

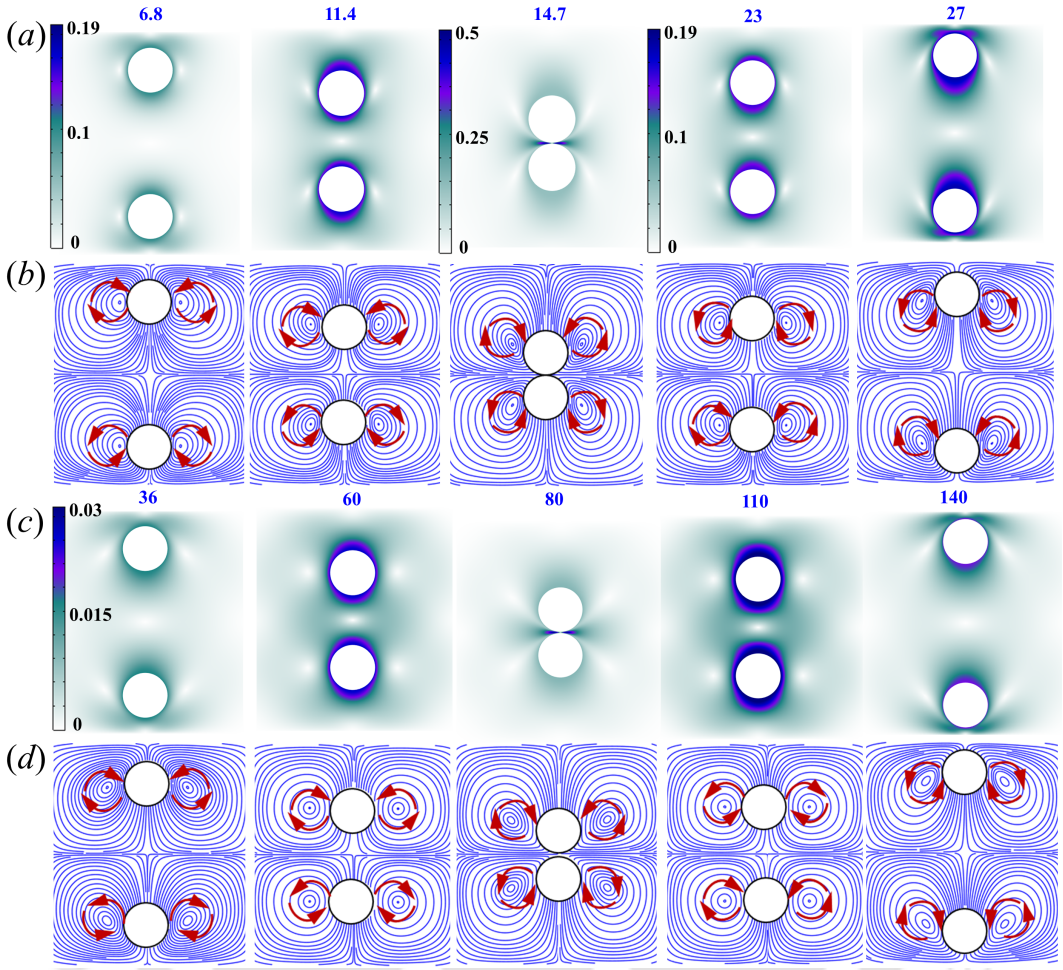

Figure 3.16: Simulated time sequence snapshots of (a) fluid velocity and (b) streamline fields for viscosity of the fluid $\mu_{rf} = 0.01$ Pa.s. (c) Fluid velocity and (d) streamline fields for viscosity of the fluid $\mu_{rf} = 0.1$ Pa.s. The particles considered are of equal size with radius of 500 μm each. The other parameters used for the simulations are, $E_0 = 9$ kVcm^{-1} and $\varepsilon_{rf} = 3$. The time indicated above the snapshots have units of milliseconds. The velocities indicated by the color scales have units of ms^{-1}.

liquid medium at the various stages of migrations of a pair of equal and unequal sized particles under electric field, respectively. The plots suggest that, as the spherical particles move in confined space between the electrodes, they entrain the liquid surrounding them. Subsequently, high fluid velocities are observed near the front and rear ends of the particles, as shown in the first 3 frames of the image sets (a) and (c) of figures 3.16 and 3.17. The liquid velocity in between the particles increase as the particles approach each other with the increase in their speed. In the process,

the liquid in-between drains out and during the collision the ejection of the liquid happen at a relatively higher velocity. Following this, once the particles separate and move towards the electrodes, they again entrain liquid with them until they collide with the electrodes, as shown by the last frames after collision of the image sets (*a*) and (*c*) of figures 3.16 and 3.17.

Once the particles attain the steady to-and-fro oscillatory motion between the

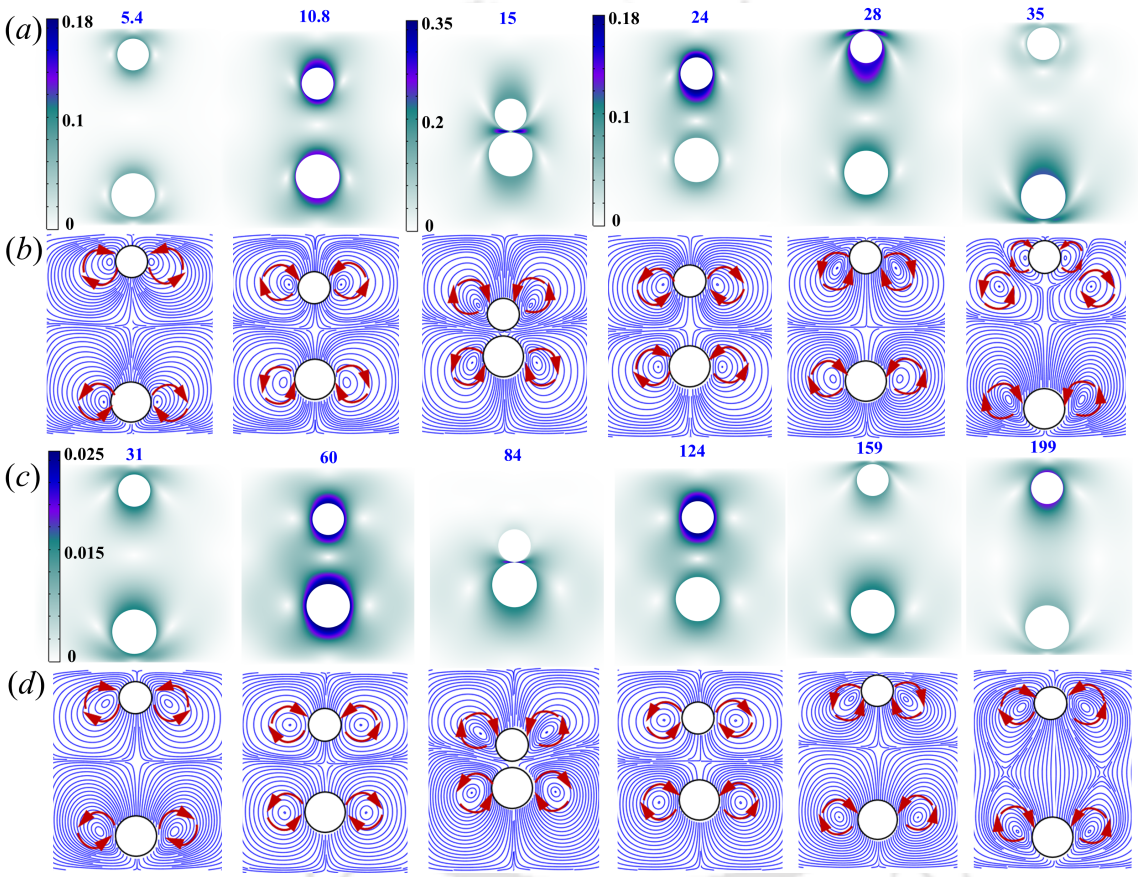

Figure 3.17: Simulated time sequence snapshots of (*a*) fluid velocity and (*b*) streamline fields for viscosity of the fluid $\mu_{rf} = 0.01$ Pa.s. (*c*) Fluid velocity and (*d*) streamline fields for viscosity of the fluid $\mu_{rf} = 0.1$ Pa.s. The particles considered are of unequal size with the radius of the bigger particle being 550 μm and the smaller being 400 μm. The other parameters used for the simulations are, $E_0 = 9$ kVcm^{-1} and $\varepsilon_{rf} = 3$. The time indicated above the snapshots have units of milliseconds. The velocities indicated by the color scales have units of ms^{-1}.

electrodes, a pair of counter rotating circulation loops are found to appear across each particle near their equatorial regions. The arrows on the streamline plots denote the directions of the liquid flows in the zones of recirculations. In such a

situation, the local stagnation points appear at the centres of the loops, where the liquid velocities nearly vanish, as shown in the image sets (b) and (d) of figures 3.16 and 3.17. As the particles move towards or away from each other, a stagnation point develops at the axial region between the particles with the liquid around it moving in opposite directions. Examining the stream line plots for $\mu_{rf} = 0.01$ Pa.s and $\mu_{rf} = 0.1$ in figures 3.16 and 3.17, it can be seen that the circulation loops are centred much close to the particle in case of $\mu_{rf} = 0.01$ Pa.s compared to $\mu_{rf} = 0.1$ Pa.s. Interestingly, the recirculation zones are of similar size, for a very synchronized motion of the particles with an 'elastic' collision in the middle. However, if 'inelastic' collision takes between unequal sized particles, the size and shapes of the recirculation zones in the surrounding liquid medium are asymmetric as shown in figures 3.17(b) and (d). Further, a comparison between the images of figure 3.17(b) and (d) suggest that the recirculations near the electrodes are also suppressed for the high viscosity case and the velocity of liquid ejection between the particle and electrode is smaller (figures 3.17(b) and (d)). The results also suggest that the multi-particle assemblages shown in the figure 3.2 are expected to have array of such flow patterns around the particles while undergoing incessant to-and-fro motion between the electrodes.

Apart from the flow structures in the surrounding liquid, the viscosity of the fluid also influences the kinetics of the particle migration. For example, figures 3.16 and 3.17 show that the velocity of particle oscillations decrease with increase in the liquid viscosity, due to increase in the hydrodynamic drag force. Interestingly, the point of collision can also be modulated by tuning the viscosity of the liquid. Figure 3.20(a) shows the variations of the positions (h) of two unequal particles with time for two different liquid viscosities. The figure suggests that as the liquid viscosity increases, the point of collision shifts upwards. With the increase in viscosity of the liquid medium, the drag force experienced by each of the particles increases, with the electrical force acting on them remaining constant. In case of the smaller particle, for $\mu_{rf} = 0.1$ Pa.s, due to increase in the viscous drag, the net force acting downwards, decreases more compared to the net upward force experienced by the bigger particle. Hence, the smaller particle travels lesser distance downwards before its collision with the bigger particle. This in turn, shifts the point of collision slightly upwards for $\mu_{rf} = 0.1$ Pa.s. compared to $\mu_{rf} = 0.01$ Pa.s.

Vorticity ($\boldsymbol{\omega} = \boldsymbol{\nabla} \times \boldsymbol{v_f}$) fields show the local fluid rotation or spinning near a

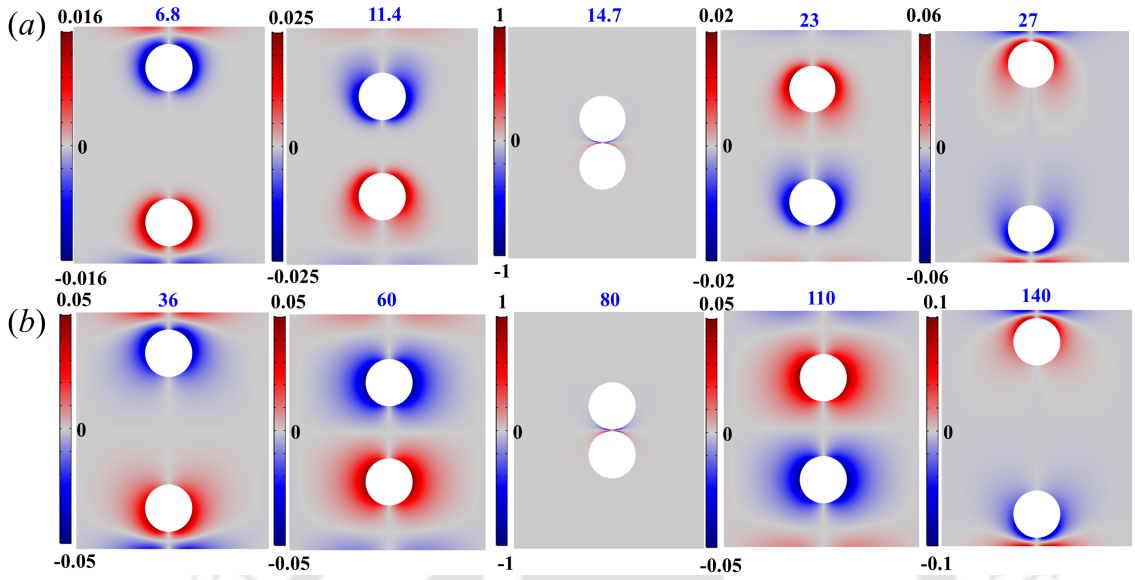

Figure 3.18: Simulated time sequence snapshots of azimuthal vorticity (ω_θ) fields for (a) viscosity of the fluid $\mu_{rf} = 0.01$ Pa.s. and (b) viscosity of the fluid $\mu_{rf} = 0.1$ Pa.s. The particles considered are of equal size with radius of 500 μm each. The other parameters used for the simulations are, $E_0 = 9$ kVcm^{-1} and $\varepsilon_{rf} = 3$. The time indicated above the snapshots have units of milliseconds. The ω_θ values indicated by the color scales are normalized with the maximum values. For $\mu_{rf} = 0.01$ Pa.s the values are normalized by $\omega_\theta = 6 \times 10^4$ s^{-1} and for $\mu_{rf} = 0.1$ Pa.s the values are normalized by $\omega_\theta = 3000$ s^{-1}.

point. Figure 3.18 shows the azimuthal vorticity ($\omega_\theta = \frac{\partial v_{fr}}{\partial z} - \frac{\partial v_{fz}}{\partial r}$) fields, for equal sized particles, where v_{fr} and v_{fz} denote the r and z directional fluid velocities, respectively. Figure 3.19 denotes the vorticity fields for unequal sized particles. At the surface of the solid, the fluid velocity goes to zero (no-slip condition), which results in very high velocity gradients in the regions surrounding the particles, leading to the generation of vorticity in the fluid. Figures 3.18 and 3.19 show that regions of strong positive and negative vorticity develop in the liquid, in the immediate vicinity of the particles. Interestingly, the first three frames of the image sets shown in figures 3.18 and 3.19 show a common-flow-up configuration (CFUp) of twin vortices accompanying the bottom-particle during its motion towards the top particle [273]. Again in the same set of images, the vortices surrounding the top-particle show a common-flow-down arrangement (CFDn) during its motion towards the bottom one. This can be more explicitly understood by the arrows on the first three frames of image sets (b) and (d) of the figures 3.16 and 3.17. Importantly, the 2nd, 3rd, and

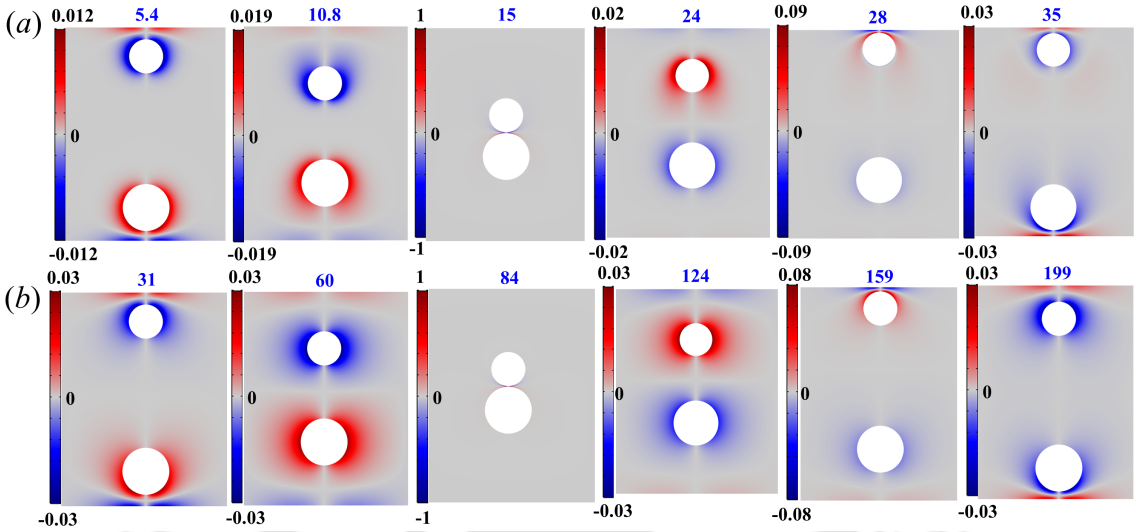

Figure 3.19: Simulated time sequence snapshots of azimuthal vorticity (ω_θ) fields for (a) viscosity of the fluid $\mu_{rf} = 0.01$ Pa.s. and (b) viscosity of the fluid $\mu_{rf} = 0.1$ Pa.s. The particles considered are of unequal size with the radius of the bigger particle being 550 µm and the smaller being 400 µm. The other parameters used for the simulations are, $E_0 = 9$ kVcm^{-1} and $\varepsilon_{rf} = 3$. The time indicated above the snapshots have units of milliseconds. The ω_θ values indicated by the color scales are normalized with the maximum values. For $\mu_{rf} = 0.01$ Pa.s the values are normalized by $\omega_\theta = 8 \times 10^4$ s^{-1} and for $\mu_{rf} = 0.1$ Pa.s the values are normalized by $\omega_\theta = 5000$ s^{-1}.

4$^{\text{th}}$ frames of the image sets (a) and (b) of figure 3.18 and 3.19 (and the corresponding images on the figures 3.16 and 3.17), suggest that after the collision there is a reversal of the direction of the rotations in the vortices. In such a situation, the top-particle moving towards the top-electrode is accompanied by a pair of CFUp vortices whereas the bottom one is surrounded by a pair of CFDn vortices until it arrives the bottom electrode. In case of the unequal sized particles, after the collision, the smaller particles travels faster towards the top electrode and for a brief period of time, both the particles travel downwards. Thus, the last images of the image sets shown in shown in figure 3.19, depict negative vorticity fields around both the particles. It can be seen from both figures 3.18 and 3.19 that, the magnitudes of vorticity are higher for $\mu_{rf} = 0.01$ Pa.s compared to $\mu_{rf} = 0.1$ Pa.s. This is because the velocity gradient in the lower viscosity fluid near the solid are greater than the higher viscosity fluid.

Another point of difference in the ω_θ fields is that, they are much diffused in case of $\mu_{rf} = 0.1$ Pa.s compared to $\mu_{rf} = 0.01$ Pa.s. The vorticity transport equation

can be written as: $\frac{\partial \boldsymbol{\omega}}{\partial t} + (\boldsymbol{v_f} \cdot \boldsymbol{\nabla})\,\boldsymbol{\omega} = (\boldsymbol{\omega} \cdot \boldsymbol{\nabla})\,\boldsymbol{v_f} + \nu \nabla^2 \boldsymbol{\omega}$, where, ν refers to the kinematic viscosity of the fluid. The second term on the left hand side of the equation denotes the convection of vorticity while the second term of the right hand side of the equation refers to the diffusion of vorticity with diffusivity, ν. Since, the fluid velocities are very less, the convection of vorticity can be ignored. Thus, the vorticity is transported from the regions near the surface of the solid mainly by diffusion. The length scale of the diffusion can be defined as $\sim \sqrt{\nu t}$. Thus, for $\mu_{rf} = 0.1$ Pa.s, ν is greater compared to $\mu_{rf} = 0.01$ Pa.s. Also, the time for diffusion is greater due to lower velocity in case of $\mu_{rf} = 0.1$ Pa.s. Thus, the vorticity is transported to a larger distance compared to $\mu_{rf} = 0.01$ Pa.s, and thus, the ω_θ fields is case of $\mu_{rf} = 0.1$ are more diffused compared to $\mu_{rf} = 0.01$ Pa.s.

Finally, the relative permittivity (ε_{rf}) of the fluid is another important parameter affecting the oscillation characteristics of the particles. Generally, relative permittivity in conjunction with the fluid conductivity are more important in determining the particle dynamics. But in the present study the fluid medium is considered as non-conductive. Hence, the variation of fluid conductivity is not considered. Figures 3.20(b) and (c) show the positions (h) of the particles with time for varying values of ε_{rf}. Figure 3.20(b) denotes the case of equal sized particles and

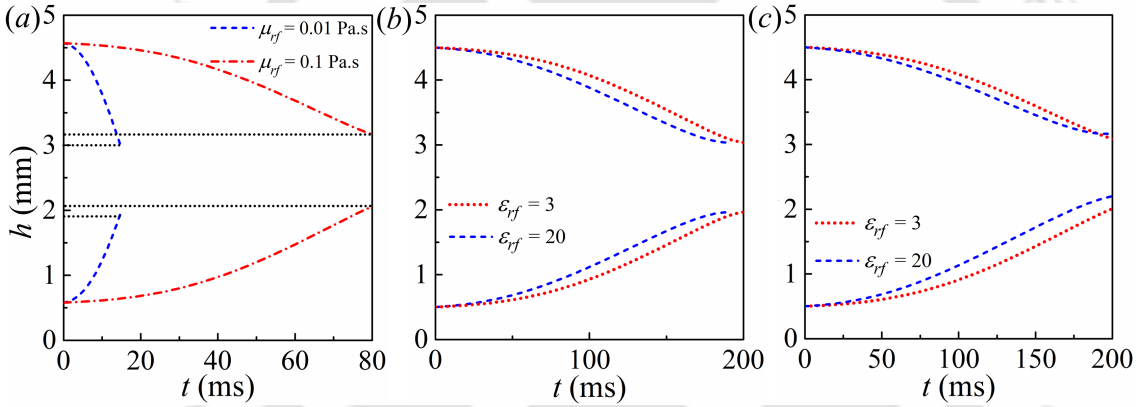

Figure 3.20: Simulated variations of the positions of the centres of the particles (h) from the lower electrode at $z = 0$ with time (t) for (a) two unequal particles with the radius of the bigger particle being 550 μm and the smaller being 400 μm for different values of μ_{rf}, (b) two equal particles with radius of 500 μm each and (b) two unequal particles with the radius of the bigger particle being 550 μm and the smaller being 400 μm for different values of ε_{rf}. The other parameters used for (a) are, $E_0 = 9$ kVcm^{-1} and $\varepsilon_{rf} = 3$. The other parameters used for (b) and (c) are, $E_0 = 9$ kVcm^{-1} and $\mu_{rf} = 0.25$ Pa.s.

3.20(*c*) refers to unequal sized particles with the smaller particle being at top. Both the figures indicate that the velocity of the particles increase with increasing fluid permittivity. As ε_{rf} increases, the electric field around the particle increases due to increasing bound charge density, leading to a greater Coulombic force acting on the particle. Thus, the particle speed is expected to increase under such circumstances.

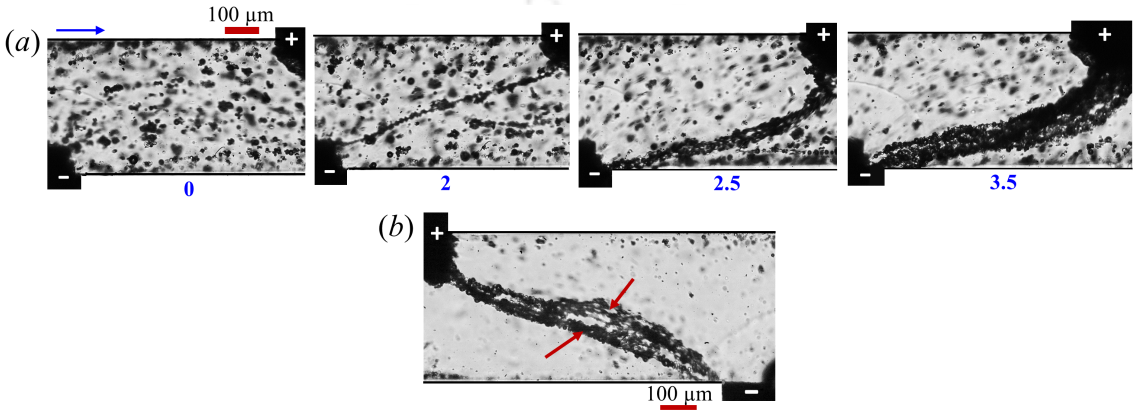

Figure 3.21: (*a*) Experimental time sequence snapshots of chaining of glass particles (∼10 µm radius) under application of 12 kVcm^{-1} average electric field, inside a 400 µm diameter microfluidic channel. (*b*) Experimental micrograph depicting the rotation of the chain of glass microparticles under application of 12 kVcm^{-1} average electric field, inside a 400 µm) diameter microfluidic channel. The experiments were visualized under a microscope at 10x magnification. The images correspond to the top view of the particles. The arrow on the first image indicates the direction of the flow.

3.6 Applications

The experiments shown here can also be extended to a number of futuristic microfluidic applications. For example, the particle chains in a PLFF (e.g. figure 3.2) can also be formed inside a microchannel with the help of an externally applied electric field to cause an on-demand restriction or opening of the flow. Such motions of a chain of glass microparticles inside a microfluidic set-up are shown in the figure 3.21. The details related to the fabrication of the channels can be found elsewhere [266]. In these experiments, silicone oil suspended with glass particles was flown through the channel. The experiments uncover various stages of chain formation, which initiate with the collision and charging of a few glass particles with

electrodes. Subsequently, the particles undergo oscillations between the electrodes and also between other particles. Some particles do not collide with the electrodes or other particles and escape to the downstream with the flow. Each collision between a pair of charged particles or between a pair of charged chains, or between a charged particle and a chain lead to charge reversal of the colliding components, which sustains the to-and-fro motions of the particles or chains in the void space available within the chains. Over a period of time, such motions of the charged particles increase their packing density between the electrodes to form a 'garland' of glass articles between the electrodes (shown by arrows in figure 3.21(b)).

Remarkably, at a very high field intensity, the garland like morphology is also found to show an anti-clock wise unsteady stick-slip motion in which the Coulombic force active between the electrodes enables one-half of the chained particles in the garland to move in the opposite direction of the other half. In fact, each of the two-halves of the 'garland' have opposite charge, which is reflected from their occasional joining due to the Coulombic attraction. In a way, the large collection of particles between the electrodes developed a pathway to electric field discharge. The discharge is less when the particles or the chains moved while the same is significant when the movements of the particles are sluggish or stationary. Most of the particle movements in the multi-particle experiments in the figures 3.2 and 3.21 largely follow the various combinations of the two-particle motions described in the study. On the other hand, from the electrorheological point of view, the assemblage shown in the figures 3.2 and 3.21 also hint towards the on-demand generation of localized power law behaviours inside microfluidic systems under the guidance of electric field.

3.7 Conclusions

We explore the pathways to the self-organization of a collection of microparticles inside a dielectric fluid under the influence of an external electric field. The electric is applied in such a manner that the electrodes are in direct contact with the fluid of significantly low electrical conductivity, which leads to the flow of a very weak leakage current through the fluid upon application of a high intensity filed. In such a PLFF, embedding the particles of different size or surface conductivity effectively help in improving the net capacitance of the fluid of low dielectric permittivity. Subsequently, the particles self-organize in the direction of the applied field creating

optimal channels for electric field discharge between the electrodes. The particles move when there is a build-up of potential difference while they become stationary when the electric field discharge through them. A combined experimental and computational study provides an insight to the dynamics of such systems by considering a two-particle system, undergoing oscillatory motions upon application of electric field. The major observations are,

1. Unlike the single particle motion between a pair of electrodes, in the multi-particle system, the particles also gather charge during the collisions in between themselves. Importantly, for such a system, the oscillatory to-and-fro motions of the particles are observed between, a pair of particles, a pair of chains, a particle and a chain, an electrode and a particle, and between the electrodes. Charge transfer followed by charge reversal between the particles near contact are found to be the necessary driving forces for the reversal of the directions of motions.

2. The finer features of the multi-particle assemblage are explored employing a model two-particle system. The experiments together with the numerical simulations for such systems uncover that the time of contact and charge reversal increases with reduction in the applied field intensity or the surface conductivity of the particles. The equal sized particles exhibit a synchronized oscillatory pattern. Their speeds of approach prior to contact and the speeds of separation, subsequent to contact and charge reversal, are reasonably identical. Unequal sized particles on the other hand show asymmetric trajectories, in such a manner that the speed of the smaller particle increases marginally after contact, while the bigger particle demonstrates a rather sluggish behaviour after contact. Experiments with unequal sized particles, also reveal that after contact between the particles, the union of the particles moves in the direction of the bigger particle briefly, before the charge reversal and separation of the particles take place. In these processes the equal sized particles under electric field driven 'elastic' collisions, while the collisions between unequal particles are rather 'inelastic'.

3. Numerical simulations corroborate the experimental observations when, (a) equal sized particles−contain equal and opposite amount of charges, (b) unequal sized particles−the bigger (smaller) particle contains smaller (larger)

amount of opposite charge after collision. The distributions of the simulated electric force on the particles reveal that, in a pair of equal and oppositely charged particles, each particle experiences attraction towards the electrode of opposite polarity, which overcomes the mutual attraction between the particles. Thus, the particles move apart from each other, as also observed in the experiments. On the contrary, in the case of particles carrying unequal quantities of charge of opposite polarity, when the gap between the particles is small, the particle with lesser charge experiences more attractive force towards the particle of higher charge than the electrode of opposite polarity. This causes the particle to follow the particle of higher charge, until the attractive force between it and the electrode of opposite polarity overcomes its attraction towards the particle of higher charge. Periodic to-and-fro movement of the spherical particles facilitate the formation of the recirculation zones around each particle. An array of such flow patterns around each particle can be envisaged for a multi-particle system while they undergo incessant to-and-fro motion between the electrodes. The non-slipping particle-liquid interface ensure the generation of a very high velocity gradient in the liquid medium present near a moving particle, which eventually leads to the formation of the vortices in the liquid. In a way, the electrical energy supplied to the particles facilitates their mechanical motion which in turn dissipates through the formation of vortices in the surrounding liquid medium. The size and strength of the vortices around each particle, viscosity of the liquid medium, and the dielectric contrast across the liquid-particle interface play key roles in deciding the particle speed, point of collision, and trajectory of motion in a PLFF under electric field. The location and the number of vortices around a particle can be modulated by changing the particle size and viscosity of the surrounding liquid.

4. Experiments with the multi-particle system exhibit different kinds of assemblies hinting at the onset of on-demand power law electrorheological behaviour under the guidance of electric field. Further, translating a similar system into a microfluidic channel with a unidirectional flow bias reveals the trapping of the microparticles between the electrodes.

Concisely, the study qualitatively uncovers various finer features of the oscillatory motions of particles in a liquid medium under electric field. The results suggest that an in-depth analysis on the mechanisms of charge transfer, charge reversal be-

tween the particles, and the role of the flow patterns in the liquid medium on such phenomena can be a very potent areas of future research. The phenomenon can also be harnessed for a number of futuristic applications such as microfluidic vortex generators or flow control valves, on-demand catalyst beds for reaction engineering, extraction of solid from liquid and microrheology.

Chapter 4

Electric Field Mediated Modes of Active Droplet Transport across a Deformable Interface

4.1 Abstract

We explore the migrations of a droplet across the interface of a pair of immiscible liquids under electric field. The electrohydrodynamic stress conditionally deforms the droplet, while the migration of the droplet deforms, stretches, and ruptures the biphasic carrier-target interface. The dynamics of the interfaces in such a ternary system have been analysed through high-speed imaging and simulations. Experiments together with simulations reveal the presence of the rupture and tailing modes of droplet transport across the interface. In the rupture mode, below a critical electric field Weber number (We_{E}), a quasi-steady rupture and hole-growth of the carrier film are observed, wherein the hole-radius r_{h} at the interface follow a viscosity dominated kinetics of, $r_{\mathrm{h}} \sim t$. In contrast, beyond this critical We_{E}, a fast moving prolate shaped droplet induces an inertia dominated hole-growth kinetics following, $r_{\mathrm{h}} \sim t^{0.5}$. Film drainage occurs in two stages, with the rate diminishing significantly after the film thickness nears 0.3 times the droplet radius. An analytical model, reveals velocity profiles resembling the Couette flow within the draining film during the various stages of carrier-film drainage. In the tailing mode, the droplet entrains carrier liquid approximately equal to it five times its own volume into the target liquid, wherein the length of tail can be as high as eight times the drop radius. The electric permittivity, interfacial-tensions, density and viscosity of the liquids of the ternary system are the key parameters influencing the dynamics of both the modes of migrations. The phenomena may find applications in liquid-liquid extraction, micro-reactions, ultra-low tensiometry, among others.

The contents in this chapter have been submitted for publication as S. Dutta, P. S. G. Pattader, and D. Bandyopadhyay, (2020) 'Electric Field Mediated Modes of Active Droplet Transport across a Deformable Interface'.

4.2 Introduction

Droplet, particle, or bubble laden ternary systems make frequent appearance in a plurality of industrial and laboratory processes. In general, such three-phase configurations are associated with the transport of a single (or a collection of) solid particle(s) or liquid droplet(s), or gas bubble(s) from a carrier liquid phase to a target liquid. For example, emulsification [274], painting [275], liquid-liquid extraction [118–120], separation processes involving electro-coalescence [121, 122], vesicle formation [127], micro-reactors [26, 123, 124], encapsulation and coating [125] and drug delivery [126, 128, 129] processes often encounter such 'droplet-carrier-target' ternary liquid systems. Further, the complex but rich thermodynamics [276] and kinetics [277] of such droplet laden three-phase systems have also been one of the most exciting areas of fundamental research. Of late, the emergence of droplet or digital microfluidic devices [278] and microscale extractors [137] or mixers [22, 266], composed of miniaturized and multiscale [279] processes have opened up fresh avenues in fluid dynamical research belonging to this class of systems. In such processes the advancements in the understanding of 'active' [140] or 'passive' [131] transport of droplets in ternary systems have become one of the major foci of ongoing research.

The prior-art reveals that the transport of a droplet across a liquid-liquid interface composed of the carrier and target liquid phases has been employed as a model set-up to explore the finer aspects of such configurations [163]. In this regard, the passive transport involves a droplet transfer due to the interplay of *in-situ* inertial, gravitational, or viscous forces through the engineering of the enclosing geometry or boundaries. On the contrary, active transport of drops relies on the use of external influences such as magnetic, electric, photonic, or acoustic fields, for the migrations. Previously, a number of seminal contributions have explored the routes of passive droplet transfer engendered by the inertial forces in the branched channels [131], channels with the railed boundaries [132] or around the pillars [133]. Some other passive methods have relied on using the non-inertial lift force [134–136] and interfacial tension gradients [137]. On the other hand, active droplet transfers with the help of magnetic field [138], surface acoustic waves [139] and laser [140] have also been explored.

However, such ternary configurations involve the existence of a triplet of liquid-liquid biphasic interfaces, composed of the droplet-carrier, droplet-target, and carrier-target phases, which pose significant difficulty in, (i) experimental tracking of the

migrations of the dispersed droplet phase in the carrier and target phases; (ii) simultaneous tracing of the spatiotemporal dynamics of the three interfaces; (iii) setting up of the governing equations with appropriate boundary conditions for the simulations; (iv) obtaining the analytical or numerical solutions of the same for theoretical or computational analyses; and (v) the inclusion of the effects of the external fields in the theoretical and experimental set-ups.

Previous studies indicate that the migration of a solid particle through a liquid-liquid interface has been a much easier system to follow experimentally owing to the non-deformability of the solid-carrier or solid-target interfaces [141–153]. Prior-art suggests that the breaking of the liquid-liquid interface during the migration of a solid particle from the carrier liquid to the target involves the film-drainage and tailing modes [167]. In the film-drainage mode, the solid particle crosses the interface in a quasi-static manner, with the slow drainage of the carrier fluid film trapped in between the particle and target phases, followed by the rupture of the carrier film. On the other hand, the tailing mode initiates as the particle tows a column of the carrier phase into the target liquid keeping the film ahead of it non-ruptured.

It has been observed that for the film-drainage mode, the flow profile within the film (thickness, h) is parabolic or half-parabolic at the various stages of film-draining. Further, the rate of film thinning is found to follow a $h \propto t^{-1/2}$ law, when gravity is dominant [141,142] and $h \propto t^{-1/4}$ law otherwise [173]. The point of rupture of the carrier film trapped between the target and solid phases can be predicted from the magnitude of the Bond number, $Bo = (\rho_2 - \rho_1)\, g r_s^2/\sigma_{12}$, where, ρ, g, r, and σ_{12}, denote the density, acceleration due to gravity, particle radius, and interfacial tension, respectively. Subscripts 1, 2 and s, denote the carrier liquid, target liquid and solid, respectively. For low Bo, the film around the particle is constricted into a dimple, near the pseudo-contact line and the film rupture takes place there. In another case of detachment, the particle submergence may be high, so that the dimple position nears the critical angle $\sim 3\pi/4$. Under this circumstance, the particle detaches before complete drainage of the film around its surface [152]. For high Bo, the constriction develops near the axial region such that, the film rupture takes place near the advancing pole of the particle [280].

The tailing mode for the solid particle transfer in a liquid-liquid carrier-target system occurs if the forces favouring the particle migration are very high as compared to the restoring interfacial tension force. As the particle passes through the interface, the tail of the carrier liquid is stretched before pinching off to release

the particle into the target liquid [143, 151–153]. The size and shape of the tail varies with the density contrast (ρ_2/ρ_1) or viscosity contrast (μ_2/μ_1) across the carrier-target interface as well as with the magnitudes of Bo [144, 153], Archimedes $\left(Ar = \rho_1 V_1 r/\mu_1, \text{where}, V_1 = \{(\rho_s - \rho_1)\, rg\}^{1/2}\right)$, and Reynolds numbers [151, 152]. Here, ρ_s denotes the density of the solid particle. Importantly, a short-tail is found to recede towards the carrier fluid after pinch-off while a long-tail may undergo a Plateau-Rayleigh instability to form droplets of carrier liquid in the target phase [152, 167].

There has also been considerable research on the breakthrough of a bubble or cluster of bubbles through the interface between two immiscible liquids [144, 154–166]. Similar to the solid particles, bubble migrations can also be broadly divided into the film drainage and the tailing modes. Such modes of bubble migrations can be predicted from the magnitudes of the Bond numbers, $Bo_1 = ((\rho_b - \rho_1)\, gr_b^2/\sigma_{1b})$ and $Bo_2 = ((\rho_b - \rho_2)\, gr_b^2/\sigma_{2b})$, which are defined based on the physical properties of the target and carrier liquids. Here the subscripts 1, 2 and b denote, the carrier fluid, the target fluid and the bubble, respectively [167]. In the presence of a free surface, the film encircling the bubble, undergoes an exponential decay [160, 281], which slows down significantly in case of an interface [163]. The studies unveil that the rate of film-drainage diminishes significantly with the increase in Bo and Bo_1, due to increasing deformability of the bubble-carrier and bubble-target interfaces [163, 281]. Importantly, a plug velocity profile can be observed in such draining films [160, 163, 173], while the film rupture nucleates near the upper pole of the advancing bubble where the carrier film thickness is minimum [163, 166]. In contrast, at a higher Bo, the bubble migrations are accompanied by the tailing mode owing to the lower interfacial restoring forces. In this regard, the detailed analyses of the tail geometry, entrained volume of carrier fluid, and bubble velocities have been reported in the past [159, 163, 166].

In comparison to the migrations of the solid particles or gas bubbles, the migration of a liquid droplet across a carrier-target liquid-liquid interface has been a rather less explored configuration [168]. In particular, the studies related to the passive transport of the liquid droplets in a carrier liquid have had a major focus on the exploration of the various characteristics of the film drainage and rupture, prior to the coalescence of droplets into a bath of the same liquid [122, 159, 169–181]. Such studies reveal that the film thickness may undergo a power law decay with a parabolic or half velocity profile in the draining film when the droplet has a signifi-

cantly higher viscosity, ($\mu_d/\mu_1 \gg 1$) [142,168,173–175,282].). Here, the subscripts 1 and d denote the drop containing fluid and the drop, respectively. In contrast, for the case with $\mu_d/\mu_1 \leq 1$, a fast film drainage can be expected, leading to a film rupture near the advancing pole of the droplet [174,175]. Importantly, most of these studies explore the passive modes of transfer of droplet, bubbles, or solid particles across the interface. The field induced active migrations of liquid droplets across a biphasic carrier-target liquid interface is a ternary system, which remains to be one of the very interesting but unexplored systems from any of experimental, theoretical, and computational point of views.

In view of this background, herein, electrical force has been harnessed to cause an active transfer of a charged droplet from a carrier to a target liquid phase in a 'drop-carrier-target' ternary liquid system. Figure 4.1 schematically shows the experimental and computational set-ups in which the migration of a water droplet (C) from a heavier carrier liquid (B) to a lighter target liquid (A) has been engendered by an electrohydrodynamic (EHD) field. The density of the water droplet ensures that it is initially placed on the bottom electrode to acquire charge from the same before undergoing an electrophoretic migration towards the anode at the top. On the way, the water droplet encounters the carrier-target interface before it breaks across or deforms the same to display an array of unprecedented film-drainage and tailing modes of active transport mechanisms. The configuration is particularly interesting because the presence of three liquids of different density, viscosity and surface tension is expected to alter the film-drainage, rupture, and tailing characteristics, as the droplet breaks across the target-carrier interface under the influence of the electric field. Further, the EHD stresses generated at the triplet of droplet-carrier, droplet-target, and target-carrier interfaces also stimulate a number of novel interfacial morphologies during the droplet transfer from the carrier to the target phase. An array of high-speed images of the phenomena uncover the finer features of the dynamics associated with the drainage of the carrier film, its rupture and the tailing of the carrier fluid into the target phase.

Most importantly, the ternary system shown in the figure 4.1 is a significantly challenging system to model analytically and computationally, because it requires simultaneous tracking of three interfaces composed of liquids A and B, B and C, and C and A [283]. In the present study, we propose a set of governing equations along with appropriate boundary conditions, which is capable of resolving the fluid dynamics of such intricate motions of coupled interfaces. A unique diffuse-interface

phase-field formulation [277, 283–288] has been utilized to track the interfaces under a computational fluid dynamics (CFD) framework, to characterize the salient features associated with the migration dynamics. The CFD simulations reveal a host of interesting insights related to the film-drainage, rupture, and tailing of the carrier fluid as the droplet pierces through the carrier-target interface under the effect of electric field. The roles of the flow patterns in the form of recirculations inside the carrier and target fluids on the various morphologies of the carrier-target interface have also been explored. Finally, analytical models have been proposed to evaluate the rate of the film drainage of the carrier fluid, and the critical field required to engender the droplet migration.

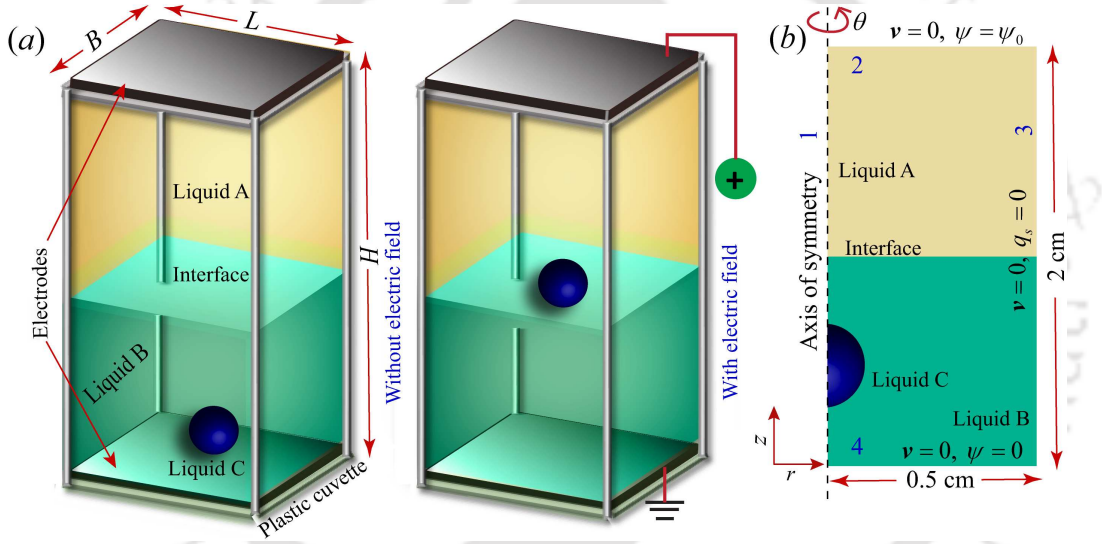

Figure 4.1: (*a*) Schematic representation of the experimental set-up. The lower density fluid A sits above the higher density fluid B inside a plastic cuvette 1 cm×1 cm×2 cm ($L \times B \times H$). A droplet of water (fluid C) is initially placed inside fluid B. The system is subjected to electric eld from a direct current (DC) high voltage source through Cu electrodes. A positive potential is applied to the top electrode while the bottom electrode is grounded. (*b*) Schematic diagram of the computational domain for computational fluid dynamics (CFD) simulations with the dimensions.

4.3 Experimental Methodology

Figure 4.1(*a*) shows that the target fluid A with a lower density was placed above the carrier fluid B of higher density inside a plastic cuvette of dimensions 1 cm×1 cm×2 cm ($L \times B \times H$). A drop of water (0.1 % w/v aqueous NaCl solution, 0.017

M) was used as phase C with, radius, $r_C \approx 1$ mm, density, $\rho_C \approx 1000$ kgm^{-3}, viscosity, $\mu_C \approx 0.001$ Pa.s, dielectric constant, $\varepsilon_C \approx 80$, and conductivity $\zeta_C \approx 0.2$ Sm^{-1}. The usage of dilute aqueous salt solution as phase C helped in improving the electrical conductivity of the droplet to facilitate motion under a lower electric field. The carrier fluid (B) used during the experiments was silicone oil (Merck, density, $\rho_B \approx 960$ kgm^{-3}, viscosity, $\mu_B \approx 0.3$ Pa.s, dielectric constant, $\varepsilon_B \approx 2.7$ [221], and electrical conductivity, $\zeta_B \approx 10^{-13}$ Sm^{-1} [231]) and the target liquids (A) were chosen from oleic acid (Merck, density, $\rho_A \approx 860$ kgm^{-3}, viscosity, $\mu_A \approx 0.02$ Pa.s , dielectric constant, $\varepsilon_A \approx 2.3$ [289], and electrical conductivity, $\zeta_A \approx 10^{-13}$ Sm^{-1} [290]) and soybean oil (local vendor, $\rho_A \approx 920$ kgm^{-3}, viscosity, $\mu_A \approx 0.05$ Pa.s, dielectric constant, $\varepsilon_A \approx 3.1$ [222], and electrical conductivity, $\zeta_A \approx 10^{-11} - 10^{-10}$ Sm^{-1} [291]). Thus, silicone oil-water-oleic acid ($\sigma_{AB} \approx 0.01$ Nm^{-1}, $\sigma_{BC} \approx 0.035$ Nm^{-1} and $\sigma_{AC} \approx 0.04$ Nm^{-1}) and silicone oil-water-soybean oil ($\sigma_{AB} \approx 0.001$ Nm^{-1}, $\sigma_{BC} \approx 0.035$ Nm^{-1} and $\sigma_{AC} \approx 0.038$ Nm^{-1}) were the combinations of liquids used in the experiments for the droplet-carrier-target three-phase liquid configurations.

Electric field was applied with the help of copper electrodes connected to a direct current (DC) high voltage source (SES Instruments Pvt. Ltd, EHT-II). The electrode in contact with liquid B was grounded and the electrode touching liquid A was connected to the positive terminal of the high voltage source. It may be noted that on application of electric field, instabilities are also induced in liquids A and B, like internal circulations and interfacial perturbations. These secondary effects cannot be curbed totally during the experiments, however, to alleviate the effects, both liquids A and B were chosen with weak electrical conductivity and nearly matching electrical permittivity (permittivity ratio, $\varepsilon_A/\varepsilon_B \approx 0.85 - 1.1$). The experiments were recorded using a high-speed camera (Photron, Fastcam Mini UX-100) integrated with a zooming lens, at 1000 fps (frames per second), unless stated otherwise. Significant care was taken to place the droplet at the centre of the cuvette and away from the walls before application of electric field in order to minimize the wall effects. All the experiments were carried out at room temperature (22 ± 2°C). The cuvettes were washed with detergents and rinsed repeatedly with ethanol and de-ionised (DI) water after every experiment. Further care was taken to avoid any scratches on the cuvettes during washing. The cuvettes were changed after every three experiments. The viscosities of the fluids were measured using interfacial rheometer (Anton Paar, Physica MCR 301). The interfacial tensions were measured using an automatic surface tensiometer (KYOWA DY-300). During

the experiments, the high density of the water droplet (C) ensured that it was placed on the bottom electrode in a cuvette inside the carrier liquid (B) of intermediate density. Following this, the target liquid (A) of lowest density was poured before the three immiscible liquids were subjected to a DC field. The droplet acquired charge from the grounded electrode placed in contact with liquid B and underwent movement towards the interface between liquids A and B. The droplet and the carrier-target liquid-liquid interfaces exhibited various interfacial phenomena based on the physical properties of the three liquids and the magnitude of electric force, which are discussed in detail in the subsequent sections.

4.4 Theoretical Formulation

Although the experiments were conducted in the rectangular cuvettes, a two dimensional (2-D) axisymmetric domain was chosen for the numerical simulations to minimize the computational load. Figure 4.1(b) shows the axisymmetric domain used for the numerical simulations wherein the liquids A and B are placed inside a cylindrical domain and a droplet of liquid C is placed in the liquid B. The axis of symmetry coincides with the axis of the cylinder ($r = 0$). The bottom wall of the cylinder is considered to be grounded while the top wall is modelled as a positive terminal of a DC source. We assume that the application of the electric field helps the droplet in acquiring charge from the grounded electrode and enables it to migrate towards the oppositely charged anode owing to the net electrostatic attraction. Subsequently, the droplet C shows an electrophoretic motion towards the anode at the top before crossing the liquid-liquid interface between the carrier B and the target A on the way.

4.4.1 Governing Equations

The problem under consideration involves three immiscible liquids namely A, B and C subjected to an electric field. The liquids are assumed to be Newtonian and incompressible, which allow the flow field to be governed by the continuity and momentum equations as follows,

$$\boldsymbol{\nabla} \cdot \boldsymbol{v} = 0, \tag{4.1}$$

$$\rho\left(\frac{\partial \boldsymbol{v}}{\partial t}+\boldsymbol{v}\cdot\boldsymbol{\nabla}\boldsymbol{v}\right)=-\boldsymbol{\nabla}p+\boldsymbol{\nabla}\cdot\left[\mu\left(\boldsymbol{\nabla}\boldsymbol{v}+\boldsymbol{\nabla}\boldsymbol{v}^{\mathrm{T}}\right)\right]+\rho\boldsymbol{g}+\boldsymbol{F}_E+\boldsymbol{F}_S. \tag{4.2}$$

Here, ρ, $\boldsymbol{v}$, p, μ, and $\boldsymbol{g}$ denote the density, velocity, pressure, viscosity and acceleration due to gravity, respectively. The electrical body force acting on the fluids, denoted by $\boldsymbol{F}_E$, is given by,

$$\boldsymbol{F}_E=q\boldsymbol{E}-\frac{1}{2}|\boldsymbol{E}|^2\boldsymbol{\nabla}\varepsilon+\boldsymbol{\nabla}\left(\rho\frac{|\boldsymbol{E}|^2}{2}\frac{\partial\varepsilon}{\partial\rho}\right), \tag{4.3}$$

where q, $\boldsymbol{E}$ and ε denote the volumetric charge density, electric field intensity and permittivity of the fluids, respectively. The first term of eq.(4.3) represents the Coulombic force acting on the free charges residing in the liquids. The second term accounts for the dielectrophoretic force acting the bound charges. The last term accounts for the electrostrictive force, which is generally combined with the pressure term of the momentum equation [292] and is neglected in the present study. The electric field intensity is given by, $\boldsymbol{E}=-\boldsymbol{\nabla}\psi$, where ψ is the electric potential.

Further, the present study also employs a part of the Taylor-Melcher leaky dielectric (TMLD) Model [292] to elucidate the physics associated with the electric field in a more comprehensive manner. However, it is important to note here that the numerical model chosen for the simulations employ a diffuse interface method, which is unlike the requirement of a sharp interface in the TMLD model. For solving electrohydrodynamic problems with such diffuse interface methods, continuum surface force representations of the electric force have been derived based on the TMLD framework [293, 294]. In such methods, the volumetric charge density is approximated as, $q=\varepsilon_0\left(\zeta\boldsymbol{E}\right)\cdot\boldsymbol{\nabla}\left(\varepsilon/\zeta\right)$. Such methods are found to be fairly accurate for solving problems with diffused deformable interfaces of fluids because they incorporate the roles of the fluid conductivities in the charge estimation at the fluid-fluid interface. However, in the present study, this strategy cannot be employed for two main reasons. Firstly, the uncharged droplet has a conductivity of $\sim 10^{-1}$ Sm^{-1}, while the oils used as the carrier and target phases have conductivities of the order of $\sim 10^{-13}-10^{-11}$ Sm^{-1}. Thus, the conductivity contrasts across the interfaces are rather high $(10^{10}-10^{12})$, which eventually makes the problem very 'stiff' from the numerical perspective, often leading to divergence [295]. In order to tackle this problem, most of the existing numerical approaches employ a decent conductivity contrast of 10^3 across the interface to simulate water-in-oil systems [191], which

can't be used for a precise quantitative emulation of the systems reported here. Thus, in the present study, the free charge density, q, is not defined in terms of the fluid conductivities. Secondly, the droplet acquires charge from the electrodes and the Coulomb force acting on the net droplet charge drives the motion. In such a situation, it is rather difficult to enforce an accurate boundary condition to estimate the transfer of charge to the droplet and measure its conductivity after the contact. In view of this background, the simulations are carried out by defining a net charge on the droplet, which it is expected to acquire after contacting the electrode.

Since, a dilute salt solution is used for the droplet phase (C), it is expected that an electrical double layer (EDL) may be formed around the droplet. The typical values of the Debye length in aqueous systems range between $10^{-10}-10^{-7}$ m [272,296]. Resolution of such thin layers in a computational domain of characteristic length $\sim O(10^{-3})$ m is numerically difficult. Thus, following the method of [272], it is considered that the entire charge on the droplet is homogeneously distributed throughout its volume. The potential distribution in the domain is then governed by the Poisson's equation as,

$$\nabla^2\psi = -\frac{q}{\varepsilon}. \tag{4.4}$$

The immiscible droplet-carrier, droplet-target, and carrier-target interfaces of the ternary system are tracked by a diffuse-interface phase field formulation [277, 284–286, 288]. Each of the phases (A, B and C) is measured by a phase field or order parameter (ϕ_i), which gives the concentration of one of the components in the mixture. The order parameters are assumed to satisfy the relation,

$$\sum_{i=\mathrm{A,B,C}} \phi_i = 1. \tag{4.5}$$

The free energy density of the system is represented as,

$$f(\phi) = \Psi(\phi) + \frac{1}{2}\lambda\left|\boldsymbol{\nabla}\phi\right|^2. \tag{4.6}$$

For ternary systems, Boyer & Lapuerta [287] proposed an expression for the free energy density by extrapolation of the diphasic Cahn-Hilliard free energy [297] to the tri-phasic systems. The bulk free energy density represented by $\Psi(\phi)$ is given

by a triple well-structured function [283, 287] as,

$$\begin{aligned}\Psi(\phi) &= \frac{12}{\delta}\left[\sigma_{\mathrm{AB}}\phi_{\mathrm{A}}^2\phi_{\mathrm{B}}^2+\sigma_{\mathrm{AC}}\phi_{\mathrm{A}}^2\phi_{\mathrm{C}}^2+\sigma_{\mathrm{BC}}\phi_{\mathrm{B}}^2\phi_{\mathrm{C}}^2+\phi_{\mathrm{A}}\phi_{\mathrm{B}}\phi_{\mathrm{C}}\left(\Sigma_{\mathrm{A}}\phi_{\mathrm{A}}+\Sigma_{\mathrm{B}}\phi_{\mathrm{B}}+\Sigma_{\mathrm{C}}\phi_{\mathrm{C}}\right)\right] \\ &+ \frac{12}{\delta}\left(\Lambda\phi_{\mathrm{A}}^2\phi_{\mathrm{B}}^2\phi_{\mathrm{C}}^2\right). \end{aligned} \tag{4.7}$$

Here, σ_{AB}, σ_{BC} and σ_{AC}, denote the interfacial tensions between the phases. The parameter Σ_i is given by,

$$\Sigma_i = \sigma_{ij}+\sigma_{ik}-\sigma_{jk} \qquad \forall i \in (\mathrm{A},\mathrm{B},\mathrm{C}). \tag{4.8}$$

Physically the coefficient Σ_i gives the extent of spreading of phase 'i' at the interface between phases 'j' and 'k'. If Σ_i is less than zero, spreading is total, else it is partial. The additional bulk free energy, Λ, is taken as zero if $\Sigma_i > 0$, for all the phases, otherwise its value is chosen to be greater than zero. The parameter, δ, controls the thickness of the diffuse interface. The second term of eq.(4.6) represents the gradient or capillary energy $\Omega(\phi)$ and for ternary systems this energy is formulated as,

$$\Omega(\phi) = \frac{3}{8}\delta\left[\Sigma_{\mathrm{A}}\left|\boldsymbol{\nabla}\phi_{\mathrm{A}}\right|^2+\Sigma_{\mathrm{B}}\left|\boldsymbol{\nabla}\phi_{\mathrm{B}}\right|^2+\Sigma_{\mathrm{C}}\left|\boldsymbol{\nabla}\phi_{\mathrm{C}}\right|^2\right]. \tag{4.9}$$

The sign and magnitude of the bulk free energy, $\Psi(\phi)$, indicate the separation of the phases into the pure components while the sign and magnitude of capillary or gradient free energy indicate the mixing of the phases. The free energy density represented by eq. (4.6), can thus be re-written for a ternary system as,

$$\begin{aligned}\Psi(\phi) &= \frac{12}{\delta}\left[\sigma_{\mathrm{AB}}\phi_{\mathrm{A}}^2\phi_{\mathrm{B}}^2+\sigma_{\mathrm{AC}}\phi_{\mathrm{A}}^2\phi_{\mathrm{C}}^2+\sigma_{\mathrm{BC}}\phi_{\mathrm{B}}^2\phi_{\mathrm{C}}^2+\phi_{\mathrm{A}}\phi_{\mathrm{B}}\phi_{\mathrm{C}}\left(\Sigma_{\mathrm{A}}\phi_{\mathrm{A}}+\Sigma_{\mathrm{B}}\phi_{\mathrm{B}}+\Sigma_{\mathrm{C}}\phi_{\mathrm{C}}\right)\right] \\ &+ \frac{12}{\delta}\left(\Lambda\phi_{\mathrm{A}}^2\phi_{\mathrm{B}}^2\phi_{\mathrm{C}}^2\right)+\frac{3}{8}\delta\left[\Sigma_{\mathrm{A}}\left|\boldsymbol{\nabla}\phi_{\mathrm{A}}\right|^2+\Sigma_{\mathrm{B}}\left|\boldsymbol{\nabla}\phi_{\mathrm{B}}\right|^2+\Sigma_{\mathrm{C}}\left|\boldsymbol{\nabla}\phi_{\mathrm{C}}\right|^2\right]. \end{aligned} \tag{4.10}$$

The chemical potential of the system is represented as,

$$\xi = \frac{\partial\left[\int_V f(\phi)\,\mathrm{d}V\right]}{\partial\phi}. \tag{4.11}$$

According to the hypothesis of van der Waals [298], $\int_V f(\phi)\,\mathrm{d}V$ has to be minimum for the diffuse interface to be at equilibrium which means that,

$$\xi_i = \frac{\partial\left[\int_V f(\phi_i)\,\mathrm{d}V\right]}{\partial\phi_i} = \beta\,\Psi'(\phi_i) - \alpha\nabla^2\phi_i = \text{constant}. \tag{4.12}$$

For the ternary system the relation given by eq.(4.12) becomes,

$$\xi_i = \frac{4\Sigma_T}{\delta}\sum_{j\neq i}\left\{\frac{1}{\Sigma_j}\left(\partial_i\,\Psi(\phi_i) - \partial_j\,\Psi(\phi_i)\right)\right\} - \frac{3}{4}\delta\Sigma_i\nabla^2\phi_i, \tag{4.13}$$

where, $\frac{3}{\Sigma_T} = \frac{1}{\Sigma_\mathrm{A}} + \frac{1}{\Sigma_\mathrm{B}} + \frac{1}{\Sigma_\mathrm{C}}$. If the mass flux is assumed to be proportional to the gradient of chemical potential, the Cahn-Hilliard equation [299] for the evolution of ϕ_i, can be written as,

$$\frac{\partial\phi_i}{\partial t} + \boldsymbol{\nabla}\cdot(\boldsymbol{v}\phi_i) = \boldsymbol{\nabla}\cdot\left(\frac{\Pi_0}{\Sigma_i}\boldsymbol{\nabla}\phi_i\right). \tag{4.14}$$

Here, Π_0, is the mobility tuning parameter. The surface tension force, $\boldsymbol{F}_S$, in eq. (4.2) can be represented as,

$$\boldsymbol{F}_S = \sum_{i=\mathrm{A,B,C}}\xi_i\boldsymbol{\nabla}\phi_i. \tag{4.15}$$

4.4.2 Boundary Conditions

Axisymmetric boundary conditions were applied for all the variables at the axis of symmetry, as shown in figure 4.1(*b*). The wetted wall and no-slip boundary conditions ($\boldsymbol{v} = 0$), were enforced on boundaries 2, 3 and 4. A pressure point constraint was employed, to set a point at zero reference gauge pressure. For the electrostatic equations, Dirichlet boundary conditions of, $\psi = \psi_0$ and $\psi = 0$, were applied at boundaries 2 and 4, respectively, where ψ_0 is the applied potential. Zero surface charge ($\boldsymbol{n}\cdot\varepsilon\boldsymbol{E} = 0$), was maintained at boundary 3. The physical properties such as density (ρ), viscosity (μ), permittivity (ε) and volumetric charge density (q), in the computational domain were defined as, $x = x_\mathrm{A}\phi_\mathrm{A} + x_\mathrm{B}\phi_\mathrm{B} + x_\mathrm{C}\phi_\mathrm{C}$. The charge acquired by the droplet from the lower electrode was calculated experimentally (refer to Appendix C.1) and plugged into the numerical simulations.

4.4.3 Solution Methodology

The governing equations mentioned in section 4.4.1 along with the boundary conditions mentioned in section 4.4.2, were solved using the Galerkin finite element method, employing the commercial software COMSOL Multiphysics^{TM}. The domain was discretized with approximately 8×10^4 triangular elements with refinement along the walls and the interfaces. Second order elements, were used for the velocity, phase field parameter and electric potential and first order elements were used for the pressure calculations. Streamline and crosswind diffusions, were used for the consistent stabilization of the momentum equation. The interface thickness tuning parameter, was set to be equal to the maximum mesh size in the domain. The MUltifrontal Massively Parallel Sparse direct solver (MUMPS), was used for solving the equations. For the integration of the equations, the time dependant solver was set to a second order backward difference formulae with backward Euler for consistent initialization. Free time stepping was used and the relative tolerance of the integration steps was set to 10^{-4}. The validation of the numerical method and the grid convergence study are given in appendices C.2 and C.3, respectively.

4.5 Results and Discussion

4.5.1 Non-Dimensional Parameters

The 'drop-carrier-target' three-phase configuration is a very complex system to analyse because of the presence of multitude of physical properties associated with the liquids. Thus, for the sake of brevity in the analysis, the discussion of the results are focussed on the most relevant parameters governing the dynamics. For this purpose, the droplet radius has been chosen as the characteristic length while the ratios of the densities, viscosities, interfacial tensions, and electric permittivities are expressed in the following dimensionless forms – density ratios: $\rho^*_{AB} = \rho_A/\rho_B$, $\rho^*_{BC} = \rho_B/\rho_C$, $\rho^*_{AC} = \rho_A/\rho_C$, and $\rho^* = (\rho_C - \rho_B)/(\rho_B - \rho_A)$, viscosity ratios: $\mu^*_{AB} = \mu_A/\mu_B$, $\mu^*_{BC} = \mu_B/\mu_C$ and $\mu^*_{AC} = \mu_A/\mu_C$, ratios of electric permittivities: $\varepsilon^*_{AB} = \varepsilon_A/\varepsilon_B$, $\varepsilon^*_{BC} = \varepsilon_B/\varepsilon_C$ and $\varepsilon^*_{AC} = \varepsilon_A/\varepsilon_C$, ratios of interfacial tensions: $\sigma^*_1 = \sigma_{AC}/\sigma_{BC}$, $\sigma^*_2 = \sigma_{AB}/\sigma_{BC}$ and $\sigma^*_3 = \sigma_{AB}/\sigma_{AC}$, where the subscripts denote the respective phases. The acquired charge, Q_0, is normalized by the theoretical value of charge acquired by a conductor in contact with an electrode, Q_{th} $\left(= (2/3)\pi^3 {r_C}^2 \varepsilon_B E_0\right)$ [108], $Q^* = Q_0/Q_{th}$, where, E_0, is the average electric field intensity. The velocity is scaled

by the term $r_C\varepsilon_B E_0^2/\mu_B$, while the dimensionless time is defined as, $\mu_B/\varepsilon_B E_0^2$. The electric force acting on the droplet can be scaled as, $F_E^* = F_E/r_C^2\varepsilon_B E_0^2$. The electric field Weber numbers, We_E and We_E^1, are defined as, $We_E = r_C\varepsilon_B E_0^2/\sigma_{AB}$ and $We_E^1 = r_C\varepsilon_B E_0^2/\sigma_{BC}$, respectively, and give the ratios of electric forces acting on the droplet to the capillary forces. The Bond numbers, Bo and Bo_1, are defined as, $Bo = gr_C^2(\rho_B - \rho_A)/\sigma_{AB}$ and $Bo_1 = gr_C^2(\rho_B - \rho_A)/\sigma_{BC}$, respectively, and give the ratios of the gravitational to the capillary forces.

4.5.2 Film Drainage Mode

4.5.2.1 The Phenomena

The migration of a water droplet−phase C, from its initial position inside silicone oil−phase B, towards oleic acid−phase A is shown in figures 4.2$(a-d)$, for different electric field intensities. The image set in row (a) shows that, for $We_E \approx 0.25$, the droplet undergoes a marginal deformation before approaching the A-B interface, and is halted at the interface due to the downward interfacial tension force. In the process, the droplet momentarily maintains a metastable engulfed position at the A-B interface. Subsequently, while the droplet attempts to break the interface and move towards the upper electrode, the thin silicone oil film ruptures. Following this, the water droplet attains morphology following Neumann's triangle, at the A-B interface [300]. The behavior observed here is very similar to the previously studied cases of buoyancy driven motion of small bubbles trapped at the interface [155, 160, 162, 163, 166].

The image (viii) in the panel (a) also shows that after a brief stay at the A-B interface the droplet rebounds into the phase B before starting a journey towards the lower electrode. As the density of phase A is moderately lower than phase B ($\rho_A^* \approx 0.86$), the apparent weight of the droplet increases after film rupture, which may cause a dynamic force imbalance forcing the droplet to fall down. The conductivity of the upper phase is also marginally higher than phase B. Thus, after film rupture, as a portion of the droplet is inside phase A, it is possible that some of the charges on the droplet relax (relaxation time, $\tau = \varepsilon/\zeta$) [108] quickly into A, leading to a sudden decrease in the electrical force acting on it. This effect combined with the increase in the apparent weight of the droplet, may be responsible for the downward flight of the droplet. Over a period of time, the droplet shows a time-periodic motion between the A-B interface and lower electrode under these circumstances.

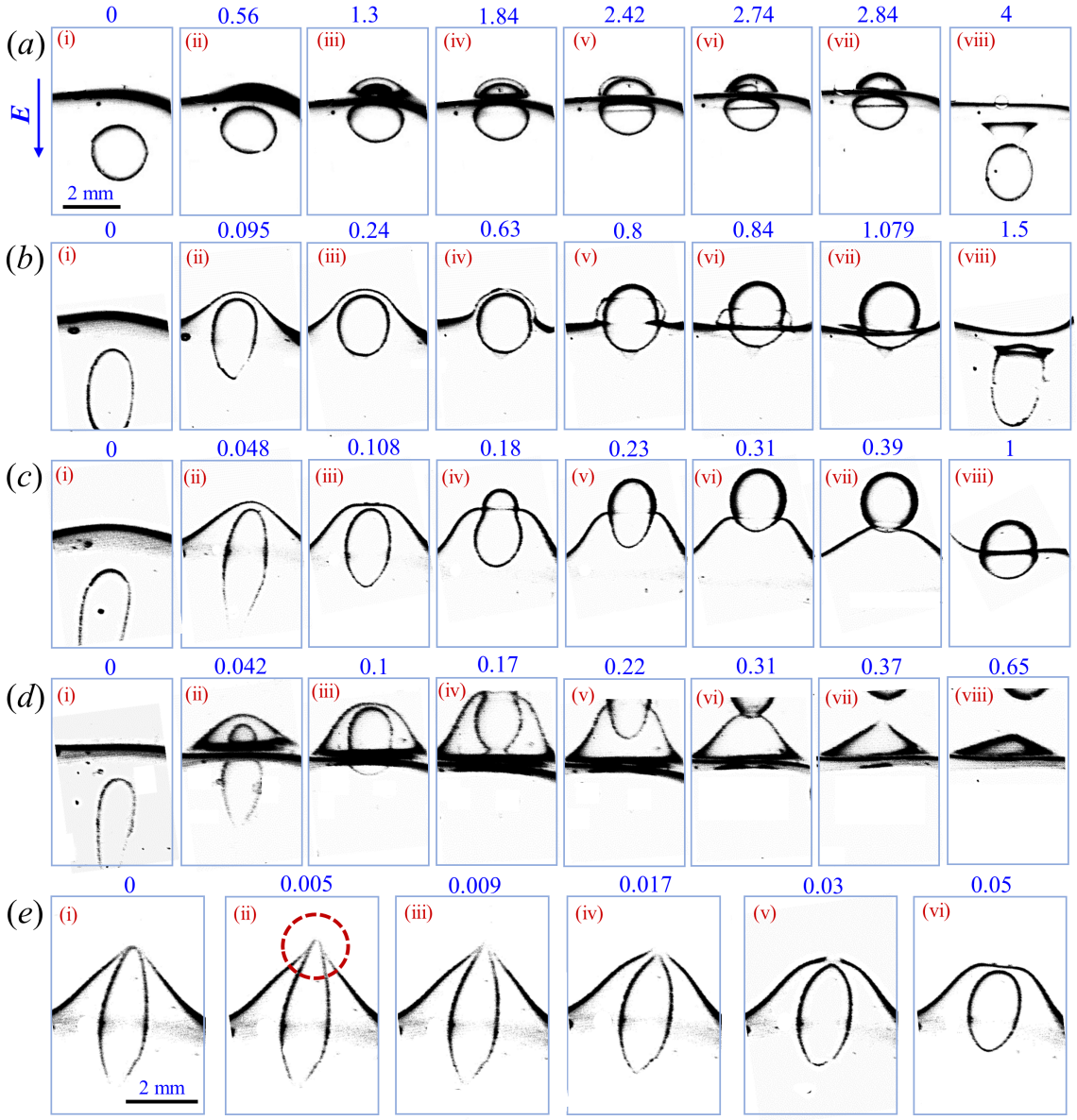

Figure 4.2: Experimental time sequence snapshots demonstrating the trajectory of an aqueous droplet (phase C) immersed in silicone oil (phase B) and advancing towards oleic acid (phase A) under application of (*a*) 3.2 kVcm^{-1}, $We_{\mathrm{E}} \approx 0.25$, $We^{1}_{\mathrm{E}} \approx 0.07$, (*b*) 3.5 kVcm^{-1}, $We_{\mathrm{E}} \approx 0.3$, $We^{1}_{\mathrm{E}} \approx 0.084$, (*c*) 3.75 kVcm^{-1}, $We_{\mathrm{E}} \approx 0.35$, $We^{1}_{\mathrm{E}} \approx 0.1$, and (*d*) 4 kVcm^{-1}, $We_{\mathrm{E}} \approx 0.4$, $We^{1}_{\mathrm{E}} \approx 0.11$. (*e*) Drop dynamics between images (ii) and (iii) of (*c*). The other dimensionless numbers associated with (*a*)−(*e*) are, $Bo \approx 0.1$, $Bo_1 \approx 0.03$, $\rho^{*}_{\mathrm{AB}} \approx 0.895$, $\rho^{*}_{\mathrm{BC}} \approx 0.96$, $\rho^{*}_{\mathrm{AC}} \approx 0.86$, $\rho^{*} \approx 0.4$, $\mu^{*}_{\mathrm{AB}} \approx 0.07$, $\mu^{*}_{\mathrm{BC}} \approx 300$, $\mu^{*}_{\mathrm{AC}} \approx 20$, $\varepsilon^{*}_{\mathrm{AB}} \approx 0.85$, $\varepsilon^{*}_{\mathrm{BC}} \approx 0.034$, $\varepsilon^{*}_{\mathrm{AC}} \approx 0.03$, $\sigma^{*}_{1} \approx 1.14$, $\sigma^{*}_{2} \approx 0.28$, and $\sigma^{*}_{3} \approx 0.25$. The time shown above each snapshot has unit of seconds.

The image set in the row (b) shows that, at $We_{\mathrm{E}} \approx 0.3$, the droplet deforms into prolate shape due to the higher Maxwell stress acting at the B-C interface under a stronger electric field [292]. However, the prolate droplet relaxes into spherical shape due the combined actions of interfacial and viscous forces after colliding with the A-B interface. Following this, a stronger upward pull by the electrical body force helps the droplet to pierce the A-B interface and partially pass to the phase A, after causing the rupture of silicone oil film in between (images (v)−(vii)). The image panel in (c) shows that for $We_{\mathrm{E}} \approx 0.35$, the B-C interface of the droplet undergoes a larger distortion in shape as compared to image set (b) due to the increase in the strength of the Maxwell stresses at a higher field intensity. The droplet proceeds at a much higher speed towards the interface and the apex of the prolate droplet impinges into the interface before causing a localized rupture of the thin film (image (iii)). The droplet than squeezes its way out of the hole formed while the film drainage takes place simultaneously over the upper part of the droplet. Interestingly, for the motions shown in the image panels (b) and (c), only a part of the drop can pierce through the A-B interface before they again migrate towards the lower electrode after spending a brief amount of time at the A-B interface. A close observation of the drop dynamics in the time gap corresponding to images (ii) and (iii) of panel (c), shown in figure (e), reveals that, as the prolate droplet with a Taylor cone impinges the A-B interface, it undergoes Rayleigh instability leading to ejection of droplets from it, as hinted by image (ii) of (e) (marked by red circle). The ejected droplet could be captured due to imaging limitations. After ejection, the prolate drop loses a part of its net charge and relaxes into an almost spherical drop due to capillary and viscous forces. The image set in the row (d) shows that, at a still higher field at $We_{\mathrm{E}} \approx 0.4$, the electrical force enables the droplet to completely pierce through the A-B interface for its transfer into phase A. Importantly, the transfer of the droplet to the phase A ensures that the same does not revert back to the phase B, which is unlike the cases shown with the image sets (a)−(c).

To gain in-depth information of the inter-phase drop immigration, CFD simulations have been carried out considering an axisymmetric domain of 0.5 cm radius and 2 cm height, as shown in figure 4.1(b). For computational simplification, the contact angles between the phases were maintained at 90°. The droplet was assigned the theoretical value of charge, Q_{th}, unless stated otherwise. Figure 4.3 shows the simulated migration of a water droplet initially placed inside silicone oil and moving towards oleic acid under electric field. This computational system is qualitatively

similar to the experiments discussed in figure 4.2.

The image panel in figure 4.3(a) demonstrates the simulated time sequence snap-

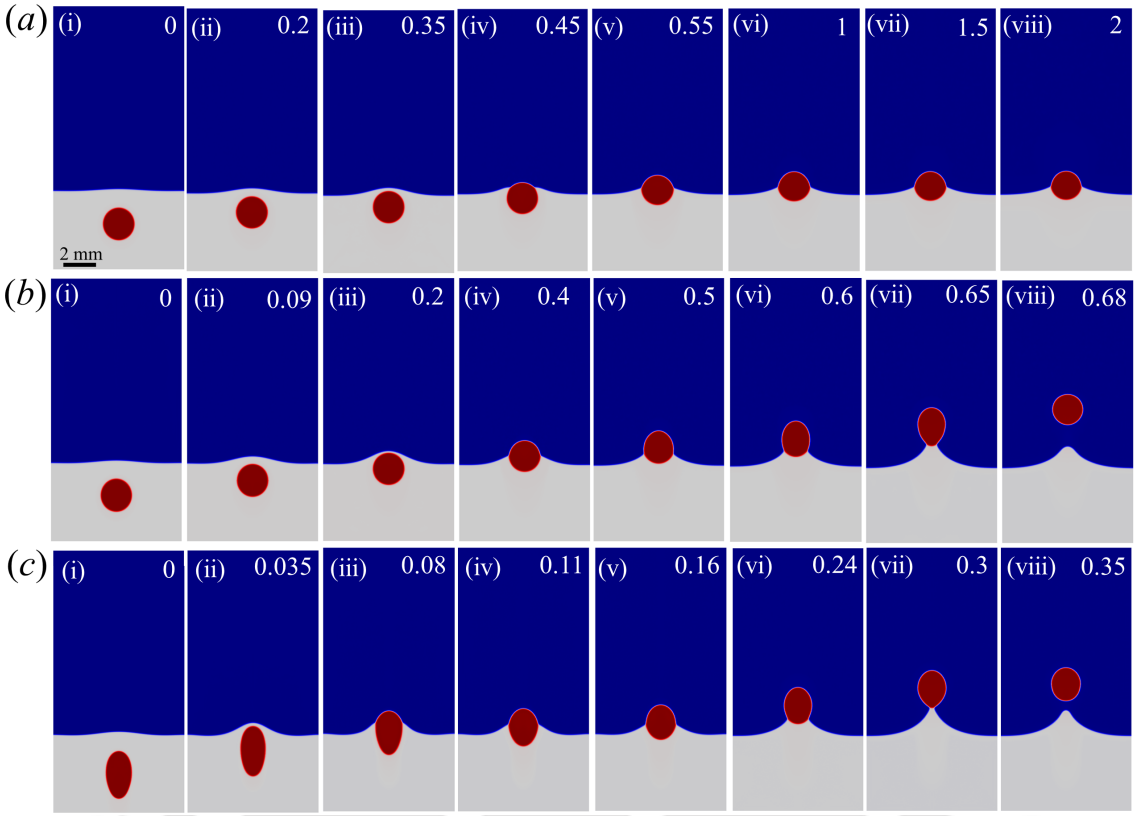

Figure 4.3: Simulated time sequence snapshots showing the motion of an aqueous droplet (phase C) immersed in silicone oil (phase B) and advancing towards oleic acid (phase A) under (a) $We_{\mathrm{E}} = 0.25$, $We^{1}_{\mathrm{E}} = 0.07$, ($b$) $We_{\mathrm{E}} = 0.3$, $We^{1}_{\mathrm{E}} = 0.084$ and (c) $We_{\mathrm{E}} = 0.4$, $We^{1}_{\mathrm{E}} = 0.11$. The other dimensionless numbers associated with ($a - c$) are, $Bo = 0.1$, $Bo_1 \approx 0.03$, $\rho^{*}_{\mathrm{AB}} = 0.895$, $\rho^{*}_{\mathrm{BC}} = 0.96$, $\rho^{*}_{\mathrm{AC}} = 0.86$, $\rho^{*} = 0.4$, $\mu^{*}_{\mathrm{AB}} = 0.07$, $\mu^{*}_{\mathrm{BC}} = 300$, $\mu^{*}_{\mathrm{AC}} = 20$, $\varepsilon^{*}_{\mathrm{AB}} = 1.4$, $\varepsilon^{*}_{\mathrm{BC}} = 0.034$, $\varepsilon^{*}_{\mathrm{AC}} = 0.05$, $\sigma^{*}_{1} = 1.14$, $\sigma^{*}_{2} = 0.28$, and $\sigma^{*}_{3} = 0.25$. The time shown above each snapshot has unit of seconds.

shots of the migration of the droplet at $We_{\mathrm{E}} = 0.25$ and $\sigma^{*}_{2} = 0.28$. The droplet travels towards the interface under the effect of electric field before the film between the droplet and interface starts thinning out. Thereafter, the droplet squeezes the interstitial fluid and the intermediate film ruptures to form a hole. The hole radius then quickly grows and the droplet attains a static equilibrium by assuming a configuration following Neumann's construction involving the surrounding three-phases at the interface. This behaviour is qualitatively similar to the image set (a) of figure 4.2. However, unlike the experiments, the droplet does not fall back to the bottom

electrode in the simulations. This is because the fluids A and B are considered to be purely dielectric in the simulations, whereas they have very weak conductivity in the experiments. Thus, when the film above the droplet breaks, it is expected that the electrical force acting on the droplet decreases in the experiments. It may also be noted that the simulations are carried out with the droplet containing the theoretical amount of charge, which remains constant throughout the migration. Thus, the simulated droplet experiences more force at a given We_{E} than the experimental droplet. These are the primary reasons behind the slightly faster dynamics of the simulated droplet.

The image set in the row (b) of figure 4.3 shows that at a higher field at $We_{\mathrm{E}} = 0.3$, the droplet approaches the interface almost undeformed, unlike the small deformation seen in experimental migration of figure 4.2(b). During the experiments, artefacts like slight non-alignment of the electrodes create additional local non-uniformity in the electric field distribution which intensifies at higher fields. Thus, in case of the experimental drop, a slight deformation is observed. After the film drainage, the droplet lingers on the interface for some time and then enters into the target liquid. The image set (c) of figure 4.3 shows the droplet dynamics at $We_{\mathrm{E}} = 0.4$. In this case, similar to the experimental observation of figure 4.2(d), the droplet deforms into a prolate shape. The prolate droplet approaches the A-B interface and due to thinning of the film beyond a critical thickness, it ruptures (image (iii)). Unlike, the experiments, ejection of droplets from the Taylor cone are not observed in the simulations. The the droplet slows down at the interface (images (iv) to (vi)) before squeezing its way out of the ruptured carrier film (images (vii) and (viii)), when the driving electrical force overpowers the restricting interfacial tension and viscous forces. This behaviour is qualitatively very similar to the image sets (c) and (d) of figure 4.2. As the droplet moves ahead with a higher velocity, the meniscus recedes to form a small neck (image (viii)), as observed in the experiments.

Image sets (a) and (b) in the figure 4.4 show the normalized azimuthal vorticity $\left(\omega_\theta = \dfrac{\partial v_r}{\partial z} - \dfrac{\partial v_z}{\partial r}\right)$ fields and the streamline fields, respectively, associated with the migration of the droplet at $We_{\mathrm{E}} = 0.4$, corresponding to figure 4.3(c). Interestingly, a pair of circulation loops are generated along the horizontal axis, as the droplet moves towards the interface against the viscous drag of the carrier fluid. The vorticity is positive in these regions with the maximum vorticity occurring in the periphery of the droplet, as shown in the frame (ii). Regions of negative vorticity

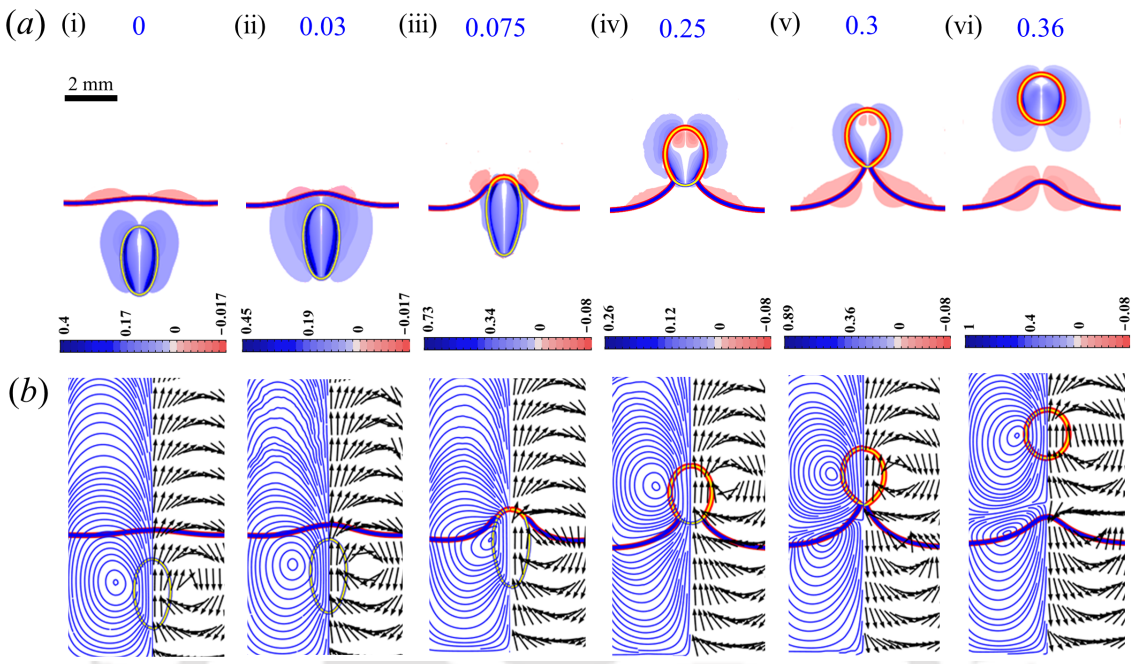

Figure 4.4: Simulated time sequence snapshots demonstrating the (a) normalized azimuthal vorticity fields $\left(\omega_\theta = \dfrac{\partial v_r}{\partial z} - \dfrac{\partial v_z}{\partial r}\right)$ and (b) streamline fields, during the trajectory of an aqueous droplet (phase C) immersed in silicone oil (phase B) and advancing towards oleic acid (phase A) at $We_{\mathrm{E}} = 0.4$ and $We_{\mathrm{E}}^{1} = 0.11$. The other dimensionless numbers associated with (a) and (b) are, $Bo = 0.1$, $Bo_1 \approx 0.03$, $\rho^*_{\mathrm{AB}} = 0.895$, $\rho^*_{\mathrm{BC}} = 0.96$, $\rho^*_{\mathrm{AC}} = 0.86$, $\rho^* = 0.4$, $\mu^*_{\mathrm{AB}} = 0.07$, $\mu^*_{\mathrm{BC}} = 300$, $\mu^*_{\mathrm{AC}} = 20$, $\varepsilon^*_{\mathrm{AB}} = 1.4$, $\varepsilon^*_{\mathrm{BC}} = 0.034$, $\varepsilon^*_{\mathrm{AC}} = 0.05$, $\sigma^*_1 = 1.14$, $\sigma^*_2 = 0.28$, and $\sigma^*_3 = 0.25$. The time shown above each snapshot has unit of seconds. The vorticity values are normalized by the maximum vorticity. The blue (pink) regions denote positive (negative) vorticity, respectively.

close to the interface, are generated due to relaxation of the interface. As the droplet ruptures the carrier film and rises above (frames (iv) and (v)), a small column of carrier phase B is formed due to the progressive entrainment of the contact line. In such a scenario, the regions of high positive vorticity are concentrated around the rising droplet, while low negative vorticity occur in the shear layer along the A-B interface. As the column gets sufficiently stretched (images (v) and (vi)) the lower part of the column starts receding back (as visible in the direction of the arrows in the streamline fields), while the part immediately below the droplet still moves upwards. The downward moving column entrains the carrier liquid A, causing circulation along the interface. Negative vorticity fields are thus, induced along the

receding column due to difference in velocities between the fluid inside and outside the column.

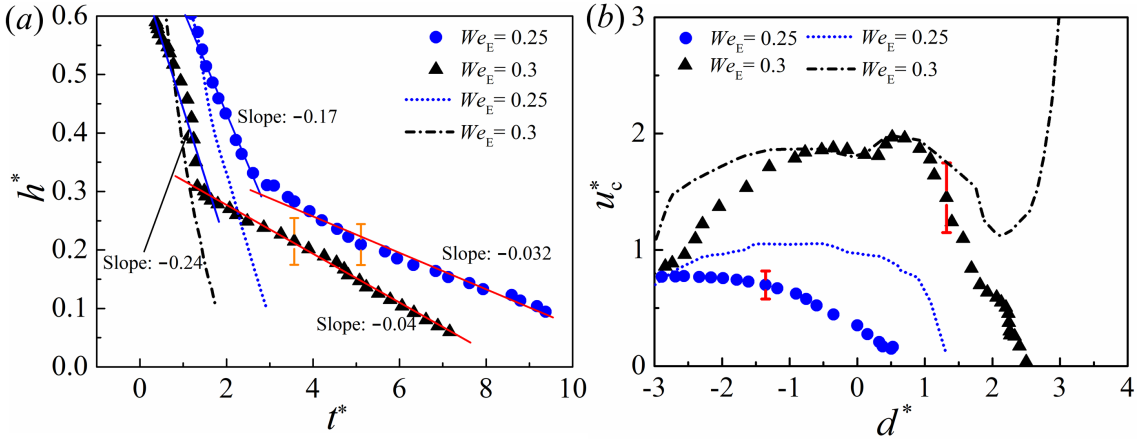

Figure 4.5: Comparisons of the normalized (a) film thickness (h^*) with time (h^*) and (b) rising velocity of the droplet (u_C^*) as a function of the distance of the uppermost point of the droplet from the undisturbed interface (d^*). The solid points indicate the experimental data and the lines correspond to the simulated values. The other dimensionless numbers associated with (a) and (b) are same as figures 4.2 and 4.3. It may be noted that the velocity and time are normalized considering the average field intensity E_0, corresponding to $We_E = 0.3$.

4.5.2.2 Quantitative Analysis

Figure 4.5(a) shows the comparisons of the experimental and computational variations of the normalized film thickness (h^*) of the carrier liquid trapped between the droplet and the target liquid as a function of the normalized time (t^*). Figure 4.5(a) shows that the experimental film thickness decreases almost linearly but in two stages. At $We_E \approx 0.25$, the film thins quickly with a slope of -0.17, at the initial stage of thinning of the carrier liquid. The rate of film thinning diminishes with a slope of -0.032 as the film thickness becomes comparable to 0.3 times the droplet radius. On the other hand, at a slightly higher electric field at $We_E \approx 0.3$, while the thickness decreases faster compared to $We_E \approx 0.25$, at the initial stage of drainage, the drainage becomes sluggish later with a slope of -0.04. The figure confirms that electric field has almost no influence on the quasi-steady drainage of the film beyond a critical film thickness of $h^* \approx 0.3$. As discussed elaborately in section 4.5.1, as the two boundaries of the film come close to each other, the shearing action increases. A constant shear stress profile develops in the draining film, leading to

decrease in the velocity of the drainage. Thus, the rate of film thinning decreases in the second stage. The simulated trends, however, suggest a one-stage thinning of the carrier film. The simulated results reasonably agree with the experimental ones in the initial stage of drainage, while overpredict the sluggish second stage when the carrier film becomes ultrathin. It is hypothesized that various types of interactions that may be present between the two interfaces during their close proximity in the experiments, are totally unaccounted for in the simulations, which may be the major reason behind this discrepancy [169]. Importantly, both the experimental and simulated trends for this carrier-droplet-target ternary liquid system vary from the previously observed exponential decay patterns for bubbles [163, 289] and power law patterns for solid particles [141, 151, 173].

Figure 4.5(b) shows the comparisons of the experimental and computational variations of the rising velocity of the droplet (u_{C}^{*}) as functions of the distance of the uppermost point of the droplet from the undisturbed interface (d^{*}). The experimental plot for $We_{\mathrm{E}} = 0.3$ shows that the electric force empowers the droplet resting on the lower electrode to move from the carrier liquid towards the target liquid. While translating, after reaching a peak velocity in the carrier liquid B, the droplet experiences a dip in the velocity when its upper part approaches the interface. As the interfacial film gets thinner due to drainage, there occurs a slight increase in the velocity of the droplet, which increases further as the film ruptures and begin to retract. However, as the droplet crosses the interface, the net weight of the droplet increases because of the lesser density of the target liquid. Also, an additional weight of the column of the carrier liquid B due the connection through contact line with the droplet, provides a downward pull. Subsequently, the droplet comes to a halt as the downward forces overpower the electrical pull towards the target liquid. The computational velocity profiles of the droplet shown in figure 4.5(b) mimic the experimental observations reasonable well. The overall simulated velocities are found to be slightly higher compared to the experimental ones due to reasons mentioned above in the description of figure 4.3.

4.5.2.3 Carrier Film Rupture

As an aqueous droplet suspended in silicone oil moves under electric field towards silicone oil-oleic acid interface (figure 4.2), the upper part of the droplet is first enveloped by a thin layer of silicone oil. The time scale of drainage of the thin

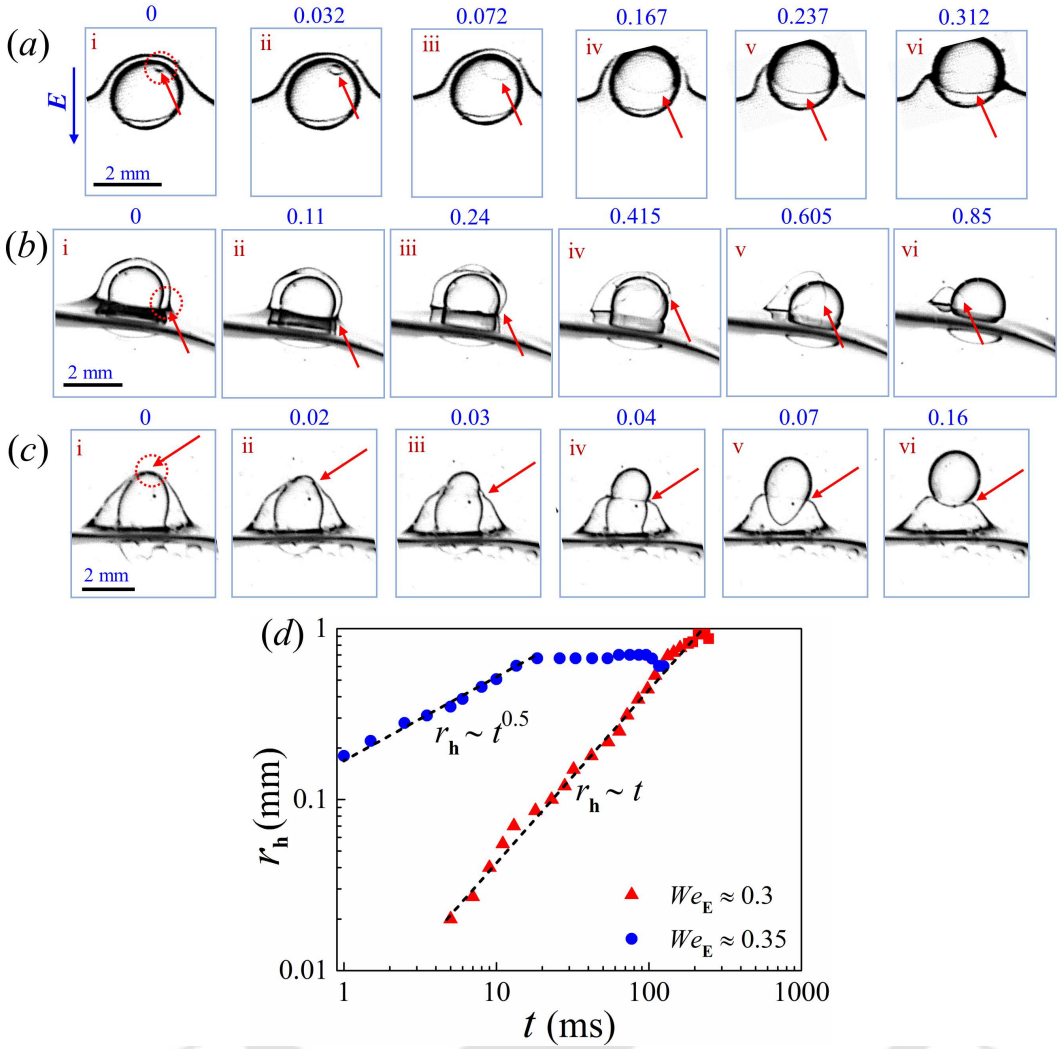

Figure 4.6: Experimental time sequence snapshots demonstrating the drainage and rupture of the surrounding thin film during the migration of a water droplet from silicone oil to oleic acid. (a) The rupture starts slightly off-centre with the hole expanding over the droplet almost symmetrically at, $E_0 = 3.5$ kVcm^{-1}, $We_E \approx 0.3$ and $We_E^1 \approx 0.084$. (b) The rupture takes place at one periphery of the film with the film falling sideways of the droplet at, $E_0 = 3.5$ kVcm^{-1}, $We_E \approx 0.3$ and $We_E^1 \approx 0.084$. (c) The advancing droplet punches a hole at the interface and squeezes out through the expanding hole at, $E_0 = 3.75$ kVcm^{-1}, $We_E \approx 0.35$ and $We_E^1 \approx 0.1$. (d) Variation of the radius of the hole formed after rupture (r_h) with time t. The other dimensionless numbers associated with (a)$-$(d) are, $Bo \approx 0.1$, $Bo_1 \approx 0.03$, $\rho^*_{AB} \approx 0.895$, $\rho^*_{BC} \approx 0.96$, $\rho^*_{AC} \approx 0.86$, $\rho^* \approx 0.4$, $\mu^*_{AB} \approx 0.07$, $\mu^*_{BC} \approx 300$, $\mu^*_{AC} \approx 20$, $\varepsilon^*_{AB} \approx 0.85$, $\varepsilon^*_{BC} \approx 0.034$, $\varepsilon^*_{AC} \approx 0.03$, $\sigma^*_1 \approx 1.14$, $\sigma^*_2 \approx 0.28$, and $\sigma^*_3 \approx 0.25$. The time shown above each snapshot has unit of seconds.

film decreases with increase in the strength of the applied field. As the film drains, its thickness becomes very small at certain points, which ultimately rupture under the influence of van der Waals forces. Figure 4.6 summarizes various modes of film rupture under different experimental conditions. Image set (a) shows an off-centre rupture (marked by dotted circle) of the thin carrier film at $We_{\mathrm{E}} \approx 0.3$, near the upper pole of the droplet. The rupture takes place under a quasi-static condition with the hole expanding symmetrically around the droplet. The radius of the hole grows with time following the rule, $r_{\mathrm{h}} \sim t$ as shown in figure 4.6(d). Image set (b) shows another case at $We_{\mathrm{E}} \approx 0.3$, wherein the droplet on reaching the interface slides to one of the sides to thin out the carrier film and cause rupture, as highlighted by the circle. The hole grows visually asymmetrically and the film falls off in manner similar to turning of a page. At a slightly higher field at $We_{\mathrm{E}} \approx 0.35$, another distinct rupture process is observed, as shown by the image set (c). In this case, the upper pole of the elongated droplet pierces through the carrier film and the rate of increase in the hole-radius follows the rule, $r_{\mathrm{h}} \sim t^{0.5}$, as shown in figure 4.6(d).

It is well known that the dynamics of hole-growth involves the inertial, viscous, and capillary forces competing with each other. Prior-art suggests that when the Ohnesorge number, $Oh = \mu/\sqrt{\rho r \sigma}$- a ratio of viscous to capillary driven inertial forces, is less than 1, the coalescence of drops is inertia dominated. In such a scenario, the breaking of the intermediate film and the subsequent hole-growth kinetics follow the rule, $r_{\mathrm{h}} \sim t^{0.5}$ [122, 169, 178, 180, 301, 302]. On the other hand, for the viscosity dominated regime ($Oh > 1$), the hole radius grows linearly with time [177–179, 302]. In the present study, the parameters set result in $Oh \approx 3.5$ and we observe a viscosity dominated hole-growth kinetics, $r_{\mathrm{h}} \sim t$, for $We_{\mathrm{E}} \leq 0.3$ whereas an inertia dominated regime with $r_{\mathrm{h}} \sim t^{0.5}$, for $We_{\mathrm{E}} > 0.3$. In a way, for $We_{\mathrm{E}} \leq 0.3$, the relatively slower kinetics of hole-growth is governed by the dominance of destabilizing capillary force over the retarding viscous force. However, for $We_{\mathrm{E}} > 0.3$, a faster hole-growth kinetics is governed by an interplay of capillary, viscous, and inertial forces. Previously, Aryafar & Kavehpour [181] reported that the electro-coalescence of a droplet to a planar interface is independent of the electric field when $Oh > 3$. In contrast, the results shown above suggest that the magnitude of We_{E} indeed play an important role in changing the shape of the droplet from spherical to prolate alongside increasing its speed towards the interface. This eventually leads to a transition from viscosity dominated carrier film rupture to an inertia dominated one with the enhancement of the strength of the electric field.

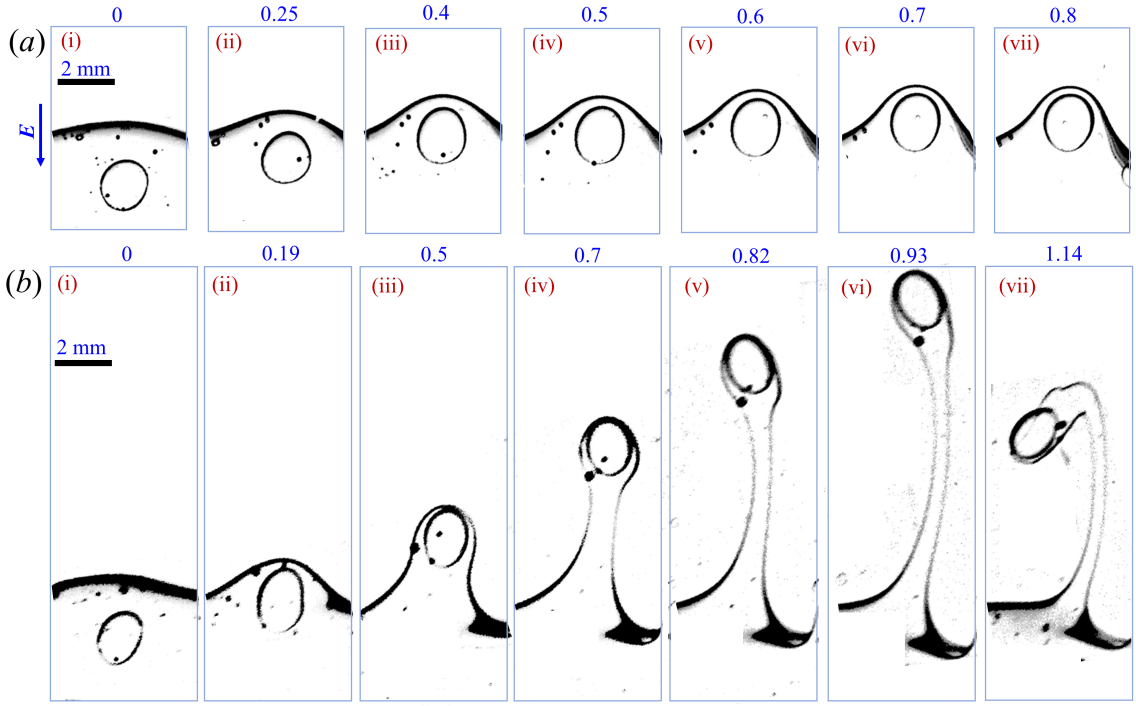

Figure 4.7: Experimental time sequence snapshots demonstrating the trajectory of an aqueous droplet (phase C) immersed in silicone oil (phase B) and advancing towards soybean oil (phase A) under application of (*a*) $E_0 \approx 3$ kVcm^{-1}, $We_E \approx 2.15$, $We_E^1 \approx 0.06$ and (*b*) $E_0 \approx 3.5$ kVcm^{-1}, $We_E \approx 3$, $We_E^1 \approx 0.084$. The other dimensionless numbers associated with (*a*) and (*b*) are, $Bo \approx 0.4$, $Bo_1 \approx 0.01$, $\rho^*_{AB} \approx 0.96$, $\rho^*_{BC} \approx 0.96$, $\rho^*_{BC} \approx 0.92$, $\rho^* \approx 1$, $\mu^*_{AB} \approx 0.17$, $\mu^*_{BC} \approx 300$, $\mu^*_{AC} \approx 50$, $\varepsilon^*_{AB} \approx 1.15$, $\varepsilon^*_{BC} \approx 0.034$, $\varepsilon^*_{AC} \approx 0.039$, $\sigma_1^* \approx 1.08$, $\sigma_2^* \approx 0.028$, and $\sigma_3^* \approx 0.026$. The time shown above each snapshot has unit of seconds.

4.5.3 Tailing Mode

4.5.3.1 The Phenomena

The tailing mode of droplet migration is observed for significantly lower interfacial tensions between phases A and B. The motion of a water droplet (phase C) from silicone oil (phase B) towards soybean oil (phase A) under electric field is shown in figure 4.7. Image set (*a*) shows that at $We_E \approx 2.15$, the droplet advances towards the A-B interface with a marginal deformation. The droplet then pushes the interface with the front covered by a thin film of silicone oil. The downward acting forces of interfacial tension, gravity and viscosity then balance the upward acting electrical force, such that it achieves a metastable equilibrium, before falling back under the effects of the forces, as mentioned previously in section 4.5.2. However, the image

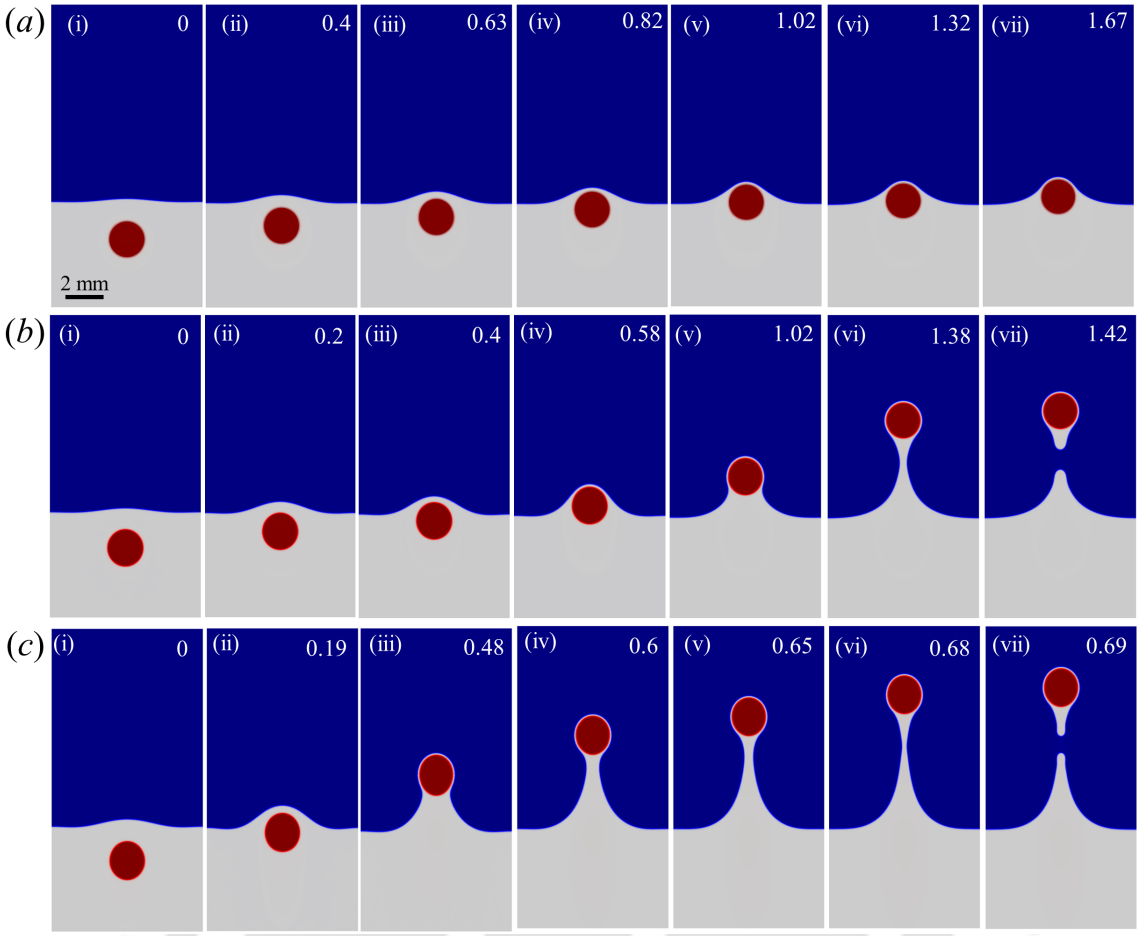

Figure 4.8: Simulated trajectory of an aqueous droplet (phase C) immersed in silicone oil (phase B) and advancing towards soybean oil (phase A) at (*a*) $We_{\mathrm{E}} = 0.7$, $We_{\mathrm{E}}^{1} \approx 0.02$, (*b*) $We_{\mathrm{E}} = 2.15$, $We_{\mathrm{E}}^{1} \approx 0.06$ and (*c*) $We_{\mathrm{E}} = 3$, $We_{\mathrm{E}}^{1} \approx 0.084$. The other dimensionless numbers associated with $(a-c)$ are, $Bo = 0.4$, $Bo_1 = 0.01$, $\rho^*_{\mathrm{AB}} = 0.96$, $\rho^*_{\mathrm{BC}} = 0.96$, $\rho^*_{\mathrm{BC}} = 0.92$, $\rho^* = 1$, $\mu^*_{\mathrm{AB}} = 0.17$, $\mu^*_{\mathrm{BC}} = 300$, $\mu^*_{\mathrm{AC}} = 50$, $\varepsilon^*_{\mathrm{AB}} = 1.15$, $\varepsilon^*_{\mathrm{BC}} = 0.034$, $\varepsilon^*_{\mathrm{AC}} = 0.039$, $\sigma^*_1 = 1.08$, $\sigma^*_2 = 0.028$, and $\sigma^*_3 = 0.026$. The time shown above each snapshot has unit of seconds.

set (*b*) shows that at $We_{\mathrm{E}} \approx 3$, the droplet moves up with its front covered by an unruptured carrier film and a tail of the same attached to the rear end. With time, the droplet covered by the carrier film enters the target liquid before the droplet motion is interrupted by its contact with the upper electrode. The thin film around the droplet ruptures instantaneously post its contact with the upper electrode and the drop falls back with the tail attached to its rear end, as shown in image vii. The tailing mode of transfer has been previously observed in the case of bubbles [159, 161, 163, 166] and solid spheres [147, 152, 153], under conditions of low

interfacial tensions, high-viscosity of the carrier liquid and comparable densities of the carrier and target liquids.

Figure 4.8 shows the simulated trajectory during the migration of a water droplet from silicone oil towards soybean oil under electric field, which is qualitatively similar to the system discussed in figure 4.7. Image set (a) shows that for $We_{\mathrm{E}} = 0.7$ and $\sigma_2^* = 0.028$, the droplet after pushing the interface for a brief period of time comes to a halt. The image sets (b) and (c) for $We_{\mathrm{E}} = 2.15$ and $We_{\mathrm{E}} = 3$, respectively, show that the droplet moves upwards with a tail of the carrier liquid, as observed previously in the experiments. As the droplet rises the tail gets stretched axially, leading to the creation of a neck at almost the central part of the tail (image (vii)). Break-up occurs and the neck pinches-off with the droplet entraining a part of liquid B, while the remaining part falls back. This behaviour is qualitatively similar with the experimental observations shown in figure 4.7(b). In the experiments, however, the droplet touches the upper electrode before the pinch-off of the tail. It may be noted that in case of the simulations, the critical voltage required for the droplet to breakthrough the interface is lower compared to the experiments. For $We_{\mathrm{E}} = 2.15$, figure 4.7(a) shows that the droplet gets stuck at the interface, while 4.8(b) shows that the droplet moves into the target liquid towing a tail of the carrier liquid. This difference is primarily due to higher charge assigned to the simulated droplet compared to the experiments.

Image sets (a) and (b) in figure 4.9 show the vorticity and streamline fields for the case discussed in the image set (c) of figure 4.8. The images show that, as the droplet rises above, positive vorticity fields appear within and around the regions entrained by the drop. The interface curvature increases sharply at the rear end of the droplet, near the junction between the film and the rising tail (image (iv)). A few regions of low negative vorticity fields also appear behind the droplet, which originate from the negative radial velocities due to the stretching of tail (images (iv)$-$(vii)). The lower part of the tail starts receding back while the upper part moves with the droplet, as the droplet moves further upwards (images (iv)$-$(vii)). The arrows in the streamline fields indicate such opposing velocities in the tail, which eventually lead to the pinch-off. Regions within the tail have negative downward velocities, while the layer of the outer fluid (fluid A) adjacent to the tail is still entrained upwards, causing a recirculating zone. Negative vorticity fields are observed on both sides of the receding interfacial regions owing to the velocity gradients. Importantly, the axisymmetric simulations lead to the formation of the symmetric vortices across the

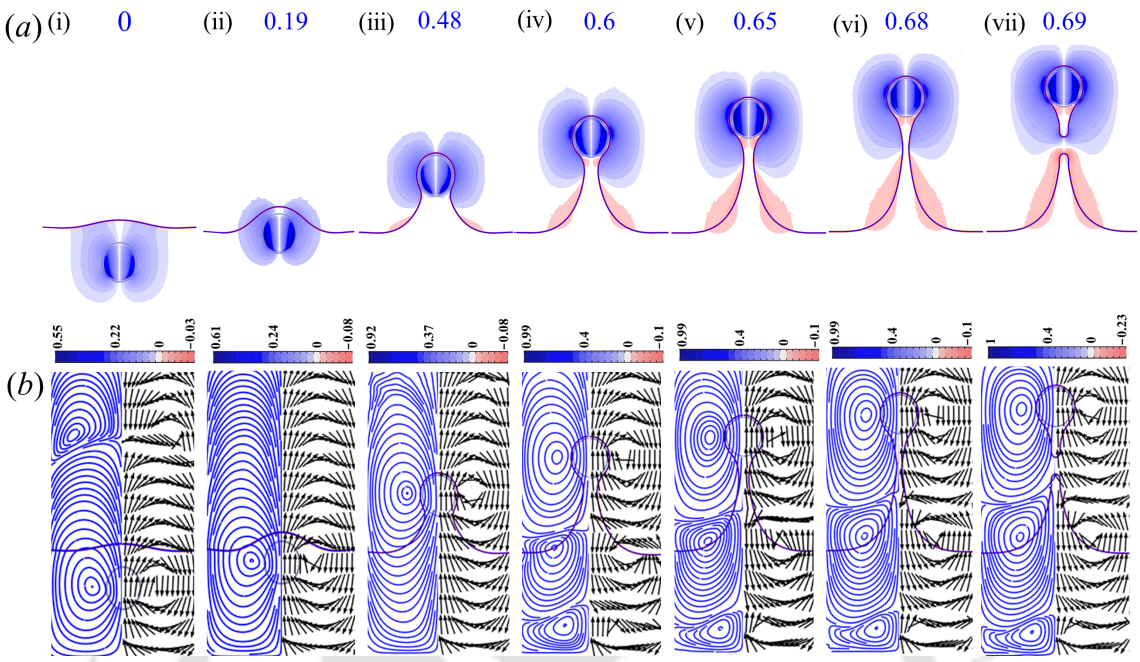

Figure 4.9: Simulated time sequence snapshots demonstrating the (a) normalized azimuthal vorticity fields $\left(\omega_\theta = \frac{\partial v_r}{\partial z} - \frac{\partial v_z}{\partial r}\right)$ and (b) streamline fields during the trajectory of an aqueous droplet (phase C) immersed in silicone oil (phase B) and advancing towards soybean oil (phase A) at $We_{\mathrm{E}} = 3$ and $We_{\mathrm{E}}^{1} = 0.084$. The other dimensionless numbers associated with (a) and (b) are, $Bo = 0.4$, $Bo_1 = 0.01$, $\rho^*_{\mathrm{AB}} = 0.96$, $\rho^*_{\mathrm{BC}} = 0.96$, $\rho^*_{\mathrm{BC}} = 0.92$, $\rho^* = 1$, $\mu^*_{\mathrm{AB}} = 0.17$, $\mu^*_{\mathrm{BC}} = 300$, $\mu^*_{\mathrm{AC}} = 50$, $\varepsilon^*_{\mathrm{AB}} = 1.15$, $\varepsilon^*_{\mathrm{BC}} = 0.034$, $\varepsilon^*_{\mathrm{AC}} = 0.039$, $\sigma^*_1 = 1.08$, $\sigma^*_2 = 0.028$, and $\sigma^*_3 = 0.026$. The time shown above each snapshot has unit of seconds. The vorticity values are normalized by the maximum vorticity. The blue (pink) regions denote positive (negative) vorticity, respectively.

axis, which ensure a straight and upward motion of the droplet towards the target liquid. However, in the experiments, one can envisage the formation of asymmetric vortices surrounding the tail, which may be the major reason behind non-linear upward motion of the droplet and the curvature observed in the tail of the image set (b) in figure 4.7.

4.5.3.2 Quantitative Analysis

Figure 4.10(a) shows the comparisons of the experimental and simulated variations of the rising velocities of the droplet (u^*_{C}), as functions of the distance of the uppermost point on the droplet, from the position of the undisturbed interface (d^*). The figure

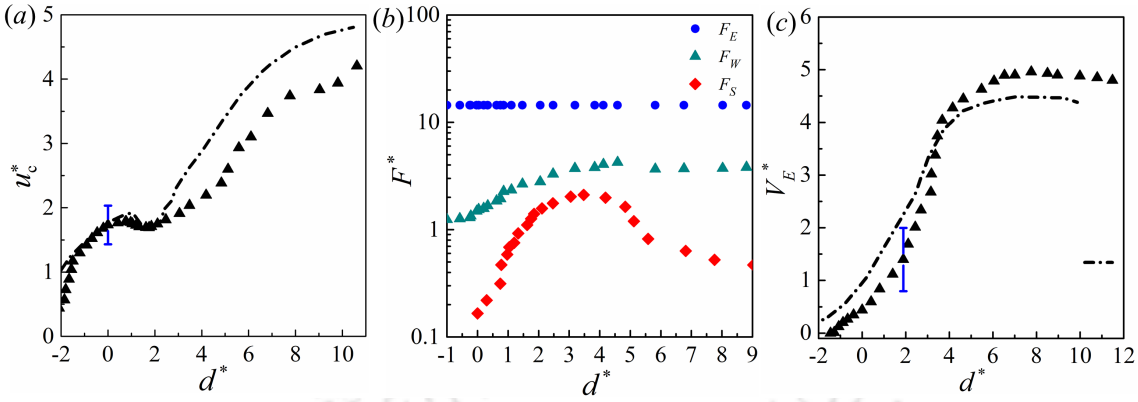

Figure 4.10: Variations of the normalized (a) rising velocities of the droplet (u_{C}^*) as functions of the distance of the uppermost point of the droplet from the undisturbed interface (d^*) (b) forces acting on the droplet (F^*) as functions of d^*, and (c) entrained volume (V_E^*) with d^* for $We_{\mathrm{E}} \approx 3$ and $We_{\mathrm{E}}^1 = 0.084$. The solid points indicate the experimental data and the lines correspond to the simulated values. The other dimensionless numbers associated with $(a)-(c)$ are, $Bo = 0.4$, $Bo_1 = 0.01$, $\rho_{\mathrm{AB}}^* = 0.96$, $\rho_{\mathrm{BC}}^* = 0.96$, $\rho_{\mathrm{BC}}^* = 0.92$, $\rho^* = 1$, $\mu_{\mathrm{AB}}^* = 0.17$, $\mu_{\mathrm{BC}}^* = 300$, $\mu_{\mathrm{AC}}^* = 50$, $\varepsilon_{\mathrm{AB}}^* = 1.15$, $\varepsilon_{\mathrm{BC}}^* = 0.034$, $\varepsilon_{\mathrm{AC}}^* = 0.039$, $\sigma_1^* = 1.08$, $\sigma_2^* = 0.028$, and $\sigma_3^* = 0.026$. The forces are normalized by the factor $-\ r_{\mathrm{C}}^2 \varepsilon_{\mathrm{B}} E_0^2$. The entrained volume V_E is normalized by the droplet volume V_{C}.

shows that starting from rest inside the highly viscous carrier liquid, the velocity of the droplet increases as it rises up under the action of the electric field. The droplet experiences a dip in the velocity near the interface ($1 \leq d^* \leq 2$) before accelerating again after entering in the target liquid of lesser viscosity ($\mu_{\mathrm{AB}}^* = 0.17$). Figure 4.10$(b)$ shows the normalized electrical force (F_E^*), net weight (F_W^*) and interfacial force (F_S^*), acting on the droplet as functions of d^* for the experiments. The expressions for F_E^*, F_W^* and F_S^* are discussed in section 4.5.5.2. For the experimental calculations, the electrical force acting on the droplet was assumed to be constant Coulomb force. The plots suggest that the electrical force is overwhelmingly stronger than the other two, which is the major reason behind the droplet migration. The plot 4.10(b) shows that the net weight of the droplet increases as it passes from the carrier to target liquid because the latter is of less density than the former. There is an increase in the interfacial tension force owing to the increase in the interfacial area, as the drop crosses the interface. Thus, a marginal reduction in the velocity of the droplet is observed in the region $1 \leq d^* \leq 2$. Beyond this region, the F_W^* enhances marginally while a decrease in F_S^* alongwith the lower viscous dissipation in A, leads to an overall increase in the velocity of the droplet. The simulated velocities

accurately map the experimental ones until $d^* \approx 3$, after which the simulated values are slightly higher. As already mentioned, the simulations are carried out with the droplet containing the theoretical amount of charge, which remains constant throughout the migration. In the experiments, however, the charge relaxation from the drop to outer fluid is expected to be higher in the target soybean oil due to its higher conductivity compared to silicone oil, Thus, the electrical force on the drop is expected to decrease as the drop moves into the target oil, which is why the experimental velocities are low compared to the simulations.

Figure 4.10(c) depicts the comparisons of the experimental and simulated values of the normalized volume of the carrier fluid entrained by the rising droplet (V_E^*) as a function of d^*. Here the entrained volume is inclusive of the droplet volume V_C. The plots show that, as the droplet crosses the interface towing a column of carrier fluid, V_E^* increases to reach a maximum value, nearly five times that of the drop volume at $d^* \approx 8$. Thereafter, receding of the column leads to decrease in V_E^* beyond $d^* \approx 8$ and the figure 4.10(c) indicates a pinch-off in the simulations at the point of discontinuity.

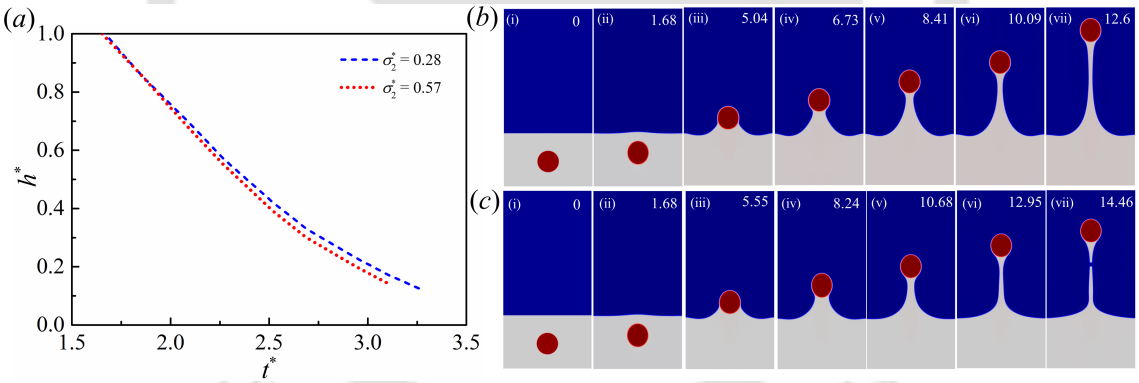

Figure 4.11: (a) Variation of the normalized simulated film thickness (h^*) as a function of time (t^*) for the rupture mode. The time sequence plots for the tailing mode of droplet migration for, (b) $\sigma_2^* = 0.028$ and (c) $\sigma_2^* = 0.143$. The other parameters used for $(a-c)$ are, $\rho_{AB}^* = 0.947$, $\rho_{AC}^* = 0.9$, $\rho_{BC}^* = 0.95$, $\rho^* = 1$, $\mu_{AB}^* = 1$, $\mu_{BC}^* = 40$, $\sigma_1^* = 1$, $\varepsilon_{AB}^* = 1$, $\varepsilon_{BC}^* = 0.0375$, and $We_E^1 = 0.11$. The time shown above each snapshot is dimensionless.

4.5.4 Parametric Study

4.5.4.1 Variation of the Interfacial Tension, σ_{AB}

Figure 4.11 shows the simulated variations of the film thickness (h^*) with time (t^*) for the rupture mode of droplet migration. The figure shows that the film drainage is marginally faster for $\sigma_2^* = 0.57$ compared to $\sigma_2^* = 0.28$ as the interfacial tension σ_{AB} increases. A higher interfacial tension signifies a more immobile interface, which deforms less due to an upward push by the droplet. Thus, the area of the gap region between the droplet and the interface is less, compared to a lower value of σ_{AB}, at a particular instant. This may lead to a thinner carrier liquid film and a faster film drainage, as compared to the case where the interface is more deformable [159, 163, 174]. Figures 4.11(b) and 4.11(c) show the motions of the droplet for the tailing mode of migration for $\sigma_2^* = 0.028$ and $\sigma_2^* = 0.143$, respectively. The figures show that, as σ_{AB} increases, the drop velocity decreases due to increase in the interfacial tension force. The volume of the carrier fluid entrained by the drop also decreases beyond a value of d^*, before the eventual pinching-off of the column. As the droplet moves upwards, the top part of the column moves with it, while the bottom part recedes downwards due to gravity as shown in figure 4.9(b). In case of lower σ_{AB}, due to higher deformability of the interface, the upper part of the column moves faster ahead compared to the receding part. Thus, the column extends deeper into the target fluid. As σ_{AB} increases, the movement of the upper part of the column becomes more restricted, while the lower part recedes at the same rate. Due to the competing upward and downward forces acting on the column, a constriction is created and the column pinches off.

4.5.4.2 Variation of the Density Ratio, ρ_{AB}^*

Figures 4.12(a) and 4.12(b) depict the variations of the film thickness (h^*) as a function of time (t^*) and the rising velocity of the droplet (u_C^*) as a function of d^*, respectively, that are associated with the rupture mode of droplet migration. Figure 4.12(a) suggests that the variation of ρ_{AB}^* does not have much influence on the rate of film drainage. Figure 4.12(b) suggests that as the density of phase A decreases, the velocity of the droplet reduces significantly after crossing the interface. The reason behind this trend is that the reduction in ρ_{AB}^* increases the downward gravitational force F_W acting on the droplet as it crosses the interface.

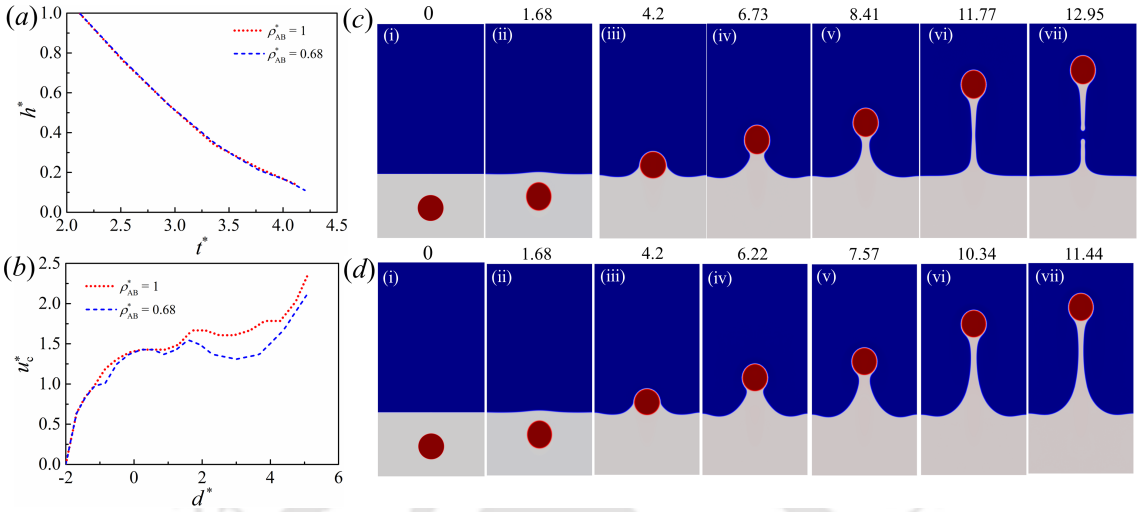

Figure 4.12: Variation of the simulated normalized (a) film thickness (h^*) as a function of time (t^*) and (b) rising velocity of the droplet (u_C^*) as a function of d^* for the rupture mode. The time sequence plots for the tailing mode of droplet migration for, (c) $\rho_{AB}^* = 0.625$ and (d) $\rho_{AB}^* = 0.94$. The other parameters used for (a) and (b) are, $\rho_{BC}^* = 0.96$, $\mu_{AB}^* = 1$, $\mu_{BC}^* = 40$, $\sigma_1^* = 1$, $\sigma_2^* = \sigma_3^* = 0.29$, $\varepsilon_{AB}^* = 1$, $\varepsilon_{BC}^* = 0.0375$, and $We_E^1 = 0.11$. The other parameters used for (c) and (d) are, $\rho_{BC}^* = 0.96$, $\mu_{AB}^* = 1$, $\mu_{BC}^* = 40$, $\sigma_1^* = 1$, $\sigma_2^* = \sigma_3^* = 0.029$, $\varepsilon_{AB}^* = 1$, $\varepsilon_{BC}^* = 0.0375$, and $We_E^1 = 0.11$. The time shown above each snapshot is dimensionless.

Figures 4.12(c) and 4.12(d) show the motions of the droplet in the tailing mode of migration for, $\rho_{AB}^* = 0.625$ and $\rho_{AB}^* = 0.94$, respectively. It can be observed that the droplet migrates with almost equal velocity until a particular value of d^*, after which there is a reduction in the velocity of the droplet for $\rho_{AB}^* = 0.625$, due to increase in F_W. Images (iv)−(vii) of figures 4.12(c) and 4.12(d) suggest that V_E^* decreases with decrease in the density of phase A. For $\rho_{AB}^* = 0.625$, the lower part of the column of B retracts back fast, due to lower density of A, while the upper part moves slowly with the droplet leading to faster drainage. Thus, V_E^* values are lower compared to $\rho_{AB}^* = 0.94$.

4.5.4.3 Variation of the Viscosity Ratio, μ_{AB}^*

Figures 4.13(a) and 4.13(b) demonstrate the simulated rising characteristics of the droplet for the rupture mode with varying viscosity contrast between the carrier and target liquids (μ_{AB}^*). Figure 4.13(a) suggests that the film drains at a faster rate as the viscosity of the target liquid decreases. A lower viscosity target liquid provides less resistance towards the drainage on one side of the film, causing the liquid within

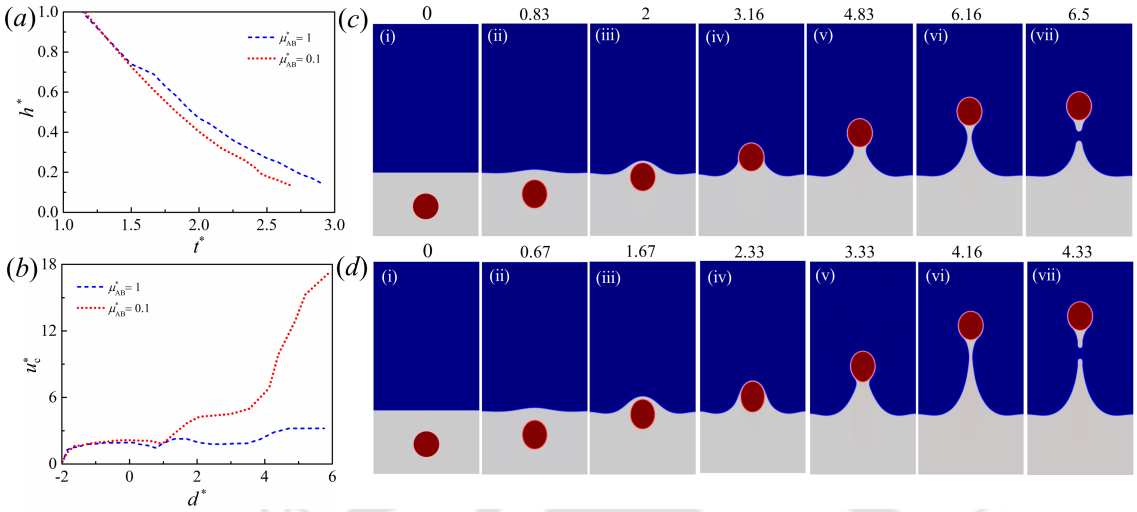

Figure 4.13: Variation of the simulated normalized (a) film thickness (h^*) as a function of time (t^*) and (b) rising velocity of the droplet (u_C^*) as a function of d^* for the rupture mode. The time sequence plots during the tailing mode of droplet migration for, (c) $\mu_{AB}^* = 1$ and (d) $\mu_{AB}^* = 0.2$. The other parameters used for (a) and (b) are, $\rho_{AB}^* = 0.89$, $\rho_{BC}^* = 0.96$, $\rho_{AC}^* = 0.86$, $\rho^* = 0.4$, $\mu_{BC}^* = 200$, $\sigma_1^* = 1$, $\sigma_2^* = \sigma_3^* = 0.29$, $\varepsilon_{AB}^* = 1$, $\varepsilon_{BC}^* = 0.0375$, and $We_E^1 = 0.11$. The other parameters used for (c) and (d) are, $\rho_{AB}^* = 0.94$, $\rho_{BC}^* = 0.96$, $\rho_{AC}^* = 0.9$, $\rho^* = 0.66$, $\mu_{BC}^* = 200$, $\sigma_1^* = 1$, $\sigma_2^* = \sigma_3^* = 0.029$, $\varepsilon_{AB}^* = 1$, $\varepsilon_{BC}^* = 0.0375$, and $We_E^1 = 0.11$. The time shown above each snapshot is dimensionless.

to squeeze out faster. Figure 4.13(b) shows that the velocity of the droplet is higher in case of $\mu_{AB}^* = 0.1$, due to lower viscous dissipation in the target liquid.

Figures 4.13(c) and 4.13(d) show the motion of the droplet for the tailing mode of migration. The figures suggest increase in the velocity of the droplet with decreasing viscosity of the target liquid. It also suggests that until some distance above the undisturbed interface, the drop entrains approximately equal volumes for both $\mu_{AB}^* = 1$ and $\mu_{AB}^* = 0.2$. For $\mu_{AB}^* = 1$, V_E^* attains maximum value at a lower value of d^* compared to $\mu_{AB}^* = 0.2$. As the lower part of the entrained column recedes back in case of $\mu_{AB}^* = 1$, the upper part of the column is pulled upwards, relatively slowly by the droplet, compared to that in the case of $\mu_{AB}^* = 0.2$, due to higher dissipation. Thus, in case of $\mu_{AB}^* = 1$, the drainage of the carrier liquid is faster and the column becomes constricted at a relatively small d^* compared to $\mu_{AB}^* = 0.2$. In case of $\mu_{AB}^* = 0.2$, the upper part of the column moves much faster with the droplet, compared to the receding lower part. As a result, the entrained column becomes longer and the stretching of the column causes a constriction to occur at the upper

part of the column causing the pinching-off.

4.5.4.4 Variation of the Drop Viscosity Ratio, μ^*_{BC}

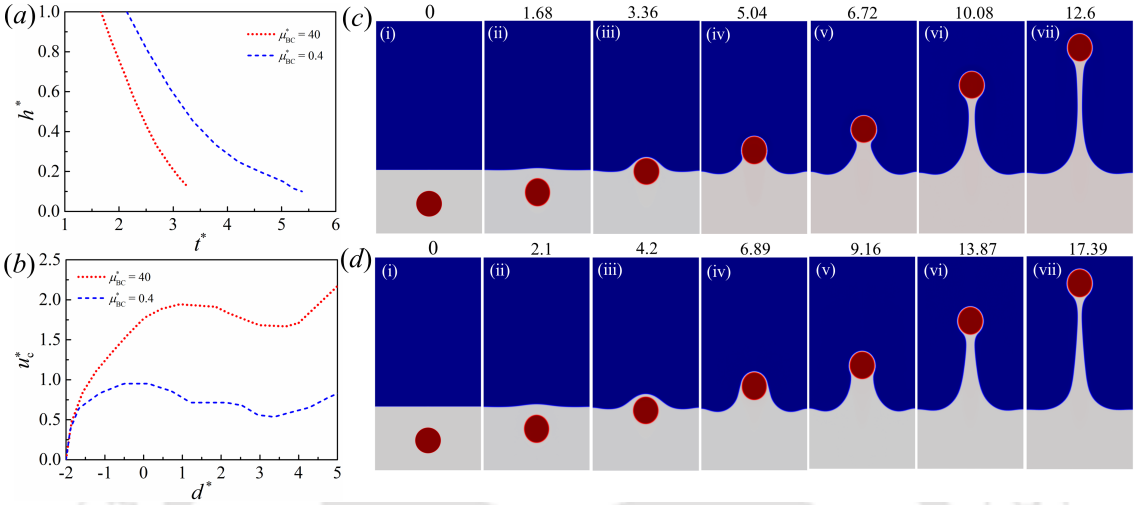

Figure 4.14: Variation of the simulated normalized (a) film thickness (h^*) as a function of time (t^*) and (b) rising velocity of the droplet (u^*_C) as a function of d^* for the rupture mode. The time sequence plots during the tailing mode of droplet migration for, (c) $\mu^*_{BC} = 40$ and (d) $\mu^*_{BC} = 0.4$. The other parameters used for (a) and (b) are, $\rho^*_{AB} = 0.89$, $\rho^*_{BC} = 0.96$, $\rho^*_{AC} = 0.86$, $\rho^* = 0.4$, $\mu^*_{AB} = 1$, $\sigma^*_1 = 1$, $\sigma^*_2 = \sigma^*_3 = 0.29$, $\varepsilon^*_{AB} = 1$, $\varepsilon^*_{BC} = 0.0375$, and $We^1_E = 0.11$. The other parameters used for (c) and (d) are, $\rho^*_{AB} = 0.94$, $\rho^*_{BC} = 0.96$, $\rho^*_{AC} = 0.9$, $\rho^* = 0.66$, $\mu^*_{AB} = 1$, $\sigma^*_1 = 1$, $\sigma^*_2 = \sigma^*_3 = 0.029$, $\varepsilon^*_{AB} = 1$, $\varepsilon^*_{BC} = 0.0375$, and $We^1_E = 0.11$. The time shown above each snapshot is dimensionless.

Figures 4.14(a) and 4.14(b) demonstrate the rising characteristics of the droplet, for the rupture mode, with varying viscosity ratio between the droplet and the carrier liquid (μ^*_{BC}). Figure 4.14(a) suggests that the film drainage is faster for the lower viscosity droplet [159, 174, 175]. This is because a less viscous drop enables an increase in the drainage rate of the carrier film due to low viscous resistance across the carrier-droplet interface. Figure 4.14(b) suggests that the droplet with lower viscosity ($\mu^*_{BC} = 40$) moves much faster as compared the one with higher viscosity ($\mu^*_{BC} = 0.4$).

Figures 4.14(c) and 4.14(d) demonstrate the rising characteristics of the droplet, for the tailing mode. Similar to the observations for the rupture mode, figures 4.14(c) and 4.14(d) show that the droplet along with the column rises faster when the droplet viscosity is lower ($\mu^*_{BC} = 40$). In case of the lower viscosity drop, the

velocity at the drop-liquid interface is higher, thus causing greater drainage of the carrier liquid compared to the higher viscosity drop. Thus, the entrained volumes, V_E^*, are slightly lower for $\mu_{BC}^* = 40$ as compared to $\mu_{BC}^* = 0.4$, as shown in images (iii)−(vii).

4.5.4.5 Variation of the Drop Dielectric Constant, ε_{BC}^*

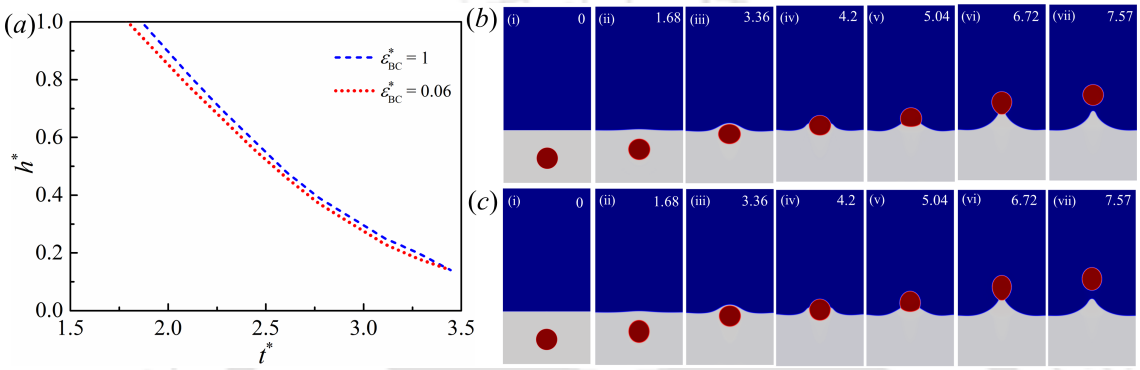

Figure 4.15: (a) Variation of the simulated normalized film thickness (h^*) as a function of time (t^*) for the rupture mode. The time sequence plots during the rupture mode of droplet migration for, (b) $\varepsilon_{BC}^* = 1$ and (c) $\varepsilon_{BC}^* = 0.06$. The other parameters used for $(a-c)$ are, $\rho_{AB}^* = 0.89$, $\rho_{BC}^* = 0.96$, $\rho_{AC}^* = 0.86$, $\rho^* = 0.4$, $\mu_{AB}^* = 1$, $\mu_{BC}^* = 40$, $\sigma_1^* = 1$, $\sigma_2^* = \sigma_3^* = 0.29$, $\varepsilon_{AB}^* = 1$, and $We_E^1 = 0.11$. The time shown above each snapshot is dimensionless.

Figures 4.15$(a-c)$ demonstrate the rising characteristics of the droplet for the rupture mode, with varying dielectric constant of the drop (ε_{BC}^*). Figures 4.15(b) and 4.15(c) depict that the droplet velocities are nearly similar for both $\varepsilon_{BC}^* = 1$ and $\varepsilon_{BC}^* = 0.06$. The gradient of electric permittivity across the B-C interface in case of $\varepsilon_{BC}^* = 0.06$ causes the droplet to deform into a prolate shape as evident from the images (ii)−(vii) of figure 4.15(c). In case of $\varepsilon_{BC}^* = 1$, due to similar dielectric constants of the drop and and the carrier liquid, the polarisation force is absent and the drop rises as a sphere. The slight increase in the drainage rate for $\varepsilon_{BC}^* = 0.06$ as shown in figure 4.15(a) is due to the deformation of the droplet under the action of of the polarisation force.

Figures 4.16(a) and 4.16(b) demonstrate the motions of the droplet during the tailing mode for, $\varepsilon_{BC}^* = 0.3$ and $\varepsilon_{BC}^* = 0.04$, respectively. It is observed that the velocities of the droplet remain the same for both the cases along with the values of the V_E^*. Due to higher gradient in permittivity across the B-C interface in case

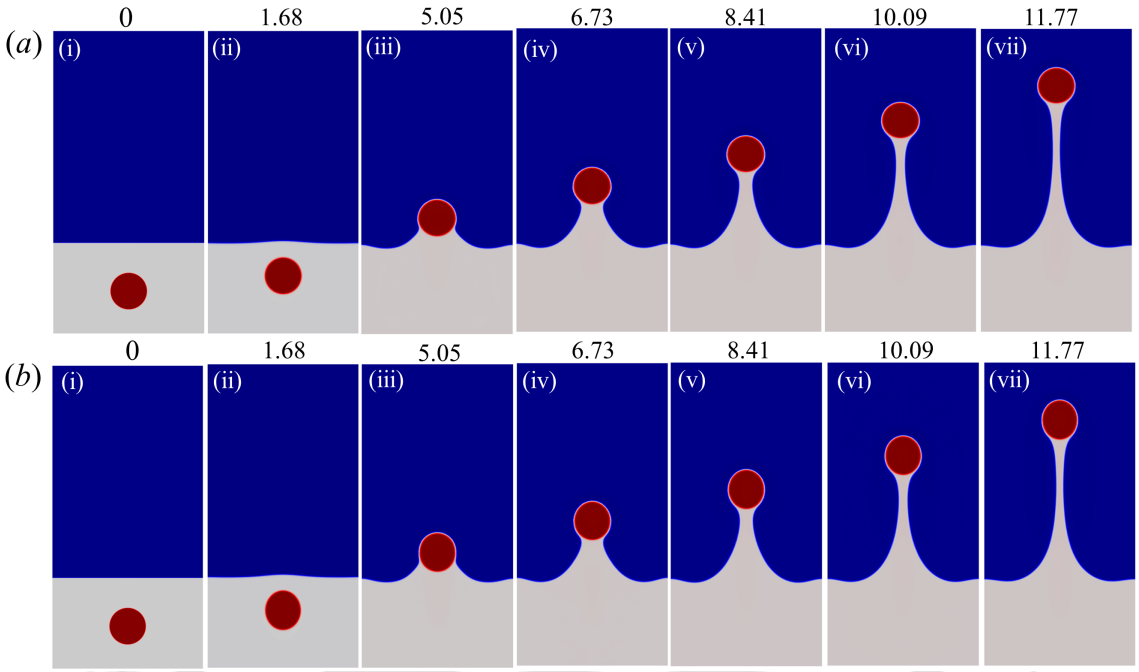

Figure 4.16: The time sequence plots during the tailing mode of droplet migration for, (a) $\varepsilon^*_{\mathrm{BC}} = 0.3$ and (b) $\varepsilon^*_{\mathrm{BC}} = 0.04$. The other parameters used are, $\rho^*_{\mathrm{AB}} = 0.95$, $\rho^*_{\mathrm{BC}} = 0.95$, $\rho^*_{\mathrm{AC}} = 0.9$, $\rho^* = 1$, $\mu^*_{\mathrm{AB}} = 1$, $\mu^*_{\mathrm{BC}} = 40$, $\sigma^*_1 = 1$, $\sigma^*_2 = \sigma^*_3 = 0.029$, $\varepsilon^*_{\mathrm{AB}} = 1$, and $We^1_{\mathrm{E}} = 0.11$. The time shown above each snapshot is dimensionless.

of $\varepsilon^*_{\mathrm{BC}} = 0.04$ compared to $\varepsilon^*_{\mathrm{BC}} = 0.3$, the droplet deforms more in the case of the former, as shown in figure 4.16(b).

4.5.4.6 Variation of the Dielectric Constants of the Carrier and Target Fluids, $\varepsilon^*_{\mathrm{AB}}$

Figures 4.17$(a-e)$ demonstrate the rising characteristics of the droplet for the rupture mode, with varying dielectric constants between carrier and target liquids ($\varepsilon^*_{\mathrm{AB}}$). The permittivity of the droplet was kept constant for all the simulations. Figures 4.17(a) and 4.17(b) depict the variations of the film thickness (h^*) as a function of time (t^*). Figures 4.17$(c-e)$ show the motions of the droplet for different values of $\varepsilon^*_{\mathrm{AB}}$. It can be seen from figures 4.17$(c-e)$ that the velocity of the droplet increases with increase in permittivity of the target liquid and decreases with the increase in the permittivity of the carrier liquid. As the permittivity of the target phase increases, the increase in the gradient of permittivity across the A-B interface leads to an increase in the electric field intensity between the droplet and the A-B

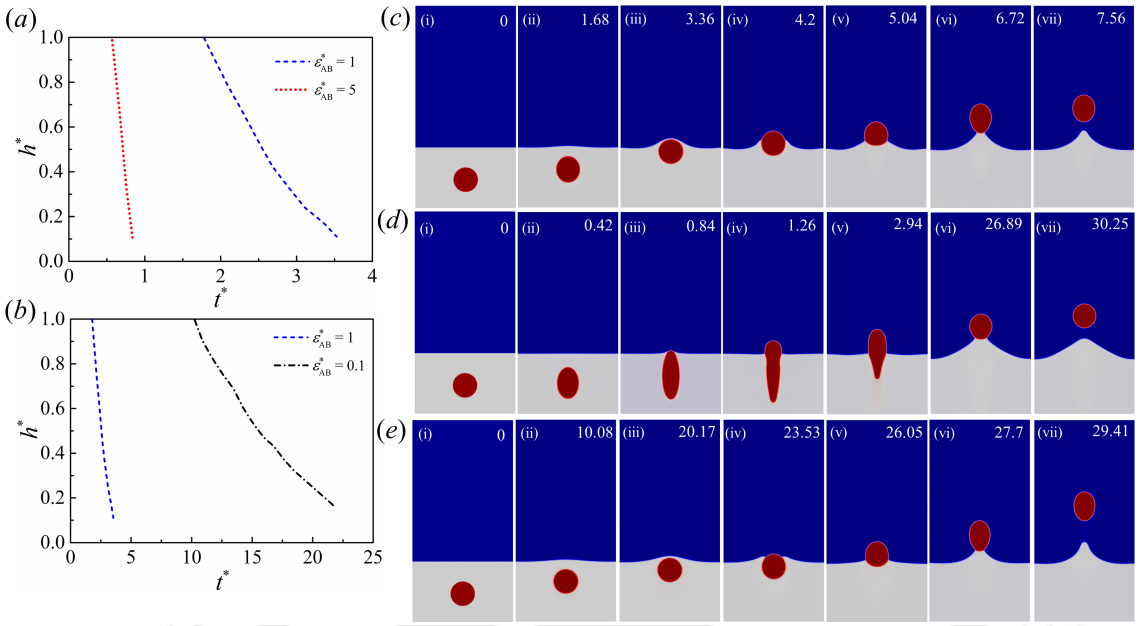

Figure 4.17: (a), (b) Variation of the simulated normalized film thickness (h^*) as a function of time (t^*) for the rupture mode. The time sequence plots during the rupture mode of droplet migration for, (c) $\varepsilon^*_{AB} = 1$, (d) $\varepsilon^*_{AB} = 5$ and (e) $\varepsilon^*_{AB} = 0.1$. The other parameters used for $(a-e)$ are, $\rho^*_{AB} = 0.89$, $\rho^*_{BC} = 0.96$, $\rho^*_{AC} = 0.86$, $\rho^* = 0.4$, $\mu^*_{AB} = 1$, $\mu^*_{BC} = 40$, $\sigma^*_1 = 1$, $\sigma^*_2 = \sigma^*_3 = 0.29$, and $We^1_E = 0.11$. The permittivity of the droplet was kept constant for all the simulations. The time shown above each snapshot is dimensionless.

interface. The droplet, thus, experiences more force which deforms it significantly alongwith increasing its speed of migration, as shown in figure 4.17(d). Thus, the drainage rate is significantly high for $\varepsilon^*_{AB} = 5$ compared to $\varepsilon^*_{AB} = 1$, as shown in figure 4.17(a). On the other hand, as the permittivity of the carrier phase increases, the gradient of permittivity between the B-C interface decreases, resulting in the droplet experiencing less upward electrical force, thus, reducing its speed as shown in figure 4.17(e). This is why the drainage rate is significantly less for $\varepsilon^*_{AB} = 0.1$ compared to $\varepsilon^*_{AB} = 1$, as shown in figure 4.17(b).

Figure 4.18 demonstrates the motion of the droplet for the tailing mode, with varying dielectric constants between carrier and target liquids (ε^*_{AB}). Figures 4.18$(a-c)$ show that the droplet velocity increases with increasing permittivity of the target phase and decreases with increasing permittivity of the carrier phase due to reasons mentioned above. In the tailing mode, due to low interfacial tension between the A-B interface, the liquid column undergoes significant changes in terms of

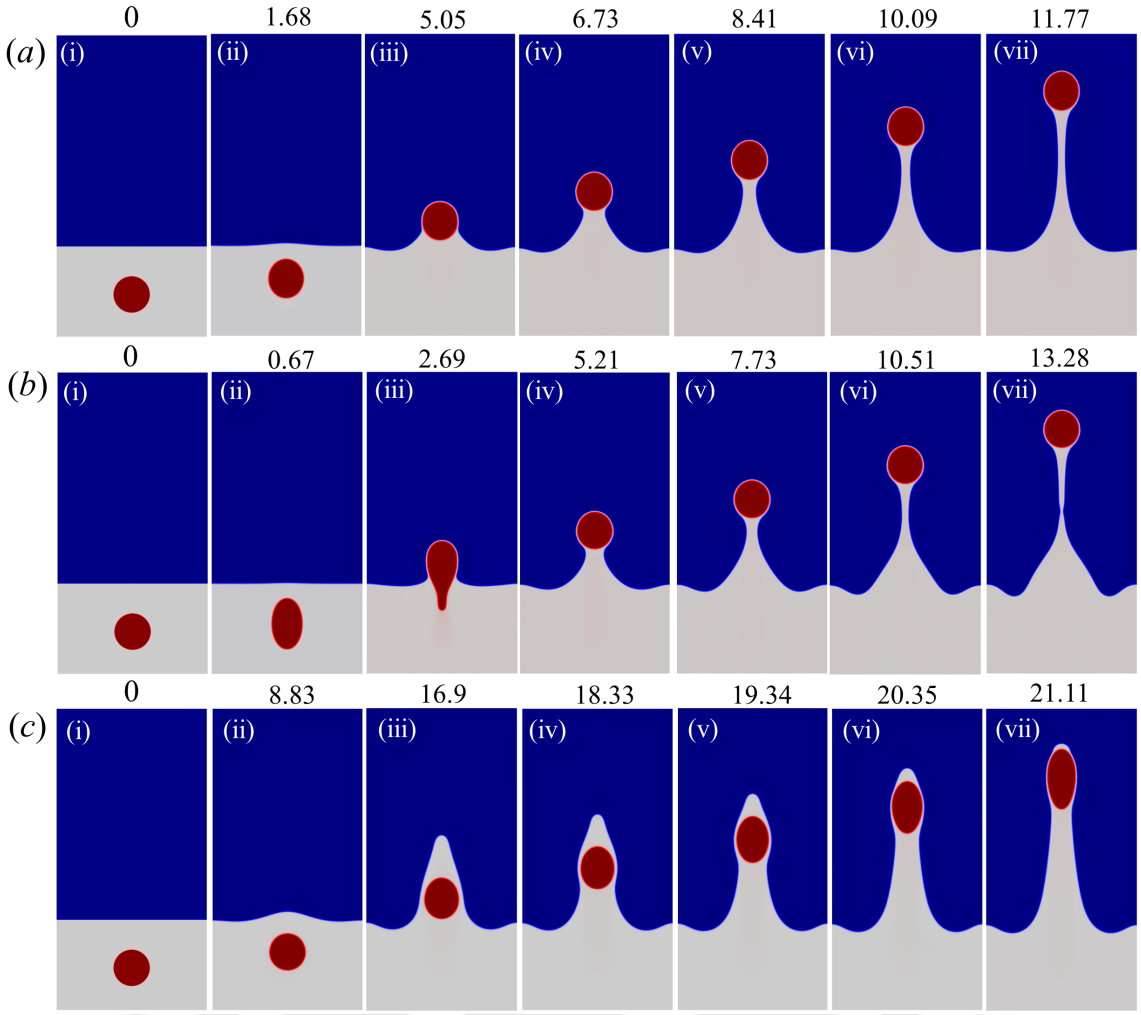

Figure 4.18: The time sequence plots for the tailing mode of droplet migration for (a) $\varepsilon^*_{\mathrm{AB}} = 1$, (b) $\varepsilon^*_{\mathrm{AB}} = 3.33$, and (c) $\varepsilon^*_{\mathrm{AB}} = 0.1$. The other parameters used for $(a-c)$ are, $\rho^*_{\mathrm{AB}} = 0.95$, $\rho^*_{\mathrm{BC}} = 0.95$, $\rho^*_{\mathrm{AC}} = 0.9$, $\rho^* = 1$, $\mu^*_{\mathrm{AB}} = 1$, $\mu^*_{\mathrm{BC}} = 40$, $\sigma^*_1 = 1$, $\sigma^*_2 = \sigma^*_3 = 0.029$, and $We^1_{\mathrm{E}} = 0.11$. The permittivity of the droplet was kept constant for all the simulations. The time shown above each snapshot is dimensionless.

shape and V^*_E, as evident from figures 4.18$(a-c)$. In case of $\varepsilon^*_{\mathrm{AB}} = 3.33$, as shown in (b), the increased permittivity gradient between the A-B interface increases the interface undulations during the droplet motion (images (iv)$-$(vii)) causing changes in the shape of the tail and V^*_E compared to $\varepsilon^*_{\mathrm{AB}} = 1$. For $\varepsilon^*_{\mathrm{AB}} = 0.1$, due to low interfacial tension of the A-B interface, the electrical force acting on it due to the increased permittivity gradient between A and B, exceeds than that acting on the droplet. Thus, the interface moves upwards faster as shown in images (iii)$-$(vi). The increase in the electric field intensity between the droplet and the A-B interface

during this time, causes the droplet to deform into a prolate shape.

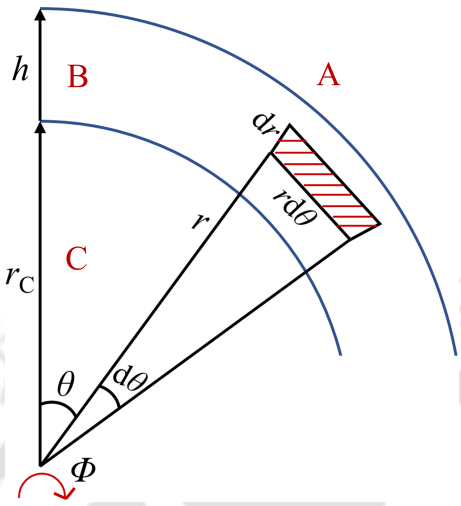

Figure 4.19: Schematic illustration of an element of the draining film. The notations A, B, and C denote the respective phases.

4.5.5 Analytical Models

4.5.5.1 An Analytical Model for the Estimation of Film-Drainage and Velocity Profile

In order to explain the experimental results alongside evaluating a few missing parameters, a simple analytical model (AM) has been developed to estimate the rate of film drainage of the carrier fluid alongwith the velocity profile within it.

Figure 4.19 shows the schematic representation of a part of the draining film of carrier phase B, sandwiched between the target phase A and the droplet phase C. In order to derive analytical expressions for the velocity profile within the film and the kinetics of the approach of the droplet towards the A-B interface, we assume that the film thickness (h) is uniform and is very thin as compared to r_C [141]. Further, the area of contact between the drop and the film is also assumed to be constant. In addition, we consider that the fluid flow within the film occurs in a direction tangential to the drop surface in such a manner that there is no pressure gradient that exists in the radial direction. The drainage of the film is also assumed to be axisymmetric. Subsequently, the force balance on the element shown in figure 4.19

can be written in the following form neglecting the acceleration,

$$-r\frac{\partial p}{\partial \theta}+\frac{\partial}{\partial r}\left(\mu_{\mathrm{B}} r^2 \frac{\partial v_\theta}{\partial r}\right)-r^2 \sin\theta \rho_{\mathrm{B}} g=0. \tag{4.16}$$

Now, to get the velocity profile within the draining film from (4.16), the boundary conditions of v_θ, at the surface of the drop and at the A-B interface must be carefully defined. At both the surfaces, v_θ will have non-zero values due induced circulations inside the droplet and also in phase A. It is intuitive that the value of v_θ at the A-B interface will be very small, and hence for the purpose of simplification, we consider $v_\theta = 0$ at the A-B interface. It has been shown that for a fully circulating drop, the velocity at the drop surface can be written as [168, 303],

$$v_\theta = \frac{\mu_{\mathrm{B}}}{2}\frac{V_i}{\mu_{\mathrm{B}}+\mu_{\mathrm{C}}}\sin\theta, \tag{4.17}$$

where, V_i is the instantaneous velocity of the droplet. Thus, the velocity profile in the film with $v_\theta\big|_{r=r_{\mathrm{C}}} = \frac{\mu_{\mathrm{B}}}{2}\frac{V_i}{\mu_{\mathrm{B}}+\mu_{\mathrm{C}}}\sin\theta$ and $v_\theta\big|_{r=r_{\mathrm{C}}+h} = 0$, is given by,

$$\begin{aligned} 2\mu_{\mathrm{B}} v_\theta \;=\; & \frac{\partial p}{\partial \theta}\left(r+\frac{r_{\mathrm{C}}(r_{\mathrm{C}}+h)}{r}-2r_{\mathrm{C}}-h\right)+\left[\frac{\mu_{\mathrm{B}}^2}{\mu_{\mathrm{B}}+\mu_{\mathrm{C}}}\frac{r_{\mathrm{C}}}{h}\sin\theta V_i\right]\left[\frac{r_{\mathrm{C}}+h}{r}-1\right] \\ + \;& \sin\theta\rho_{\mathrm{B}} g\left[\frac{r^2}{3}+\frac{(2r_{\mathrm{C}}+h)(h+r_{\mathrm{C}})r_{\mathrm{C}}}{3r}-r_{\mathrm{C}}\left(r_{\mathrm{C}}+h+\frac{h^2}{3r_{\mathrm{C}}}\right)\right]. \end{aligned} \tag{4.18}$$

If the velocity of approach of the two surfaces towards each other is defined as u, then the shrinkage in film volume up to an angle θ is given by $A_{cap}u$, where A_{cap} is the area of the spherical cap shown in figure 4.19 and given by $A_{cap} = 2\pi {r_{\mathrm{C}}}^2(1-\cos\theta)$. Alternatively, the volume outflow at an angle θ can also be written as $2\pi\sin\theta\int_{r_{\mathrm{C}}}^{r_{\mathrm{C}}+h} r v_\theta\, \mathrm{d}r$. Thus, the pressure distribution can be expressed as,

$$-\frac{\partial p}{\partial \theta}=\frac{12\mu_{\mathrm{B}} r_{\mathrm{C}}^2 u(1-\cos\theta)}{h^3\sin\theta}+g\rho_{\mathrm{B}} r_{\mathrm{C}}\sin\theta-\frac{3\mu_{\mathrm{B}}^2}{\mu_{\mathrm{B}}+\mu_{\mathrm{C}}}\frac{r_{\mathrm{C}}}{h^2}V_i\sin\theta. \tag{4.19}$$

Considering $p = p'$ at $\theta = \theta'$, (4.19) can be integrated as,

$$p-p'=\frac{12\mu_{\mathrm{B}} r_{\mathrm{C}}^2 u}{h^3}\log\frac{(\cos\theta+1)}{(\cos\theta'+1)}+g\rho_{\mathrm{B}} r_{\mathrm{C}}(\cos\theta-\cos\theta')-\frac{3\mu_{\mathrm{B}}^2}{\mu_{\mathrm{B}}+\mu_{\mathrm{C}}}\frac{r_{\mathrm{C}}}{h^2}V_i(\cos\theta-\cos\theta'). \tag{4.20}$$

The downward force F_d on the sphere can be evaluated as, $2\pi r_C^2 \int_0^{\theta'} p \sin\theta \cos\theta \, d\theta$, which gives,

$$F_d = \pi r_C^2 p' \sin^2\theta' + \frac{12\mu_B r_C^4 u}{h^3}\frac{(\cos\theta'-1)^2}{2} + \frac{\pi g \rho_B r_C^3}{3}(\cos^3\theta' - 3\cos\theta' + 2) - \frac{\pi \mu_B^2}{\mu_B+\mu_C}\frac{r_C^3}{h^2}V_i(\cos^3\theta' - 3\cos\theta' + 2). \quad (4.21)$$

Here, the terms $\pi r_C^2 p' \sin^2\theta' + \frac{\pi g \rho_B r_C^3}{3}(\cos^3\theta' - 3\cos\theta' + 2)$, signify the downward force acting on the droplet due to hydrostatic pressure in the film. Thus, net force balance on the droplet can be written as,

$$F_u = F_d - \pi r_C^2 p' \sin^2\theta' - \frac{\pi g \rho_B r_C^3}{3}(\cos^3\theta' - 3\cos\theta' + 2). \quad (4.22)$$

where, $F_u = k r_C^2 \varepsilon_B E_0^2 - V_C(\rho_C - \rho_B)g$. The approach velocity can be written as, $u = -\frac{\partial h}{\partial t}$. Now integrating (4.22) with the condition, $h = h_0$ at $t = 0$ and considering $v_\theta\big|_{r=r_C} = 0$ gives, the relation between the gap thickness, h, and time, t, as,

$$t = \frac{6\pi\mu_B r_C^4}{F_u}\frac{(\cos\theta'-1)^2}{2}\left(\frac{1}{h^2} - \frac{1}{h_0^2}\right). \quad (4.23)$$

Using $v_\theta\big|_{r=r_C} = \frac{\mu_B}{2}\frac{V_i}{\mu_B+\mu_C}\sin\theta$, eq. (4.23) modifies to,

$$t = \frac{A_1\left[\log\left\{\frac{B_1 h^2 + C_1}{B_1 h_0^2 + C_1}\right\} - 2\log\frac{h}{h_0}\right]}{2C_1}. \quad (4.24)$$

Here, $A_1 = 6\pi\mu_B r_C^4(\cos\theta'-1)^2$, $B_1 = F_u$ and $C_1 = \frac{\pi\mu_B^2}{\mu_B+\mu_C} r_C^3 V_i(\cos^3\theta' - 3\cos\theta' + 2)$.

Figure 4.20(a) shows a comparison of the h^* vs. t^* plots obtained from the experiments and the analytical model. The plots of the AM shown in figure 4.20(a) correspond to eq.(4.23), obtained by considering $v_\theta\big|_{r=r_C} = 0$, i. e. the case of film drainage over a solid particle. For the calculation of the analytical variations of film thickness, the value of θ' was taken as $\pi/2$ and $h_0^* = 1$. The figure illustrates that the values of h^* predicted by the AM are relatively higher in comparison to

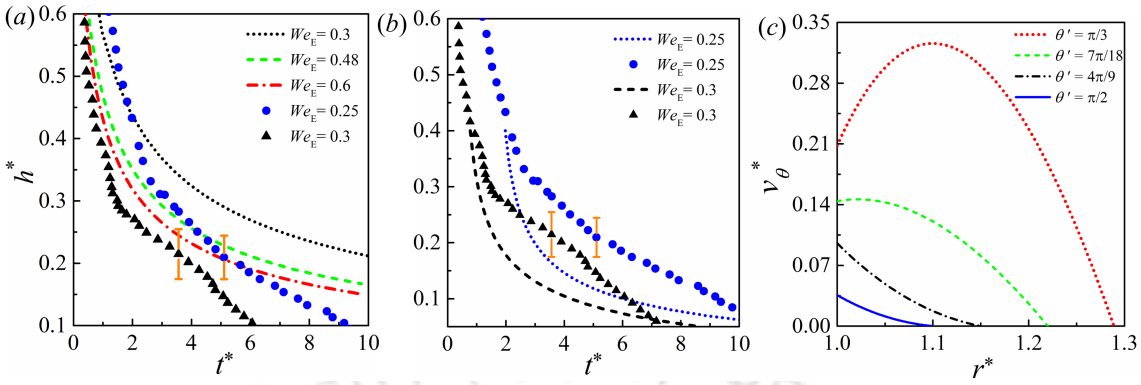

Figure 4.20: Comparisons of the variations of the normalized film thickness (h^*) with time (t^*) of the experimental values with the results obtained from the AM considering (a) $v_\theta\big|_{r=r_C} = 0$ and (b) $v_\theta\big|_{r=r_C} = \frac{\mu_B}{2}\frac{V_i}{\mu_B+\mu_C}\sin\theta$. ($c$) Variations of the normalized velocity within the film (v_θ^*) with r^* obtained from the analytical model at $We_E = 0.3$. It may be noted that the velocity and time are normalized considering the average field intensity, E_0, corresponding to $We_E = 0.3$. The dotted, evenly broken, and unevenly broken lines in (a) and the dotted and evenly broken lines in (b), correspond to the analytical model and the solid symbols correspond to the experimental values. The other parameters used for the analytical calculations are, $r_C = 1$ mm, $\rho_B = 960$ kgm^{-3}, $\rho_C = 1000$ kgm^{-3}, $\mu_B = 0.3$ Pa.s, $\mu_C = 0.001$ Pa.s , $k = (2/3)\pi^3$, $\varepsilon_B = 2.7\varepsilon_0$ Fm^{-1}, $\sigma_{AB} = 0.01$ Nm^{-1}.

the experiments and the film thickness decreases rather slowly. One of the primary reasons behind this trend can be traced back to the velocity boundary conditions at the surface of the drop ($v_\theta\big|_{r=r_C} = 0$) and the interface ($v_\theta\big|_{r=r_C+h} = 0$). The velocity of the flowing liquid in the carrier film is considered to be zero at the interface in the AM, whereas in reality a finite velocity is always present at the interface due to recirculation in phase A, during the drainage of the carrier liquid. Also, since the drainage velocity is essentially non-zero at the surface of the drop, the drainage rates obtained from the AM for $v_\theta\big|_{r=r_C} = 0$, are less compared to the experiments. Figure 4.20(b) shows the comparisons of the h^* versus t^* obtained from the AM for $v_\theta\big|_{r=r_C} = \frac{\mu_B}{2}\frac{V_i}{\mu_B+\mu_C}\sin\theta$ (given by equation (4.24)), with the corresponding experimental values. The values of h_0 and θ' used in the analytical calculations were obtained from the experimental data. The instantaneous velocity, V_i, has been evaluated from the following force balance equations,

$$F_E = F_S + F_W + F_D, \tag{4.25}$$

$$kr_C^2\varepsilon_B E_0^2 = 2\pi r_C\sigma_{AB}\sin\theta'^2 + g\rho_C V_C - g\rho_B\left(V_C - V_S\right) - g\rho_A V_S + g\left(\rho_B - \rho_A\right)V_R + 6\pi\mu_B r_C V_i. \quad (4.26)$$

Here, F_D is the drag force acting on the droplet and is estimated using the Stokes' drag. The figure highlights that the drainage rates predicted by the AM considering non-zero velocity at the surface, are slightly higher compared to the experimental results. The dissimilarities are mainly due to inaccuracies involved in estimation of V_i.

Figures 4.20(c) shows the variations of the velocity of the draining fluid (v_θ^*) with time. The expression of v_θ^*, obtained from the AM is given in eq. (4.17). The values of the various parameters used for the calculations, were obtained from the experimental result shown in figure 4.2(b). Figure 4.20(c) shows that at $\theta' = \pi/3$, when the gap thickness is ∼0.3 times of the droplet radius, the velocity profile within the draining film is nearly parabolic. As the film thickness reduces to ∼0.2 times of the droplet radius, at $\theta' = 7\pi/18$, the profile becomes nearly half-parabolic. The velocity profiles predicted by the AM are nearly linear for $\theta' = 4\pi/9$ and $\theta' = \pi/2$ with further reduction in the thickness of the film. Thus, the velocity profiles in the draining film, emulate the Couette flow profiles between parallel plates. When the film thickness is moderate and the interfaces are not very close, the shearing action due to the presence of the boundaries, becomes gradually less in the middle part of the film. Thus, the velocity profile shows a maximum near the middle for $\theta' = \pi/3$. The shearing action increases due to close proximity of both the boundaries as the film thins during the draining process. Subsequently, a constant shear stress profile across the film leads to a linear velocity profile.

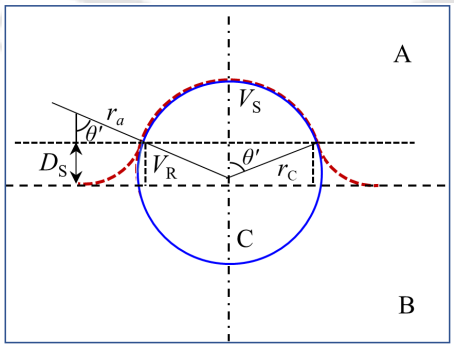

Figure 4.21: Schematic illustration of the quasi-static equilibrium of a droplet (C) at the interface between two liquids A and B during its upward migration under the influence of an electric field.

4.4.5.2 An Analytical Model for the determination of the Critical Electric Field for Droplet Migration

One of the important parameters to estimate, from both fundamental and application point of views is the critical field strength required for the migration of a droplet to the target liquid. The estimation of the exact critical conditions, requires the solution of a dynamic force balance on the droplet, considering the drag and the inertia forces acting on the body, along with the gravitational, interfacial and electric forces. In this study, however, we consider a static force balance, as the droplet velocity is found to be sufficiently low during its approach to the interface interface, to reasonably omit the contributions of the inertial effects.

Figure 4.15 shows a situation wherein a droplet of liquid C moving under the combined influence of an upward electric force and a downward net gravitational force comes to a quasi-steady equilibrium at the interface between liquids A and B, due to the downward acting interfacial force. If it is assumed that the droplet is totally wetted and the thickness of the film attached to the droplet above the pseudo-contact line is negligible, a static force balance on the droplet following previous literature [143, 151, 163] can be written as,

$$F_S + F_W = F_E, \tag{4.27}$$

$$2\pi r_{\mathrm{C}}\sigma_{\mathrm{AB}}\sin^2\theta + g\rho_{\mathrm{C}}V_{\mathrm{C}} - g\rho_{\mathrm{B}}\left(V_{\mathrm{C}} - V_{\mathrm{S}}\right) - g\rho_{\mathrm{A}}V_{\mathrm{S}} + g\left(\rho_{\mathrm{B}} - \rho_{\mathrm{A}}\right)V_{\mathrm{R}} = kr_{\mathrm{C}}^2\varepsilon_{\mathrm{B}}E_0^2. \tag{4.28}$$

Here, the first term of (4.28) denotes the interfacial tension force, F_S, exerted on the droplet by liquid A-liquid B interface. The second term denotes the weight of the droplet of volume V_{C}. The third and the fourth terms denote the buoyant forces acting on the portions of the droplet submerged in liquids B and A, respectively. The fourth term denotes the additional downward force acting on the droplet due to shift in the meniscus [304] and is given by the net weight of the cylinder of liquid B that is immersed in liquid A. These terms are collectively defined as the net gravitational force, F_W, acting on the droplet. The fifth term denotes the approximate electrical Coulomb force acting on the droplet [112, 305]. Here, 'k' denotes a constant that signifies the amount of charge acquired by the droplet from the electrode immersed in liquid B and E_0 denotes the average applied electric field intensity. In case of the droplet acquiring the theoretical amount charge from the electrode, $k = (2/3)\pi^3$ [108]. The volume of the spherical cap V_{S} as shown in

figure 4.21, can be written as, $V_S = (\pi r_C^3/3)(2 - 3\cos\theta' + \cos^3\theta')$, assuming the droplet rise to be axisymmetric along a vertical line passing through the centre of the droplet. Here, θ' is the angle between the axis of symmetry and the line passing through the point of intersection of the meniscus with the $z = D_S$ plane passing through the pseudo-contact line. The volume V_R of the cylindrical column is given by, $V_R = \pi {r_C}^2 \sin^2\theta' D_S$. Thus, equation (4.28) can be re-written as,

$$\begin{aligned} k r_C^2 \varepsilon_B {E_0}^2 &= 2\pi r_C \sigma_{AB} \sin^2\theta' + \frac{4\pi r_C^3(\rho_C - \rho_B)g}{3} + \pi {r_C}^2 D_S \sin^2\theta'(\rho_B - \rho_A)g \\ &+ \frac{\pi r_C^3(2 - 3\cos\theta' + \cos^3\theta')(\rho_B - \rho_A)g}{3}. \end{aligned} \tag{4.29}$$

The non-dimensional form of equation (4.29) can be written as,

$$kWe_E = 2\pi\sin^2\theta' + \frac{4}{3}\pi\rho^* Bo + \frac{\pi}{3}(2 - 3\cos\theta' + \cos^3\theta')Bo + \pi Bo {D_S}^* \sin^2\theta'. \tag{4.30}$$

Equation (4.30) can be solved if the position of the pseudo-contact line D_S^* from the undisturbed interface is known. The Young-Laplace equation defining the hydrostatic balance at the intersection of the pseudo-contact line with the meniscus can be written as,

$$(\rho_B - \rho_A)g D_S = \sigma_{AB} \boldsymbol{\nabla} \cdot \boldsymbol{n}, \tag{4.31}$$

where, $\boldsymbol{n}$ is the unit normal vector to the meniscus. An accurate solution of equation (4.31) can be obtained by solving it numerically with appropriate boundary conditions [152, 306, 307]. However, we follow the procedure used by Maru *et al.* [143] and Bonhomme *et al.* [163], wherein the shape of the meniscus between the pseudo-contact line and the undisturbed interface, as shown in figure 4.21 is considered to be a circular arc of radius r_a. Equation (4.31) can now be written as,

$$(\rho_B - \rho_A)g D_S = \sigma_{AB}\left(\frac{1}{r_a} - \frac{1}{r_C}\right). \tag{4.32}$$

The non-dimensional form of (4.32) leads to the following expression after substitution of, $D_S = r_a(1 - \cos\theta')$,

$$D_S^* = \frac{-1 + \sqrt{1 + 4Bo(1 - \cos\theta')}}{2Bo}. \tag{4.33}$$

On substituting the values of D_S^* in equation (4.30) the electric field needed to migrate a droplet of a particular size can be roughly estimated. To determine the critical cap angle θ'_c and the electric field Weber number $We_{E,c}$, eq. (4.30) is differentiated w. r. t. θ' and equated to zero which gives,

$$\frac{\mathrm{d}(kWe)}{\mathrm{d}\theta'} = 4\pi \sin\theta'_c \cos\theta'_c + \pi Bo \sin^3\theta'_c + \frac{\pi Bo \sin^3\theta'_c}{\sqrt{1+4Bo(1-\cos\theta'_c)}} + \frac{\pi \sin\theta'_c \cos\theta'_c}{\sqrt{1+4Bo(1-\cos\theta'_c)}} = 0. \tag{4.34}$$

Equation (4.34) was solved numerically using the Newton-Raphson method, to get the θ'_c. Substituting the values of θ'_c in eq. (4.30), gives the $We_{E,c}$ required for the droplet migration.

Figure 4.22(a) shows the variation of We_E with normalized cap angle $\theta'^* =$

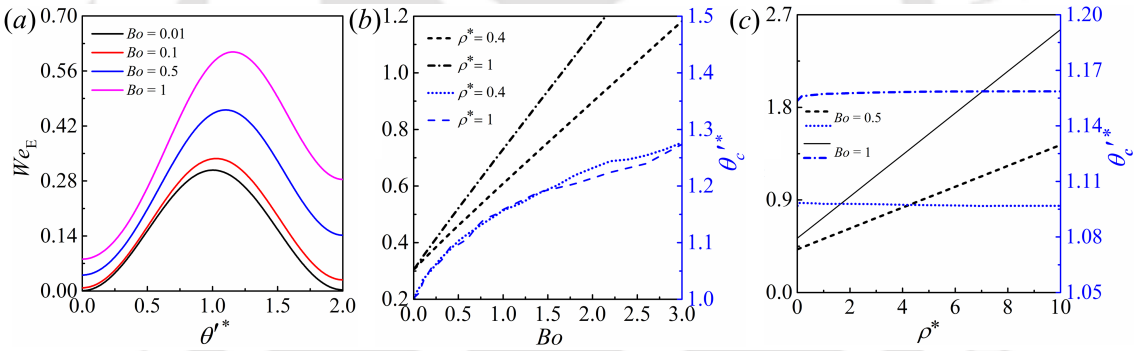

Figure 4.22: (a) Variation of the electric field Weber number (We_E) with the cap angle (θ'^*) for $\rho^* = 0.4$. Variations of the critical electric field Weber number ($We_{E,c}$) with the critical cap angle (θ'^*_c) with (b) Bond number (Bo) and (c) density ratio (ρ^*). It may be noted that the angles are normalized by $\pi/2$ rad.

$\theta'/(\pi/2)$ at different Bo. The plots suggest that We_E increases to a maximum with θ'^* before decreasing and the maxima correspond to the critical $We_{E,c}$ and θ'^*_c for the drop migration. The prior-art [143] suggests that for $We_E < We_{E,c}$, there can be a pair of θ'^* for which the facilitating and retarding forces for droplet motion are balanced such that it can attain two metastable equilibria. It may be expected that, upon application of an upward force, the droplet may oscillate back to its first metastable state, till θ'^* is smaller than that of the second metastable state. The droplet will no longer be in equilibrium, if θ'^* exceeds the angle for the second metastable equilibrium and will move into the target fluid.

Figure 4.22(b) shows the variations of the critical electric field Weber number ($We_{\mathrm{E},c}$) and the critical cap angle (θ'^{*}_{c}) with Bo. The plots show that $We_{\mathrm{E},c}$ and θ'^{*}_{c} increase with increasing Bo. The Bo increases with the increase in the drop size (r_{C}), density difference between liquids A and B ($\rho_{\mathrm{B}} - \rho_{\mathrm{A}}$), or decrease in the interfacial tension σ_{AB}. As the size of the droplet increases, the gravitational forces acting on it increase, which leads to an increase in the electric force to maintain a static balance. Similarly, with increase in $\rho_{\mathrm{B}} - \rho_{\mathrm{A}}$, the net weight of the droplet (F_W) increases leading to an increase in $We_{\mathrm{E},c}$. Importantly, the values of $We_{\mathrm{E},c}$ and θ'^{*}_{c} agree reasonably well with the experimental results shown in the image set (b) of figure 4.2, where the droplet is at equilibrium at the interface at $We_{\mathrm{E}} \approx 0.3$. However, when $\rho^{*} = 1$ and $Bo = 0.4$, the theoretical model shows $We_{\mathrm{E},c} = 0.47$, which is significantly lower than the experimental value of $We_{\mathrm{E},c} \approx 2.15$, shown in the image set (a) of figure 4.7. The exclusion of the viscous drag in the static model may be one of the factors behind this anomaly. Inaccuracies related to the measurement of the ultra-low IFT in case of figure 4.7(a), may be another factor behind the imprecise prediction by the static model. Figure 4.22(c) shows the variations of $We_{\mathrm{E},c}$ and θ'^{*}_{c} with the density ratio ρ^{*} at constant Bo. An increase in ρ^{*} increases the net gravitational force (F_W) on the droplet, which in turn causes the necessity of a stronger electric field to maintain a static equilibrium. Therefore, $We_{\mathrm{E},c}$ increases with increasing ρ^{*}.

4.6 Prospective Applications

The results discussed above, reveal that the rupture (silicone oil-oleic acid, $\sigma_{\mathrm{AB}} \approx 0.01$ Nm^{-1}) and tailing (silicone oil-soybean oil, $\sigma_{\mathrm{AB}} \approx 0.001$ Nm^{-1}) modes of droplet transfer, are very distinguishable even under conditions of ultra-low interfacial tensions (μIFT). The μIFTs are often encountered in industrially relevant processes such as enhanced oil recovery [308], emulsions in food industry [309], and microemulsions [310]. Such processes require the accurate measurement of the μIFTs, which is a challenging task. This is because, the conventional methods of Wilhelmy plate and Du Noüy Ring suffer from disadvantages of poor force resolutions at the interface [311]. In the recent past, a host of strategies have been proposed for the accurate determination of μIFTs employing, laser interface manipulation [311], thermal capillary waves [312], optical tweezers [313] and magnetic field [138]. In this context, the proposed phenomena can be a promising method for the determination

of μIFTs. Especially, the rupture mode of droplet motion is expected to provide the critical electric field force required to break the carrier-target interface, following equation (4.30). Subsequently, a calibration can be obtained to develop a correlation between the critical field required to rupture the interface by varying the carrier-target liquids of known interfacial tensions. Finally, the calibration can be employed to determine the interfacial tensions of unknown combinations of carrier-target liquids. The method has some inherent advantages such as, it is simple in operation, does not alter the chemical composition of the liquids by addition of reagents, is cost-effective, and suitable for lab-on-chip applications. The proposed phenomena can also be harnessed for a multitude of applications which include liquid-liquid extraction, separation and purification, micro-reactions, drug encapsulation for drug delivery, and preparation of vesicles.

4.7 Conclusions

The dynamics of an electric field induced droplet migration in an immiscible carrier-target liquid interface have been explored. Experimental investigations are corroborated by three-phase CFD simulations and analytical models. The major findings of the study are,

1. The electric field induced droplet migrations from a carrier to a target liquid can be broadly divided into the rupture and tailing modes, similar to bubbles and solid particles. However, the use of electric field allows an active droplet transport across the carrier-target biphasic interface, which enables a number of novel outcomes. An undeformed droplet at a low electric field migrates slowly and cause a viscosity dominated quasi-static carrier film drainage and rupture. In this situation, the hole radius grows as, $r_{\mathrm{h}} \sim t$, similar to viscosity dominated regime of drop coalescence on a liquid bath. On the other hand, at a higher electric field, a deformed prolate shaped droplet impinges on the interface at a much higher speed to stimulate an inertia dominated carrier film rupture and drainage. The hole-growth kinetics follow a much faster $r_{\mathrm{h}} \sim t^{0.5}$ relation in such a scenario.

2. In the rupture mode, the drainage of the film proceeds in two distinct stages. The rate of film-drainage is faster until the film thickness reduces to $\sim$0.3 times the drop radius, after which there is a significant reduction in the rate

of film drainage. CFD simulations predict similar rates of drainage as the first stage of the experiments. However, for the thinner films, the simulated rates of drainage are significantly higher than the experiments. An analytical model of static film drainage predicts slightly higher rates of carrier film drainage compared to the experiments. The analytical model predicts velocity profiles within the draining film. The profile is found to be nearly parabolic for thicker films, which eventually becomes almost linear with decrease in film thickness, resembling that of Couette flow. The shearing of the moving interfaces at a close proximity results in a constant shear stress profile within the film. This causes the pressure drop in the draining film to be negligibly small, resulting in a linear velocity profile.

3. The tailing mode is observed for very low values of interfacial tensions between the carrier and target phases. In this case, the carrier film ahead of the droplet does not rupture and the drop moves upwards towing a long tail of the carrier liquid. Simulations predict regions of positive vorticity around the rising droplet and negative vorticity fields around the lower receding part of the tail. Both experiments and simulations predict the maximum volume of the carrier liquid entrained by the droplet to be approximately five times the volume of the droplet. The maximum occurs at a distance of approximately eight times the droplet radius from the undisturbed interface.

4. Increase in the density and decrease in the viscosity of the target liquid, increase the droplet velocity after crossing the interface. The decrease in droplet viscosity also increases the overall velocity of the droplet. The rate of film drainage increases with the increase in interfacial tension between the carrier and target phases, decrease in viscosity of the target phase and decrease in the droplet viscosity. The rate of the drainage remains unaffected by the density contrast between the carrier and the target phases. As the interfacial tension between the carrier and target phases increases, the height of the column entrained by the droplet decreases. Decrease in the density and increase in viscosity of the target liquid and increase in the drop viscosity, are found to decrease the height of the column at pinch-off. The maximum volume entrained by the droplet also decreases, under such conditions.

5. Increase in the electric permittivity of the drop increases the deformation of

the drop, without affecting its velocity. In both the rupture and tailing modes, increase in the electric permittivity of the target phase, increases the droplet deformation and velocity. Increase in the permittivity of the carrier phase, however, leads to reduction in droplet velocity. In the tailing mode, changes in the permittivity of the target and carrier phases, lead to significant changes in the column size and shape and hence, the entrained volumes.

6. A quasi-static analytical model predicts the critical electric field required for droplet migration and the critical cap angle, which increases with, (a) increasing density contrast between carrier and target liquids, (b) increasing size of the droplet and (c) increasing the interfacial tension between the carrier and target liquids. The critical electric field also increases with increase in density of the droplet, while the cap angle is not influenced by it.

In summary, the study unveils some unique behaviours of the electric field driven migrations of an aqueous droplet across a carrier-target interface. Such motions can be harnessed for a variety of applications such as liquid-liquid extraction, separation and purification, micro-reactions, tensiometry. In depth analysis with a wider range of liquids along with the study of secondary electric field effects on the migration of drops have been kept as future scope of the research work.

Chapter 5

Mechanisms of Electric Field Mediated Drop Coalescence or Non-coalescence

5.1 Abstract

Experimental investigations with high-speed imaging reveal asymmetric 'cone-cone' to 'cone-groove' deformations of the approaching poles of two uneven sized oppositely charged drops during electro-coalescence/non-coalescence. Three dimensional simulations and an analytical model confirm the occurrence of a third 'groove-groove' configuration at close proximity. Experiments corroborated with simulations show the emergence of asymmetric liquid 'tentacles' on the Taylor cone of the smaller droplet prior to contact.

The contents in this chapter have been submitted for publication as S. Dutta, J. Chaudhuri, P. S. G. Pattader and D. Bandyopadhyay, (2021) 'Asymmetric 'Tentacles' Formation in Coalescing/Non-Coalescing Drops'.

5.2 Introduction

The physics associated with the electric field driven droplet coalescence or non-coalescence has garnered immense scientific curiosity owing to its prevalence in a multitude of processes such as dehydration in petroleum industry [182], ink-jet printing technology [183], electro-wetting [184], chemical and biological assays on lab-on-chip platforms [185], among others. While electro-coalescence studies are centered at the dynamics associated with interstitial film drainage and rupture [122], non-coalescence studies focus on the determination of critical driving conditions and the liquid bridge dynamics [186–191]. After perusal of literature, it can be ascertained that all studies in this front are motivated to explore the critical conditions or bridge dynamics considering symmetric mode of contact between the drops. All existing numerical or analytical models also illustrate the spatiotemporal dynamics of the liquid bridge considering a symmetric contact as an initial condition. Since the drops are seldom equal sized in experiments, it is anticipated that the assumption of symmetric contact may not be always true. Some recent experimental studies report the existence of a symmetric 'cone-cone' mode of contact between uneven sized water droplets in silicone oil and an asymmetric 'cone-dimple' contact in castor oil [187,314]. However, the aspect of asymmetric contact has not been explored in great detail.

In this chapter, we attempt to experimentally uncover the salient features associated with the pre-contact and contact dynamics of two oppositely charged droplets. High resolution three dimensional numerical simulations shed light on the underlying physics associated with the experimental observations. An analytical model relying on general linear stability analysis (GLSA) of a liquid tri-layer under electric field, serves to further substantiate the experimental and numerical observations. The findings may be instrumental in realizing more practical and robust models to accurately map the finer details of the contact phase dynamics of coalescing/non-coalescing drops.

5.3 Experimental Methodology

The experimental set-up shown in figure 5.1(a) contains a well of dimensions 5 mm×5 mm×2 cm ($l \times b \times h$), craved inside poly-dimethyl-siloxane (PDMS, SLYGARD 184 silicone elastomer, Dow Corning) block [266]. For the preparation of the

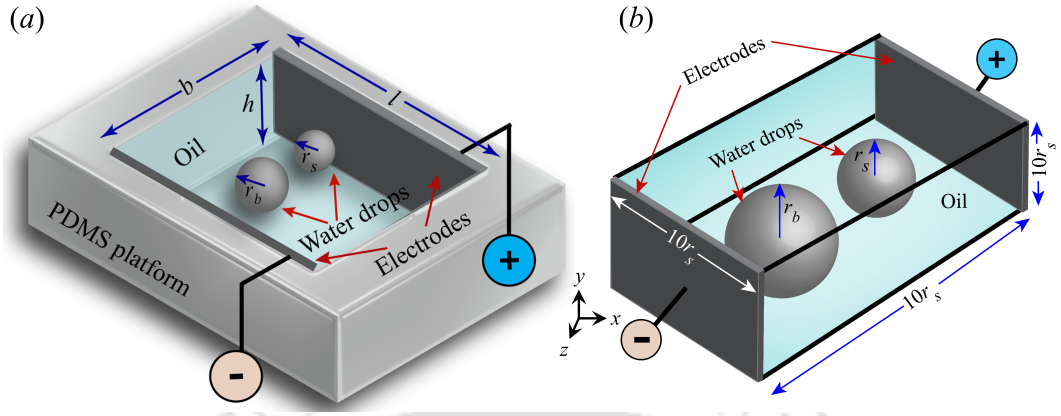

Figure 5.1: (*a*) Schematic diagram of the experimental well 5 mm×5 mm×2 cm ($l \times b \times h$), containing two water droplets suspended inside silicone oil. Aluminium plate electrodes are inserted on two sides of the well for application of electric field via a high voltage DC power source. (*b*) Schematic representation of the three-dimensional (3-D) computational domain for the numerical simulations.

well, a template of the size of the well was fixed on a glass plate and the aluminium electrodes were affixed on its sides. The entire set up was surrounded with double sided tapes and liquid PDMS (mixed with cross linker in 10:1 ratio) was poured into it. Following this, the set-up was cured inside a vacuum oven at 80° C for roughly 3 h. The cured and hardened set-up was then taken out and the templates were carefully removed. The fabricated well was then repeatedly washed with de-ionised water and ethanol and dried. Electric field was applied via the aluminium electrodes with the help of a high voltage direct current (DC) power source (SES Instruments Pvt. Ltd, EHT-II). Silicone oil (Merck, density, $\rho_m \approx 970$ kgm^{-3}, viscosity at 25° C, $\mu_m \approx 0.3$ Pa.s, electrical conductivity, $\sigma_m \approx 10^{-12}$ Sm^{-1} [231], and dielectric constant, $\varepsilon_m \approx 2.7$) was used as the suspending fluid. De-ionised (DI) water (density, $\rho_d \approx 1000$ kgm^{-3}, viscosity at 25° C, $\mu_d \approx 0.001$ Pa.s, electrical conductivity, $\sigma_d \approx 10^{-6}$ Sm^{-1}, and dielectric constant, $\varepsilon_d \approx 80$) was used as the drop phase. The experiments were performed under a microscope (Leica, DM 2500) and recorded using a high-speed camera (Photron, Fastcam Mini UX-100).

5.4 Details of the Numerical Simulations

5.4.1 Computational Domain

A three-dimensional (3-D) computational domain of dimensions $10r_s \times 10r_s \times 10r_s$ was considered for the present analysis. A representative schematic diagram (not to scale) of the computational domain adopted for the study is shown in figure 5.1(b). Two unequal sized water droplets were suspended in the oil phase as shown in the schematic diagram. The radii of the smaller and relatively bigger water droplets were r_s and r_b, respectively. The electric field was applied in the positive z-direction in the computational domain. The drops were assumed to be initially spherical. We have explored the same problem with different domain sizes and found the dynamics to be insensitive to any further increase in the domain size.

5.4.2 Governing Equations

The hydrodynamics of the system considered in the present study are governed by the continuity and incompressible Navier-Stokes equations and the electric field effects are described using the EHD model. In order to track the interface, an advection equation for the volume fraction of a particular fluid, ϕ (which is 1 and 0 for the droplet and surrounding medium, respectively) is solved using the Volume-of-Fluid (VOF) approach. The mutually immiscible fluids are considered to be Newtonian and incompressible, thereby the governing equations of the flow field are given by,

$$\rho\left(\frac{\partial \boldsymbol{v}}{\partial t} + \boldsymbol{v}\cdot\boldsymbol{\nabla}\boldsymbol{v}\right) = -\boldsymbol{\nabla}P + \mu\nabla^2\boldsymbol{v} + \gamma\boldsymbol{\kappa}\boldsymbol{n}\delta\left(\boldsymbol{x}-\boldsymbol{x}_f\right) + \boldsymbol{F}_E, \tag{5.1}$$

$$\boldsymbol{\nabla}\cdot\boldsymbol{v} = 0, \tag{5.2}$$

$$\frac{\partial \phi}{\partial t} + \boldsymbol{\nabla}\cdot(\boldsymbol{v}\phi) = 0. \tag{5.3}$$

Here, $\boldsymbol{v} = (u, v, w)$ represents the velocity field, wherein u, v and w are the components of velocity in x, y and z directions, respectively; t represents time; P denotes the pressure field; $\boldsymbol{\kappa}\,(\equiv \boldsymbol{\nabla}\cdot\boldsymbol{n})$ is the curvature of the interface, wherein $\boldsymbol{n}\,(\equiv \boldsymbol{\nabla}\phi/|\boldsymbol{\nabla}\phi|)$ is the unit normal pointing outward of the interface. The function $\delta\left(\boldsymbol{x}-\boldsymbol{x}_f\right)$, is a delta function (denoted by δ hereafter) that is zero everywhere except at the interface, where, $\boldsymbol{x} = \boldsymbol{x}_f$ is the position vector of a point at the interface.

The Gauss's law can be written in terms of the electric displacement ($\boldsymbol{D} = \varepsilon_0 \varepsilon \boldsymbol{E}$) as, $\boldsymbol{\nabla} \cdot \boldsymbol{D} = \boldsymbol{\nabla} \cdot (\varepsilon_0 \varepsilon \boldsymbol{E}) = q$, where, q and ε denotes the volumetric charge density, and dielectric constants of the fluids, respectively. In the absence of magnetic field, the Maxwell Faraday equation can be simplified to, $\boldsymbol{\nabla} \times \boldsymbol{E} = 0$, which signifies that the electric field is irrotational. In that case, the electric field can be written in terms of electric potential as, $\boldsymbol{E} = -\boldsymbol{\nabla}\psi$. For leaky dielectric liquids, the Gauss's law can be rewritten in terms of electric potential as, $\boldsymbol{\nabla} \cdot (\varepsilon_0 \varepsilon \boldsymbol{\nabla}\psi) = -q$. The volumetric charge density q is governed by the balance of ohmic conduction and convection of charges in the following form,

$$\frac{\partial q}{\partial t} + \boldsymbol{\nabla} \cdot (\boldsymbol{v} q) = -\boldsymbol{\nabla} \cdot (\sigma \boldsymbol{E}) \,. \tag{5.4}$$

For leaky dielectric fluids, the electrical relaxation time scale is significantly smaller than the time scale of fluid motion and hence the charge accumulates at the interface almost instantaneously. Therefore, for a quasi-static system, equation (5.4) can be simplified as,

$$\frac{\partial q}{\partial t} + \boldsymbol{\nabla} \cdot (\sigma \boldsymbol{E}) = 0. \tag{5.5}$$

The effect of the electric field is incorporated into the momentum equation (equation (5.1)) by the volumetric electrostatic force ($\boldsymbol{F}_E$) expressed as,

$$\boldsymbol{F}_E = \boldsymbol{\nabla} \cdot \boldsymbol{\tau}_e = \boldsymbol{\nabla} \cdot \left[\varepsilon_0 \varepsilon_i \left\{ \boldsymbol{E}_i \otimes \boldsymbol{E}_i - \frac{1}{2} (\boldsymbol{E}_i \cdot \boldsymbol{E}_i) \mathbf{I} \right\} \right]. \tag{5.6}$$

The first term in the right-hand side of the equation (5.6) represents the Columbic force which acts between the free charges present in the system. The second term denotes the dielectric force, which is generated due to the polarization of the fluid medium. The third term in the right-hand side of equation (5.6) is termed as electrostrictive force, which is included with the pressure term in Navier-Stokes equation in equation (5.1) due to the assumption of incompressibility of the liquids [315].

5.4.3 Non-dimensional Governing Equations

Considering diameter of the smaller drop ($2r_s$) to be the characteristic length scale and U (to be discussed later) to be the characteristic velocity of the drops, the

dimensionless variables can be expressed as,

$$x = 2x'r_s, y = 2y'r_s, z = 2z'r_s, t = 2t'\left(\frac{r_s}{U}\right), \boldsymbol{v} = \boldsymbol{v}U, P = P'\left(\rho_d U^2\right), \delta = \frac{\delta'}{2r_s},$$
$$\boldsymbol{E} = \boldsymbol{E'}E_0, \psi = \psi'\Psi_0, q = q'q_0, \rho = \rho'\rho_m, \mu = \mu'\mu_m, \varepsilon = \varepsilon'\varepsilon_m, \text{ and } \sigma = \sigma'\sigma_m. \quad (5.7)$$

Removing the prime ($\prime$) notations, we get the dimensionless forms of the governing equations as,

$$\rho\left(\frac{\partial \boldsymbol{v}}{\partial t} + \boldsymbol{v}\cdot\boldsymbol{\nabla}\boldsymbol{v}\right) = -\boldsymbol{\nabla}P + \frac{1}{Re}\mu\nabla^2\boldsymbol{v} + \frac{1}{We}\boldsymbol{\kappa}\boldsymbol{n}\delta + \frac{Ca_E}{We}\varepsilon_0\left[\boldsymbol{\nabla}\cdot(\varepsilon\boldsymbol{E})\,\boldsymbol{E} - \frac{1}{2}|\boldsymbol{E}|^2\boldsymbol{\nabla}\varepsilon\right], \quad (5.8)$$

$$\boldsymbol{\nabla}\cdot\boldsymbol{v} = 0, \quad (5.9)$$

$$\frac{\partial \phi}{\partial t} + \boldsymbol{\nabla}\cdot(\boldsymbol{v}\phi) = 0, \quad (5.10)$$

$$\frac{\partial q}{\partial t} + \frac{1}{R_E}\boldsymbol{\nabla}\cdot(\sigma\boldsymbol{E}) = 0. \quad (5.11)$$

The fluid properties (ρ, μ, ε and σ) are evaluated using the weighted average method as [316], $\Sigma = \Sigma_d\phi + \Sigma_m(1-\phi) = \left(\frac{\Sigma_d}{\Sigma_m}\right)\phi + (1-\phi) = \Sigma_r\phi + (1-\phi)$. Here, $\Sigma_r = \frac{\Sigma_d}{\Sigma_m}$ is the ratio of the fluid properties. The dimensionless numbers are defined as, $Re = \frac{2\rho_m U r_s}{\mu_m}$, $We = \frac{2\rho_m U^2 r_s}{\gamma}$, $R_E = \frac{U q_0}{E_0\sigma_m}$ and $Ca_E = \frac{2\varepsilon_0\varepsilon_m E_0^2 r_s}{\gamma}$. The characteristic velocity (U) or the advection of the droplet can be estimated as [292], $U = \frac{2\varepsilon_0\varepsilon_m E_0^2 r_s}{\mu_m} = \frac{2\varepsilon_0\varepsilon_m E_0^2 r_s}{\gamma}\left(\frac{\gamma}{\mu_m}\right) = Ca_E\left(\frac{\gamma}{\mu_m}\right) \approx O\left(10^{-2}\right)$. Since, the order of magnitude of U is small in this case, we can safely assume that, $O(Re)$ and $O(We)$ is relatively small in our case.

5.4.4 Boundary Conditions

The initial and boundary conditions implemented to solve the governing equations were such that, in the beginning (at $t = 0$), both the surrounding medium and the liquid droplets were considered to be static. No slip and impermeability conditions were applied at the walls ($u = v = w = 0$). The external electric field was applied by imposing constant voltage boundary conditions with $\psi = \Psi_0$ at the top wall ($z = H$) of the computational domain, while the lower wall ($z = 0$) was grounded ($\psi = 0$). With respect to the electric field, free slip boundary conditions ($\partial\psi/\partial x =$

$\partial\psi/\partial y = 0$) were applied to all the other walls of the domain.

5.4.5 Solution Methodology

A volume-of-fluid (VOF) method with dynamic adaptive grid refinement over the droplet interface was employed to simulate the EHD deformation of the liquid droplets. The finite volume open source code GERRIS [317] was used to carry out the numerical simulations which employs a staggered grid approach with second order accuracy in space and time. All the scalar variables and the vector components were defined at the cell-centers and the cell faces, respectively. The temporal discretization was handled by the fractional-step projection method, whereas, the advection terms were discretized using a second-order upwind scheme. A height function based balanced continuum-surface force formulation was incorporated to model the effect of surface tension [293]. GERRIS is capable of minimizing the amplitude of spurious currents, scaled with $(r_s/\gamma)^{0.5}$ where γ is the surface tension coefficient, to less than 10^{-12} as compared with other numerical simulations employing level-set (LS) [318], CLSVOF [319] and front tracking [320]. The EHD toolbox available in the code architecture was also used in order to model the influence of the applied electric field. Moreover, a dynamic load balancing algorithm was incorporated in the solver to efficiently distribute the computational load across the processors during the course of the simulations. The solver is equipped with the adaptive mesh refinement (AMR) technique, which provides a large number of grid points/cells over the interface separating the fluids, while keeping a relatively coarser grid elsewhere, thereby optimizing the computational load and time.

5.4.6 Grid Convergence Study

The mesh refinement was done based on the gradient of volume fraction along with the volume fraction function itself. The smallest dimensionless cell sizes corresponding to grid levels 9, 10, 11, and 12 were 1.953×10^{-3}, 0.976×10^{-3}, 0.488×10^{-3}, and 0.245×10^{-3}, respectively. A detailed grid refinement study revealed that a minimum cell size about 1000 times smaller than the drop radius corresponding to level 9 refinement was necessary to observe the finer details. However, a much finer grid was needed to reproduce the evolution of the finer 'tentacles'. This was accomplished using up to 12 levels of grid refinement, which means separating the domain locally into two smaller cells 12 times in each direction (the size of the smallest cell is

212 times smaller than the domain). In our simulations, this corresponds to ~ 5000 cells per drop radius. At this level of refinement, an equivalent uniform grid would have more than 68 billion cells $[(2^{12})^3]$, while our simulation had of the order of 1 billion cells which reduced the overall computational load. The minimum level of refinement in the domain was kept at 9, equivalent to a uniform grid of 512×512 cells. The results in the main manuscript are at level 12, calculated on 8 processors and 64 CPU cores, thereby allowing a systematic investigation of the parameter space.

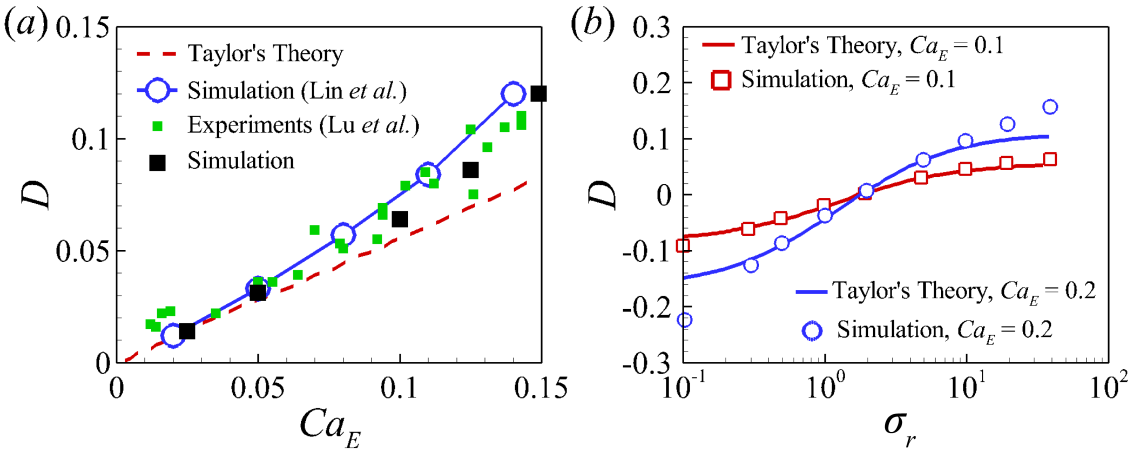

Figure 5.2: Deformation (D) of droplet under electric field with the variation of (a) Ca_E and (b) σ_r, respectively. The parameters associated with the simulations are, $\rho_r = 1$, $\mu_r = 0.003$, $\varepsilon_r = 26.67$, $\sigma_r = 1000$ for (a), $Re = 0.067$, and $R_E = 0.1$.

5.4.7 Model Validation

Although this solver has been validated extensively for simulating a wide range of complex fluid flow problems involving bubbles and drops, the numerical scheme adopted for the present study is validated thoroughly by comparing our results with prior literatures. For validation of the present numerical model, we consider a discrete liquid-droplet of radius r_s suspended in a continuous medium. The DC electric field with varying intensities (E_0) are introduced to the system along the z-direction. The electric field induced deformation of a liquid-droplet suspended in the continuous medium is assisted by the EHD stresses at the liquid-liquid interface originating from the accumulations of, (i) induced charges across the interface owing to the dielectric contrast ($\varepsilon_r = \varepsilon_d/\varepsilon_m$) and (ii) free charges owing to the difference in the

electrical conductivities ($\sigma_r = \sigma_d/\sigma$) of the liquid mediums. In this formulation, the subscripts 'd' and 'm' represent disperse and continuous medium, respectively. The presence of the electric field introduces Maxwell stresses along the interface, which facilitates the small and large deformations depending on the applied electric field intensity. The components of capillary forces at the interface aid as well as oppose the deformation depending upon the sign of the radius of curvature of the interface. The interplay between the surface tension, Maxwell stresses, inertial forces, and viscous stresses decides the final shape of droplet.

It may be noted here that the deformation of the droplet (D) can be analytically evaluated from the leaky dielectric model of Taylor as [321], $D = (L-W)/(L+W) = 0.56Ca_E f(\sigma_r, \varepsilon_r, \mu_r)/(2+\sigma_r)^2$, where the notations L and W represent the length and width of the deformed droplet, respectively. The electrical capillary number is defined as, $Ca_E = 2r_s\varepsilon_0\varepsilon_m E_0^2/\gamma$ and $f(\sigma_r, \varepsilon_r, \mu_r) = \sigma_r^2 + 1 - 2\varepsilon_r + 0.6(\sigma_r - \varepsilon_r)(2 + 3\mu_r)/(1+\mu_r)$ is the Taylor's 'discriminating function' [321]. In particular, Taylor's theory suggests that a droplet can easily deform into a prolate ($D > 0$) or oblate ($D < 0$) shape with the variations in E_0, γ, σ_r, and ε_r, under the influence of an external electric field. Figure 5.2 shows the accuracy of the present numerical model in predicting the deformation of the discrete droplet for varying Ca_E and σ_r with the deformations obtained from the analytical calculations of Taylors theory [321], experiments, and numerical results [322].

5.5 Details of the General Linear Stability Analysis (GLSA)

Figure 5.3 shows the schematic representation of three layers of liquids that are places between two electrodes. One of the electrodes is connected to the positive terminal of a voltage source while the other is grounded. The linear stability analysis is carried with a cartesian coordinate system as the reference frame, with the x and z axes perpendicular to each other on the same plane. The distance between the electrodes is d. The base state heights of the lower and upper interfaces without application of electric field are $h_{1,0}$ and $h_{2,0}$, respectively, from the lower electrode at $z = 0$. On application of electric field, the perturbed heights of the lower and upper interfaces are denoted by $h_1(x,t)$ and $h_2(x,t)$, respectively. The parameters ρ_i, μ_i, σ_i and ε_i ($i = 1, 2, 3$) denote the density, viscosity, conductivity and dielectric constants of the liquids, respectively. The interfacial tensions of the lower and upper interfaces are denoted by γ_{12} and γ_{23}, respectively.

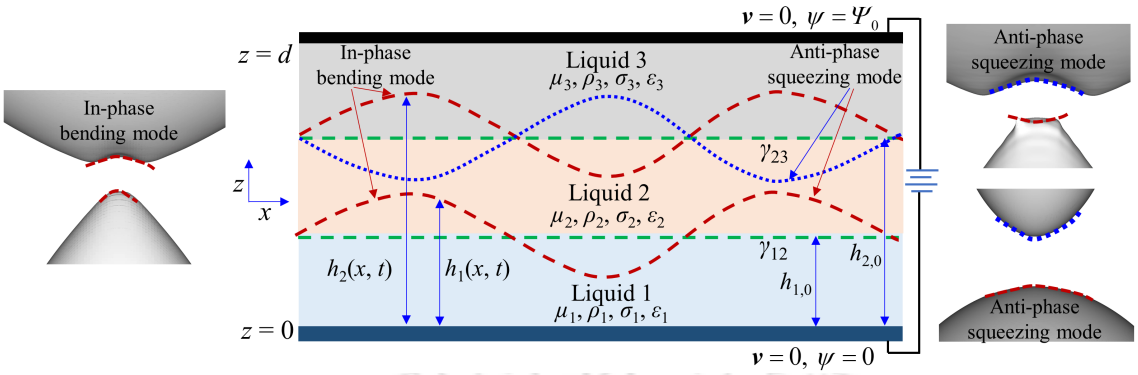

Figure 5.3: Schematic representation of a tri-layer of leaky dielectric fluids sandwiched between an anode ($\psi = \Psi_0$) and a cathode ($\psi = 0$) that are located at a distance of d apart. The base distances of the lower and upper interfaces are located at heights $h_{1,0}$ and $h_{2,0}$ from the cathode at $z = 0$. The perturbed heights of the lower and upper interfaces are denoted by $h_1(x,t)$ and $h_2(x,t)$, respectively.

5.5.1 Governing Equations and Boundary Conditions

5.5.1.1 Electric Field

The irrotational electric field ($\boldsymbol{E}_i = -\boldsymbol{\nabla}\psi_i$) inside the fluids considering electroneutrality are governed by the Laplace's equation as,

$$\nabla^2\psi_i = 0. \tag{5.12}$$

Here, ψ_i represents the electric potential. The boundary conditions used for solving the electric field are: (i) Dirichlet boundary conditions at the anode and the cathode: at $z = 0$, $\psi_1 = 0$ and at $z = d$, $\psi_3 = \Psi_0$, (ii) At the interfaces the normal components of electric fields satisfy: at $z = h_1$, $\{(-\varepsilon_0\varepsilon_2\boldsymbol{\nabla}\psi_2) - (-\varepsilon_0\varepsilon_1\boldsymbol{\nabla}\psi_1)\} \cdot \boldsymbol{n}_1 = q_1$ and at $z = h_2$, $\{(-\varepsilon_0\varepsilon_3\boldsymbol{\nabla}\psi_3) - (-\varepsilon_0\varepsilon_2\boldsymbol{\nabla}\psi_2)\} \cdot \boldsymbol{n}_2 = q_2$, (iii) The continuity of the tangential components of the electric fields at the interfaces give: at $z = h_1$, $\psi_1 = \psi_2$ and $z = h_2$, $\psi_2 = \psi_3$. Here, $\boldsymbol{n}_i$ represents the unit normal vector to the interface.

5.5.1.2 Electro-hydrodynamic Field

Considering the liquids to be Newtonian and incompressible, the flow field is defined by the continuity and momentum equations neglecting gravity and acceleration as,

$$\boldsymbol{\nabla} \cdot \boldsymbol{v}_i = 0, \tag{5.13}$$

$$-\boldsymbol{\nabla} P_i + \boldsymbol{\nabla} \cdot (\boldsymbol{\tau}_{h,i} + \boldsymbol{\tau}_{e,i}) = 0. \tag{5.14}$$

Here, $\boldsymbol{v}_i$ denote the velocity vector with u_i and v_i as the x and z components, respectively and P_i denote the pressure. The term $\boldsymbol{\tau}_{h,i} = \mu_i \left(\boldsymbol{\nabla} \boldsymbol{v}_i + \boldsymbol{\nabla} \boldsymbol{v}_i{}^{\mathrm{T}}\right)$ denotes the hydrodynamic stress tensor. The term $\boldsymbol{\tau}_{e,i} = \varepsilon_0 \varepsilon_i \left[\boldsymbol{E}_i \otimes \boldsymbol{E}_i - 0.5 \left(\boldsymbol{E}_i \cdot \boldsymbol{E}_i\right) \mathbf{I}\right]$ denotes the Maxwell stress tensor and acts only at the interfaces between the fluids. For the solution of the flow field the following boundary conditions are enforced.

(i) No-slip velocity boundary conditions at the electrodes:

at $z = 0$, $\boldsymbol{v}_1 = 0$ and at $z = d$, $\boldsymbol{v}_3 = 0$.

(ii) Continuity of velocities at the interfaces:

at $z = h_1$, $\boldsymbol{v}_1 = \boldsymbol{v}_2$ and at $z = h_2$, $\boldsymbol{v}_2 = \boldsymbol{v}_3$.

(iii) Tangential stress balance at the interfaces:

at $z = h_1$, $\boldsymbol{t}_1 \cdot (\boldsymbol{\tau}_{h,1} + \boldsymbol{\tau}_{e,1}) \cdot \boldsymbol{n}_1 = \boldsymbol{t}_1 \cdot (\boldsymbol{\tau}_{h,2} + \boldsymbol{\tau}_{e,2}) \cdot \boldsymbol{n}_1$ and,

at $z = h_2$, $\boldsymbol{t}_2 \cdot (\boldsymbol{\tau}_{h,2} + \boldsymbol{\tau}_{e,2}) \cdot \boldsymbol{n}_2 = \boldsymbol{t}_2 \cdot (\boldsymbol{\tau}_{h,3} + \boldsymbol{\tau}_{e,3}) \cdot \boldsymbol{n}_2$. Here, $\boldsymbol{t}_i$ represents the unit tangent to the interface.

(iv) Normal stress balances at the interfaces give:

at $z = h_1$,

$\{-p_2 \mathbf{I} + \boldsymbol{n}_1 \cdot (\boldsymbol{\tau}_{h,2} + \boldsymbol{\tau}_{e,2}) \cdot \boldsymbol{n}_1\} - \{-p_1 \mathbf{I} + \boldsymbol{n}_1 \cdot (\boldsymbol{\tau}_{h,1} + \boldsymbol{\tau}_{e,1}) \cdot \boldsymbol{n}_1\} = \gamma_{12} \boldsymbol{\nabla} \cdot \boldsymbol{n}_1$ and,

at $z = h_2$,

$\{-p_3 \mathbf{I} + \boldsymbol{n}_2 \cdot (\boldsymbol{\tau}_{h,3} + \boldsymbol{\tau}_{e,3}) \cdot \boldsymbol{n}_2\} - \{-p_2 \mathbf{I} + \boldsymbol{n}_2 \cdot (\boldsymbol{\tau}_{h,2} + \boldsymbol{\tau}_{e,2}) \cdot \boldsymbol{n}_2\} = \gamma_{23} \boldsymbol{\nabla} \cdot \boldsymbol{n}_2$.

(v) The kinematic conditions for the evolution of the interfaces take the form:

at $z = h_1$, $\dfrac{\partial h_1}{\partial t} + u_1 \dfrac{\partial h_1}{\partial x} = w_1$ and at $z = h_2$, $\dfrac{\partial h_2}{\partial t} + u_2 \dfrac{\partial h_2}{\partial x} = w_2$.

(vi)The conservation equations of the interfacial charge are given by:

at $z = h_1$, $\dfrac{\partial q_1}{\partial t} + \boldsymbol{v}_1 \boldsymbol{\nabla}_S q_1 - q_1 \boldsymbol{n}_1 \cdot (\boldsymbol{n}_1 \cdot \boldsymbol{\nabla}) \boldsymbol{v}_1 = (\sigma_1 \boldsymbol{E}_1 - \sigma_2 \boldsymbol{E}_2) \cdot \boldsymbol{n}_1$ and,

at $z = h_2$, $\dfrac{\partial q_2}{\partial t} + \boldsymbol{v}_2 \boldsymbol{\nabla}_S q_2 - q_2 \boldsymbol{n}_2 \cdot (\boldsymbol{n}_2 \cdot \boldsymbol{\nabla}) \boldsymbol{v}_2 = (\sigma_2 \boldsymbol{E}_2 - \sigma_3 \boldsymbol{E}_3) \cdot \boldsymbol{n}_2$.

5.5.2 Linear Stability Analysis

In order to carry out a general linear stability analysis (GLSA), the flow and electric variables are expressed by the following linear modes:

$$[u_i, w_i, P_i, h_i, q_i, \psi_i] = [0, 0, P_{i,0}, h_{i,0}, q_{i,0}, \psi_{i,0}] + \left[\tilde{u}_i, \tilde{w}_i, \tilde{P}_i, \tilde{h}_i, \tilde{q}_i, \tilde{\psi}_i\right] \mathrm{e}^{\omega t + \mathrm{i} k x}. \tag{5.15}$$

Here, the variables with subscript '0' denote the base state parameters and the those with subscript 'tilde' are the perturbed variables. The term ω denotes the growth

coefficient of the perturbations and k denotes the wavenumber.

5.5.2.1 Base State Analysis

The Laplace's equation 5.12 in the base state is given by,

$$\psi''_{i,0} = 0. \tag{5.16}$$

Here, 'dash' represents derivative w.r.t z. The solution of equation 5.16 can be written as,

$$\psi_{i,0} = A_i z + B_i. \tag{5.17}$$

The coefficients A_i $(i = 1, 2, 3)$ and B_i $(i = 1, 2, 3)$ along with the base state charge $q_{i,0}$ are evaluated using the boundary conditions:
(i) At $z = 0$, $\psi_{1,0} = 0$ and at $z = d$, $\psi_{3,0} = \Psi_0$.
(ii) At $z = h_{1,0}$, $\varepsilon_0\varepsilon_1\psi'_{1,0} - \varepsilon_0\varepsilon_2\psi'_{2,0} = q_{1,0}$ and at $z = h_2$, $\varepsilon_0\varepsilon_2\psi'_{2,0} - \varepsilon_0\varepsilon_3\psi'_{3,0} = q_{2,0}$.
(iii) At $z = h_{1,0}$, $\psi_{1,0} = \psi_{2,0}$ and at $z = h_{2,0}$, $\psi_{2,0} = \psi_{3,0}$.
(iv) At $z = h_{1,0}$, $\sigma_1\psi'_{1,0} - \sigma_2\psi'_{2,0} = 0$ and at $z = h_{2,0}$, $\sigma_2\psi'_{2,0} - \sigma_3\psi'_{3,0} = 0$.
In the present study, layer 2 is considered to be non-conducting as it represents the silicon oil layer between the water droplets. Thus, $\sigma_2 = 0$ and conditions shown in (iv) reduce to: at $z = h_{1,0}$, $\psi'_{1,0} = 0$ and at $z = h_{2,0}$, $\psi'_{3,0} = 0$. On solving the system of equations, the values obtained are: $A_1 = 0$, $A_2 = \dfrac{-\Psi_0}{h_{1,0} - h_{2,0}}$, $A_3 = 0$, $B_1 = 0$, $B_2 = \dfrac{\Psi_0}{h_{1,0} - h_{2,0}}$, $B_3 = \Psi_0$, $q_{1,0} = \dfrac{\varepsilon_0\varepsilon_2\,\Psi_0}{h_{1,0} - h_{2,0}}$, and $q_{2,0} = \dfrac{-\varepsilon_0\varepsilon_2\,\Psi_0}{h_{1,0} - h_{2,0}}$.

5.5.2.2 Perturbed State Analysis

The linearized perturbed form of the Laplace's equation (5.12) can be written as,

$$\tilde{\psi}''_i - k^2\tilde{\psi}_i = 0. \tag{5.18}$$

The general solution of equation (5.18) is given by,

$$\tilde{\psi}_i = C_i e^{kz} + D_i e^{-kz}. \tag{5.19}$$

The coefficients $C_i (i = 1, 2, 3)$ and $D_i (i = 1, 2, 3)$ are evaluated from the following boundary conditions,

(i) At, $z = 0$, $\tilde{\psi}_1 = 0$ and at $z = d$, $\tilde{\psi}_3 = 0$.
(ii) At, $z = h_{1,0}$, $\varepsilon_0\varepsilon_1\tilde{\psi}'_1 - \varepsilon_0\varepsilon_2\tilde{\psi}'_2 = \tilde{q}_1$ and at, $z = h_{2,0}$, $\varepsilon_0\varepsilon_2\tilde{\psi}'_2 - \varepsilon_0\varepsilon_3\tilde{\psi}'_3 = \tilde{q}_2$
(iii) At, $z = h_{1,0}$, $(\tilde{\psi}_1 - \tilde{\psi}_2) = \tilde{h}_1\left(\psi'_{2,0} - \psi'_{1,0}\right)$, and,
at $z = h_{2,0}$, $(\tilde{\psi}_2 - \tilde{\psi}_3) = \tilde{h}_2\left(\psi'_{3,0} - \psi'_{2,0}\right)$
The linearized perturbed form of the kinematic condition of the evolution of the height at the interface $z = h_{i,0}$ becomes,

$$\tilde{h}_i = \frac{\tilde{w}_i}{\omega}. \tag{5.20}$$

The conservation of interfacial charge at the interface $z = h_{i,0}$ in the linearized perturbed form can be written as,

$$\tilde{q}_i = \frac{1}{\omega}\left(\sigma_{i+1}\tilde{\psi}'_{i+1} - \sigma_i\tilde{\psi}'_i - \mathrm{i}kq_{i,0}\tilde{u}_i\right). \tag{5.21}$$

The linearized perturbed forms of the continuity and the x and z directional momentum equations are given by,

$$\tilde{u}_i = \frac{-\tilde{w}'_i}{\mathrm{i}k}, \tag{5.22}$$

$$-\mathrm{i}k\tilde{P}_i + \mu_i\left(\tilde{u}''_i - k^2\tilde{u}_i\right) = 0, \tag{5.23}$$

$$-\tilde{P}'_i + \mu_i\left(\tilde{w}''_i - k^2\tilde{w}_i\right) = 0. \tag{5.24}$$

On eliminating $\tilde{P}_i$, eqs. (5.22–5.24) reduce to the following biharmonic equation,

$$\tilde{w}''''_i - 2k^2\tilde{w}''_i + k^4\tilde{w}_i = 0. \tag{5.25}$$

Equation (5.25) has a general solution of the form,

$$\tilde{w}_i = (F_i + G_iz)\,e^{kz} + (H_i + J_iz)\,e^{-kz}. \tag{5.26}$$

The coefficients $F_i(i = 1, 2, 3)$, $G_i(i = 1, 2, 3)$, $H_i(i = 1, 2, 3)$, and $J_i(i = 1, 2, 3)$ are evaluated from the following boundary conditions,
(i) At $z = 0$, $\tilde{u}_1 = \tilde{w}_1 = 0$ and at $z = d$, $\tilde{u}_3 = \tilde{w}_3 = 0$.
(ii) At $z = h_1$, $\tilde{u}_1 = \tilde{u}_2$, $\tilde{w}_1 = \tilde{w}_2$ and at $z = h_2$, $\tilde{u}_2 = \tilde{u}_3$, $\tilde{w}_2 = \tilde{w}_3$.
(iii) Continuity of tangential stress at the interfaces give,
at $z = h_1$,

$\mu_1\left(\tilde{u}_1' + \mathrm{i}k\tilde{w}_1\right) - \mu_2\left(\tilde{u}_2' + \mathrm{i}k\tilde{w}_2\right) + \mathrm{i}k\varepsilon_0\left(\varepsilon_1\psi_{1,0}'\tilde{\psi}_1 - \varepsilon_2\psi_{2,0}'\tilde{\psi}_2 + \varepsilon_1\psi_{1,0}'^2\tilde{h}_1 - \varepsilon_2\psi_{2,0}'^2\tilde{h}_1\right) = 0,$

at $z = h_2$,

$\mu_2\left(\tilde{u}_2' + \mathrm{i}k\tilde{w}_2\right) - \mu_3\left(\tilde{u}_3' + \mathrm{i}k\tilde{w}_3\right) + \mathrm{i}k\varepsilon_0\left(\varepsilon_2\psi_{2,0}'\tilde{\psi}_2 - \varepsilon_3\psi_{3,0}'\tilde{\psi}_3 + \varepsilon_2\psi_{2,0}'^2\tilde{h}_2 - \varepsilon_3\psi_{3,0}'^2\tilde{h}_2\right) = 0.$

(iv)) Normal stress balance at the interfaces yield,

at $z = h_1$, $\tilde{P}_1 - \tilde{P}_2 + 2\mu_2\tilde{w}_2' - 2\mu_1\tilde{w}_1' + \varepsilon_0\left(\varepsilon_2\psi_{2,0}'\tilde{\psi}_2' - \varepsilon_1\psi_{1,0}'\tilde{\psi}_1'\right) - k^2\gamma_{12}\tilde{h}_1 = 0,$

at $z = h_2$, $\tilde{P}_2 - \tilde{P}_3 + 2\mu_3\tilde{w}_3' - 2\mu_2\tilde{w}_2' + \varepsilon_0\left(\varepsilon_3\psi_{3,0}'\tilde{\psi}_3' - \varepsilon_2\psi_{2,0}'\tilde{\psi}_2'\right) - k^2\gamma_{23}\tilde{h}_2 = 0.$

On substituting the general solutions of $\tilde{u}_i$, $\tilde{w}_i$, and $\tilde{P}_i$ obtained from eqs. (5.22–5.26) in the 12 boundary conditions mentioned from (i)−(iv) and using equations (5.20) and (5.21), a set of 12 homogenous linear algebraic equations are obtained in terms of the 12 coefficients $F_i(i = 1, 2, 3)$, $G_i(i = 1, 2, 3)$, $H_i(i = 1, 2, 3)$, and $J_i(i = 1, 2, 3)$. The dispersion relation $\omega = f(k)$ is obtained by the equating the determinant of the coefficient matrix of the 12 linear equations to zero. For the sake of brevity, the dispersion relation is not supplied with the text. The algebraic operations are performed with the aid of the commercial software package MATHEMATICA™.

5.6 Results and Discussion

Under the action of electric field, the droplets gather charge from the contacting electrodes and during their motion towards the opposite electrode they either coalesce or bounce off depending on the strength of the applied electric field [305]. Using high speed imaging, we aim to disclose the pre-contact and contact dynamics of such phenomena.

The sequences of experimental micrographs shown in figure 5.4$(a - c)$ demonstrate the formation and subsequent break-up of the bridge between two de-ionised (DI) water drops suspended in silicone oil at different electric field intensities. Post contact between the oppositely charged droplets, a liquid bridge is formed between them which grows up to a critical diameter before shrinking and eventually pinching-off. The comparisons of the time scales of the process at electric fields of 4 kVcm^{-1}, 5 kVcm^{-1} and 6 kVcm^{-1} shown in image panels (a), (b) and (c), respectively, suggest that electric field intensifies the formation and subsequent break-up of the bridge formed between the droplets. Figure 5.5(a) shows the variation of the tangent of the cone angle (α) with the electric field capillary number (Ca_E) for the contact between

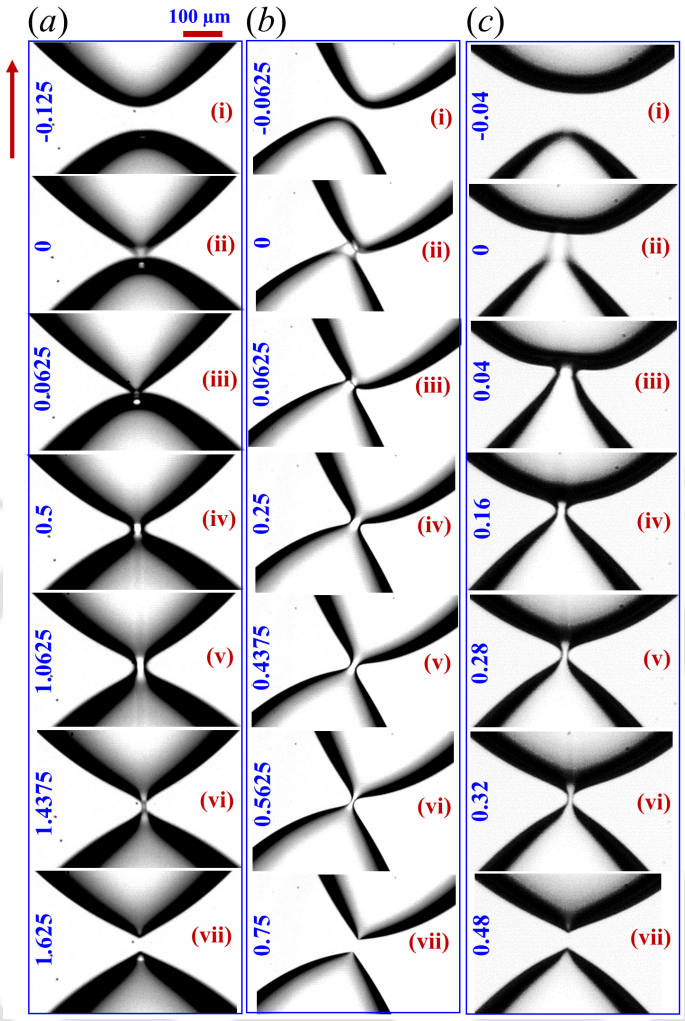

Figure 5.4: Experimental micrographs demonstrating the formation and pinch-off of the liquid bridge between two DI water droplets suspended in silicone oil at electric field intensity of (*a*) 4 kVcm^{-1}, (*b*) 5 kVcm^{-1}, and (*c*) 6 kVcm^{-1}. The arrow demonstrates the direction of the electric field. The time shown on each image has unit of milliseconds.

two water drops immersed in silicon oil. The variation of the bridge radius (r_{bridge}) formed between the drops with time is shown in figure 5.5(*b*). Beyond a critical electric field, the cone angle α at contact between the droplets reaches a value which creates positive capillary pressure within the bridge. The liquid inside the bridge is then pumped towards the bulk of the droplet, leading to bridge break-up and subsequent drop non-coalescence [186–188]. Figure 5.5(*a*) suggests the critical angle for non-coalescence to be approximately 20° which is fairly similar to the observations of Anand *et al.* [187]. The cone angle is found to follow a rule in accordance with

the observations of Ristenpart *et al.* [186].

Images (i) and (ii) of each panel and particularly panel (*c*) suggest marked

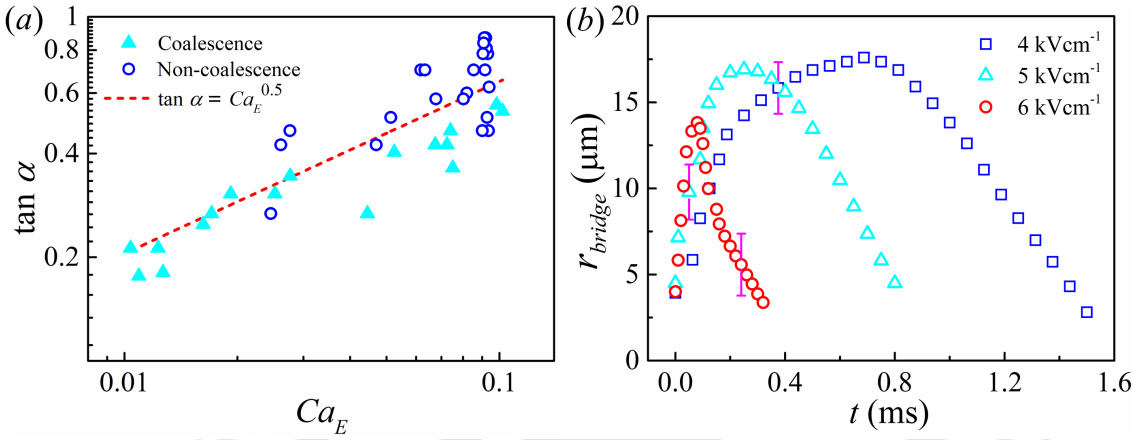

Figure 5.5: Variation of the (*a*) tangent of the cone angle (α) with the electric field capillary number (Ca_E) and (*b*) the radius of the liquid bridge (r_b) with time during contact of two oppositely charged water droplets moving inside silicone oil.

asymmetry of the approaching ends of the droplets. The drops at contact assume a 'lock and key' type of configuration as the protruding edge of one drop indents the other. Such asymmetric contact between unevenly sized droplets has been recently observed during non-coalescence of water drops in castor oil [187, 191]. In case of the drops suspended in silicone oil, Anand *et al.* (2019), however reports symmetric 'cone-cone' configuration in the pre-contact phase for unevenly sized drops [187, 314]. They hypothesize that the lower conductivity of silicone oil compared to castor oil causes relatively lesser charge loss from the poles of the droplets in the pre-contact phase. Thus, a greater electrostatic attractive force exists between the droplets with silicone oil in the interstitial gap compared to castor oil, which leads to the droplets assuming a symmetric 'cone-cone' configuration in the former and a 'cone-dimple' configuration in the later. The results shown in the figure 5.4 however, are contradictory, wherein the uneven sized water drops suspended in silicone oil medium also show asymmetric 'cone-cone' (C−C) configuration in the pre-contact phase. This observation hints at the possible role of the asymmetry of the droplet sizes (and hence droplet charges) rather than the conductivity of the surrounding medium, on the pre and contact phase dynamics of the droplets.

Figure 5.6 demonstrates the pre-contact and contact configurations assumed by two unequal sized oppositely charged droplets under electric field. Images (i)

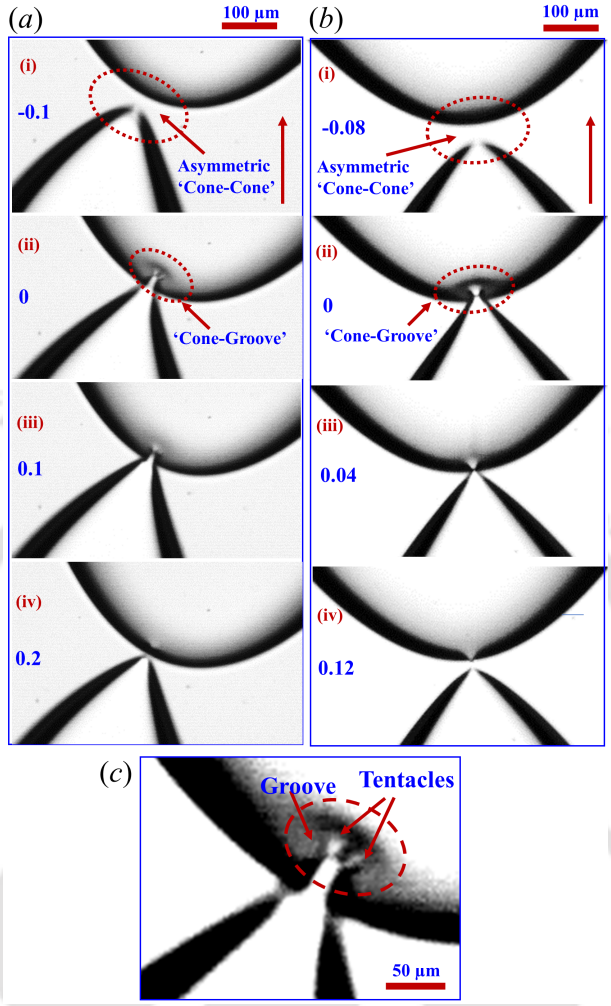

Figure 5.6: Time sequence experimental micrographs demonstrating the pre-contact and contact dynamics of two asymmetrical water droplets suspended in silicone oil at electric field intensity of (*a*) 5.5 kVcm^{-1}, and (*b*) 6.5 kVcm^{-1}. The arrows on the first images demonstrate the direction of the electric field. The time shown on each image has unit of milliseconds. (*c*) Magnified portion of image (ii) of panel (*a*) demonstrating the 'tentacles' (shown by the arrows on the image) protruding out of the Taylor cone of the lower droplet.

of both panels (*a*) and (*b*) demonstrate the pre-contact phase wherein the lower droplet of smaller size exhibits a Taylor cone (TC) while the upper bigger droplet shows a marginal prolate deformation to assume an asymmetric 'C−C' configuration. As the drops near each other, the TC on the smaller droplet sharpens while the bigger droplet exhibits a 'depression' or 'groove' at the approaching end to form a 'cone-groove' (C−G) configuration as illustrated in images (ii) of panels (*a*) and

(b). A closer look at the magnified image (ii) of panel (a) which is shown in figure 5.6(c) suggests the bifurcation of the TC on the smaller droplet into liquid 'tentacles' (illustrated by arrows on the image). The 'tentacles' then indent the 'groove' formed on the bigger droplet to form a 'lock and key' configuration at the contact phase. Thereafter the 'tentacles' join to form a liquid bridge between the droplets as illustrated in figure 5.4, which pinches off to cause electric field induced droplet non-coalescence.

To shed more light into the underlying physics of such droplet interactions un-

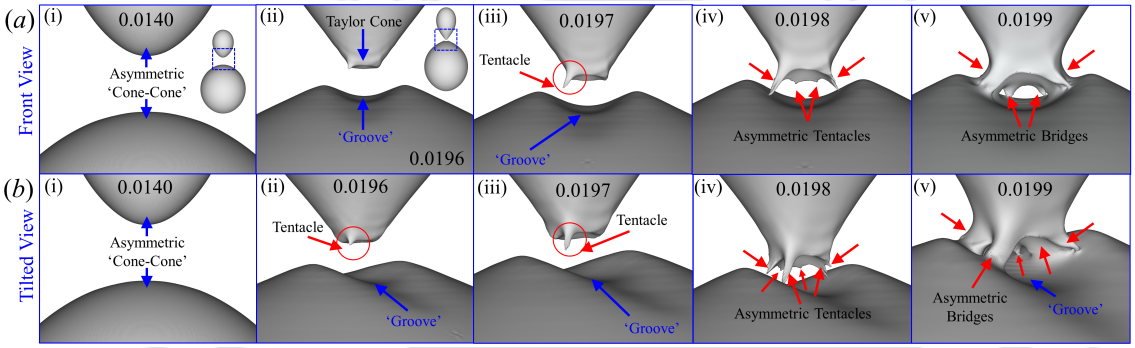

Figure 5.7: Time sequence computational snapshots demonstrating the pre-contact and contact dynamics of two asymmetrical water droplets suspended in an insulating oil under electric field from (a) front view and (b) tilted side view. The numbers in each image represent the dimensionless time. The other parameters used in the simulations are, $\frac{r_s}{r_b} = 0.5$, $\rho_r = 1$, $\mu_r = 0.003$, $\epsilon_r = 29.63$, $\sigma_r = 1000$, $Re = 0.067$, $We = 0.0067$, $R_E = 0.1$, and $Ca_E = 0.3$.

der electric field, a series of three-dimensional computational fluid dynamics (CFD) simulations were performed employing the open source code GERRIS [317]. The details of the CFD simulations are provided in section 5.4. Figure 5.7 illustrates the simulated pre-contact and contact dynamics of two uneven sized droplets (smaller droplet of radius r_s and bigger droplet of radius r_b) embedded in an insulating oil under the exposure of electric field. Inset of image (i) in figure 5.7(a) shows the pre-contact configuration of the two approaching droplets at $Ca_E = 0.3$, wherein the smaller droplet exhibits a sharp TC while the bigger droplet is marginally deformed into a prolate shape. This observation is qualitatively similar to image (i) of figure 5.4(c) and images (i) of figures 5.6(a) and 5.6(b). The magnified portion of the two approaching ends of the droplets (highlighted by the rectangle on the inset in image (i)) reveal the formation of a 'groove' at the approaching pole of the

prolate bigger droplet as shown in images (i) of panels (a) and (b). The union of the TC on the smaller droplet and the 'groove' on the bigger one engenders a 'lock and key' conformation. Another noteworthy observation in image (i) is the seemingly flat tip of the TC on the smaller droplet. As the drops approach more closer towards each other, images (ii) of both panels (a) and (b) reveal that the flat tip of the TC is squeezed inside the smaller drop to form a relatively smaller 'groove' at the pole. Interestingly, this smaller 'groove' formation is augmented by the appearance of 'tentacle' like liquid pillars. With further increase in proximity between the drops, images (iii) of panels (a) and (b) reveal the formation of more asymmetric 'tentacles' from the periphery of the 'groove' on the smaller droplet, which can be thought of as hierarchical TCs emerging from the initial TC on the smaller droplet. This asymmetric liquid 'tentacles' are analogous to the flexible limbs found in some invertebrates like hydra, jellyfish, corals and the arms of octopuses. The liquid 'tentacles' then progressively join the plateau around the 'groove' on the bigger droplet. This phenomenon is equivalent to the 'phagocytosis' by unicellular organisms like amoeba or the 'grasping of food' with the aid of the flexible tentacles by invertebrates. Images (iv) of both panels (a) and (b) unveil that upon contact with the plateaued region of the bigger droplet the 'tentacles' thicken to form a metastable structure consisting of a multitude of asymmetric liquid bridges forming a 'liquid cage' around the insulating oil. These individual liquid bridges then eventually collapse to form a single symmetrical bridge between the two drops as shown in the experimental images in figure 5.4.

Under the effect of electric field, the leaky dielectric spherical drops first deform into prolate shape [321]. As the deformed droplets near each other, the approaching pole of the smaller droplet is expected to experience higher Maxwell stress compared to the adjacent pole of the bigger droplet, owing to the smaller area of the polar region of the former. Thus, the advancing pole of the smaller droplet quickly extends into a TC with a sharp tip, while the bigger droplet undergoes marginal deformation. As the TC advances against a slowly draining highly viscous oil medium ($\mu_r = 0.003$), a high-pressure region is formed in between the two adjacent poles as shown in image (i) of figure 5.8(a). This hydrodynamic pressure over-powers the combined action of the Maxwell stress and the capillary pressure acting on the advancing pole of the bigger droplet creating the 'groove' on it as demonstrated in image (ii) of figure 5.8. Image (iii) of figure 5.8(b) highlights the translocations of the volumetric charge density with sparse charge density on the 'groove' (marked

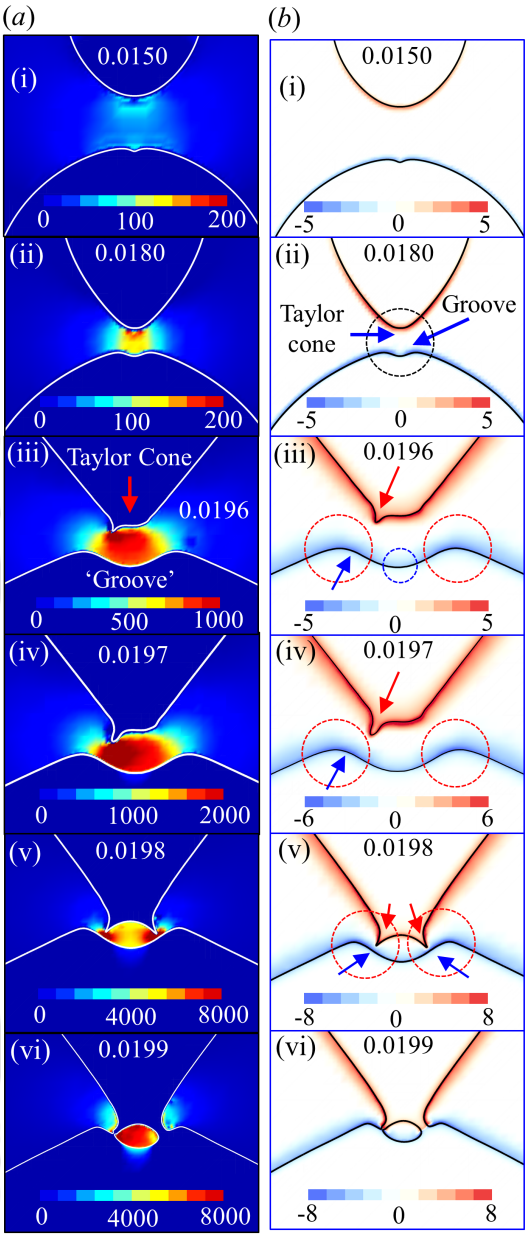

Figure 5.8: Time sequence computational snapshots demonstrating the (a) pressure and (b) volumetric charge distributions in a 2-D cross sectional view during the approach of two unequal sized droplets towards each other under the effect of electric field corresponding to figure 5.7. The numbers in each image represent the dimensionless time. The other parameters employed in the simulations are same as of figure 5.7.

by blue circle) and high concentrations of charge on the plateaued region (marked by red circles). The interaction of the charges present on the plateau of the bigger

droplet with the oppositely charged TC on the smaller droplet initiates the formation of the liquid 'tentacle' from the TC as shown in images (iii) and (iv) of panel (b). With further decrease in distance between the droplets, the pressure build-up in the interstitial oil film dents the already flattened tip of the TC to create a 'groove' on the smaller droplet similar to the bigger one as depicted in image (v) of panel (a). Image (v) of panel (b) shows the formation of additional 'tentacles' due to similar charge interactions as described in images (iii) and (iv) of panel (b). The conjoined tentacles in image (vi) of panel (a) form a number of asymmetric liquid bridges which eventually merge to form a single symmetric bridge between the droplets.

To better understand the dynamics associated with the transition of the

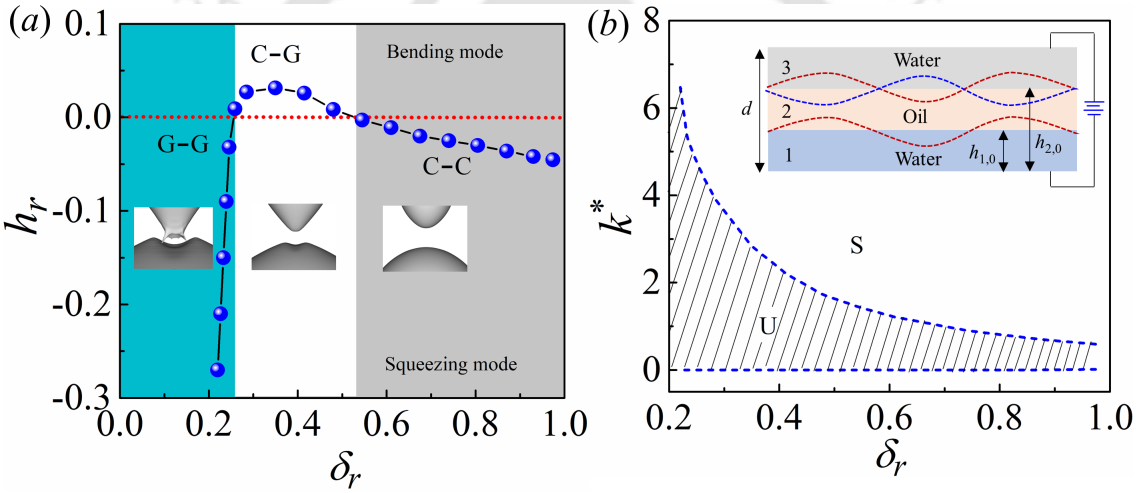

Figure 5.9: Variation of the (a) ratio of the linear amplitude of deformations (h_r) and (b) dimensionless wavenumbers (k^*) with dimensionless distance between the upper and lower layers (δ_r). The turquoise, white and grey regions denote the 'groove-groove' (G−G), 'cone-groove' (C−G), and 'cone-cone' (C−C) formations of the upper and lower interfaces, respectively. The red dotted line demarcates the bending and squeezing modes of interfacial deformations. The other parameters used for the GLSA are, $d = 50\mu$m, $h_{20} = 3.33h_{10}$, $\delta_r = \dfrac{h_{20} - h_{10}}{d}$,$h_r = \dfrac{\tilde{h_1}}{\tilde{h_2}}$, $\mu_1 = \mu_3 = 0.001$ Pa.s, $\mu_2 = 0.3$ Pa.s, $\sigma_1 = \sigma_3 = 10^{-6}$ Sm^{-1}, $\sigma_2 = 0$ Sm^{-1}, $\epsilon_1 = \epsilon_3 = 80$, $\epsilon_2 = 2.7$, $\gamma_{12} = \gamma_{23} = 0.03$ Nm^{-1}, and $\Psi_0 = 100$ V.

'cone-groove' to 'groove-groove' configuration as discussed in figures 5.7 and 5.8, a GLSA was carried out on a tri-layer of liquids acted upon by an electric field, the details of which are provided section 5.5. The upper and lowers layers (liquid 1 and 3) of the tri-layer configuration qualitatively represent the water drops and the

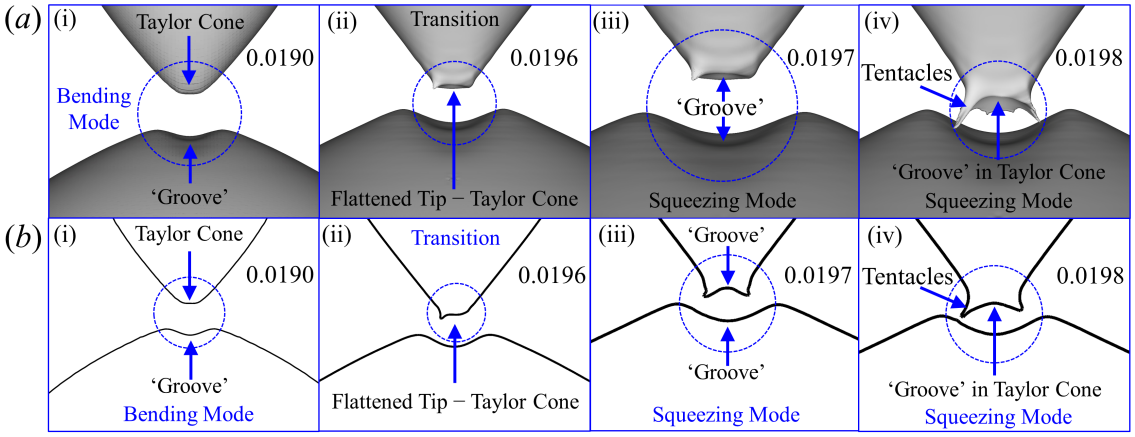

Figure 5.10: Time sequence computational snapshots indicating the bending (C–G) to squeezing (G−G) transition of the oil-water interfaces near the approaching poles of the unequal sized droplets from (a) three-dimensional (3-D) and (b) cross-sectional view. The other parameters used in the simulations are, $\frac{r_s}{r_b} = 0.5$, $\rho_r = 1$, $\mu_r = 0.003$, $\epsilon_r = 29.63$, $\sigma_r = 1000$, $Re = 0.067$, $We = 0.0067$, $R_E = 0.1$, and $Ca_E = 0.3$.

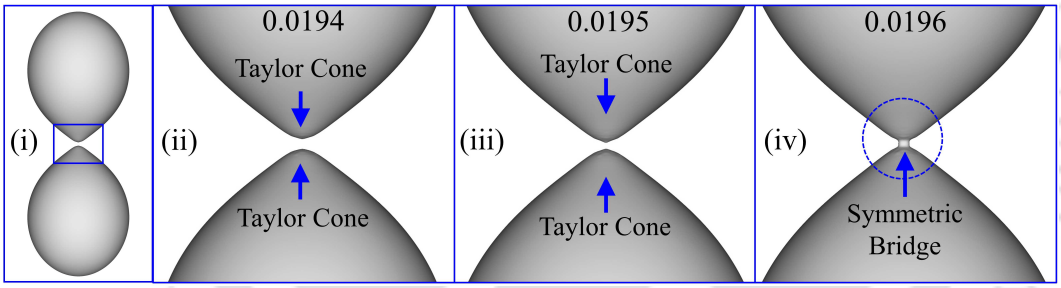

Figure 5.11: Time sequence computational snapshots indicating a pair of Taylor cones and a singular symmetric bridge formation in case of two equal sized droplets under the exposure of electric field.

sandwiched layer (liquid 2) represents the surrounding oil medium. Figure 5.9(a) demonstrates the variation of the ratio of the linear amplitude of deformations (h_r) with the dimensionless thickness of the sandwiched oil layer (δ_r) under electric field. The plot suggests that when the distance between the layers 1 and 3 is greater than a critical value, h_r displays negative values indicating the anti-phase squeezing mode of deformations of the twin oil-water interfaces. This region may be compared to the asymmetric 'C−C' (grey region) deformations of the water droplets at relatively large distance from each other as seen in the experimental micrographs (images (i)) of figure 5.6. The white region in the plot with positive values of h_r denotes the in-phase bending mode of deformations of the oil-water interfaces. This region can

be compared to the 'C−G' kind of configuration attained by the droplets as shown in experimental figures 5.4 and 5.6 and simulated figures 5.7 and 5.8. When the two interfaces come very close to each other (turquoise region), h_r values again become negative, indicating squeezing mode of interfacial deformations. This region parallels the 'G−G' transitions of the approaching ends of the water droplets as depicted in the computational snapshots in figures 5.7 and 5.8. It may be noted that, the experimental figure 5.6 demonstrates the 'C−G' configuration of the droplet pair at close proximity. The formation of a groove on the Taylor cone of the smaller droplet could not be captured owing to the imaging limitations. However, the simulations together with the GLSA provide sufficient evidence of the transition from the 'C−G' to the 'G−G' configurations at a later stage during the close approach of the droplets. This transition from 'C−C' to 'C−G' to 'G−G' is also shown in the simulated figure 5.10. It is also observed from the GLSA that when the thickness of the water layers 1 and 3 remain similar the value of h_r is always -1 suggesting the prevalence of anti-phase squeezing mode of interfacial deformations. This hints at the universally symmetric 'C−C' configuration of equal sized droplets which is also validated by the simulated results shown in figure 5.11. The neutral stability plot shown in gure 5.9(b) indicates a decrease in the wavelength of the instabilities with increasing proximity between the layers 1 and 3.

5.7 Conclusions

To summarize, the study unravels the pre-contact and contact dynamics of two oppositely charged uneven water droplets during coalescence/non-coalescence under electric field. Experiments reveal asymmetric 'C−C' to 'C−G' transitions with decreasing distance between the droplets. Simulations in conjunction with GLSA reveal the existence of an additional 'G−G' transition before the final contact between the droplets. Experiments and simulations also disclose the formation of asymmetric 'tentacles' emerging from the periphery of the 'grooved' Taylor cone on the smaller droplet which eventually extend into the bigger droplet forming a liquid bridge between the droplets.

Chapter 6

Conclusions and Future Scopes of Work

6.1 Conclusions

The dissertation documents the findings associated with electric field mediated phenomena in four different types of liquid-liquid and solid-liquid systems. The thesis attempts to uncover the physics associated with such field induced processes both experimentally as well as numerically. The study also discusses a host of relevant prospective applications of the proposed phenomena. The first topic of the thesis which is discussed in chapter two, contains a combined theoretical and experimental study to uncover the salient features of electric field induced instabilities in viscosity stratified flow of a pair of miscible dielectric fluids inside a microchannel. The third chapter of the dissertation documents a combined experimental and numerical study that throws light on the dynamics of electric field induced particle oscillations and pattern formations in insulating liquids. In the fourth chapter of the dissertation, a combined experimental and numerical study uncovers the modes of electric field induced active transfer of an aqueous droplet from a carrier liquid to a target liquid. The fifth chapter of the thesis discusses the salient features associated with electric field induced coalescence/non-coalescence of aqueous droplets in a non-conducting oil.

The key results of the studied phenomena along with the prospective applications of the same and scopes of future research are discussed point-wise in the following sections.

6.1.1 Electric Field Mediated von Kármán Vortices in Stratified Microflows: Transition from Linear Instabilities to Coherent Mixing

In this study, we harness the classical electro-hydrodynamic phenomenon of ion injection from metallic electrodes into dielectric liquids to cause electro-convection and subsequent mixing of two liquid streams. Experiments are conducted on a pressure-driven flow of a pair of miscible, non-conducting and viscosity stratified liquids inside a microchannel. A general linear stability analysis (GLSA) is carried out to identify the critical conditions for the initiation of the instabilities and to unveil the characteristics of the same. Computational fluid dynamics (CFD) studies are carried out to validate the physics underlying the experimental findings. The

main conclusions of the study are:

1. Experiments uncover four distinct regimes of the instabilities. The linear regime I corresponds to the onset of the instability waves beyond a critical field intensity. With increase in the applied voltage, the regime II marks the initiation of the non-linear regime with the appearance of time-periodic vortices in the downstream of the electrode region. With further increase in the electric field intensity, regime III initiates with smaller, high-frequency vortices that lead to the intermixing of the flow streams. An abrupt jump in the Strouhal number marks the transition of regime II to III. Regime IV initiates at very high field intensities, wherein the flow becomes unstructured and chaotic. Regime IV finally leads to the total mixing of the two fluids in the downstream region.

2. A general linear stability analysis reveals that the EHD instabilities of such systems appear only beyond a critical field intensity. The presence of five distinctive instability modes are confirmed by the GLSA. They are distinguished as: electric field mode I (E-I), electric field mode II (E-II), viscous mode (V), diffusive mode (D), and the K-mode. The E-I-mode is expected to initiate in the bulk of the lower viscosity fluid at the lower values of Ra^{ψ}. At very high values of Ra^{ψ} the E-II-mode manifests in the higher viscosity fluid. Beyond a critical viscosity difference between the fluids the V-mode appears in the mixed interfacial region. The application of electric field facilitates the onset of the V-mode compared with the regular pressure driven flows. Due to steep variation of perturbation concentration across the interface, the D-mode appears in the mixed interfacial region at higher values of Sc. Again, presence of the electric field facilitates the early onset of the D-mode in the regular pressure driven flows. The shorter wavelength K-mode of instability appears due to contrast of the ionic mobility in the fluids.

3. The most important parameters governing the nature of the instabilities are: the location of the interface (h), the thickness of the interface (δ), the level of charge injection (I^q), the strength of the applied EHD field (Ra^{ψ}), the viscosity contrast across the diffused interface (V^L), and the diffusivity across the interface (Sc). The E-I-mode remains nearly unaffected for relatively small variations in the dielectric constants of the fluids (E^L). Increase in the applied

field intensity, increase in the charge injection levels, and reduction of the overall viscosity of the fluids facilitate the initiation of the E-I-mode and E-II-modes. In the linear regime, the experimental and theoretical values obtained for the critical electric field strength, wave speed, and wavelength of the E-I-mode of instability are found to be in reasonable qualitative agreement.

4. Among all the regimes, the chaotic regime IV with coherent flow patterns is found to be the most suitable one from the perspective of mixing. At the immediate downstream of the electrodes that are inserted in the channel, the electric field engender the most efficient intermixing of the layers. The degree of mixing decreases at the far downstream of the channel, due to viscous damping of the perturbations induced by the electric field. The increase in the strength of the applied field and the number of electrodes inserted across the channel increases the mixing efficiency. Interestingly, the mixing and de-mixing processes has been observed to be reversible because the flow immediately restores to its stratified configuration on switching off the electric field.

To conclude, the study unveils pathways to integrate the influence of an external electrostatic field with a microfluidic device to remotely control the mixing of the fluid layers. The phenomenon can be of significance in improving the efficiency of multifarious cutting-edge microfluidic applications which include mixing, pumping, heat-exchange, mass transfer, and reaction engineering. In depth investigation of the coherent and chaotic regimes, alongwith a spatial stability analysis of the system has been kept as future scope of research work.

6.1.2 Genesis of Electric Field assisted Microparticle Assemblage in a Dielectric Fluid

The third chapter explores the salient features of the electric field induced organizations of collections of microparticles suspended in a dielectric liquid. A combined experimental and numerical study provides an approximate model describing the dynamics of the oscillatory motions in such electric field driven particle assemblies. The major observations of the study are:

1. In a multi-particle system, the particles transfer charge during the collisions in between themselves and also with the electrodes. The oscillatory to-and-fro motions of the particles are observed between, a pair of particles, a pair of

chains, a particle and a chain, an electrode and a particle, and between the electrodes, for such a system. Charge transfer followed by charge reversal between the particles near contact are found to be the necessary driving forces for the reversal of the directions of motions. Both conductive and non-conductive particles undergo oscillatory motions between the electrodes upon application of electric field beyond a critical value. The contact time during which the charge transfer takes place between a particle and an electrode or between two particles, decreases with increasing electric field. The conductive particles are found to acquire more charge compared to the non-conductive particles in relatively lesser times.

2. A model two-particle system is employed to explore the unique facets of the multi-particles assemblies. The experiments together with the numerical simulations for such systems reveal that equal sized particles exhibit synchronized oscillatory patterns. Their speeds of approach prior to contact and the speeds of separation, subsequent to contact and charge reversal, are reasonably identical. The trajectories of the unequal sized particles are asymmetric in such a manner that the speed of the smaller particle increases marginally after contact, while the bigger particle demonstrates a rather sluggish behaviour after contact. In the experiments with unequal sized particles, it is observed that, post contact the union of particles moves in the direction of the bigger particle briefly, during which time the charge transfer is assumed to take place. The smaller particle then reverses its direction and moves towards the electrode. The bigger particle on the other hand, after its disengagement from the union, continues its motion in the original direction, before finally reversing its direction of motion. In these processes the equal sized particles thus undergo electric field driven 'elastic' collisions, while the collisions between unequal particles are rather 'inelastic'.

3. Numerical simulations with equal sized conductive particles, carrying the theoretical amount of charges of opposite polarity, are found to exhibit qualitatively similar separation patterns as predicted by the experiments. This observation suggests that equal sized particles transfer approximately equal magnitude of charges between each other, such that after contact, they contain equal and opposite amount of charges. Simulations with one of the particles containing less magnitude of charge of opposite polarity, suggest trends similar to

the experiments with unequal sized particles. In such simulations, for a very brief time post contact between the particles, the particle with lesser net charge shows preference of motion towards the particle of higher charge with opposite polarity than the electrode of opposite polarity. With increase in separation between the particles, the particle with less charge slowly reverses its direction of motion towards the electrode of opposite polarity. This observation suggests that in the experiments with unequal particles, the bigger particle after contact with the smaller particle, retains less charge of opposite polarity than the smaller particle. The distance traversed by the less charged particle in the direction of the higher charged particle increases with the increase in the difference between the values of their charges. The charging time at contact between the particles decreases with increasing field intensities. The distribution of the simulated electric force on the particles reveal that, in the case of two particles carrying equal and opposite magnitude of charge each particle experiences attraction towards the electrode of opposite polarity, which overcomes the mutual attraction between the particles. Thus, the particles move apart from each other, as also observed in the experiments. However, in the case of particles carrying unequal quantities of charge of opposite polarity, the particle with lesser charge experiences more attractive force towards the particle of higher charge than the electrode of opposite polarity when the gap between the particles is less. This causes the particle to follow the particle of higher charge, until the attractive force between it and the electrode of opposite polarity overcomes its attraction towards the former. This observation suggests that in the experiments with unequal particles, the bigger particle carrying lesser charge after contact, must experience more attractive force towards the smaller particle, causing it to move towards it for a very brief period of time after disengagement.

4. Recirculation zones around each particle are generated due to the repeated oscillations of the spherical particles. For a multi-particle system with the particles undergoing incessant to-and-fro motion between the electrodes, an array of such flow patterns can be envisaged to be generated in the surrounding fluid. The non-slipping particle-liquid interface ensure the generation of a very high velocity gradient in the liquid medium present near a moving particle, which eventually leads to the formation of the vortices in the liquid. The

length scale of vorticity diffusion increases with increasing viscosity creating more diffused vorticity fields. The viscosity of the liquid medium and the dielectric contrast across the liquid-particle interface play key roles in deciding the particle speeds, points of collisions, and trajectories of motions in a particle laden fluid flow under electric field. The location and the number of vortices around a particle can be modulated by changing the particle size and viscosity of the surrounding liquid.

5. Experiments with the multi-particle systems show morphologies resembling layering or chaining of microparticles inside the fluid medium hinting at the onset of on-demand power law electrorheological behaviour under remote guidance of the electric field. Further, translating a similar system into a microfluidic channel with a unidirectional fluid flow bias reveals the trapping of the microparticles between the electrodes to form an electrostatic 'garland'. At a very high field intensity the garland like morphology also shows a rotational stick-slip motion motion. Importantly, most of the finer features of the particle motions observed in the multi-particle systems can be followed in a greater detail employing the two-particle system.

In summary, the study throws light on the various oscillatory patterns shown by different types of particles under electric field, along with the explanations of the mechanisms driving those motions. In-depth analysis of the mechanisms of charge transfer between the particles and the factors affecting the rate of charge transfer are very instrumental in accurately describing these systems and can be a rich area of further research.

6.1.3 Electric Field Mediated Modes of Active Droplet Transport across a Deformable Interface

In the fourth chapter a combined experimental and numerical study unveils the dynamics of an electric field induced droplet migration in an immiscible carrier-target liquid interface. The major findings of the study are:

1. Similar to the case of bubbles and solid particles, electric field induced droplet migrations can be broadly divided into the two regimes: (a) the rupture mode and (b) the tailing mode. The study suggests that, even under conditions of ultra-low interfacial tensions between the carrier and target liquids, the rupture

mode of migration may occur. Experiments reveal that for low vales of electric fields, the droplet undergoes little deformation before reaching the interface. The film drainage and rupture take place in a quasi-static manner. With increase in field intensity beyond a critical value, the droplet is first distorted into a prolate shape. It then impinges the interface, to squeeze its way out of the hole, into the target liquid, in a dynamic fashion. Three phase CFD simulations, reproduce the experimental observations, qualitatively, with the exception of changes in drop shape. The primary reason lies in the omission of the dielectrophoretic forces in the numerical model.

2. According to the experimental observations, the drainage of the film proceeds in two distinct stages, though the time scales vary with the strength of the applied field. Drainage is fast, until the film thickness reduces to almost 0.3 times the radius of the drop, after which there is a significant reduction in the rate of film drainage. CFD simulations predict similar rates of drainage as the experiments in the first stage. However, for the thinner films, the simulated rates of drainage in the second stage deviate significantly from the experiments. An analytical model of static film drainage predicts slightly higher rates of carrier film drainage compared to the experiments. The analytical model predicts velocity profiles within the draining film resembling that of the Couette flow. The profile is almost parabolic for higher values of film thickness, which eventually becomes almost linear with decrease in the thickness. The increase in shearing action, due to close proximity of the moving boundaries, leads to a constant shear stress profile, within the film. This causes the pressure drop in the draining film to be negligibly small, thus resulting in a linear velocity profile. Hence, the drainage rates are significantly reduced in the second stage.

3. Experiments reveal two distinct modes of film rupture. At lower values of electric fields, the rupture takes place at a slightly off-centre position near the advancing pole of the droplet. The hole radius grows as $r_h \sim t$, similar to the viscosity dominated regime of drop coalescence on a liquid bath. Beyond a critical value of electric field, as the droplet punches a hole near the advancing pole of the droplet, the hole grows quickly as $r_h \sim t^{0.5}$, in the initial stage. After a while, the radius of the hole remains almost constant till the droplet squeezes its way out. The initial stage in this case, resembles the inertia dominated regime of drop coalescence on a liquid bath. It may be noted that

along with the capillary forces (favouring) and viscous forces (retarding), at higher electric fields, the forces associated with the relaxation of the distorted prolate droplet, play important roles in controlling the dynamics of the opening of the hole.

4. The tailing mode is observed for very low values of interfacial tensions between the carrier and target phases. Experiments as well as simulations predict very slight change in the velocity of the droplet as it crosses the interface. In this mode, the thin film, ahead of the droplet does not rupture, as the drop moves upwards towing the long tail of the carrier liquid. Simulations predict, regions of positive vorticity around the rising droplet and negative vorticity fields around the lower receding part of the tail. Both experiments and simulations predict the maximum volume of the carrier liquid entrained by the droplet (including the droplet volume), to be approximately twice the volume of the droplet itself. The maximum occurs at a distance of approximately eight times the droplet radius from the undisturbed interface.

5. Increase in the density contrast and decrease in the viscosity contrast between the carrier and target liquids, increases the droplet velocities after crossing the interface. The decrease in droplet viscosity also increases the overall velocity of the droplet. The rate of film drainage increases with the increase in interfacial tension between the carrier and target phases, decrease in viscosity of the target phase and decrease in the droplet viscosity. The rate of the drainage remains unaffected by the density contrast between the carrier and the target phases. As the interfacial tension between them increases, the height of the column entrained by the droplet decreases, with the pinch-off occurring at the rear end of the column. Decrease in the density and increase in viscosity contrasts between the carrier and target liquids and increase in the drop viscosity, are found to decrease the height of the column at pinch-off. The maximum volume entrained by the droplet also decreases, under such conditions.

6. A quasi-static analytical model predicts that the critical electric field required for droplet migration and the the critical cap angle increases with (a) increasing density contrast between the carrier and the target fluids, (b) increasing the size of the droplet and (c) decreasing the interfacial tension between the carrier and the target fluids. It is also observed that the critical electric field also

increases with increase in density of the droplet, while the cap angle is not influenced by it.

In summary, the study unveils the dynamics associated with the electric field driven migrations of an aqueous droplet across the interface between liquid pairs with very low interfacial tensions between them. The phenomena can be harnessed for a variety of applications such as liquid-liquid extraction, separation and purification, micro-reactions, ultra-low tensiometry, and a host of biological applications related cell research, preparation of vesicles etc. In depth analysis with a wider range of liquids alongwith the study of secondary electrical effects of interface perturbations and drop shape distortions, on the migration dynamics, are kept as future scope of the research work.

6.1.4 Mechanisms of Electric Field Mediated Drop Coalescence or Non-coalescence

The fifth chapter documents the findings associated with the electric field induced drop coalescence/non-coalescence in an insulating oil. The pre-contact and contact dynamics of two oppositely charged uneven water droplets are studied in details via experiments and three dimensional numerical simulations. A general linear stability analysis is carried out to extract the finer details of the phenomena. Experiments reveal that for unequal sized droplets the contact is always asymmetric irrespective of the suspending medium. Experiments also reveal asymmetric 'cone-cone' ('C−C') to 'cone-groove' ('C−G') transitions of the approaching poles of the droplets with decreasing distance between them. Simulations in conjunction with GLSA reveal that, before the final contact the approaching poles of the droplets undergo a third 'groove-groove' ('G−G') transition. Experiments and simulations also disclose the formation of asymmetric liquid bridges resembling 'tentacles' from the periphery of the 'grooved' Taylor cone on the smaller droplet. These 'tentacles' on the smaller droplet eventually extend into the bigger droplet, forming a liquid bridge between the droplets.

6.2 Future Scopes of Work

The phenomena discussed in the dissertation can open up avenues for a number of areas of fundamental research. The experiments discussed in the thesis have the

potential to be harnessed for a multitude of applications. In this section the prospective scopes of the four objectives of the thesis are discussed pointwise,

(i) The phenomenon of electric field induced instabilities in miscible microchannel flows may be tuned to achieve a variety of cutting-edge microfluidic applications which require mixing and pumping of fluid streams. The phenomenon can also also be utilized for efficient heat-exchange, mass transfer, and micro-reactions. The investigations of the critical conditions and the characteristics of the instabilities in a multi-electrode channel may yield more interesting features of the phenomena. Experiments with more than two fluids may be yield promising results. From the point-of-view of fundamental research, the phenomena may be extrapolated into a number of relevant and interesting research problems. For example, the coherent and chaotic regimes which are observed at high electric fields may be investigated to ascertain the onset of turbulence inside such systems. A non-linear stability analysis along-with a spatial stability analysis may be potent areas of further research. Also, three dimensional numerical simulations of the discussed phenomena mimicking the actual experimental set-up may yield further novel features and forms a lucrative research problem.

(ii) The phenomena of electric field induced particle oscillations can be harnessed for a number of futuristic applications such as microfluidic vortex generators, flow control valves, on-demand catalyst beds for reaction engineering, extraction of solid from liquid and micro-rheology. The in-depth analysis of the mechanisms driving the charge transfer to cause charge reversal of the particles at contact may yield useful data to more accurately model such field driven assemblies. In this regard, molecular simulations may be suitable for deciphering the kinetics of charge transfer and reversal. Three dimensional simulations mimicking the actual experimental conditions may yield more interesting outcomes. The role of the flow patterns in the liquid medium on such phenomena can be a very potent area of future research. Experiments and simulations in the micro/nano channels can be prospective areas of research.

(iii) The electric field driven migrations of droplets through liquid-liquid interfaces can be harnessed for a multitude of applications such as liquid-liquid extraction, separation and purification, micro-reactions and tensiometry. The in-depth experimental and numerical analysis with a wider range of liquids may yield further interesting features. The study of the secondary electric field effects on the migration of drops may be also be the future scope of the research work. Three di-

mensional numerical simulations exactly mimicking the experimental conditions are expected to be instrumental in accurately modelling the experimental observations. Molecular simulations may also be carried out to study the complex dynamics of interaction of the electric double layers near the three phase contact line.

(iv) The findings from the study of electric field mediated drop coalescence/non-coalescence may be instrumental in realizing more practical and robust models to accurately map the finer details of the contact phase dynamics of such phenomena. Molecular simulations of the phenomenon may yield very useful informations on the charge during the pre-contact phase where liquid tentacles of the smaller droplet indent the groove on the bigger. Molecular simulations may also elucidate the charge transfer and reversal dynamics during the formation and break-up of the liquid bridge, which to this day are very poorly understood. The knowledge obtained from the study may be utilized for applications such as ink-jet printing, dehumidifiers, separation of water from crude, emulsification processes, chemical and biological assays, and electro-wetting.

References

[1] Vilkner T., Janasek D., and Manz A. (2004) 'Micro total analysis systems. recent developments', *Anal. Chem.*, vol. 76(12), pp. 3373–3386.

[2] Haeberle S. and Zengerle R. (2007) 'Microfluidic platforms for lab-on-a-chip applications', *Lab Chip*, vol. 7, pp. 1094–1110.

[3] Mark D., Haeberle S., Roth G., von Stetten F., and Zengerle R. (2010) 'Microfluidic lab-on-a-chip platforms: requirements, characteristics and applications', *Chem. Soc. Rev.*, vol. 39, pp. 1153–1182.

[4] Samiei E., Tabrizian M., and Hoorfar M. (2016) 'A review of digital microfluidics as portable platforms for lab-on a-chip applications', *Lab Chip*, vol. 16, pp. 2376–2396.

[5] Reyes D.R., Iossifidis D., Auroux P.A., and Manz A. (2002) 'Micro total analysis systems. 1. introduction, theory, and technology', *Anal. Chem.*, vol. 74(12), pp. 2623–2636.

[6] Wang J., Ibáñez A., Chatrathi M.P., and Escarpa A. (2001) 'Electrochemical enzyme immunoassays on microchip platforms', *Anal. Chem.*, vol. 73(21), pp. 5323–5327.

[7] Doyle P.S., Bibette J., Bancaud A., and Viovy J.L. (2002) 'Self-assembled magnetic matrices for dna separation chips', *Science*, vol. 295(5563), pp. 2237–2237.

[8] Christodoulides N., Tran M., Floriano P.N., Rodriguez M., Goodey A., Ali M., Neikirk D., and McDevitt J.T. (2002) 'A microchip-based multianalyte assay system for the assessment of cardiac risk', *Anal. Chem.*, vol. 74(13), pp. 3030–3036.

[9] Rhee S.W., Taylor A.M., Tu C.H., Cribbs D.H., Cotman C.W., and Jeon N.L. (2005) 'Patterned cell culture inside microfluidic devices', *Lab Chip*, vol. 5, pp. 102–107.

[10] Bromberg A. and Mathies R.A. (2003) 'Homogeneous immunoassay for detection of tnt and its analogues on a microfabricated capillary electrophoresis chip', *Anal. Chem.*, vol. 75(5), pp. 1188–1195.

[11] Luka G., Ahmadi A., Najjaran H., Alocilja E., DeRosa M., Wolthers K., Malki A., Aziz H., Althani A., and Hoorfar M. (2015) 'Microfluidics integrated biosensors: A leading technology towards lab-on-a-chip and sensing applications', *Sensors*, vol. 15(12), pp. 30011–30031.

[12] Yao X., Zhang Y., Du L., Liu J., and Yao J. (2015) 'Review of the applications of microreactors', *Renew. Sustain. Energy Rev.*, vol. 47, pp. 519–539.

[13] Mizuno K., Nishiyama Y., Ogaki T., Terao K., Ikeda H., and Kakiuchi K. (2016) 'Utilization of microflow reactors to carry out synthetically useful organic photochemical reactions', *J. Photochem. Photobiol. C.*, vol. 29, pp. 107–147.

[14] Leary T., Yeganeh M., and Maldarelli C. (2020) 'Microfluidic study of the electrocoalescence of aqueous droplets in crude oil', *ACS omega*, vol. 5(13), pp. 7348–7360.

[15] Ates H.C., Brunauer A., von Stetten F., Urban G.A., Güder F., Merkoçi A., Früh S.M., and Dincer C. (2020) 'Integrated devices for non-invasive diagnostics', *Adv. Funct. Mater.*, vol. 2010388, pp. 1–18.

[16] Sachdeva S., Davis R.W., and Saha A.K. (2021) 'Microfluidic point-of-care testing: Commercial landscape and future directions', *Front. Bioeng. Biotechnol.*, vol. 8, p. 1537.

[17] Siedlik M.J., Yang Z., Kadam P.S., Eberwine J., and Issadore D. (2021) 'Micro- and nano-devices for studying subcellular biology', *Small*, vol. 17(2005793), pp. 1–12.

[18] Hakke V., Sonawane S., Anandan S., Sonawane S., and Ashokkumar M. (2021) 'Process intensification approach using microreactors for synthesizing nanomaterials—a critical review', *Nanomaterials*, vol. 11(1), p. 98.

[19] Stone H.A., Stroock A.D., and Ajdari A. (2004) 'Engineering flows in small devices: microfluidics toward a lab-on-a-chip', *Annu. Rev. Fluid Mech.*, vol. 36, pp. 381–411.

[20] Dittrich P.S. and Manz A. (2006) 'Lab-on-a-chip: microfluidics in drug discovery', *Nat. Rev. Drug Discov.*, vol. 5(3), pp. 210–218.

[21] Sackmann E.K., Fulton A.L., and Beebe D.J. (2014) 'The present and future role of microfluidics in biomedical research', *Nature*, vol. 507(7491), pp. 181–189.

[22] Stroock A.D., Dertinger S.K.W., Ajdari A., Mezić I., Stone H.A., and Whitesides G.M. (2002) 'Chaotic mixer for microchannels', *Science*, vol. 295(5555), pp. 647–651.

[23] El Moctar A.O., Aubry N., and Batton J. (2003) 'Electro-hydrodynamic micro-fluidic mixer', *Lab Chip*, vol. 3(4), pp. 273–280.

[24] Di Carlo D. (2009) 'Inertial microfluidics', *Lab Chip*, vol. 9(21), pp. 3038–3046.

[25] Zhang J., Yan S., Yuan D., Alici G., Nguyen N.T., Warkiani M.E., and Li W. (2016) 'Fundamentals and applications of inertial microfluidics: a review', *Lab Chip*, vol. 16(1), pp. 10–34.

[26] Janasek D., Franzke J., and Manz A. (2006) 'Scaling and the design of miniaturized chemical-analysis systems', *Nature*, vol. 442(7101), p. 374.

[27] Hertzog D.E., Ivorra B., Mohammadi B., Bakajin O., and Santiago J.G. (2006) 'Optimization of a microfluidic mixer for studying protein folding kinetics', *Anal. Chem.*, vol. 78(13), pp. 4299–4306.

[28] Bertsch A., Heimgartner S., Cousseau P., and Renaud P. (2001) 'Static micromixers based on large-scale industrial mixer geometry', *Lab Chip*, vol. 1(1), pp. 56–60.

[29] Verma M.K.S., Ganneboyina S.R., Vinayak R.R., and Ghatak A. (2008) 'Three-dimensional multihelical microfluidic mixers for rapid mixing of liquids', *Langmuir*, vol. 24(5), pp. 2248–2251.

[30] Hinsmann P., Frank J., Svasek P., Harasek M., and Lendl B. (2001) 'Design, simulation and application of a new micromixing device for time resolved infrared spectroscopy of chemical reactions in solution', *Lab Chip*, vol. 1(1), pp. 16–21.

[31] Simonnet C. and Groisman A. (2005) 'Chaotic mixing in a steady flow in a microchannel', *Phys. Rev. Lett.*, vol. 94(13), p. 134501.

[32] Jha B., Cueto-Felgueroso L., and Juanes R. (2011) 'Fluid mixing from viscous fingering', *Phys. Rev. Lett.*, vol. 106(19), p. 194502.

[33] Rife J., Bell M., Horwitz J., Kabler M., Auyeung R., and Kim W. (2000) 'Miniature valveless ultrasonic pumps and mixers', *Sens. Actuat. A: Phys.*, vol. 86(1), pp. 135–140.

[34] Yi M., Qian S., and Bau H.H. (2002) 'A magnetohydrodynamic chaotic stirrer', *J. Fluid Mech.*, vol. 468, pp. 153–177.

[35] Oddy M., Santiago J., and Mikkelsen J. (2001) 'Electrokinetic instability micromixing', *Anal. Chem.*, vol. 73(24), pp. 5822–5832.

[36] Zhao H. and Bau H.H. (2007) 'Microfluidic chaotic stirrer utilizing induced-charge electro-osmosis', *Phys. Rev. E*, vol. 75(6), p. 066217.

[37] Harnett C.K., Templeton J., Dunphy-Guzman K.A., Senousy Y.M., and Kanouff M.P. (2008) 'Model based design of a microfluidic mixer driven by induced charge electroosmosis', *Lab Chip*, vol. 8(4), pp. 565–572.

[38] Chen C.H., Lin H., Lele S.K., and Santiago J.G. (2005) 'Convective and absolute electrokinetic instability with conductivity gradients', *J. Fluid Mech.*, vol. 524, pp. 263–303.

[39] Posner J.D. and Santiago J.G. (2006) 'Convective instability of electrokinetic flows in a cross-shaped microchannel', *J. Fluid Mech.*, vol. 555, pp. 1–42.

[40] Posner J.D., Pérez C.L., and Santiago J.G. (2012) 'Electric fields yield chaos in microflows', *Proc. Nat. Acad. Sci.*, vol. 109(36), pp. 14353–14356.

[41] Wang J., Wang B., and Qiu H. (2014) 'Coalescence and breakup of oppositely charged droplets', *Sci. Rep.*, vol. 4(1), pp. 1–6.

[42] Ding Z. and Wong T.N. (2015) 'Electrohydrodynamic instability of miscible core–annular flows with electrical conductivity stratification', *J. Fluid Mech.*, vol. 764, pp. 488–512.

[43] Wang G., Yang F., Zhao W., and Chen C.P. (2016) 'On micro-electrokinetic scalar turbulence in microfluidics at a low reynolds number', *Lab Chip*, vol. 16(6), pp. 1030–1038.

[44] Ko S.H., Lee H., and Kang K.H. (2008) 'Hydrodynamic flows in electrowetting', *Langmuir*, vol. 24(3), pp. 1094–1101.

[45] Otsubo Y. and Edamura K. (1998) 'Viscoelasticity of a dielectric fluid in nonuniform electric fields generated by electrodes with flocked fabrics', *Rheol. Acta*, vol. 37(5), pp. 500–507.

[46] Skotak M. and Larsen G. (2006) 'Solution chemistry control to make well defined submicron continuous fibres by electrospinning: the (ch3ch2ch2o)4ti/acoh/poly(n-vinylpyrrolidone) system', *J. Mater. Chem.*, vol. 16, pp. 3031–3039.

[47] Chakraborty S., Liao I.C., Adler A., and Leong K.W. (2009) 'Electrohydrodynamics: A facile technique to fabricate drug delivery systems', *Adv. Drug Deliv. Rev.*, vol. 61(12), pp. 1043–1054.

[48] Atten P. and Gosse J.P. (1969) 'Transient of one-carrier injections in polar liquids', *J. Chem. Phys.*, vol. 51(7), pp. 2804–2811.

[49] Watson P.K., Schneider J.M., and Till H.R. (1970) 'Electrohydrodynamic stability of space-charge-limited currents in dielectric liquids. ii. experimental study', *Phys. Fluids*, vol. 13(8), pp. 1955–1961.

[50] Hopfinger E.J. and Gosse J.P. (1971) 'Charge transport by selfâgenerated turbulence in insulating liquids submitted to unipolar injection', *Phys. Fluids*, vol. 14(8), pp. 1671–1682.

[51] Atten P. (1974) 'Electrohydrodynamic stability of dielectric liquids during transient regime of space-charge-limited injection', *Phys. Fluids*, vol. 17(10), pp. 1822–1827.

[52] Lacroix J.C., Atten P., and Hopfinger E.J. (1975) 'Electro-convection in a dielectric liquid layer subjected to unipolar injection', *J. Fluid Mech.*, vol. 69(3), pp. 539–563.

[53] Denat A., Gosse B., and Gosse J. (1979) 'Ion injections in hydrocarbons', *J. Electrostat.*, vol. 7, pp. 205–225.

[54] Alj A., Denat A., Gosse J.P., Gosse B., and Nakamura I. (1985) 'Creation of charge carriers in nonpolar liquids', *IEEE Trans. Electr. Insul.*, vol. EI-20(2), pp. 221–231.

[55] Suh Y.K. (2012) 'Modeling and simulation of ion transport in dielectric liquids - fundamentals and review', *IEEE Trans. Dielectr. Electr. Insul.*, vol. 19(3), pp. 831–848.

[56] Malraison B. and Atten P. (1982) 'Chaotic behavior of instability due to unipolar ion injection in a dielectric liquid', *Phys. Rev. Lett.*, vol. 49(10), p. 723.

[57] Oliveri S., Atten P., and Castellanos A. (1987) 'The stability of a planar layer of insulating liquid subjected to charge injection and rotation', *Phys. Fluids*, vol. 30(7), pp. 1948–1955.

[58] Castellanos A. (1991) 'Coulomb-driven convection in electrohydrodynamics', *IEEE Trans. Electr. Insul.*, vol. 26(6), pp. 1201–1215.

[59] McCluskey F..M.J., Atten P., and Perez A.T. (1991) 'Heat transfer enhancement by electroconvection resulting from an injected space charge between parallel plates', *Int. J. Heat Mass Transfer*, vol. 34(9), pp. 2237–2250.

[60] Allen P. and Karayiannis T. (1995) 'Electrohydrodynamic enhancement of heat transfer and fluid flow', *Heat Recov. Syst. CHP*, vol. 15(5), pp. 389–423.

[61] Bart S.F., Tavrow L.S., Mehregany M., and Lang J.H. (1990) 'Microfabricated electrohydrodynamic pumps', *Sensor Actuat. A-Phys.*, vol. 21(1), pp. 193–197.

[62] Petitjeans P. and Maxworthy T. (1996) 'Miscible displacements in capillary tubes. part 1. experiments', *J. Fluid Mech.*, vol. 326, pp. 37–56.

[63] Sahu K.C. and Govindarajan R. (2016) 'Linear stability analysis and direct numerical simulation of two-layer channel flow', *J. Fluid Mech.*, vol. 798, pp. 889–909.

[64] Shrimpton J.S. and Yule A.J. (1999) 'Characterisation of charged hydrocarbon sprays for application in combustion systems', *Exps. Fluids*, vol. 26(5), pp. 460–469.

[65] Albrecht D.R., Underhill G.H., Mendelson A., and Bhatia S.N. (2007) 'Multiphase electropatterning of cells and biomaterials', *Lab Chip*, vol. 7(6), pp. 702–709.

[66] Delannay R., Valance A., Mangeney A., Roche O., and Richard P. (2017) 'Granular and particle-laden flows: from laboratory experiments to field observations', *J. Phys. D: Appl. Phys.*, vol. 50(5), p. 053001.

[67] Ku D.N. (1997) 'Blood flow in arteries', *Annu. Rev. Fluid Mech.*, vol. 29(1), pp. 399–434.

[68] Be'er A. and Ariel G. (2019) 'A statistical physics view of swarming bacteria', *Movement Ecology*, vol. 7(9), pp. 1–17.

[69] Yuan H.G., Kalfas G., and Ray W.H. (1991) 'Suspension polymerization', *Journal of Macromolecular Science, Part C: Polymer Reviews*, vol. 31(2-3), pp. 215–299.

[70] Lee P.Y., Costumbrado J., Hsu C.Y., and Kim Y.H. (2012) 'Agarose gel electrophoresis for the separation of dna fragments', *J. Vis. Exp.*, vol. 62, p. e3923.

[71] Hendrickson G. (2006) 'Electrostatics and gas phase fluidized bed polymerization reactor wall sheeting', *Chem. Eng. Sci.*, vol. 61(4), pp. 1041–1064.

[72] Adan A., Alizada G., Kiraz Y., Baran Y., and Nalbant A. (2017) 'Flow cytometry: basic principles and applications', *Crit. Rev. Biotech.*, vol. 37(2), pp. 163–176.

[73] Liao X., Makris M., and Luo X.M. (2016) 'Fluorescence-activated cell sorting for purification of plasmacytoid dendritic cells from the mouse bone marrow', *J. Vis. Exp.*, vol. 117, p. e54641.

[74] Hunter R.J., *Zeta potential in colloid science: principles and applications*, vol. 2 (Academic press, 2013).

[75] Xu X., Ray R., Gu Y., Ploehn H.J., Gearheart L., Raker K., and Scrivens W.A. (2004) 'Electrophoretic analysis and purification of fluorescent single-walled carbon nanotube fragments', *J. Am. Chem. Soc.*, vol. 126(40), pp. 12736–12737.

[76] Nakata S., Hata M., Ikura Y.S., Heisler E., Awazu A., Kitahata H., and Nishimori H. (2013) 'Motion with memory of a self-propelled object', *J. Phys. Chem. C*, vol. 117(46), pp. 24490–24495.

[77] Dumazer G., Sandnes B., Ayaz M., Måløy K., and Flekkøy E.G. (2016) 'Frictional fluid dynamics and plug formation in multiphase millifluidic flow', *Phys. Rev. Lett.*, vol. 117(2), p. 028002.

[78] Yariv E. (2004) 'Inertia-induced electrophoretic interactions', *Phys. Fluids*, vol. 16(4), pp. L24–L27.

[79] Swaminathan T.N. and Hu H.H. (2004) 'Particle interactions in electrophoresis due to inertia', *J. Colloid Interface Sci.*, vol. 273(1), pp. 324–330.

[80] Talary M.S., Burt J.P.H., Tame J.A., and Pethig R. (1996) 'Electromanipulation and separation of cells using travelling electric fields', *J. Phys. D: Appl. Phys.*, vol. 29(8), p. 2198.

[81] Choi S. and Park J.K. (2005) 'Microfluidic system for dielectrophoretic separation based on a trapezoidal electrode array', *Lab Chip*, vol. 5(10), pp. 1161–1167.

[82] Barrett L.M., Skulan A.J., Singh A.K., Cummings E.B., and Fiechtner G.J. (2005) 'Dielectrophoretic manipulation of particles and cells using insulating ridges in faceted prism microchannels', *Anal. Chem.*, vol. 77(21), pp. 6798–6804.

[83] Barbulovic-Nad I., Xuan X., Lee J.S., and Li D. (2006) 'Dc-dielectrophoretic separation of microparticles using an oil droplet obstacle', *Lab Chip*, vol. 6(2), pp. 274–279.

[84] Cui H.H., Voldman J., He X.F., and Lim K.M. (2009) 'Separation of particles by pulsed dielectrophoresis', *Lab Chip*, vol. 9(16), pp. 2306–2312.

[85] Kang K. and Dhont J.K.G. (2010) 'Electric-field induced transitions in suspensions of charged colloidal rods', *Soft Matter*, vol. 6(2), pp. 273–286.

[86] Liu B., Besseling T.H., Hermes M., Demirörs A.F., Imhof A., and Van Blaaderen A. (2014) 'Switching plastic crystals of colloidal rods with electric fields', *Nat. Commun.*, vol. 5, p. 3092.

[87] Crassous J.J. and Demirörs A.F. (2017) 'Multiscale directed self-assembly of composite microgels in complex electric fields', *Soft Matter*, vol. 13(1), pp. 88–100.

[88] Leunissen M.E., Sullivan M.T., Chaikin P.M., and Van Blaaderen A. (2008) 'Concentrating colloids with electric field gradients. i. particle transport and growth mechanism of hard-sphere-like crystals in an electric bottle', *J. Chem. Phys.*, vol. 128(16), p. 164508.

[89] Juárez J.J., Mathai P.P., Liddle J.A., and Bevan M.A. (2012) 'Multiple electrokinetic actuators for feedback control of colloidal crystal size', *Lab Chip*, vol. 12(20), pp. 4063–4070.

[90] Edwards T.D. and Bevan M.A. (2014) 'Controlling colloidal particles with electric fields', *Langmuir*, vol. 30(36), pp. 10793–10803.

[91] Jones T.B. and Jones T.B., *Electromechanics of particles* (Cambridge University Press, 2005).

[92] Velev O.D. and Bhatt K.H. (2006) 'On-chip micromanipulation and assembly of colloidal particles by electric fields', *Soft Matter*, vol. 2(9), pp. 738–750.

[93] Suzuki M., Yasukawa T., Shiku H., and Matsue T. (2007) 'Negative dielectrophoretic patterning with colloidal particles and encapsulation into a hydrogel', *Langmuir*, vol. 23(7), pp. 4088–4094.

[94] Gangwal S., Cayre O.J., and Velev O.D. (2008) 'Dielectrophoretic assembly of metallodielectric janus particles in ac electric fields', *Langmuir*, vol. 24(23), pp. 13312–13320.

[95] Zhang C., Khoshmanesh K., Mitchell A., and Kalantar-Zadeh K. (2010) 'Dielectrophoresis for manipulation of micro/nano particles in microfluidic systems', *Anal. Bioanal. Chem.*, vol. 396(1), pp. 401–420.

[96] Kadaksham A.T.J., Singh P., and Aubry N. (2004) 'Dielectrophoresis of nanoparticles', *Electrophoresis*, vol. 25(21-22), pp. 3625–3632.

[97] Ai Y. and Qian S. (2010) 'Dc dielectrophoretic particle–particle interactions and their relative motions', *J. Colloid Interface Sci.*, vol. 346(2), pp. 448–454.

[98] Hossan M.R., Dillon R., Roy A.K., and Dutta P. (2013) 'Modeling and simulation of dielectrophoretic particle-particle interactions and assembly', *J. Colloid Interface Sci.*, vol. 394, pp. 619–629.

[99] Moncada-Hernandez H., Nagler E., and Minerick A.R. (2014) 'Theoretical and experimental examination of particle-particle interaction effects on induced dipole moments and dielectrophoretic responses of multiple particle chains', *Electrophoresis*, vol. 35(12-13), pp. 1803–1813.

[100] Hossan M.R., Gopmandal P.P., Dillon R., and Dutta P. (2016) 'A comprehensive numerical investigation of dc dielectrophoretic particle? particle interactions and assembly', *Colloids Surf., A*, vol. 506, pp. 127–137.

[101] Velev O.D., Gangwal S., and Petsev D.N. (2009) 'Particle-localized ac and dc manipulation and electrokinetics', *Annu. Rep. Prog. Chem., Sect. C: Phys. Chem.*, vol. 105, pp. 213–246.

[102] Kang S. (2014) 'Dielectrophoretic motion of two particles with diverse sets of the electric conductivity under a uniform electric field', *Comput. Fluids*, vol. 105, pp. 231–243.

[103] Winslow W.M. (1949) 'Induced fibration of suspensions', *J. Appl. Phys.*, vol. 20(12), pp. 1137–1140.

[104] Bonnecaze R.T. and Brady J.F. (1992) 'Dynamic simulation of an electrorheological fluid', *J. Chem. Phys.*, vol. 96(3), pp. 2183–2202.

[105] Davis L.C. (1993) 'The metal-particle/insulating oil system: An ideal electrorheological fluid', *J. Appl. Phys.*, vol. 73(2), pp. 680–683.

[106] Cho A.Y.H. (1964) 'Contact charging of micron-sized particles in intense electric fields', *J. Appl. Phys.*, vol. 35(9), pp. 2561–2564.

[107] Soria C., Ramos A., and Pérez A.T. (1997) 'The charged bouncing ball: An experimental model for period-doubling bifurcation', *Europhys. Lett.*, vol. 37(8), p. 541.

[108] Khayari A. and Perez A.T. (2002) 'Charge acquired by a spherical ball bouncing on an electrode: Comparison between theory and experiment', *IEEE Trans. Dielectr. Electr. Insul.*, vol. 9(4), pp. 589–595.

[109] Drews A.M., Lee H.Y., and Bishop K.J.M. (2013) 'Ratcheted electrophoresis for rapid particle transport', *Lab Chip*, vol. 13(22), pp. 4295–4298.

[110] Cartier C.A., Drews A.M., and Bishop K.J.M. (2014) 'Microfluidic mixing of nonpolar liquids by contact charge electrophoresis', *Lab Chip*, vol. 14(21), pp. 4230–4236.

[111] Drews A.M., Kowalik M., and Bishop K.J.M. (2014) 'Charge and force on a conductive sphere between two parallel electrodes: A stokesian dynamics approach', *J. Appl. Phys.*, vol. 116(7), p. 074903.

[112] Drews A.M., Cartier C.A., and Bishop K.J.M. (2015) 'Contact charge electrophoresis: Experiment and theory', *Langmuir*, vol. 31(13), pp. 3808–3814.

[113] Eslami G., Esmaeilzadeh E., and Pérez A.T. (2016) 'Modeling of conductive particle motion in viscous medium affected by an electric field considering particle-electrode interactions and microdischarge phenomenon', *Phys. Fluids*, vol. 28(10), p. 107102.

[114] Bishop K.J.M., Drews A.M., Cartier C.A., Pandey S., and Dou Y. (2018) 'Contact charge electrophoresis: fundamentals and microfluidic applications', *Langmuir*, vol. 34(22), pp. 6315–6327.

[115] Smythe W.B., *Static and dynamic electricity* (Taylor and Francis, 1988).

[116] Davis M.H. (1964) 'Two charged spherical conductors in a uniform electric field: forces and field strength', *Q. J. Mech. Appl. Math.*, vol. 17, pp. 499–511.

[117] Felici N.J. (1966) 'Forces and charges of small objects in contact with an electrode subjected to an electric field', *Revue Generale de l'Electricite*, vol. 75, pp. 1145–1160.

[118] Kundu A., Dumont E., Duquenne A.M., and Delmas H. (2003) 'Mass transfer characteristics in gas-liquid-liquid system', *Can. J. Chem. Eng.*, vol. 81(3-4), pp. 640–646.

[119] Gjelstad A. (2019) 'Three-phase hollow fiber liquid-phase microextraction and parallel artificial liquid membrane extraction', *TrAC Trends Anal. Chem.*, vol. 113, pp. 25–31.

[120] Li A., Zhai H., Li J., and He Q. (2020) 'Practical applications of supramolecular extraction with macrocycles', *Chem. Lett.*, vol. 49(10), pp. 1125–1135.

[121] Mhatre S., Vivacqua V., Ghadiri M., Abdullah A.M., Al-Marri M.J., Hassanpour A., Hewakandamby B., Azzopardi B., and Kermani B. (2015) 'Electrostatic phase separation: A review', *Chem. Eng. Res. Des.*, vol. 96, pp. 177–195.

[122] Kavehpour H.P. (2015) 'Coalescence of drops', *Annu. Rev. Fluid Mech.*, vol. 47, pp. 245–268.

[123] Trantidou T., Friddin M.S., Salehi-Reyhani A., Ces O., and Elani Y. (2018) 'Droplet microfluidics for the construction of compartmentalised model membranes', *Lab Chip*, vol. 18(17), pp. 2488–2509.

[124] Sohrabi S., Moraveji M.K., and Iranshahi D. (2020) 'A review on the design and development of photocatalyst synthesis and application in microfluidic reactors: Challenges and opportunities', *Rev. Chem. Eng.*, vol. 36(6), pp. 687–722.

[125] Tsai S.S.H., Wexler J.S., Wan J., and Stone H.A. (2011) 'Conformal coating of particles in microchannels by magnetic forcing', *Appl. Phys. Lett.*, vol. 99(15), p. 153509.

[126] Vasiliauskas R., Liu D., Cito S., Zhang H., Shahbazi M.A., Sikanen T., Mazutis L., and Santos H.A. (2015) 'Simple microfluidic approach to fabricate monodisperse hollow microparticles for multidrug delivery', *ACS Appl. Mater. Interfaces*, vol. 7(27), pp. 14822–14832.

[127] Matosevic S. and Paegel B.M. (2011) 'Stepwise synthesis of giant unilamellar vesicles on a microfluidic assembly line', *J. Am. Chem. Soc.*, vol. 133(9), pp. 2798–2800.

[128] Skelley A.M., Kirak O., Suh H., Jaenisch R., and Voldman J. (2009) 'Microfluidic control of cell pairing and fusion', *Nat. Methods*, vol. 6(2), pp. 147–152.

[129] Gossett D.R., Tse H.T.K., Dudani J.S., Goda K., Woods T.A., Graves S.W., and Di Carlo D. (2012) 'Inertial manipulation and transfer of microparticles across laminar fluid streams', *Small*, vol. 8(17), pp. 2757–2764.

[130] Yoon S., Kim J.A., Lee S.H., Kim M., and Park T.H. (2013) 'Droplet-based microfluidic system to form and separate multicellular spheroids using magnetic nanoparticles', *Lab Chip*, vol. 13(8), pp. 1522–1528.

[131] Li L., Boedicker J.Q., and Ismagilov R.F. (2007) 'Using a multijunction microfluidic device to inject substrate into an array of preformed plugs without cross-contamination: comparing theory and experiments', *Anal. Chem.*, vol. 79(7), pp. 2756–2761.

[132] Chung S.E., Park W., Shin S., Lee S.A., and Kwon S. (2008) 'Guided and fluidic self-assembly of microstructures using railed microfluidic channels', *Nat. Mater.*, vol. 7(7), pp. 581–587.

[133] Kantak C., Beyer S., Yobas L., Bansal T., and Trau D. (2011) 'A 'microfluidic pinball'for on-chip generation of layer-by-layer polyelectrolyte microcapsules', *Lab Chip*, vol. 11(6), pp. 1030–1035.

[134] Gol B., Tovar-Lopez F.J., Kurdzinski M.E., Tang S.Y., Petersen P., Mitchell A., and Khoshmanesh K. (2015) 'Continuous transfer of liquid metal droplets across a fluid–fluid interface within an integrated microfluidic chip', *Lab Chip*, vol. 15(11), pp. 2476–2485.

[135] Jayaprakash K.S., Banerjee U., and Sen A.K. (2016) 'Dynamics of aqueous droplets at the interface of coflowing immiscible oils in a microchannel', *Langmuir*, vol. 32(8), pp. 2136–2143.

[136] Jayaprakash K.S. and Sen A.K. (2018) 'Continuous splitting of aqueous droplets at the interface of co-flowing immiscible oil streams in a microchannel', *Soft Mater.*, vol. 14(5), pp. 725–733.

[137] Deng N.N., Wang W., Ju X.J., Xie R., and Chu L.Y. (2016) 'Spontaneous transfer of droplets across microfluidic laminar interfaces', *Lab Chip*, vol. 16(22), pp. 4326–4332.

[138] Tsai S.S.H., Wexler J.S., Wan J., and Stone H.A. (2013) 'Microfluidic ultralow interfacial tensiometry with magnetic particles', *Lab Chip*, vol. 13(1), pp. 119–125.

[139] Destgeer G., Lee K.H., Jung J.H., Alazzam A., and Sung H.J. (2013) 'Continuous separation of particles in a pdms microfluidic channel via travelling surface acoustic waves (tsaw)', *Lab Chip*, vol. 13(21), pp. 4210–4216.

[140] Fradet E., McDougall C., Abbyad P., Dangla R., Mcgloin D., and Baroud C.N. (2011) 'Combining rails and anchors with laser forcing for selective manipulation within 2d droplet arrays', *Lab Chip*, vol. 11(24), pp. 4228–4234.

[141] Hartland S. (1968) 'The approach of a rigid sphere to a deformable liquid/liquid interface', *J. Colloid I. Sci.*, vol. 26(4), pp. 383–394.

[142] Hartland S. (1969) 'The profile of the draining film between a rigid sphere and a deformable fluid-liquid interface', *Chem. Eng. Sci.*, vol. 24(6), pp. 987–995.

[143] Maru H.C., Wasan D.T., and Kintner R.C. (1971) 'Behavior of a rigid sphere at a liquid—liquid interface', *Chem. Eng. Sci.*, vol. 26(10), pp. 1615–1628.

[144] Geller A.S., Lee S.H., and Leal L.G. (1986) 'The creeping motion of a spherical particle normal to a deformable interface', *J. Fluid Mech.*, vol. 169, pp. 27–69.

[145] Abaid N., Adalsteinsson D., Agyapong A., and McLaughlin R.M. (2004) 'An internal splash: Levitation of falling spheres in stratified fluids', *Phys. Fluids*, vol. 16(5), pp. 1567–1580.

[146] Aristoff J.M. and Bush J.W.M. (2008) 'Water entry of small hydrophobic spheres', *J. Fluid Mech.*, vol. 619, pp. 45–78.

[147] Aristoff J.M., Truscott T.T., Techet A.H., and Bush J.W.M. (2010) 'The water entry of decelerating spheres', *Phys. Fluids*, vol. 22(3), p. 032102.

[148] Lee D.G. and Kim H.Y. (2011) 'Sinking of small sphere at low reynolds number through interface', *Phys. Fluids*, vol. 23(7), p. 072104.

[149] Camassa R., Khatri S., McLaughlin R.M., Prairie J.C., White B.L., and Yu S. (2013) 'Retention and entrainment effects: Experiments and theory for porous spheres settling in sharply stratified fluids', *Phys. Fluids*, vol. 25(8), p. 081701.

[150] Chen H., Xu Q., Liang S., and Li J. (2018) 'Film coating on a small sphere crossing an oil-water interface', *Phys. Rev. Fluids*, vol. 3(12), p. 124003.

[151] Pierson J.L. and Magnaudet J. (2018) 'Inertial settling of a sphere through an interface. part 2. sphere and tail dynamics', *J. Fluid Mech.*, vol. 835, pp. 808–851.

[152] Pierson J.L. and Magnaudet J. (2018) 'Inertial settling of a sphere through an interface. part 2. sphere and tail dynamics', *J. Fluid Mech.*, vol. 835, pp. 808–851.

[153] Jarvis P.A., Mader H.M., Huppert H.E., Cashman K.V., and Blundy J.D. (2019) 'Experiments on the low-reynolds-number settling of a sphere through a fluid interface', *Phys. Rev. Fluids*, vol. 4(2), p. 024003.

[154] Mercier J.L., da Cunha F.M., Teixeira J.C., and Scofield M.P. (1974) 'Influence of enveloping water layer on the rise of air bubbles in newtonian fluids', *J. Appl. Mech.*, pp. 29–34.

[155] Greene G.A., Chen J.C., and Conlin M.T. (1988) 'Onset of entrainment between immiscible liquid layers due to rising gas bubbles', *Int. J. Heat Mass Transf.*, vol. 31(6), pp. 1309–1317.

[156] Hashimoto H. and Kawano S. (1990) 'A study on encapsulated liquid drop formation in liquid-liquid-gas systems: fundamental mechanism of encapsulated drop formation', *JSME Int. J. II*, vol. 33(4), pp. 729–735.

[157] Reiter G. and Schwerdtfeger K. (1992) 'Observations of physical phenomena occurring during passage of bubbles through liquid/liquid interfaces', *ISIJ international*, vol. 32(1), pp. 50–56.

[158] Kawano S., Hashimoto H., and Suyama T. (1994) 'Buoyancy-driven accelerated motion of an encapsulated liquid drop', *JSME Int. J. Ser. B Fluids Therm. Eng.*, vol. 37(1), pp. 30–37.

[159] Manga M. and Stone H.A. (1995) 'Low reynolds number motion of bubbles, drops and rigid spheres through fluid–fluid interfaces', *J. Fluid Mech.*, vol. 287, pp. 279–298.

[160] Debrégeas G., Gennes P.G.D., and Brochard-Wyart F. (1998) 'The life and death of" bare" viscous bubbles', *Science*, vol. 279(5357), pp. 1704–1707.

[161] Dietrich N., Poncin S., Pheulpin S., and Li H.Z. (2008) 'Passage of a bubble through a liquid–liquid interface', *AIChE journal*, vol. 54(3), pp. 594–600.

[162] Uemura T., Ueda Y., and Iguchi M. (2010) 'Ripples on a rising bubble through an immiscible two-liquid interface generate numerous micro droplets', *EPL*, vol. 92(3), p. 34004.

[163] Bonhomme R., Magnaudet J., Duval F., and Piar B. (2012) 'Inertial dynamics of air bubbles crossing a horizontal fluid-fluid interface', *J. Fluid Mech.*, vol. 707, pp. 405–443.

[164] Singh K.K. and Bart H.J. (2015) 'Passage of a single bubble through a liquid–liquid interface', *Ind. Eng. Chem. Res.*, vol. 54(38), pp. 9478–9493.

[165] Díaz-Damacillo L., Ruiz-Angulo A., and Zenit R. (2016) 'Drift by air bubbles crossing an interface of a stratified medium at moderate reynolds number', *Int. J. Multiph. Flow*, vol. 85, pp. 258–266.

[166] Emery T.S., Raghupathi P.A., and Kandlikar S.G. (2018) 'Flow regimes and transition criteria during passage of bubbles through a liquid–liquid interface', *Langmuir*, vol. 34(23), pp. 6766–6776.

[167] Magnaudet J. and Mercier M.J. (2020) 'Particles, drops, and bubbles moving across sharp interfaces and stratified layers', *Annu. Rev. Fluid Mech.*, vol. 52, pp. 61–91.

[168] Shah S.T., Wasan D.T., and Kintner R.C. (1972) 'Passage of a liquid drop through a liquid—liquid interface', *Chem. Eng. Sci.*, vol. 27(5), pp. 881–893.

[169] Charles G.E. and Mason S.G. (1960) 'The mechanism of partial coalescence of liquid drops at liquid/liquid interfaces', *J. Colloid Sci.*, vol. 15(2), pp. 105–122.

[170] Princen H.M. and Mason S.G. (1965) 'The permeability of soap films to gases', *J. Colloid Sci.*, vol. 20(4), pp. 353–375.

[171] Princen H.M. and Mason S.G. (1965) 'Shape of a fluid drop at a fluid-liquid interface. ii. theory for three-phase systems', *J. Colloid Interf. Sci.*, vol. 20(3), pp. 246–266.

[172] Brown A.H. and Hanson C. (1967) 'Drop coalescence in liquid-liquid systems', *Nature*, vol. 214(5083), pp. 76–77.

[173] Jones A.F. and Wilson S.D.R. (1978) 'The film drainage problem in droplet coalescence', *J. Fluid Mech.*, vol. 87(2), pp. 263–288.

[174] Chi B.K. and Leal L.G. (1989) 'A theoretical study of the motion of a viscous drop toward a fluid interface at low reynolds number', *J. Fluid Mech.*, vol. 201, pp. 123–146.

[175] Shopov P.J. and Minev P.D. (1992) 'The unsteady motion of a bubble or drop towards a liquid-liquid interface', *J. Fluid Mech.*, vol. 235, pp. 123–141.

[176] Mohamed-Kassim Z. and Longmire E.K. (2004) 'Drop coalescence through a liquid/liquid interface', *Phys. Fluids*, vol. 16(7), pp. 2170–2181.

[177] Aarts D.G., Lekkerkerker H.N.W., Guo H., Wegdam G.H., and Bonn D. (2005) 'Hydrodynamics of droplet coalescence', *Phys. Rev. Lett.*, vol. 95(16), p. 164503.

[178] Thoroddsen S.T., Takehara K., and Etoh T.G. (2005) 'The coalescence speed of a pendent and a sessile drop', *J. Fluid Mech.*, vol. 527, p. 85.

[179] Yao W., Maris H.J., Pennington P., and Seidel G.M. (2005) 'Coalescence of viscous liquid drops', *Phys. Rev. E*, vol. 71(1), p. 016309.

[180] Aryafar H., Lukyanets A.S., and Kavehpour H.P. (2006) 'Inertia-dominated coalescence of drops', *Appl. Math. Res. Express*, vol. 2006, pp. 1–8.

[181] Aryafar H. and Kavehpour H.P. (2009) 'Electrocoalescence: effects of dc electric fields on coalescence of drops at planar interfaces', *Langmuir*, vol. 25(21), pp. 12460–12465.

[182] Eow J.S., Ghadiri M., Sharif A.O., and Williams T.J. (2001) *Chem. Eng. J.*, vol. 84(3), p. 173.

[183] Calvert P. (2001) *Chem. Mater.*, vol. 13(10), pp. 3299–3305.

[184] Baret J.C. and Mugele F. (2006) *Phys. Rev. Lett.*, vol. 96(1), p. 016106.

[185] Link D.R., Grasland-Mongrain E., Duri A., Sarrazin F., Cheng Z., Cristobal G., Marquez M., and Weitz D.A. (2006) 'Electric control of droplets in microfluidic devices', *Angew. Chem. Int. Ed.*, vol. 45(16), pp. 2556–2560.

[186] Ristenpart W., Bird J., Belmonte A., Dollar F., and Stone H.A. (2009) 'Non-coalescence of oppositely charged drops', *Nature*, vol. 461(7262), pp. 377–380.

[187] Anand V., Roy S., Naik V.M., Juvekar V.A., and Thaokar R.M. (2019) 'Electrocoalescence of a pair of conducting drops in an insulating oil', *J. Fluid Mech.*, vol. 859, pp. 839–850.

[188] Bird J.C., Ristenpart W.D., Belmonte A., and Stone H.A. (2009) *Phys. Rev. Lett.*, vol. 103(16), p. 164502.

[189] Helmensdorfer S. and Topping P. (2013) *EPL*, vol. 104(3), p. 34001.

[190] Bartlett C.T., Génério G.A., and Bird J.C. (2015) *J. Fluid Mech.*, vol. 763, pp. 369–385.

[191] Roy S., Anand V., and Thaokar R.M. (2019) *J. Fluid Mech.*, vol. 878, pp. 820–833.

[192] Wall D.P. and Wilson S.K. (1996) 'The linear stability of channel flow of fluid with temperature-dependent viscosity', *J. Fluid Mech.*, vol. 323, pp. 107–132.

[193] Craik A.D.D. (1969) 'The stability of plane couette flow with viscosity stratification', *J.Fluid Mech.*, vol. 36(4), pp. 685–693.

[194] Ranganathan B.T. and Govindarajan R. (2001) 'Stabilization and destabilization of channel flow by location of viscosity-stratified fluid layer', *Phys. Fluids*, vol. 13(1), pp. 1–3.

[195] Ern P., Charru F., and Luchini P. (2003) 'Stability analysis of a shear flow with strongly stratified viscosity', *J. Fluid Mech.*, vol. 496, pp. 295–312.

[196] Govindarajan R. (2004) 'Effect of miscibility on the linear instability of two-fluid channel flow', *Int. J. Multiphase Flow*, vol. 30(10), pp. 1177–1192.

[197] Selvam B., Merk S., Govindarajan R., and Meiburg E. (2007) 'Stability of miscible core–annular flows with viscosity stratification', *J. Fluid Mech.*, vol. 592, pp. 23–49.

[198] Selvam B., Talon L., Lesshafft L., and Meiburg E. (2009) 'Convective/absolute instability in miscible core-annular flow. part 2. numerical simulations and nonlinear global modes', *J. Fluid Mech.*, vol. 618, pp. 323–348.

[199] Talon L. and Meiburg E. (2011) 'Plane poiseuille flow of miscible layers with different viscosities: instabilities in the stokes flow regime', *J. Fluid Mech.*, vol. 686, pp. 484–506.

[200] Scoffoni J., Lajeunesse E., and Homsy G.M. (2001) 'Interface instabilities during displacements of two miscible fluids in a vertical pipe', *Phys. Fluids*, vol. 13(3), pp. 553–556.

[201] d'Olce M., Martin J., Rakotomalala N., Salin D., and Talon L. (2009) 'Convective/absolute instability in miscible core-annular flow. part 1: Experiments', *J. Fluid Mech.*, vol. 618, pp. 305–322.

[202] Ghosh S. and Usha R. (2016) 'Stability of viscosity stratified flows down an incline: Role of miscibility and wall slip', *Phys. Fluids*, vol. 28(10), p. 104101.

[203] Talon L., Goyal N., and Meiburg E. (2013) 'Variable density and viscosity, miscible displacements in horizontal hele-shaw cells. part 1. linear stability analysis', *J. Fluid Mech.*, vol. 721, pp. 268–294.

[204] Tan C.T. and Homsy G.M. (1986) 'Stability of miscible displacements in porous media: Rectilinear flow', *Phys. Fluids*, vol. 29(11), pp. 3549–3556.

[205] Preziosi L., Chen K., and Joseph D.D. (1989) 'Lubricated pipelining: stability of core-annular flow', *J. Fluid Mech.*, vol. 201, pp. 323–356.

[206] Chen C.Y. and Meiburg E. (1996) 'Miscible displacements in capillary tubes. part 2. numerical simulations', *J. Fluid Mech.*, vol. 326, pp. 57–90.

[207] Lajeunesse E., Martin J., Rakotomalala N., Salin D., and Yortsos Y.C. (1999) 'Miscible displacement in a hele-shaw cell at high rates', *J. Fluid Mech.*, vol. 398, p. 299–319.

[208] Schneider J.M. and Watson P.K. (1970) 'Electrohydrodynamic stability of space-charge-limited currents in dielectric liquids. i. theoretical study', *Phys. Fluids*, vol. 13(8), pp. 1948–1954.

[209] Atten P. and Moreau R. (1972) 'Stabilité électrohydrodynamique des liquides isolants soumis à une injection unipolaire', *J. Mécanique*, vol. 11(3), pp. 471–521.

[210] Atten P. and Lacroix J. (1979) 'Non-linear hydrodynamic stability of liquids subjected to unipolar injection', *J. Mécanique*, vol. 18, pp. 469–510.

[211] Vázquez P.A., Georghiou G.E., and Castellanos A. (2006) 'Characterization of injection instabilities in electrohydrodynamics by numerical modelling: comparison of particle in cell and flux corrected transport methods for electroconvection between two plates', *J. Phys. D: Appl. Phys.*, vol. 39(13), pp. 2754–2763.

[212] Traoré P. and Pérez A.T. (2012) 'Two-dimensional numerical analysis of electroconvection in a dielectric liquid subjected to strong unipolar injection', *Phys. Fluids*, vol. 24(3), p. 037102.

[213] Wu J., Traoré P., Vázquez P.A., and Pérez A.T. (2013) 'Onset of convection in a finite two-dimensional container due to unipolar injection of ions', *Phys. Rev. E*, vol. 88, p. 053018.

[214] Wu J., Pérez A.T., Traoré P., and Vázquez P.A. (2015) 'Complex flow patterns at the onset of annular electroconvection in a dielectric liquid subjected to an arbitrary unipolar injection', *IEEE Trans. Dielect. Electr. Insul.*, vol. 22(5), pp. 2637–2645.

[215] Zhang M., Martinelli F., Wu J., Schmid P., and Quadrio M. (2015) 'Modal and non-modal stability analysis of electrohydrodynamic flow with and without cross-flow', *J. Fluid Mech.*, vol. 770, pp. 319–349.

[216] Zhang M. (2016) 'Weakly nonlinear stability analysis of subcritical electrohydrodynamic flow subject to strong unipolar injection', *J. Fluid Mech.*, vol. 792, pp. 328–363.

[217] Wang B.F. and Sheu T.W.H. (2016) 'Numerical investigation of electrohydrodynamic instability and bifurcation in a dielectric liquid subjected to unipolar injection', *Comput. Fluids*, vol. 136, pp. 1–10.

[218] Timung S., Chaudhuri J., Borthakur M.P., Mandal T.K., Biswas G., and Bandyopadhyay D. (2017) 'Electric field mediated spraying of miniaturized droplets inside microchannel', *Electrophoresis*, vol. 38(11), pp. 1450–1457.

[219] van der Maesen F. (1949) 'The absolute dielectric constant of benzene', *Physica*, vol. 15(5-6), pp. 481–483.

[220] de Sousa F.F., Moreira S.G.C., Shirsley J., Nero J.D., and Alcantara Jr P. (2009) 'Dielectric properties of oleic acid in liquid phase', *J. Bionanoscience*, vol. 3(2), pp. 139–142.

[221] Ren Q.Y., Wang L.F., and Huang Q.A. (2016) 'A new method for real-time measuring the temperature-dependent dielectric constant of the silicone oil', *IEEE Sens. J.*, vol. 16(24), pp. 8792–8797.

[222] Spohner M., 'Study of the dielectric properties of vegetable oils and their constituents', in 'Diagnostic of Electrical Machines and Insulating Systems in Electrical Engineering (DEMISEE)', (2016), pp. 16–19.

[223] Mccluskey F.M.J. and Atten P. (1988) 'Modifications to the wake of a wire across poiseuille flow due to a unipolar space charge', *J. Fluid Mech.*, vol. 197, pp. 81–104.

[224] Pontiga F., Castellanos A., and Malraison B. (1995) 'Some considerations on the instabilities of nonpolar liquids subjected to charge injection', *Phys. Fluids*, vol. 7(6), pp. 1348–1356.

[225] Tobazeon R., Haidara M., and Atten P. (1984) 'Ion injection and kerr plots in liquids with blade-plane electrodes', *J. Phys. D: Appl. Phys.*, vol. 17(6), pp. 1293–1301.

[226] Atten P. and Haidara M. (1985) 'Electrical conduction and ehd motion of dielectric liquids in a knife-plane electrode assembly', *IEEE Trans. Electr. Insul.*, vol. E1-20(2), pp. 187–198.

[227] Higuera F.J. (2002) 'Electrohydrodynamic flow of a dielectric liquid due to autonomous injection of charge by a needle electrode', *Phys. Fluids*, vol. 14(1), pp. 423–426.

[228] Tsukahara Y., Hirose Y., and Otsubo Y. (2013) 'Effect of electrode materials on electrohydrodynamic flows of ethanol', *Colloids Surf. A: Physicochem. Eng. Asp.*, vol. 425, pp. 76–82.

[229] Vasilkov S.A., Chirkov V.A., and Stishkov Y.K. (2017) 'Study on high-voltage conductivity provided solely by field-enhanced dissociation in liquid dielectrics', *J. Electrosts.*, vol. 88, pp. 81–87.

[230] Bobyl V.G., Romanets R.G., and Alyab'ev V.A. (1965) 'The electrical conductivity of benzene and its monohalide derivatives in an ultrasonic field', *Soviet Physics Journal*, vol. 8, pp. 30–34.

[231] Zhang H.B., Edirisinghe M.J., and Jayasinghe S.N. (2006) 'Flow behaviour of dielectric liquids in an electric field', *J. Fluid Mech.*, vol. 558, pp. 103–111.

[232] Castellanos A. and Agrait N. (1992) 'Unipolar injection induced instabilities in plane parallel flows', *IEEE Trans Ind. Appl.*, vol. 28(3), pp. 513–519.

[233] Lara J.L., Castellanos A., and Pontiga F. (1997) 'Destabilization of plane poiseuille flow of insulating liquids by unipolar charge injection', *Phys. Fluids*, vol. 9(2), pp. 399–406.

[234] Orszag S.A. (1971) 'Accurate solution of the orr-sommerfeld stability equation', *J. Fluid Mech.*, vol. 50(4), pp. 689–703.

[235] Weideman J.A. and Reddy S.C. (2000) 'A matlab differentiation matrix suite', *ACM Trans. Math. Softw.*, vol. 26(4), pp. 465–519.

[236] Schmid P.J. and Henningson D.S., *Stability and Transition in Shear Flows* (Springer, 2001).

[237] Schmidt W.F. and Yoshino K. (2015) 'Ion mobilities in non-polar dielectric liquids: silicone oils', *IEEE Trans. Dielectr. Electr. Insul.*, vol. 22(5), pp. 2424–2427.

[238] Marath N.K. and Subramanian G. (2018) 'The inertial orientation dynamics of anisotropic particles in planar linear flows', *J. Fluid Mech.*, vol. 844, p. 357.

[239] Wong J., Lindstrom M., and Bertozzi A.L. (2019) 'Fast equilibration dynamics of viscous particle-laden flow in an inclined channel', *J. Fluid Mech.*, vol. 879, pp. 28–53.

[240] Lippert M.C. and Woods A.W. (2020) 'Experiments on the sedimentation front in steady particle-driven gravity currents', *J. Fluid Mech.*, vol. 889(A20), pp. 1–20.

[241] Mirzaeian N. and Alba K. (2018) 'Monodisperse particle-laden exchange flows in a vertical duct', *J. Fluid Mech.*, vol. 847, pp. 134–160.

[242] Jiang W. and Chen G. (2019) 'Dispersion of active particles in confined unidirectional flows', *J. Fluid Mech.*, vol. 877, pp. 1–34.

[243] Zade S., Shamu T.J., Lundell F., and Brandt L. (2020) 'Finite-size spherical particles in a square duct flow of an elastoviscoplastic fluid: an experimental study', *J. Fluid Mech.*, vol. 883(A6), pp. 1–33.

[244] Kumaran V. (2020) 'A suspension of conducting particles in a magnetic field–the particle stress', *J. Fluid Mech.*, vol. 901(A36), pp. 1–27.

[245] Kasbaoui M.H., Koch D.L., and Desjardins O. (2019) 'Clustering in euler-euler and euler-lagrange simulations of unbounded homogeneous particle-laden shear', *J. Fluid Mech.*, vol. 859, pp. 174–203.

[246] Zhang K. and Rival D.E. (2020) 'On the dynamics of unconfined and confined vortex rings in dense suspensions', *J. Fluid Mech.*, vol. 902(A6), pp. 1–19.

[247] Dsouza P.V. and Nott P.R. (2020) 'A non-local constitutive model for slow granular flow that incorporates dilatancy', *Journal of Fluid Mechanics*, vol. 888(R3), pp. 1–12.

[248] Swan J.W. and Brady J.F. (2007) 'Simulation of hydrodynamically interacting particles near a no-slip boundary', *Phys. Fluids*, vol. 19(11), p. 113306.

[249] Swan J.W. and Brady J.F. (2011) 'The hydrodynamics of confined dispersions', *J. Fluid Mech.*, vol. 687, pp. 254–299.

[250] Lu X., Soto F., Li J., Li T., Liang Y., and Wang J. (2017) 'Topographical manipulation of microparticles and cells with acoustic microstreaming', *ACS Appl. Mater. Interfaces*, vol. 9(44), pp. 38870–38876.

[251] Cheng S., Xia T., Liu M., Xu S., Gao S., Zhang G., and Tao S. (2019) 'Optical manipulation of microparticles with the momentum flux transverse to the optical axis', *Opt. Laser Technol.*, vol. 113, pp. 266–272.

[252] Yu-lan L., Biao W., and Dian-fu W. (2003) 'A theoretical medelling of the chain structure formation in electrorheological fluids', *Appl. Math. Mech.*, vol. 24(4), pp. 385–395.

[253] Feynman R.P., Leighton R.B., and Sands M. (1965) 'The feynman lectures on physics; vol. i', *American Journal of Physics*, vol. 33(9), pp. 750–752.

[254] Beer M., Kuppalu N., Stefanini M., Becker H., Schulz I., Manoli S., Schuette J., Schmees C., Casazza A., Stelzle M., and Arcangeli A. (2017) 'A novel microfluidic 3d platform for culturing pancreatic ductal adenocarcinoma cells: comparison with in vitro cultures and in vivo xenografts', *Sci. Rep.*, vol. 7(1), p. 1325.

[255] Kang K.H. and Li D. (2006) 'Dielectric force and relative motion between two spherical particles in electrophoresis', *Langmuir*, vol. 22(4), pp. 1602–1608.

[256] Im D.J., Ahn M.M., Yoo B.S., Moon D., Lee D.W., and Kang I.S. (2012) 'Discrete electrostatic charge transfer by the electrophoresis of a charged droplet in a dielectric liquid', *Langmuir*, vol. 28(32), pp. 11656–11661.

[257] Birlasekaran S. (1991) 'The measurement of charge on single particles in transformer oil', *IEEE Trans. Electr. Insul.*, vol. 26(6), pp. 1094–1103.

[258] Knutson C.R., Edmond K.V., Tuominen M.T., and Dinsmore A.D. (2007) 'Shuttling of charge by a metallic sphere in viscous oil', *J. Appl. Phys.*, vol. 101(1), p. 013706.

[259] Tobazéon R. (1996) 'Electrohydrodynamic behaviour of single spherical or cylindrical conducting particles in an insulating liquid subjected to a uniform dc field', *J. Phys. D: Appl. Phys.*, vol. 29(10), p. 2595.

[260] Elton E.S., Rosenberg E.R., and Ristenpart W.D. (2017) 'Crater formation on electrodes during charge transfer with aqueous droplets or solid particles', *Phys. Rev. Lett.*, vol. 119(9), p. 094502.

[261] Mersch E. and Vandewalle N. (2011) 'Antiphase synchronization of electrically shaken conducting beads', *Phys. Rev. E*, vol. 84(6), p. 061301.

[262] Feng J.Q. and Hays D.A. (1998) 'A finite-element analysis of the electrostatic force on a uniformly charged dielectric sphere resting on a dielectric-coated

electrode in a detaching electric field', *IEEE Trans. Ind. Appl.*, vol. 34(1), pp. 84–91.

[263] Feng J.Q. (2000) 'Electrostatic interaction between two charged dielectric spheres in contact', *Phys. Rev. E*, vol. 62(2), p. 2891.

[264] Feng J.Q. and Hays D.A. (2003) 'Relative importance of electrostatic forces on powder particles', *Powder Technol.*, vol. 135, pp. 65–75.

[265] Bichoutskaia E., Boatwright A.L., Khachatourian A., and Stace A.J. (2010) 'Electrostatic analysis of the interactions between charged particles of dielectric materials', *J. Chem. Phys.*, vol. 133(2), p. 024105.

[266] Dutta S., Ghosh A., Pattader P.S.G., and Bandyopadhyay D. (2019) 'Electric field mediated von kármán vortices in stratified microflows: Transition from linear instabilities to coherent mixing', *J. Fluid Mech.*, vol. 865, pp. 169–211.

[267] Malvern L.E., *Introduction to the Mechanics of a Continuous Medium* (Prentice Hall, 1969).

[268] Pohl H.A. (1958) 'Some effects of nonuniform fields on dielectrics', *J. Appl. Phys.*, vol. 29(8), pp. 1182–1188.

[269] Joseph G.G., Zenit R., Hunt M.L., and Rosenwinkel A.M. (2001) 'Particle-wall collisions in a viscous fluid', *J. Fluid Mech.*, vol. 433, pp. 329–346.

[270] Birwa S.K., Rajalakshmi G., Govindarajan R., and Menon N. (2018) 'Solid-on-solid contact in a sphere-wall collision in a viscous fluid', *Phys. Rev. Fluids*, vol. 3(4), p. 044302.

[271] Ruiz-Angulo A., Roshankhah S., and Hunt M.L. (2019) 'Surface deformation and rebound for normal single-particle collisions in a surrounding fluid', *J. Fluid Mech.*, vol. 871, pp. 1044–1066.

[272] Flittner R. and Přibyl M. (2017) 'Computational fluid dynamics model of rhythmic motion of charged droplets between parallel electrodes', *J. Fluid Mech.*, vol. 822, pp. 31–53.

[273] Lu G. and Zhai X. (2019) 'Analysis on heat transfer and pressure drop of a microchannel heat sink with dimples and vortex generators', *Int. J. Therm. Sci.*, vol. 145, p. 105986.

[274] Kim H., Padrino J.C., and Joseph D.D. (2011) 'Viscous effects on kelvin-helmholtz instability in a channel', *J. Fluid Mech.*, vol. 680, p. 398.

[275] Bergeron V., Bonn D., Martin J.Y., and Vovelle L. (2000) 'Controlling droplet deposition with polymer additives', *Nature*, vol. 405(6788), pp. 772–775.

[276] Cahn J.W. and Hilliard J.E. (1958) 'Free energy of a nonuniform system. i. interfacial free energy', *J. Chem. Phys.*, vol. 28(2), pp. 258–267.

[277] Jacqmin D. (2000) 'Contact-line dynamics of a diffuse fluid interface', *J. Fluid Mech.*, vol. 402, pp. 57–88.

[278] Haeberle S. and Zengerle R. (2007) 'Microfluidic platforms for lab-on-a-chip applications', *Lab Chip*, vol. 7(9), pp. 1094–1110.

[279] Mark D., Haeberle S., Roth G., Von Stetten F., and Zengerle R., 'Microfluidic lab-on-a-chip platforms: requirements, characteristics and applications', in 'Microfluidics based microsystems', (Springer, 2010), pp. 305–376.

[280] Smith P.G. and Van de Ven T.G.M. (1984) 'The effect of gravity on the drainage of a thin liquid film between a solid sphere and a liquid/fluid interface', *J. Colloid Interf. Sci.*, vol. 100(2), pp. 456–464.

[281] Pigeonneau F. and Sellier A. (2011) 'Low-reynolds-number gravity-driven migration and deformation of bubbles near a free surface', *Phys. Fluids*, vol. 23(9), p. 092102.

[282] Hartland S. (1971) 'The pressure distribution in axisymmetric draining films', *J. Colloid Interf. Sci.*, vol. 35(2), pp. 227–237.

[283] Boyer F., Lapuerta C., Minjeaud S., piar B., and Quintard M. (2010) 'Cahn–hilliard/navier–stokes model for the simulation of three-phase flows', *Transp. Porous Med.*, vol. 82, pp. 463–483.

[284] Wheeler A.A., McFadden G.B., and Boettinger W.J. (1996) 'Phase-field model for solidification of a eutectic alloy', *Proc. R. Soc. Lond. A*, vol. 452(1946), pp. 495–525.

[285] Jacqmin D., 'An energy approach to the continuum surface tension method', in '34th Aerospace sciences meeting and exhibit', (1996), p. 858.

[286] Jacqmin D. (1999) 'Calculation of two-phase navier-stokes flows using phase-field modeling', *J. Comput. Phys.*, vol. 155(1), pp. 96–127.

[287] Boyer F. and Lapuerta C. (2006) 'Study of a three component cahn-hilliard flow model', *ESAIM: Mathematical Modelling and Numerical Analysis-Modélisation Mathématique et Analyse Numérique*, vol. 40(4), pp. 653–687.

[288] Chiu P.H. and Lin Y.T. (2011) 'A conservative phase field method for solving incompressible two-phase flows', *J. Comput. Phys.*, vol. 230(1), pp. 185–204.

[289] de Sousa F.F., Moreira S.G.C., dos Santos d.S., Shirsley J., Nero J.D., and Alcantara Jr. P. (2009) 'Dielectric properties of oleic acid in liquid phase', *Journal of Bionanoscience*, vol. 3(2), pp. 139–142.

[290] Oommen T.V. and Claiborne C.C. (1999) 'High oleic acid electrical insulation fluids and method of making the same', *U. S. Patent*, vol. US5949017, pp. 1–19.

[291] Corach J., Sorichetti P.A., and Romano S.D. (2014) 'Electrical properties of vegetable oils between 20 hz and 2 mhz', *Int. J. Hydrog. Energy*, vol. 39(16), pp. 8754–8758.

[292] Saville D. (1997) 'Electrohydrodynamics: the taylor-melcher leaky dielectric model', *Annu. Rev. Fluid Mech.*, vol. 29(1), pp. 27–64.

[293] Brackbill J.U., Kothe D.B., and Zemach C. (1992) 'A continuum method for modeling surface tension', *J. Comput. Phys.*, vol. 100(2), pp. 335–354.

[294] Tomar G., Gerlach D., Biswas G., Alleborn N., Sharma A., Durst F., Welch S.W.J., and Delgado A. (2007) 'Two-phase electrohydrodynamic simulations using a volume-of-fluid approach', *J. Comput. Phys.*, vol. 227(2), pp. 1267–1285.

[295] Wehking J.D., Chew L., and Kumar R. (2013) 'Droplet deformation and manipulation in an electrified microfluidic channel', *Appl. Phys. Lett.*, vol. 103(5), p. 054101.

[296] Hrdlička J., Červenka P., Přibyl M., and Šnita D. (2010) 'Mathematical modeling of ac electroosmosis in microfluidic and nanofluidic chips using equilibrium

and non-equilibrium approaches', *J. Appl. Electrochem.*, vol. 40(5), pp. 967–980.

[297] Yue P., Feng J.J., Liu C., and Shen J. (2004) 'A diffuse-interface method for simulating two-phase flows of complex fluids', *J. Fluid Mech.*, vol. 515, p. 293.

[298] van der Waals J.D. (1979) 'The thermodynamic theory of capillarity under the hypothesis of a continuous variation of density', *J. Statist. Phys.*, vol. 20(2), pp. 200–244.

[299] Cahn J.W. and Hilliard J.E. (1959) 'Free energy of a nonuniform system. iii. nucleation in a two-component incompressible fluid', *J. Chem. Phys.*, vol. 31(3), pp. 688–699.

[300] De Gennes P.G., Brochard-Wyart F., and Quéré D., *Capillarity and wetting phenomena: drops, bubbles, pearls, waves* (Springer Science & Business Media, 2013).

[301] Culick F.E.C. (1960) 'Comments on a ruptured soap film', *J. Appl. Phys.*, vol. 31(6), pp. 1128–1129.

[302] Menchaca-Rocha A., Martínez-Dávalos A., Nunez R., Popinet S., and Zaleski S. (2001) 'Coalescence of liquid drops by surface tension', *Phys. Rev. E.*, vol. 63(4), p. 046309.

[303] Levich V.G., *Physicochemical hydrodynamics* (Prentice-Hall Inc., 1962).

[304] Keller J.B. (1998) 'Surface tension force on a partly submerged body', *Phys. Fluids*, vol. 10(11), pp. 3009–3010.

[305] Im D.J., Noh J., Moon D., and Kang I.S. (2011) 'Electrophoresis of a charged droplet in a dielectric liquid for droplet actuation', *Anal. Chem.*, vol. 83(13), pp. 5168–5174.

[306] Huh C. and Scriven L.E. (1969) 'Shapes of axisymmetric fluid interfaces of unbounded extent', *J. Colloid Interf. Sci.*, vol. 30(3), pp. 323–337.

[307] Rapacchietta A.V. and Neumann A.W. (1977) 'Force and free-energy analyses of small particles at fluid interfaces: Ii. spheres', *J. Colloid Interf. Sci.*, vol. 59(3), pp. 555–567.

[308] Rosen M.J., Wang H., Shen P., and Zhu Y. (2005) 'Ultralow interfacial tension for enhanced oil recovery at very low surfactant concentrations', *Langmuir*, vol. 21(9), pp. 3749–3756.

[309] Lekkerkerker H.N.W., De Villeneuve V.W.A., De Folter J.W.J., Schmidt M., Hennequin Y., Bonn D., Indekeu J.O., and Aarts D.G.A.L. (2008) 'Life at ultralow interfacial tension: wetting, waves and droplets in demixed colloid-polymer mixtures', *Eur. Phys. J. B*, vol. 64(3-4), pp. 341–347.

[310] Márquez A.L., Palazolo G.G., and Wagner J.R. (2007) 'Water in oil (w/o) and double (w/o/w) emulsions prepared with spans: microstructure, stability, and rheology', *Colloid Polym. Sci.*, vol. 285(10), pp. 1119–1128.

[311] Mitani S. and Sakai K. (2002) 'Measurement of ultralow interfacial tension with a laser interface manipulation technique', *Phys. Rev. E*, vol. 66(3), p. 031604.

[312] Aarts D.G.A.L., Schmidt M., and Lekkerkerker H.N.W. (2004) 'Direct visual observation of thermal capillary waves', *Science*, vol. 304(5672), pp. 847–850.

[313] Ward A.D., Berry M.G., Mellor C.D., and Bain C.D. (2006) 'Optical sculpture: controlled deformation of emulsion droplets with ultralow interfacial tensions using optical tweezers', *Chem. Commun.*, (43), pp. 4515–4517.

[314] Anand V., Juvekar V.A., and Thaokar R.M. (2019) *Colloids Surf. A Physicochem. Eng. Asp.*, vol. 568, pp. 294–300.

[315] Lai H.M., Leung P.T., Poon K.L., and Young K. (1989) 'Electrostrictive distortion of a micrometer-sized droplet by a laser pulse', *JOSA B*, vol. 6(12), pp. 2430–2437.

[316] López-Herrera J.M., Popinet S., and Herrada M.A. (2011) 'A charge-conservative approach for simulating electrohydrodynamic two-phase flows using volume-of-fluid', *J. Comput. Phys.*, vol. 230(5), pp. 1939–1955.

[317] Popinet S. (2003) *J. Comput. Phys.*, vol. 190(2), pp. 572–600.

[318] Herrmann M. (2008) 'A balanced force refined level set grid method for two-phase flows on unstructured flow solver grids', *J. Computat. Phys.*, vol. 227(4), pp. 2674–2706.

[319] Sussman M., Smith K.M., Hussaini M.Y., Ohta M., and Zhi-Wei R. (2007) 'A sharp interface method for incompressible two-phase flows', *J. Computat. Phys.*, vol. 221(2), pp. 469–505.

[320] Shin S., Abdel-Khalik S.I., Daru V., and Juric D. (2005) 'Accurate representation of surface tension using the level contour reconstruction method', *J. Computat. Phys.*, vol. 203(2), pp. 493–516.

[321] Taylor G.I. (1966) 'Studies in electrohydrodynamics. i. the circulation produced in a drop by an electric field', *Proc. R. Soc. A*, vol. 291(1425), pp. 159–166.

[322] Lin Y. (2013) 'Two-phase electro-hydrodynamic flow modeling by a conservative level set model', *Electrophoresis*, vol. 34(5), pp. 736–744.

[323] Pérez A.T. (2002) 'Charge and force on a conducting sphere between two parallel electrodes', *J. Electrostat.*, vol. 56(2), pp. 199–217.

[324] Dey K.K., Sharma D., Basu S., and Chattopadhyay A. (2008) 'Veering the motion of a magnetic chemical locomotive in a liquid', *J. Chem. Phys.*, vol. 129(12), p. 121101.

[325] Singh A.K., Dey K.K., Chattopadhyay A., Mandal T.K., and Bandyopadhyay D. (2014) 'Multimodal chemo-magnetic control of self-propelling microbots', *Nanoscale*, vol. 6(3), pp. 1398–1405.

[326] Singh A.K., Rarotra S., Pasumarthi V., Mandal T.K., and Bandyopadhyay D. (2018) 'Formic acid powered reusable autonomous ferrobots for efficient hydrogen generation under ambient conditions', *J. Mater. Chem. A*, vol. 6(19), pp. 9209–9219.

[327] Magnaudet J., Takagi S., and Legendre D. (2003) 'Drag, deformation and lateral migration of a buoyant drop moving near a wall', *J. Fluid Mech.*, vol. 476, pp. 115–157.

Appendix A

A.1 Energy Analysis

The contributions of the various forces towards production or dissipation of the disturbance kinetic energy is analysed to obtain a more comprehensive understanding of the instability phenomenon. The energy equation is obtained by first multiplying the x and z directional momentum equations (eq.(2.3)) with the complex conjugate of $\tilde{u}$ ($\tilde{u}^{\dagger}$) and $\tilde{w}$ ($\tilde{w}^{\dagger}$), respectively, then adding the equations, and subsequently, integrating them across the channel length [197]. The energy equation is given by,

$$E_{KE} = E_{RS} + E_{VD} + E_{V} + E_{E}, \tag{A.1}$$

where, E_{KE} represents the rate of change of disturbance kinetic energy, E_{RS} is the energy associated with the Reynolds stress, E_{VD} is the viscous dissipation energy, E_{V} is the rate of energy change due to viscosity stratification, and E_{E} is the energy associated with the electrical field body force component in the momentum equation. Here,

$$E_{KE} = \omega_r \int_{-1}^{1} \left(\left|\tilde{u}\right|^2 + \left|\tilde{w}\right|^2 \right) \mathrm{d}z,$$

$$E_{RS} = -\int_{-1}^{1} \left[\mathrm{Re}\left(\tilde{u}^{\dagger}\tilde{w}\right) u_0' \right] \mathrm{d}z,$$

$$E_{VD} = \frac{1}{Re^{\psi}} \int_{-1}^{1} \mu_0 \left[-\left(\left|\tilde{u}'\right|^2 + \left|\tilde{w}'\right|^2 \right) - k^2 \left(\left|\tilde{u}\right|^2 + \left|\tilde{w}\right|^2 \right) \right] \mathrm{d}z,$$

$$E_{V1} = \frac{1}{Re^{\psi}} \int_{-1}^{1} \left[\mu_0' \left\{ \mathrm{Re}\left(\tilde{u}^{\dagger}\tilde{u}' + 2\tilde{w}^{\dagger}\tilde{w}'\right) + \mathrm{Im}\left(k\tilde{u}^{\dagger}\tilde{w}\right) \right\} \right] \mathrm{d}z,$$

$$E_{V2} = \frac{1}{Re^{\psi}} \int_{-1}^{1} \left[\tilde{\mu} \left\{ \mathrm{Re}\left(\tilde{u}^{\dagger} u_0''\right) + \mathrm{Im}\left(k\tilde{w}^{\dagger} u_0'\right)\right\}\right] \mathrm{d}z,$$

$$E_{V3} = \frac{1}{Re^{\psi}} \int_{-1}^{1} \left[\tilde{\mu}' \left\{ \mathrm{Re}\left(\tilde{u}^{\dagger} u_0'\right)\right\}\right] \mathrm{d}z,$$

$$E_V = E_{V1} + E_{V2} + E_{V3},$$

$$E_E = \frac{Ra^{\psi}}{Re^{\psi}} \int_{-1}^{1} \left[\mathrm{Im}\left(k\tilde{u}^{\dagger}\psi_0''\tilde{\psi}\right) + \mathrm{Re}\left\{\tilde{w}^{\dagger}\left(\psi_0''\tilde{\psi}' + \tilde{\psi}''\psi_0' - k^2\psi_0'\tilde{\psi}\right)\right\}\right] \mathrm{d}z.$$

A.2 3-Dimensional Stability Analysis

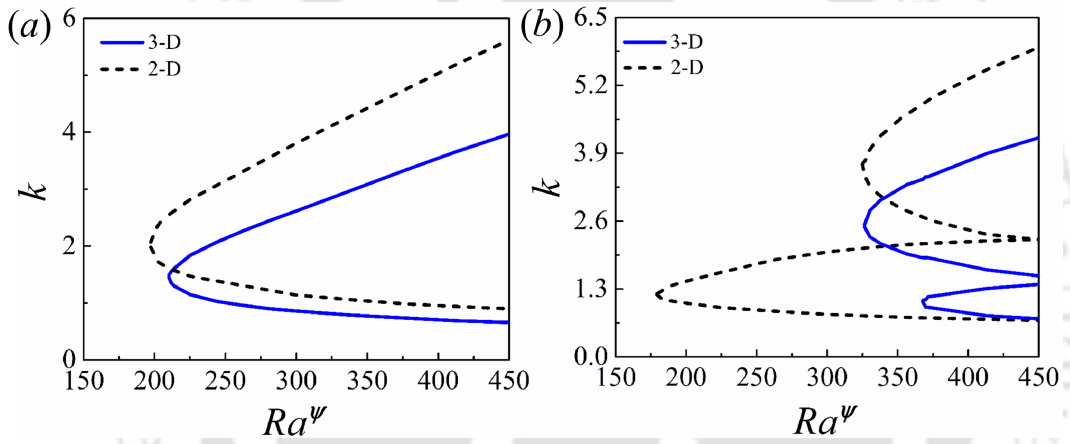

Figure A.1: Neutral stability curves (a) and (b) show the variation of stream-wise wavenumber (k) with electric Rayleigh number (Ra^{ψ}) for two-dimensional (evenly broken line) and three-dimensional (solid line) perturbations. The other parameters for (a) are, $V^L = 1$, $h = 0$, $\delta = 0.02$, $Sc = 10$, and $Re = 0.5$. The other parameters for (b) are, $V^L = 3$, $h = -0.3$, $\delta = 0.02$, $Sc = 10$, and $Re = 0.5$. The value of the span-wise wave number m is set equal to k for the three-dimensional cases.

The non-dimensional scheme is given by,

$$\left.\begin{aligned} (x, y, z, h, \delta) = R\,(x^*, y^*, z^*, h^*, \delta^*)\,, \quad (u, v, w) = \frac{K\Psi_0}{R}\,(u^*, v^*, w^*)\,, \\ \psi = \Psi_0\psi^*, \quad q = Q_0 q^*, \quad t = \frac{R^2}{K\Psi_0}t^*, \quad p = \frac{\rho K^2\Psi_0^2}{R^2}p^*, \quad \mu = \mu_1\mu^*. \end{aligned}\right\} \tag{A.2}$$

Here, u, v, and w represent the x, y and z directional velocity components, respec-

tively. The normal linear modes represented by eq. (2.19) are modified as,

$$\begin{aligned}[u,v,w,p,\psi,S,\mu]\,(x,y,z,t) &= [u_0\,(z)\,,0,0,p_0,\psi_0\,(z)\,,S_0\,(z)\,,\mu_0\,(z)] \\ &+ \left[\tilde{u},\tilde{v},\tilde{w},\tilde{p},\tilde{\psi},\tilde{S},\tilde{\mu}\right](z)\,e^{[\omega t+\mathrm{i}(kx+my)]}. \end{aligned} \tag{A.3}$$

Here, k represents the stream-wise and m represents the span-wise wavenumbers, respectively. The non-dimensional linearized momentum equation represented by eq. (2.24) becomes,

$$\begin{aligned}&Re^{\psi}\mathrm{i}k\left[(u_0-c)\left(\tilde{w}''-\left(k^2+m^2\right)\tilde{w}\right)-u_0''\tilde{w}\right] \\ &+Ra^{\psi}\left(k^2+m^2\right)\left[\psi_0'\tilde{\psi}''-\left(\psi_0'''+\left(k^2+m^2\right)\psi_0'\right)\tilde{\psi}\right]=\mu_0\tilde{w}''''+2\mu_0'\tilde{w}'''+ \\ &\left(\mu_0''-2\left(k^2+m^2\right)\mu_0\right)\tilde{w}''-2\left(k^2+m^2\right)\mu_0'\tilde{w}'+\left(\left(k^2+m^2\right)\mu_0''+\left(k^2+m^2\right)^2\mu_0\right)\tilde{w} \\ &-\mathrm{i}ku_0'\tilde{\mu}''-2\mathrm{i}ku_0''\tilde{\mu}'-\left(\mathrm{i}ku_0'''+\mathrm{i}k\left(k^2+m^2\right)u_0'\right)\tilde{\mu}.\end{aligned} \tag{A.4}$$

The charge conservation equation [eq. (2.25)] is modified as,

$$\begin{aligned}\mathrm{i}k\left[(u_0-c)\left(\tilde{\psi}''-\left(k^2+m^2\right)\tilde{\psi}\right)-\frac{\mathrm{i}}{k}\psi_0'''\tilde{w}\right]&=\psi_0'\tilde{\psi}'''+2\psi_0''\tilde{\psi}''+\left(\psi_0'''-\left(k^2+m^2\right)\psi_0'\right)\tilde{\psi}' \\ &-2\left(k^2+m^2\right)\psi_0''\tilde{\psi},\end{aligned} \tag{A.5}$$

The advection-diffusion equation of the concentration scalar becomes,

$$\mathrm{i}kRe^{\psi}Sc\left[(u_0-c)\,\tilde{S}-\frac{\mathrm{i}}{k}S_0'\tilde{w}\right]=\tilde{S}''-\left(k^2+m^2\right)\tilde{S}. \tag{A.6}$$

Equations (A.4–A.6) are solved using the boundary conditions mentioned in eqs. (2.27–2.29) and applying the numerical methodology mentioned in section 2.4.4.3 of the main text. Figure A.1 shows the comparison between neutral stability plots of the two-dimensional and three-dimensional perturbations. It may be noted that for the three-dimensional cases, $m = k$ is considered. Figure A.1(a) shows that the two dimensional perturbations are unstable at a lower value of critical Ra^{ψ} compared to the three-dimensional perturbations. Figure A.1(b) also depicts a similar trend with the two dimensional perturbations being more unstable than the three-dimensional ones. Thus, in the light of the above observation, it is evident that two dimensional

perturbations become unstable at lower values of Ra^{ψ}, compared to the three dimensional ones. Hence, only two dimensional transversal modes are considered in the analysis.

A.3 Estimation of Thickness of Mixed Layer δ

For the diffusion process, the length scale can be approximated as, $\delta \sim \sqrt{\kappa t}$. The diffusion coefficient $\kappa \sim \mathrm{O}\left(10^{-9} - 10^{-11}\right)$ m^{2}s^{-1} [62, 207], the time scale t can be approximated as, $t \sim \mathrm{O}\left(10^{-1} - 10^{-2}\right)$ s. Thus, δ is obtained as, $\delta \sim \mathrm{O}\left(10^{-5} - 10^{-6}\right)$ m. This gives the dimensionless value of $\delta \sim \mathrm{O}\left(10^{-1} - 10^{-2}\right)$ considering the characteristic length to be $\sim 10^{-4}$ m. It was further confirmed through the nonlinear CFD simulations, the details of which are mentioned in section 2.4.5. Figure A.2 shows the base state scalar (S_0) profile, for $V^L = 6$. It can be seen from the figure that the thickness of the mixed interface at the base state is ~ 0.05.

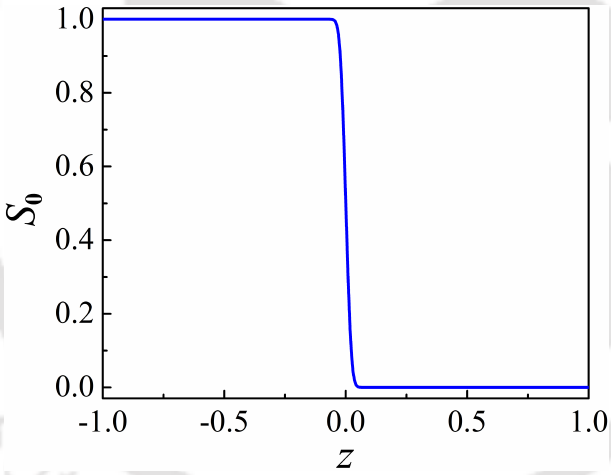

Figure A.2: The variation concentration scalar (S_0) across the channel at the base state. The parameters considered for the simulation are, $h = 0$, $Sc = 700$ and $V^L = 6$.

Appendix B

B.1 Validation of the Numerical Method

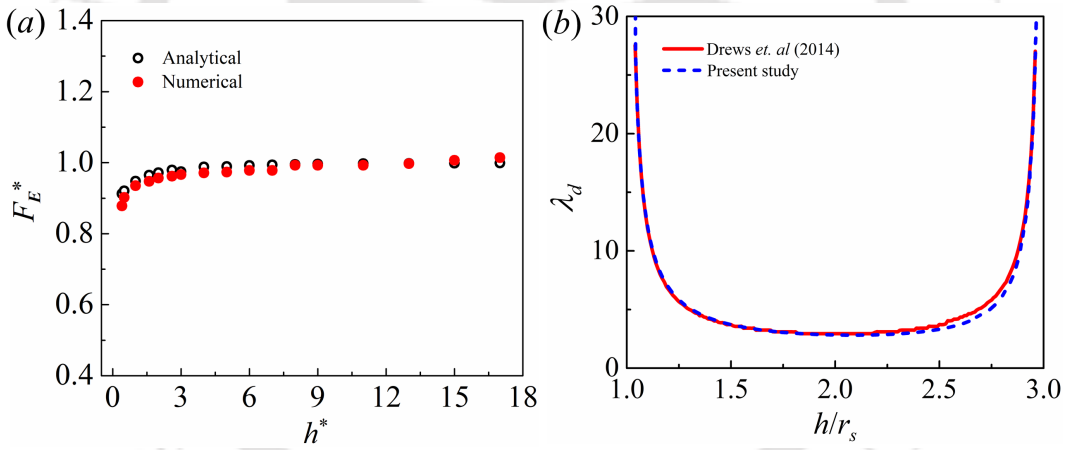

Figure B.1: (a) Variation of normalized electric force ($F_e{}^*$) acting on a solid particle with its normalized distance (h^*) from the grounded bottom electrode. The solid (hollow) symbols denote the numerically (analytically) obtained values, respectively. The other parameters used for the numerical simulations are: $r_s = 0.5$ mm, $d = 20$ mm, $\varepsilon_f = 2.5\varepsilon_0$, $q = 7\times10^{-11}$ C and $E_0 = 6$ kVcm^{-1}. (b) Variation of drag coefficient (λ_d) with normalized distance (h/r_s) of the particle from the grounded electrode at $z = 0$. The dashed (solid) line denotes values obtained numerically (analytically obtained by [111]) from the present study, respectively, for an aspect ratio (d/r_s) of 4.

For the purpose of validation of the numerical method mentioned in section 3.4 of chapter 3 the normalized electrical force $F_e{}^*\left(=\dfrac{F_e}{qE_0}\right)$ experienced by a conductive particle ($r_s = 0.5$ mm) oscillating between parallel electrodes 20 mm apart

obtained numerically is compared to the force obtained analytically by Pérez [323]. If h is defined as the distance between the centre of the particle and the grounded electrode at $z = 0$, and d as the distance between the electrodes, then the analytical expressions for the force experienced by the particles read as [113, 323] as,

$$F_e = 4\pi\varepsilon_f {r_s}^2 {E_0}^2 F_0\left(\frac{h}{r_s}\right) + qE_0F_1\left(\frac{h}{r_s}\right) + \frac{q^2}{4\pi\varepsilon_f {r_s}^2}F_2\left(\frac{h}{r_s}\right), \qquad h \leq \frac{d}{2} \tag{B.1}$$

$$F_e = -4\pi\varepsilon_f {r_s}^2 {E_0}^2 F_0\left(d-h\right) + qE_0F_1\left(d-h\right) - \frac{q^2}{4\pi\varepsilon_f {r_s}^2}F_2\left(d-h\right), \qquad h > \frac{d}{2} \tag{B.2}$$

where, E_0 is the average electric field intensity between the electrodes in absence of the solid particle. The coefficients F_0, F_1 and F_2 are defined elsewhere [323]. Figure B.1(a) shows the variation of ${F_e}^*$ with the normalized distance $h^*\left(=\dfrac{h-r_s}{r_s}\right)$ obtained numerically alongside the corresponding values obtained from equations (B.1) and (B.2). It can be seen from the figure that when the particle is sufficiently close to either electrode, the force predicted numerically (solid symbols) is marginally different from the corresponding values predicted analytically (hollow symbols), with a maximum relative error $\left(\left|\dfrac{{F_{e,}}^*{}_{numerical} - {F_{e,}}^*{}_{analytical}}{{F_{e,}}^*{}_{numerical}}\right| \times 100\%\right)$ of $\sim$ 3.8%. It may be hypothesized that presence of the particle between parallel electrodes, as considered in the numerical solution, leads to the influence of the image charges on the total force experienced by the particle, which leads to the deviation from the analytically obtained values. Figure B.1(b) predicts the comparison of the variation of dimensionless drag coefficient (λ_d) with the dimensionless position (h/r_s) of the particle between two electrodes obtained by the present numerical method to that reported analytically by Drews *et al.* [111]. The drag coefficient captures the increase in the drag force experienced by the particle due to the presence of the walls and can be calculated from the following equation,

$$\lambda_d = \frac{\boldsymbol{F}_e}{6\pi\mu_f r_s \boldsymbol{v}_s}. \tag{B.3}$$

It must be noted that equation (B.3) is valid when inertial acceleration of the particle is small compared to drag forces [111]. The plots in figure B.1(b) suggests a reasonable agreement of the values of drag coefficient obtained numerically and analytically. Both the plots suggest significant increase in the drag coefficient close to

the walls due to increase in the hydrodynamic drag force experienced by the particle.

B.2 Grid Convergence Study

(*a*)

G_R	No. of elements	$\tau_z{}^t$	Error (%)	$\tau_z{}^b$	Error (%)
A	15797	183.88846	--	-183.55259	--
B	32281	185.74894	1.0117	-185.57618	1.1024
C	46546	186.1287	0.2044	-185.99532	0.226
D	56681	186.32837	0.107	-186.19953	0.109

(*b*)

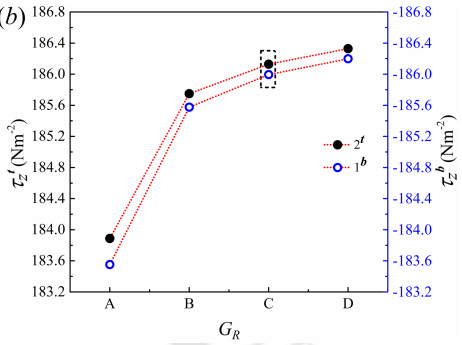

Figure B.2: (*a*) Tabulated values of the number of mesh elements corresponding to each grid resolution (G_R), the values of the z- component of the Maxwell stress tensor at the bottommost point of sphere 1 ($\tau_z{}^b$) and the topmost point of sphere 2 ($\tau_z{}^t$) at $t = 0.06$ s and the relative error for the mentioned grid resolutions. (*b*) Variation of $\tau_z{}^t$ and $\tau_z{}^b$ with the grid resolutions. The rectangular box at C represents the chosen grid resolution for the numerical simulations. The other parameters for the simulations are, $E_0 = 9$ kVcm^{-1}, $r_s = 0.5$ mm for each sphere (1 and 2), $d = 5$ mm, $\mu_f = 0.3$ Pa.s, $\varepsilon_f = 2.5\varepsilon_0$, $\rho_f = 970$ kgm^{-3} and $\rho_s = 1280$ kgm^{-3}.

To ensure the grid independence of the numerical simulation results of chapter 3, a grid convergence study was carried out by considering four grid resolutions (G_R) tabulated in figure B.2(*a*). For the purpose of the test, two equal sized spheres 1 and 2 were subjected to an electric field of magnitude 9 kVcm^{-1}. The spheres were assigned the theoretical values of charge of opposite polarity (sphere 1 positively charged and sphere 2 negatively charged). At time $t = 0$, the positions of the spheres 1 and 2 were $h = 3.8$ mm and $h = 1.3$ mm, respectively. On application of electric field the spheres were subjected to electric force and the values of the z-component of the Maxwell stress tensor at the bottommost point of sphere 1 ($\tau_z{}^b$) and the topmost point of sphere 2 ($\tau_z{}^t$) are tabulated in figure B.2(*a*) and shown in figure B.2(*b*), for four different grid resolutions. Both figures (*a*) and (*b*) suggest that the convergence improves with grid refinement. Table B.2(*a*) predicts that the relative errors in the values of $\tau_z{}^t$ and $\tau_z{}^b$ for grid resolutions C (46546 elements) and D (56681 elements), are ∼0.1%. Hence, grid C was chosen for the numerical simulations to optimize the computational load.

B.3 Characterization of the Beads

B.3.1 Materials

Iron sulphate heptahydrate ($FeSO_4.7H_2O$), hydrochloric acid (HCl) (37%), ethanol (C_2H_5OH) (99.9%), and Amberlite IR-120 particles were obtained from Merck (India). Iron (III) chloride hexahydrate ($FeCl_3{\cdot}6H_2O$), silver nitrate ($AgNO_3$), Nickel (II) chloride hexahydrate ($NiCl_2.\ 6H_2O$), and sodium borohydride ($NaBH_4$) were procured from Sigma-Aldrich (India). The aforementioned chemicals were used without further purification. The Milli-Q grade water was used in the experiments.

B.3.2 Methods

The deposition of metallic entities on the ion-exchange Amberlite IR-120 resin particles was performed by following the previously reported protocols with slight modifications [324–326]. Initially, 3 g of Amberlite IR-120 (cationic exchange resin particles) were thoroughly washed with MilliQ grade water and then immersed in 20 ml of HCl (0.3 M) and kept for 8 h at 25°C for activation. After activation, the particles were washed with water to remove the excess HCl and then dried overnight at 60°C. Thereafter, the particles were suspended overnight in a beaker containing 20 ml of 1.5 M of metal salt solution ($FeSO_4.7H_2O$, $NiCl_2.6H_2O$, $AgNO_3$) at 25°C. In case of $AgNO_3$ treatment, the beaker was completely covered with aluminium foil and was kept in dark conditions in order to prevent or slow down the light-mediated decomposition of the silver salt. The higher concentration of metallic salt solution was used in this protocol to ensure formation of densely-packed nanoparticle (NP) aggregates or metallic thin films over the resin particles rather than discrete metallic NPs, after reduction process. Following this, the particles were retrieved after metal salt treatment and then suspended in a beaker containing 5 ml of water. After this, 10 ml of $NaBH_4$ (0.8 M) was added dropwise to the suspension with vigorous stirring. The black colouration of the particles indicated the formation of iron (Fe) and nickel (Ni) coating on the polymer particles and in the case of silver (Ag) coating, a metallic silvery appearance was observed on the spherical particles. The particles were washed thrice with ethanol to prevent rapid oxidation, and vacuum dried for 1 h at 60°C. The freshly prepared metal-coated particles were used for all the experiments. The uncoated and freshly prepared metal-coated Amberlite IR-120 resin particles were characterized using Field emission scanning electron microscopy

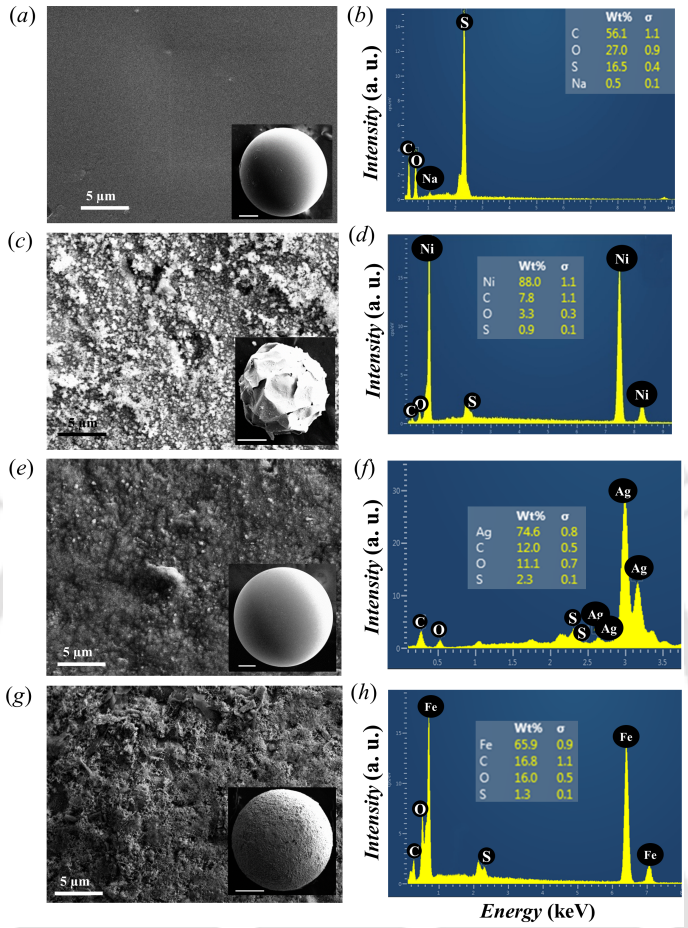

Figure B.3: (*a*) Field Emission Scanning Electron Microscopy (FESEM) image of the surface of an uncoated Amberlite IR-120 polymer resin particle. The scale bar at the bottom is of 5 µm. The inset image shows an uncoated spherical resin particle. The scale bar at the bottom is of 125 µm. (*b*) Spot Energy Dispersive X-ray (EDX) of the uncoated polymer resin. (*c*) FESEM image of the surface of a freshly prepared nickel (Ni)-coated resin particle. The scale bar at the bottom is of 5 µm. The inset image shows a spherical Ni-coated resin particle. The scale bar at the bottom is of 250 µm. (*d*) Spot EDX of spherical Ni-coated resin particle shows the elemental Ni peak. (*e*) FESEM image of the surface of a freshly prepared silver (Ag)-coated resin particle. The scale bar at the bottom is of 5 µm. The inset image shows a spherical Ag-coated resin particle. The scale bar at the bottom is of 125 µm. (*f*) Spot EDX of spherical Ag-coated resin particle shows the elemental Ag peak. (*g*) FESEM image of the surface of a freshly prepared iron (Fe)-coated resin particle. The scale bar at the bottom is of 25 µm. The inset image shows a spherical Fe-coated resin particle. The scale bar at the bottom is of 250 µm. (*h*) Spot EDX of spherical Fe-coated resin particle shows the elemental Fe peak.

(Zeiss Sigma FESEM, Germany). The FESEM images shown in figure B.3(c), figure B.3(e) and figure B.3(g) of an Amberlite IR-120 resin surface shows the presence of a homogenous thin film or coating of Ni, Ag and Fe, respectively, resulting in rough surface texture as compared to the uncoated resin (figure B.3(a)). The spot EDX analysis - figure B.3(d), figure B.3(f) and figure B.3(h) on the agglomerates confirmed the presence of the elemental Ni, Ag and Fe deposits, respectively, over the surface of the resin particles.

B.4 Experimental Determination of Charge Acquired by the Particle

In order to estimate the total charge acquired by the particle (q) in contact with the electrode, the following force balance, neglecting the acceleration of the particles, is used [112, 256],

$$qE_0 = 6\pi\mu_f r_s v_s \lambda_d. \tag{B.4}$$

The average electric field intensity is calculated as, $E_0 = \dfrac{\psi_0}{d}$, where ψ_0 is the applied potential and d is the distance between the electrodes. The term on the left-hand side of the equation is the Coulomb force acting on the charged droplet. The term on the R.H.S. of equation B.4 accounts for the drag force experienced by the particle. The dimensionless drag coefficient (λ_d) is obtained from figure 3.4(b). The frames extracted from the recorded videos are used to estimate the average speed (v_s) of the particles. Particle motions near the electrodes are not taken in the calculations.

Appendix C

C.1 Experimental Determination of Charge Acquired by the Droplet

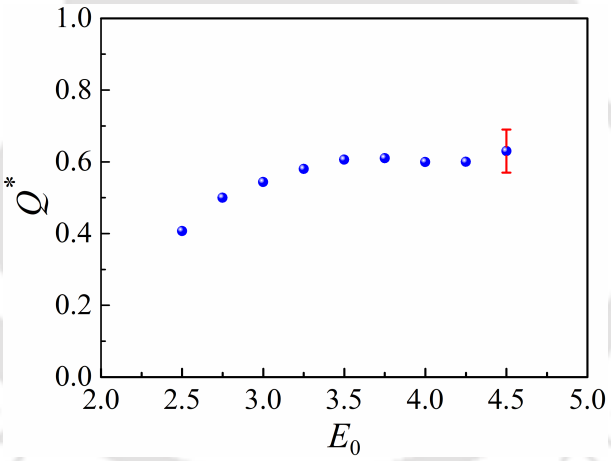

Figure C.1: Variation of the dimensionless charge ($Q^* = Q_0/Q_{th}$) acquired by the droplet ($r_C = 0.1$ cm) from the lower electrode with applied electric field intensity (E_0). The error bar indicates maximum standard deviation obtained from four sets of experiments.

In order to estimate the total charge acquired by the droplet, Q_0, in contact with the electrode, the following vertical force balance neglecting the acceleration of the droplet was used [186, 256],

$$Q_0 E_0 = \frac{4}{3}\pi r_{\mathrm{C}}^3(\rho_{\mathrm{C}} - \rho_{\mathrm{B}})g + 4\pi\mu_{\mathrm{B}} r_{\mathrm{C}} u_{\mathrm{C}} \left(\frac{3\mu^*_{\mathrm{CB}} + 2}{2\,(\mu^*_{\mathrm{CB}} + 1)}\right). \tag{C.1}$$

The average electric field intensity was calculated as, $E_0 = \psi_0/H$, where ψ_0 is the applied potential and H is the distance between the electrodes. The term on the left-hand side of the equation is the Coulomb force acting on the charged droplet. The first term of the right-hand side of eq. (C.1) is the net gravitational pull experienced by the droplet with radius r_C. The second term of the RHS of equation (C.1) accounts for the drag force experienced by the water droplet in the highly viscous oil ($\mu^*_{CB} \approx 0.0033$), calculated using the Hadamard Rybczynski drag coefficient [305]. It may be noted that during the experiments the droplet was carefully placed each time near the centre of the cuvette away from the walls. Using the expression, $4\pi\mu_B r_C u_C \left(\frac{3\mu^*_{CB}+2}{2\left(\mu^*_{CB}+1\right)}\right)\left(1-\frac{3}{8}\kappa-\frac{3}{64}\kappa^4\right)^{-1}$ [327], which contains the effect of the vertical walls, the correction factor is found to be ~ 1.02. Here, $\kappa\,(=r_C/(L/2))$ signifies the ratio of the droplet size to its distance from the wall. As, the wall correction is negligible, the wall effect is ignored in calculation of the drag force. For the calculation of Q_0 using the above-mentioned equation, a droplet of water ($r_C \approx 0.1$ cm) was placed inside phase B (silicone oil) and electric field was applied. The motion of the droplet was recorded and the frames extracted from the video was used to estimate the average speed (u_C) of the droplet. The average charge acquired by the droplets was then estimated for each value of E_0, by plugging the measured value of u_C into eq. (C.1).

Figure C.1 shows the variation of the charge acquired by the water droplet in silicone oil from the lower electrode with the applied field intensity. The plot shows that the charge acquired by the droplet increases with increase in the value of the applied field intensity. It can be also be seen from the plot that the water droplet acquires almost $40-65$ % of the theoretical value of charge, Q_{th}. Such values of charge acquisition have also been previously noted for the oscillation of water droplets of different conductivity in silicone oil [305].

C.2 Validation of the Numerical Method

In order to validate the proposed numerical method (PNM) of section 4.4, a few results reported by Shopov & Minev [175] (SM), for the approach of a drop towards a liquid-liquid interface have been reproduced. A new set of dimensionless numbers

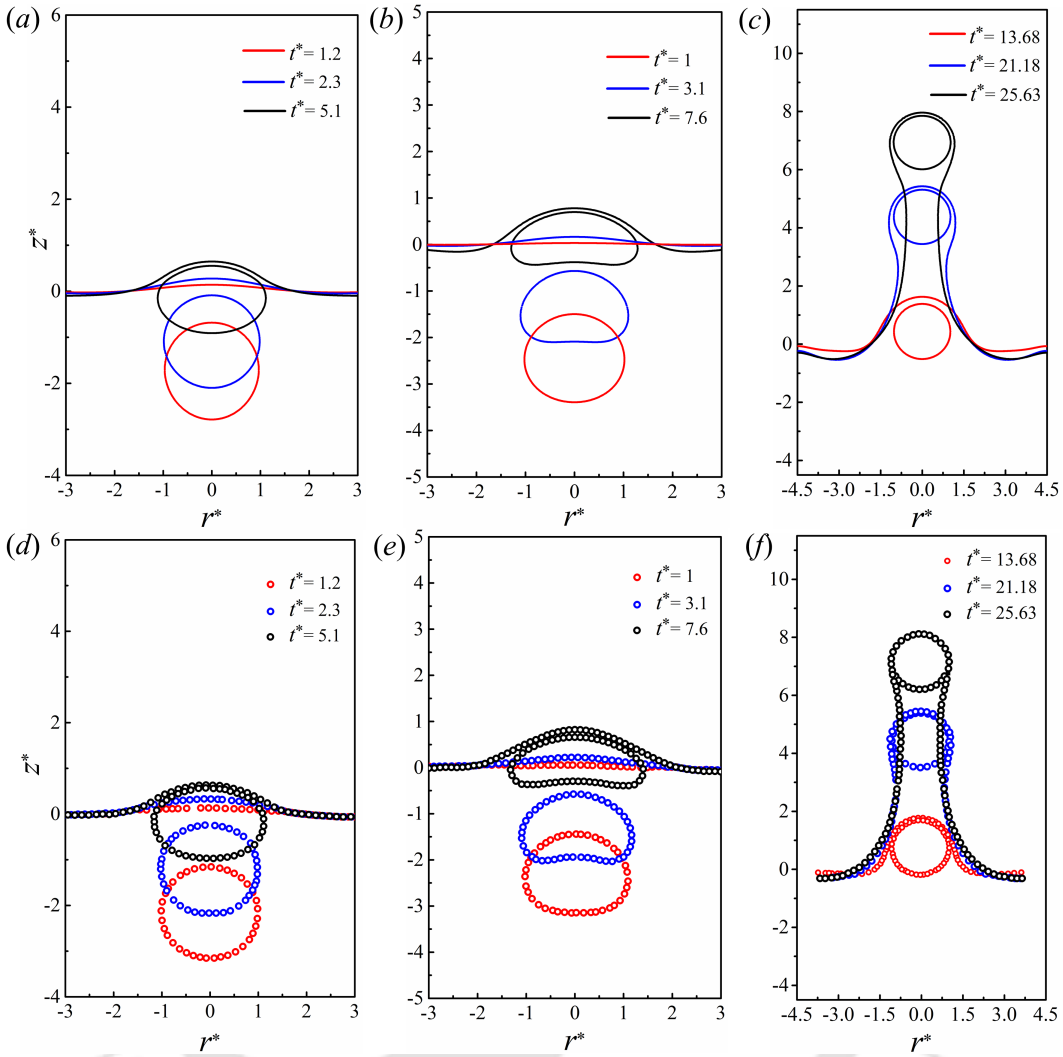

Figure C.2: Positions of a droplet moving from a carrier liquid towards the target liquid obtained from the present numerical model for (*a*) $\Re = 0.0021$, $\aleph = 3.14$, $\mu^*_{AB} = \mu^*_{CB} = 0.021$, $\sigma^*_2 = 1$, $\rho^*_{AB} = \rho^*_{CB} = 0.2$, $D = 1.5$, and $We_E = 10^{-8}$ (*b*) $\Re = 10$, $\aleph = 5$, $\mu^*_{AB} = \mu^*_{CB} = 0.333$, $\sigma^*_2 = 1$, $\rho^*_{AB} = \rho^*_{CB} = 0.2$, $D = 1.5$, and $We_E = 10^{-8}$ (*c*) $\Re = 18$, $\aleph = 1$, $\mu^*_{AB} = 0.33$, $\mu^*_{CB} = 0.36$, $\sigma^*_2 = 0.01$, $\rho^*_{AB} = 0.9$, $\rho^*_{CB} = 0.1$, $D = 3$, and $We_E = 10^{-8}$. Positions of a droplet moving from a carrier liquid towards the target liquid reported by [175] for (*a*) $\Re = 0.0021$, $\aleph = 3.14$, $\mu^*_{AB} = \mu^*_{CB} = 0.021$, $\sigma^*_2 = 1$, $\rho^*_{AB} = \rho^*_{CB} = 0.2$, and $D = 1.5$, (*b*) $\Re = 10$, $\aleph = 5$, $\mu^*_{AB} = \mu^*_{CB} = 0.333$, $\sigma^*_2 = 1$, $\rho^*_{AB} = \rho^*_{CB} = 0.2$, and $D = 1.5$, and (*c*) $\Re = 18$, $\aleph = 1$, $\mu^*_{AB} = 0.33$, $\mu^*_{CB} = 0.36$, $\sigma^*_2 = 0.01$, $\rho^*_{AB} = 0.9$, $\rho^*_{CB} = 0.1$, and $D = 3$.

are defined as reported by SM, which are,

$$\left.\begin{aligned} l = \left(\frac{3V_C}{4\pi}\right)^{1/3},\ U_0 = \frac{2(\rho_B - \rho_C)gl^2}{9\mu_B},\ \Re = \frac{lU_0\rho_B}{\mu_B},\ \aleph = \frac{gl^2(\rho_B - \rho_C)}{\sigma_{AB}} \\ \mu^*_{CB} = \frac{\mu_C}{\mu_B},\ \mu^*_{AB} = \frac{\mu_A}{\mu_B},\ \rho^*_{CB} = \frac{\rho_C}{\rho_B},\ \rho^*_{AB} = \frac{\rho_A}{\rho_B},\ D = \frac{H_1}{l},\ t^* = \frac{l}{U_0}. \end{aligned}\right\} \quad \text{(C.2)}$$

Here, l, U_0, $\Re$, and $\aleph$ denote the characteristic length, characteristic velocity, Reynolds number, and Eötvös number, respectively. The notation H_1 denotes the distance of the centre of the droplet from the position of the undisturbed interface at $t = 0$. Figures C.2$(a-c)$ show the positions of a droplet under different conditions, as predicted by the numerical method proposed in the present study. Figures C.2$(d-f)$ show the corresponding positions reported by Shopov & Minev [175]. Figure C.2(a) and C.2(d) shows the low Reynolds number ($\Re = 0.0021$) buoyancy driven motion of a drop towards a liquid-liquid interface. The drop rises almost undeformed towards the interface and deforms into an oblate shape on reaching the interface, due to combined effect of the buoyant (upwards) and interfacial tension (downward) forces. The figures suggest that the PNM mimics the results of SM quite accurately. Figures C.2(b) and C.2(e) depict the buoyancy driven motion of a drop towards a liquid-liquid interface at a relatively higher Reynolds number ($\Re = 10$) compared to figures C.2(a) and C.2(d). Here, due to increase in the inertial force, the particle is indented at the rear end. Here, the PNM shows reasonably good agreement with SM, however, droplet deformation in the former case is slightly lower. Figures C.2(c) and C.2(f) show the high Reynold number ($\Re = 10$) motion of a droplet, towards a liquid-liquid interface of very low interfacial tension ($\sigma_2^* = 0.01$). As the restricting interfacial tension force is very low compared to the buoyant force acting on the droplet, it moves up towing a long tail of the carrier liquid along with it. Nonetheless, there is a reasonably fair agreement between the droplet positions predicted by the PNM and those reported by SM. There is a slight difference in the thickness of the tail and hence in the volume of entrained fluid, which are expected to occur because of the choice of the diffuse interface thickness and/or the grid resolution. Thus, figure C.2 confirms the accuracy of the PNM used for the simulations in the present study.

C.3 Grid Convergence Study

In order to optimize the grid resolution for the numerical results of chapter 4, a grid convergence study has been carried out, as shown in figure C.3. The positions of a droplet (C) at various instants during its migration from liquid B towards liquid A are depicted in figures C.3$(a-d)$ for different grid resolutions. The corresponding variations of the distance of the top of the droplet from the undisturbed interface (d^*) with time are shown in figure C.3(e). In figure C.3(f) the relative percentage

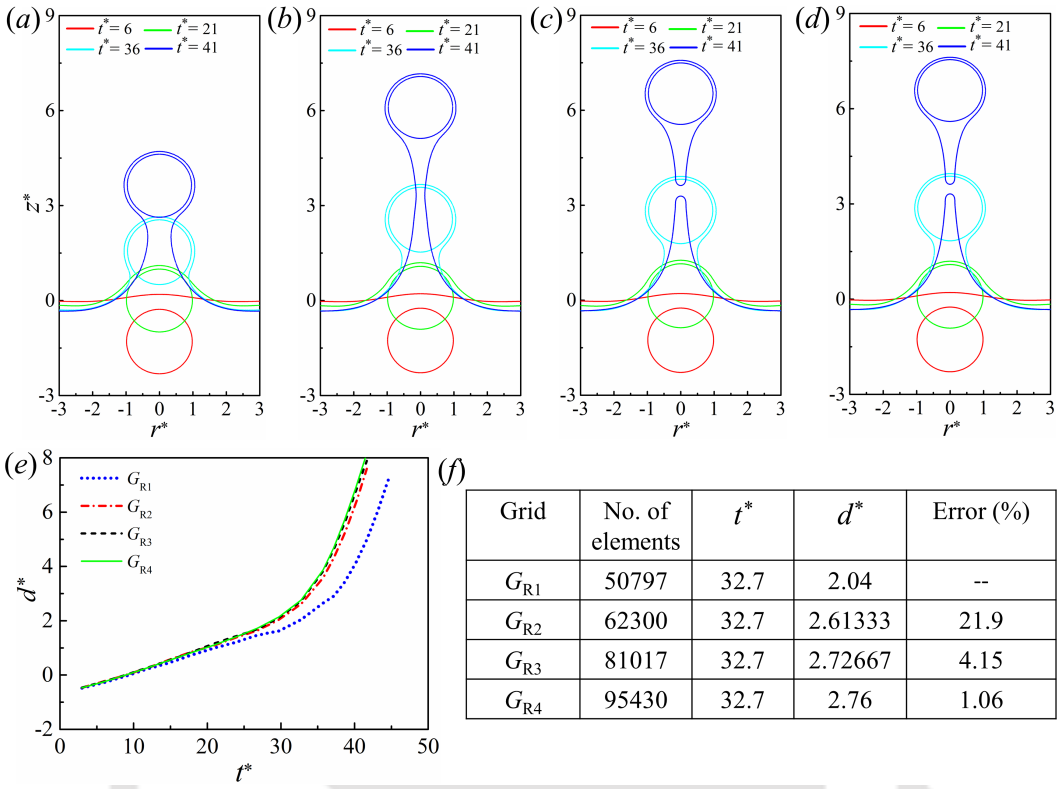

Grid	No. of elements	t^*	d^*	Error (%)
G_{R1}	50797	32.7	2.04	--
G_{R2}	62300	32.7	2.61333	21.9
G_{R3}	81017	32.7	2.72667	4.15
G_{R4}	95430	32.7	2.76	1.06

Figure C.3: Positions of a droplet (C) moving from the carrier liquid B towards the target liquid A at $We_E = 9$ at grid resolution (a) $G_{R1}(= 50797)$, (b) $G_{R2}(= 62300)$, (c) $G_{R3}(= 81017)$, and (d) $G_{R4}(= 95430)$. (e) Variation of the normalized position of the top of the droplet from the position of the undisturbed interface (d^*) with time (t^*) for the cases shown in $(a - d)$. (f) Table depicting the percentage error in the values of d^* for different grid resolutions. The other dimensionless numbers associated are, $\rho^*_A = 0.92$, $\rho^*_B = 0.96$, $\rho^* = 1$, $\mu^*_{AB} = 0.17$, $\mu^*_{BC} = 300$, $\sigma^*_1 = 1.08$, $\sigma^*_2 = 0.028$, and $\sigma^*_3 = 0.026$.

error $\left(\dfrac{d^*_{GR,i+1} - d^*_{GR,i}}{d^*_{GR,i+1}} \times 100\%\right)$ values are tabulated for the tested grid resolutions. The figures suggest that the migration characteristics are highly dependent on the grid resolutions. At low number of elements, the migration characteristics are found to be slow and the droplet rises sluggishly. The convergence of the simulated results improves with grid refinement. The figure C.3(f) suggest that the relative error in the simulated values of the droplet positions for G_{R3} and G_{R4} is $\sim$1%. Thus, to optimize the computational load simulation time, the simulations were carried out at grid resolution G_{R3}.

List of Publications

Journal Publications

1. **S. Dutta**, A. Ghosh, P. S. G. Pattader and D. Bandyopadhyay, Electric Field Mediated von Kármán Vortices in Stratified Microflows: Transition from Linear Instabilities to Coherent Mixing, ***Journal of Fluid Mechanics***, 865, 169–211, 2019.
2. **S. Dutta**, A. K. Singh, P. S. G. Pattader, and D. Bandyopadhyay, Genesis of Electric Field assisted Microparticle Assemblage in a Dielectric Fluid, ***Journal of Fluid Mechanics***, 915, 1−36, 2021.
3. **S. Dutta**, P. S. G. Pattader, and D. Bandyopadhyay, Electric Field Mediated Modes of Active Droplet Transport across a Deformable Interface, ***Manuscript Submitted and Under Review***.
4. **S. Dutta**, J. Chaudhuri, P. S. G. Pattader, and D. Bandyopadhyay, Asymmetric 'Tentacles' Formation in Coalescing/Non-Coalescing Drops, ***Manuscript Submitted and Under Review***.
5. **S. Dutta**, N. Mandal, and D. Bandyopadhyay, Paper-based α-amylase detector for point-of-care diagnostics, ***Biosensors and Bioelectronics***, 78, 447–453, 2016.
6. N. Mandal, **S. Dutta**, A. Gupta, and D. Bandyopadhyay, Paper-Based Sensors for Point-of-Care Kidney Function Monitoring, ***IEEE Sensors Journal***, 20(17), 9644–9651, 2020.

Patent Publications

1. D. Bandyopadhyay, N. Mandal, and **S. Dutta**, A transmittance-based system/kit for point-of-care quantification of biomarkers sample and use thereof, **US 10,900,909 B2**, 2021.
2. D. Bandyopadhyay, N. Mandal, and **S. Dutta**, A transmittance-based system/kit for point-of-care quantification of biomarkers sample and use thereof, **201631018620 A**, 2016.

Conference Publications

1. **S. Dutta**, P. S. G. Pattader, and D. Bandyopadhyay, Electric Field Mediated Particle Chaining - Experimental and Numerical Investigation, *International Conference on Advanced Nanomaterials and Nanotechnology* (ICANN), Guwahati, India, 18th - 21st December, 2019.
2. **S. Dutta**, P. S. G. Pattader, and D. Bandyopadhyay, Electric Field Induced Instabilities in Viscosity Stratified Miscible Microflows: Transition from Linear Instabilities to Coherent Vortices, *Annual Meeting of the American Physical Society's Division of Fluid Mechanics*, Seattle, USA, 23rd - 26th November, 2019.
3. **S. Dutta**, P. S. G. Pattader, and D. Bandyopadhyay, Electric Field Induced Instabilities in Viscosity Stratified Miscible Microflows: Transition from Linear Instabilities to Coherent Mixing, *Research Conclave*, Guwahati, India, 14th - 17th March, 2019.
4. **S. Dutta**, P. S. G. Pattader, and D. Bandyopadhyay, Electric Field Induced Active Transport of Droplets across Microfluidic Interfaces, *International Conference on Complex Fluids and Soft Matter* (COMFLU), Roorkee, India, 6th - 9th December, 2018.
5. **S. Dutta**, N. Mandal, M. Bhattacharjee, H. Nemade, A. Chattopadhyay, and D. Bandyopadhyay, Paper Based Optical alpha-Amylase Sensor, *International Conference on Translational Nanomedicine* (T-NANO), Ahmedabad, India, 15th - 17th December, 2014.
6. M. Bhattacharjee, N. Mandal, **S. Dutta**, S. Rarotra, H. Nemade, T. K. Mandal, and D. Bandyopadhyay, Controlled Drug Release: Attachment of Drugs with Magnetic Nanoparticles , *International Conference on Translational Nanomedicine* (T-NANO), Ahmedabad, India, 15th - 17th December, 2014.